AALBORG UNIVERSITY
DENMARK

Fracture Mechanics of Concrete

Ulfkjær, Jens Peder

[Link to publication from Aalborg University](#)

INSTITUTTET FOR BYGNINGSTEKNIK
DEPT. OF BUILDING TECHNOLOGY AND STRUCTURAL ENGINEERING
AALBORG UNIVERSITETSCENTER • AUC • AALBORG • DANMARK

JENS PEDER ULFKJÆR
FRACTURE MECHANICS OF CONCRETE
JULY 1992   PH.D. THESIS

FRACTURE MECHANICS OF CONCRETE

Jens Peder Ulfkjær
Department of Building Technology and Structural Engineering
University of Aalborg
Denmark

ACKNOWLEDGEMENTS

1 INTRODUCTION.

1.1 Background and Motives.

In the last two decades the research tool fracture mechanics for concrete has been developed, as it has become clear that the traditionally applied calculation tools (elasticity theory and plasticity theory), not always are applicable of describing certain phenomenons in concrete fracture. The tool has also been applied by material researches developing new ultra strong ductile materials, e.g. Compact Reinforced Composites (CRC).

The compressive strength of concrete has in the same period increased dramatically, and compressive strength over 100 MPa by using conventional techniques has been obtained. The increase in strength is followed by an increase in the brittleness of the materials, and it has been assumed that the conventional techniques do not suffice for these new brittle materials.

One of the most important models which describes the fracture process of concrete in tension is the fictitious crack model developed by Arne Hillerborg and his co-workers at the University of Lund, Sweden. The fictitious crack model is a nonlinear fracture mechanical model, based on observations made in a displacement controlled tensile test.

One of the phenomenons which can be described by using the fictitious crack model, is the well-known size effect on the bending tensile strength. It can also be proved that the brittleness of a structure is dependent on the size of the structure, explaining why large structures are cracking more than small structures.

There are two major problems by using the fictitious crack model. Firstly, that the material parameters which describe the model must be found by performing a stable deformation controlled tensile test, which is almost impossible for high strength concrete. Secondly, that it is almost always necessary to use numerical methods, and only in very special cases are analytical methods developed.

Most of the developed numerical methods are either not stable or are not able to calculate the entire load-displacement curve. The analytical methods are in general very time consuming, not accurate enough or do not describe size effects.

Therefore, it would be welcome if powerful numerical techniques, simple accurate analytical models and indirect methods for determining the constitutive parameters were developed.

1.2 Scope of Thesis.

On the basis the previous scope of this thesis is presented, as a listing of topics.

The main scope of the thesis is:

Development of numerical and analytical fracture mechanical techniques, examination of the applicability of these techniques on high strength concrete structures and to develop indirect methods for determination of the constitutive parameters.

The above scope of the thesis can be divided into the following topics and a list of general limitations.

Topics

- The development of fast numerical methods which are applicable for brittle structures and which can calculate the entire load-displacement curve.

- The development of approximate analytical methods where the calculation time is smaller than that of the numerical methods, and which enables the development of explicit analytical results.

- To develop experimental techniques which can perform stable three-point bending tests

- Perform experiments with high strength concrete in order to investigate size effects and to study the brittleness of the strong material.

- Develop methods for indirect determination of the constitutive parameters in the fictitious crack model.

Limitations.

The following limitations are general in this thesis.

- The compressive strength is assumed to be so large that compressive failure will not occur.

- The fictitious crack model will be used.

- It is in general assumed that the softening relation is piece by piece linear.

6

·   The structure outside the crack is assumed to be modelled satisfactory by linear elasticity theory.

·   In chapter 3-5 only the three-point bending geometry is considered.

1.3 Readers Guide.

In the following it is the intention to give the reader a preliminary overview of the thesis, which enables more selective reading.

After the introduction, chapter 2 is used to give an overview of the factors that governs strength and cracking of normal- and high strength concrete. Models for cracking in concrete are evaluated, and a few examples which illustrates size effects and brittleness in concrete are presented.

The chapters 3-5 are the main body in the thesis.

In chapter 3, different numerical methods which have been developed for use with the fictitious crack model are presented and stability problems by using the models are described and solved.

Chapter 4 is devoted to analytical models which take the softening behaviour of concrete into consideration. Also two models which are developed for lightly reinforced concrete are presented.

In chapter 5 an experimental investigation of 8 different beam geometries of a high strength concrete is presented. Fracture parameters by using different fracture models are presented, and size effects are observed. The numerical method is applied to determine the fracture parameters by curve fitting.

An overall summary and conclusion is given in chapter 6.

At the end of the thesis there are 6 appendixes which contain the list of notation, all the fracture results and the load displacement curves of the performed experiments.

The references in the text can be found in the list of references in the last section of the individual chapters.

2 FRACTURE AND FRACTURE MODELS OF CONCRETE.

After a description of concrete and the fracture process of concrete a review of the most important models which are used to describe concrete fracture will be given. A short presentation of linear elastic fracture mechanics (LEFM) is given with emphasis on terminology and definitions. Four different non-linear elastic fracture mechanical (NLFM) models which are widely accepted are presented. The models are compared and the applicability of each model is evaluated. Finally the terms 'size effect' and 'brittleness' is discussed and different examples and stability problems is examined by using LEFM.

2.1 Fracture of Concrete and High Strength Concrete.

Concrete is a heterogeneous anisotropic non-linear inelastic composite material that consists mainly of cement, aggregates (sand and gravel) and water. In high-strength concrete (here defined as concrete with a compressive strength above 50 MPa) mineral admixtures and water reducing additives are usually present.

Wittmann (1983) suggests to consider concrete on three different levels: the micro-level where the structure of the hydrated cement is considered, the meso-level where large inhomogeneities such as larger aggregates and flaws are taken into consideration and the macro-level where the concrete is assumed to be a homogeneous isotropic continuum. Accordingly cracks are categorized as follows:

Micro cracks :   Cracks that can only be observed by an electron microscope.
Meso cracks :   Cracks that can be observed using a conventional microscope.
Macro cracks :   Cracks that are visible to the naked eye.

Depending on the purpose of the investigation the appropriate level should be chosen. However, it will often be fruitful to develop a model at one level based on observations at a lower level. In practice models which should apply for the practical engineer will be on the macro-level.

In this chapter emphasis will be on subjects related to strength and cracking of concrete. Strength of concrete will mainly depend on the strength and stiffness of the hardened cement

paste, on the strength of the aggregates and on the bonding between the cement paste and the aggregates. The strength of the cement paste and of the aggregates will to a great extent depend on the porosity. This is explained in two different theories: fracture mechanics by Griffith (1921) and the weakest link theory by Weibull (1932). These two theories will be presented in detail later.

The difference between normal strength concrete (NSC) and high strength concrete (HSC) lies in the difference in the microstructure. According to Rice (1977) *"depends strength and fracture in ceramics critically on microstructural extremes rather than on averages"* and according to Mai (1991) *"..but we want to re-emphasize here the need to understand the physical mechanisms of the bridges and the mechanics of crack-bridging. It is such knowledge that teaches us to design better ceramics through the control of micro-structures, such as grain sizes..."*. Thus, in order to understand the fracture process, which is necessary for developing realistic fracture models, and to explain the difference between normal and high strength concrete this presentation starts on the micro-level.

2.1.1 Concrete on the Micro-level.

Each component of concrete will first be described with emphasis on NSC, then HSC will be described under the section mineral admixtures.

Portland Cement.

In the experiments performed in connection with this thesis the Danish low alkali sulphate resistant portland cement certified as PC (A/HS/EA/G)[1] was used.

Cement powder consists of particles with typical sizes of 1-50 μm, see Fig. 2.1:. The specific surface (the blaine) is typically 350 m^2/kg. By increasing the blaine it is possible to obtain high early strength. The long term strength is, however, not affected by the blaine, Swammy (1986).

The solid phases of portland cement consist of four principal minerals: alite (impure tricalcium silicate (C_3S)[2]), belite (impure dicalcium silicate (C_2S)), impure tricalcium aluminate (C_3A) and a ferrite solid solution (tetracalcium alumina ferrite (C_4AF or Fss). When these are mixed with water several chemical processes, called the **hydration process,** start. The outcome of the hydration process is the **hydration products.** The calcium silicates react with water to give calcium silicate hydrates (C-S-H) and calcium hydroxide (C-H). The aluminate and the ferrite phases react with added gypsum (calcium sulfate ($CaSO_4$)) to give

---

[1] According to the Danish code: DS-SBC 227

[2]The customary cement nomenclature is used: Calcium oxide - CaO = C; Silicium oxide - SiO_2 = S; Aluminum oxide - Al_2O_3 = A; Water - H=H_2O;
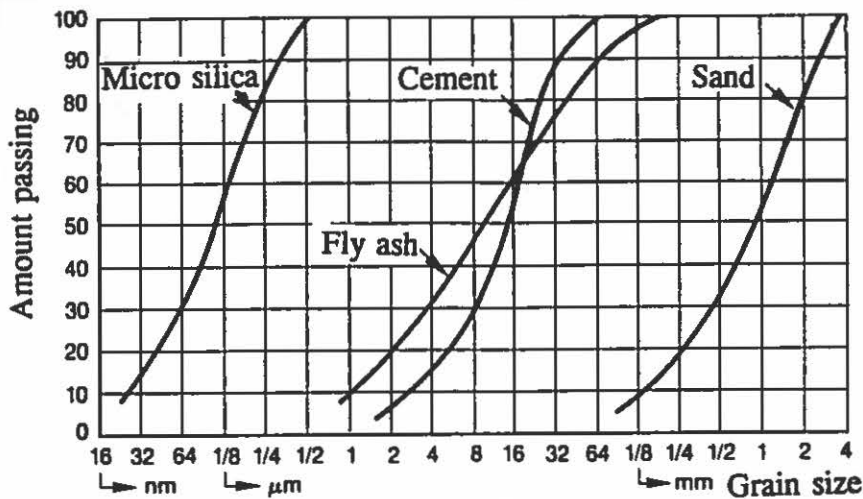
Fig. 2.1: Grain curves for micro silica, fly ash, cement and sand, Herholdt et al. (1985).

two types of products, referred to as AFt (Ettringite) and AFm, see Table 2:. If gypsum is not added the C_3A will almost instantly react with water making the setting time very short, Herholdt et al. (1985).

Clinker mineral	Contents	Hydration products	Morphology
C_3S	58%	C-S-H and C-H	Of C-S-H: Wide range of morphology; Early: Fibrillar or honeycomb structure; Later: More dense
C_2S	24%	C-S-H and C-H	Of C-H: Euhedral hexagonal habit
C_3A	4%	AFt	Hexagonal rods
C_4AF	8%	AFm	Hexagonal plates

Table 2: Constituents of cement.

The C-S-H is the most important component in concrete and together with C-H it controls the strength development and most other macroscopic properties of the hardened cement paste. The other clinker minerals and gypsum are important during cement clinker production, in regulation of setting time and important rheological properties, Skalny and Roberts (1987).

It is in general difficult to follow the hydration process, and especially in the early phases. However, some results can be given of the mechanical details of the microstructural development during hydration by using e.g. the scanning electron microscope (SEM) or the high voltage electron microscope (HVEM). In the HVEM it is possible to install an environmental cell which makes it possible to study the hydration process as early as after 10 min

mixing.

The hydration process is an exothermic reaction, and the overall progress in the hydration process can be studied under adiabatic conditions. The heat development for each clinker mineral is different and is approximately 500 J/g for the cement taken as a whole. However, the **rate-of-heat evolution** curve is, of considerable more interest since it determines the
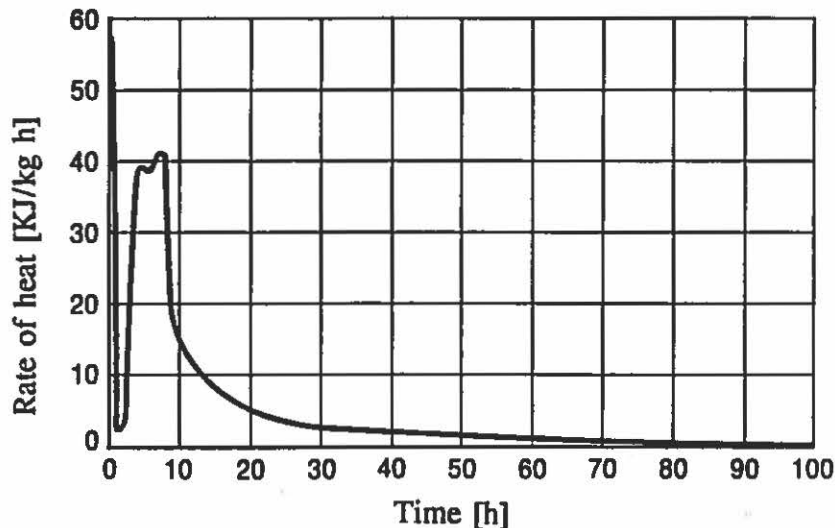
Fig. 2.2:. Rate of heat evolution curve, Herholdt et al. (1985).

temperature and the temperature gradients in the concrete. A typical rate-of-heat curve is seen in Fig. 2.2:.

By referring to the rate-of-heat evolution curve the hydration process can roughly be divided into three phases: early (0-3 hrs), middle (3-24 hrs) and late (beyond 24 hrs). An illustration of the development of the microstructure of a cement grain during hydration is shown in Fig. 2.3: a-e.

In the early phase, termed the induction period, the cement remains fluid and a large amount of heat is developed, see Fig. 2.2:. In Fig. 2.3:a. a typical anhydrous cement corn consisting of C_3S, C_3A and C_4AF is shown. The C_2S is omitted since it basically performs the same processes as (C_3S).

Immediately when the cement surface and the water come in contact the hydration starts. Calcium, aluminates and other ions are released into the solution forming an aluminate and silica rich gel layer, Skalny and Roberts (1987), Scrivener (1989) and Herholdt et al. (1985). As early as after 10 minutes hydration small rods of AFt which have nucleated in the gel, can be observed. At the end of the induction period the reaction of the tricalcium silicate begins which leads to the formation of C-S-H where the rods of AFt have nucleated. That is outside the original boundary of the cement grain which leaves a space of approximately 1 μm between the anhydrous cement grain and the AFt and the C-S-H. These products are

11
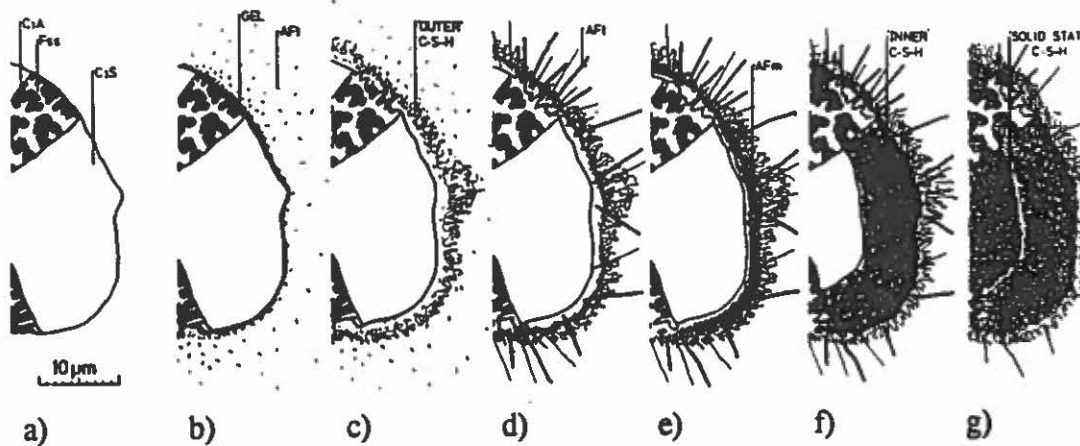
Fig. 2.3: The hydration process. a) unhydrated. b) -10 min. c) -10 hrs. d) -18 hrs. e) 1-3 days. f) -16 days. g) years, Scrivener (1989).

referred to as **the outer product**, Skalny and Roberts (1987) and Mehta and Aïtchen (1990). This mechanism continues with the formation of C-S-H at the outer surface increasing the distance between the core and the shell. After about 16 hrs the AFt rods start to grow again through the shell of C-S-H. At the end of this phase all grains smaller than 5 μm are completely hydrated leaving hollow shells of hydration products, Scrivener (1989). As the shell of hydration products thickens the shell becomes less permeable and will eventually prevent the water transport in the system which ends the second phase.

The subsequent hydration which continues infinitely will then be a slow solid state process decreasing the distance between the core and the shell. These products are often referred to as the **inner products**, Skalny and Roberts (1989), Scrivener (1989) and Mehta and Aïtchen (1990). The hydrated cement grain will thus consist of the porous outer products and the more dense inner products.

This explains why the fracture path will go through the outer products rather than the inner solid products as revealed by SEM studies of fractured surfaces. Thus, the larger amount of inner products that can be achieved the stronger is the cement paste. This is obtained by low water/cement ratios, mineral admixtures and super plasticizer, Mehta and Aïtcin (1990).

Coarse Aggregates.

The strength of the coarse aggregate, usually with maximum sizes up to 64 mm, is controlled

by the amount and sizes of cracks and by the amount of weak minerals. A high quality aggregate is therefore clean, free of clay and silt, well graded and with a high density. Certain types of aggregates have a strengths up to 200 MPa, Mehta and Aïtcin (1990). It is usually assumed that the strength of the aggregates does not have a significant influence on the compressive strength, but as shown by Aïtchen (1990) this is not the case for high-strength concrete. It is therefore evident to use high quality aggregates in high-strength concrete.

Bonding

The final important aspects in concrete strength is the role of the bonding between the cement paste and the aggregates. The aggregates depending on shape, size and surface texture will
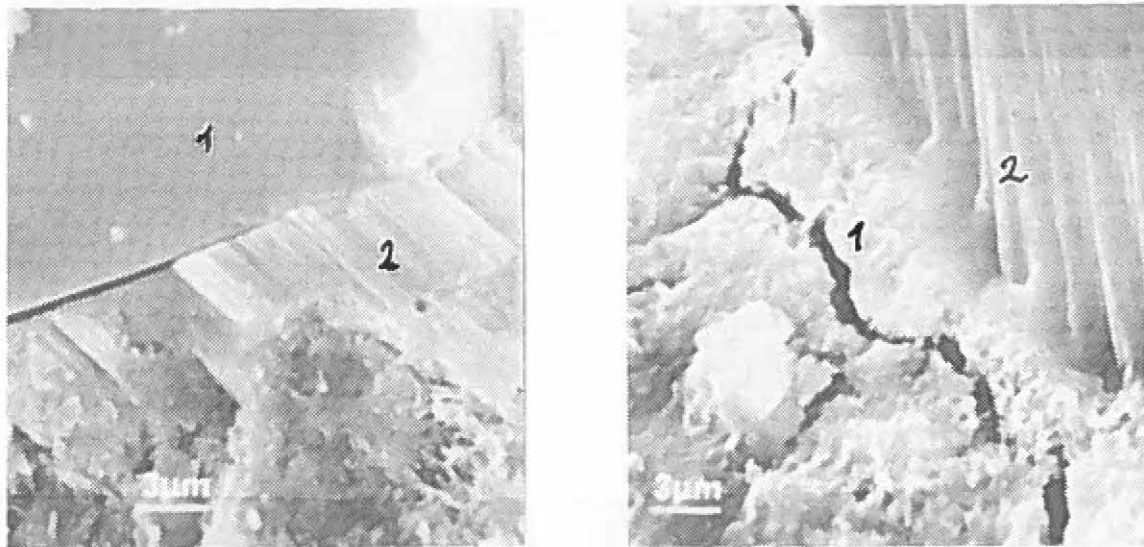
Fig. 2.4: SEM photo of the transition zone. a) (1) Silicious aggregates; crack along edge and (2) oriented C-H crystals. b) (2) Limestone aggregate; crack in cement paste beyond a zone of calcite reaction (1) and $CaSO_3$ crystals, Regourd (1984).

block the water distribution during bleeding. This leads to a locally increased water/cement ratio at the paste aggregate interface. This increase leads to a change of the microstructure next to the aggregates, termed the **transition zone** typical 40-50 μm wide. In addition to larger porosity due to the bleeding there are generally large crystals of C-H in the transition zone with a referenced orientation, Mindess (1989), see Fig. 2.4: and Fig. 2.5:. The weakest zone in the transition zone does not lie at the physical interphase but 5-10 μm away from the aggregate. The fracture will often run in the oriented C-H crystals. It is often assumed that the transition zone only represents a fraction of the entire volume of the concrete. Microscopical investigation by Diamond, Mindess and Integers (1982), has revealed that the mean distance between the aggregates is about 75 - 100 μm which means that most of the hardened cement paste lies in the transition zone. These observations indicate that the strength of the transition zone is of outermost importance in the description of concrete

13
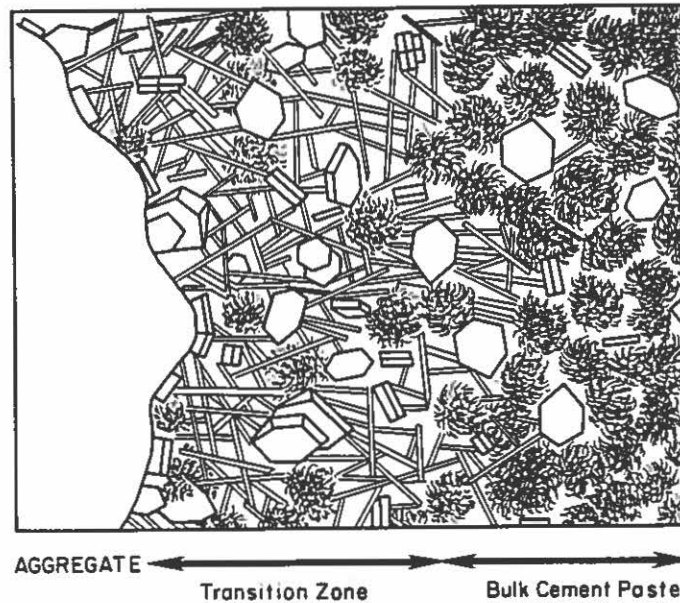
Fig. 2.5: The transition zone between the aggregates and the cement gel, Mehta (1986).

strength.

Mineral Admixtures.

The mineral admixtures are e.g. puzzolans, blast-furnace slag, fly ash and water reducing additives. Puzzulanes e.g. micro silica are extremely fine particles with a size of 20 nm- 500 nm while fly ash have almost the same size distribution as cement, see Fig. 2.1:. The micro silica is added to make the concrete more dense, i.e. it will fill out the voids which are too small for the cement corn and the hydration products, see Fig. 2.6:. Micro silica is not reacting with water but with the hydration product calcium hydroxide, making the hardened cement paste more homogeneous and dense. When micro silica is added the transition zone also changes. The micro silica will react with the oriented C-H which is the weak part of the transition zone, thus the interface between the cement gel and the aggregate is strengthened, Sarkar and Aïtcin (1987).

Since it is very difficult to disperse the small micro silica particles in the cement pastes it will always be necessary to add water reducing additives (WRA), which will increase the workability. The WRA can be categorized into three groups: a) lignosulphonates b) sulphonated melamine-formaldehyde condensates and c) sulphonated naphtalene-formaldehyde condensates. a) is also having a retarding effect and is often referred to as a plasticizer. The groups b) and c) are referred to as super plasticizer due to their low retarding effect which allows an increased dosage, FIP/CEB (1990). A combination of the two types of products will therefore often be used.

14
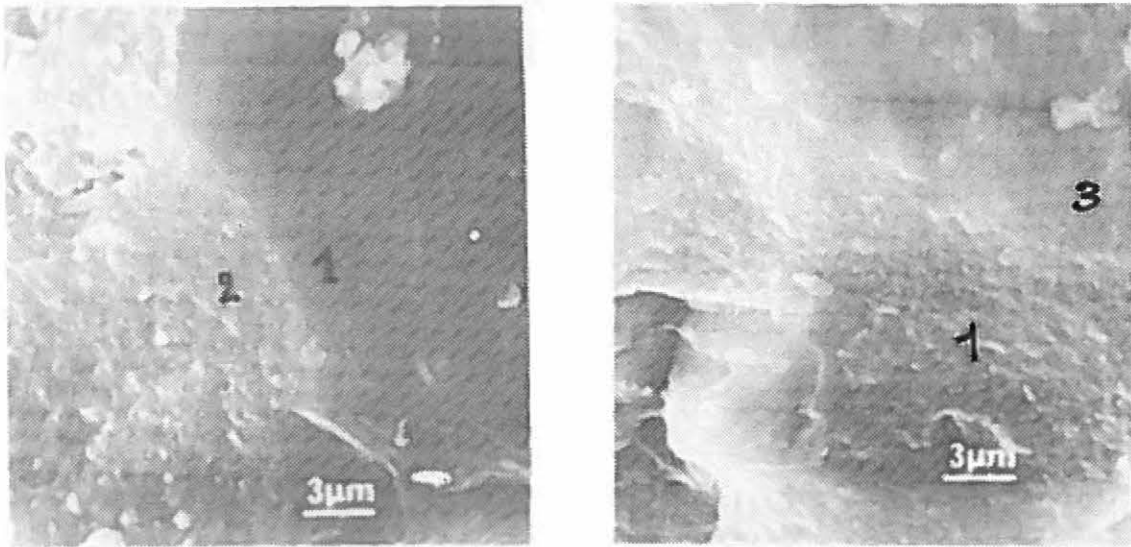
Fig. 2.6: Micro silica concrete. a) Silicious aggregates (1) no crack and no oriented crystals of C-H low porosity and amorphous C-S-H (2). b) Limestone aggregate (3) no crack amorphous C-S-H and calcite reaction (1) some C-H crystals in the matrix, Regourd (1984).

Silica fume and water reducing additives will thus change the microstructure of concrete significantly making the structure more dense, see Fig. 2.6:.

2.1.2 The Fracture Process in Compression.

Depending of the level of the investigation each part of NSC can be thought of as a composite material that consists of stronger particles which are embedded in a weaker matrix, see Table 3:.

Level	Material	Strong Particles	Weak Matrix
Micro	Cement paste	Inner Products	Outer Products
Meso	Mortar	Sand	Cement Paste
Macro	Concrete	Gravel	Mortar

Table 3:. Strong and weak particles classified depending on the considered level.

Consider the stress- strain curves for aggregates, concrete, and cement paste see. Fig. 2.7:. It is observed that the curve for the gravel is almost linear until 95% of the failure load and that the failure is very brittle. The stress-strain curves for the other materials are non-linear. This is probably due to cracking at the different levels.

15
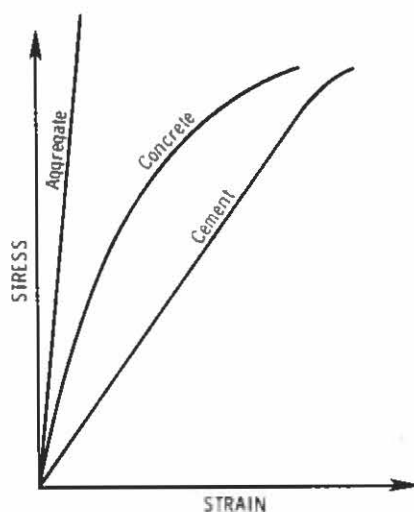
Fig. 2.7: Stress-strain curves for aggregates, concrete and cement paste, Mindess (1983).

The fracture process on the micro-level related to the stress-ss wtrain curve, has as far as the author knows, only been studied for cement paste and mortar, and only by Attiogbe and Darwin (1987). A very large study (150 specimens) of microcracking in cement paste and mortar was made in order to understand the non-linear behavior of those two materials. The examination was performed in a scanning electron microscope with a magnification of 1250 x or 2500 x (cracks with widths below 2.5 μm). They concluded that cracks run through C-S-H and C-H in the cement paste. In the mortar the cracks are also running at the interface between the sand and the cement paste. The result were presented as crack densities at different stages of loading. For both materials it was observed that a substantial amount of cracking was initial cracking. For the cement paste almost 50% of the cracking at failure were initial cracks whereas it was approximately 30% for the mortar. However, during loading the crack densities where growing more rapidly in the mortar than in the cement paste. Whereby they concluded *'Thus, sand particles appear to act as stress raisers that result in a greater degree of softening and of lower strain capacity for mortar than for cement paste'*.

Cracking on the meso-level

Due to the non-linear stress-strain curve for concrete it is beneficial to divide the ascending branch of the stress-strain curve into four regions and the descending branch as suggested by Mindess (1983), see Fig. 2.8:.

This is illustrated by Hsu et al. (1963) who by using microscope and x-ray techniques studied NSC and observed that there initially was a substantial amount of bonding cracks. According to Stroeven (1975) the increase of the specific crack area during loading is increased with 26% which corresponds to 80% of all cracks were initial. These observations are in

16
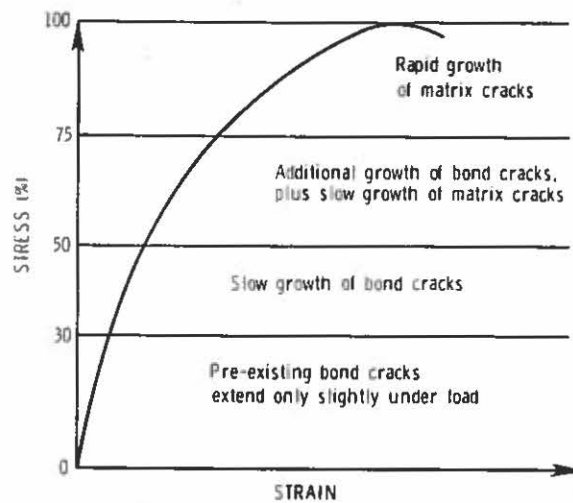
Fig. 2.8: Stress-strain curve for concrete divided into four regions, Ziegeldorf (1983).

accordance with the observation made on the micro-level. These initial cracks are properly due to swelling, shrinkage and bleeding since swelling yields tangential cracks while cracks due to creep are radial, Ziegeldorf (1983).

For loads below app. 30-50% of the ultimate load the stress-strain curve is approximately linear and there is no growth of the initial cracks. Due to crack intensities and the difference in the elasticity modulus between the mortar and the aggregates bonding cracks start to grow making the curve increasingly non-linear. Beyond 50% of the ultimate load cracks start to form in the mortar running between the aggregates parallel with the load direction (indicating tensile cracks). These cracks grow quasi-statically and this type of crack growth is often termed **slow crack growth**. At 75% of the ultimate load a more complex cracking system starts to develop and the cracks in the mortar coalesce with the bonding cracks and finally failure occur.

In HSC the same mechanisms can be observed, Smadi and Slate (1989). It can, however, be concluded:

The amount of cracking is significantly less in HSC than in NSC.
The interfacial cracking is insignificant below 60-70% of the ultimate load for HSC.
Mortar cracking is negligible below 90% of the ultimate load.

By the observations made for HSC it can be concluded that the strengthening of the transition zone limits the amount of bond cracking and the more homogeneous high-strength cement paste is more brittle.

2.1.3 The Fracture Process in Tension.

The tensile strength of concrete is a product of the above observations and the fracture process will thus be dependent on the strength of each link in the cracking process (cracking of the paste, cracking of the aggregates and debonding). In normal strength concrete the cracking process will start as debonding or as crack growth of existing micro cracks in the cement paste at approximately 80% of the peak load, then new cracks will form and some will stop due to stress redistributions and due to crack arrest (cracks stopped by stronger aggregates). These cracks are evenly distributed throughout the specimen. When the peak load is reached a large amount of cracking will **localize** in a narrow zone and eventually the crack that will split the specimen into two will form in that zone. This zone will probably develop in the weakest part of the specimen.

In high strength concrete the weakest part can both be in the aggregates and in the cement paste. If the cement paste and the transition zone are the strongest then crack initiation will probably not start as debonding but instead the crack growth will initiate in the aggregates. After the peak load is reached all cracking will be limited to the zone. By using laser holographic Ansari (1987) confirmed these observations and he further observed that the displacement profile in the narrow zone was varying in a random way.

In the following the fracture process in tension will be described on the macro-level by using a concrete rod as an example. Consider a concrete rod with the length, L subjected to a deformation controlled tensile load, P, see Fig. 2.9: . The strain is measured by the strain gauges A, B, C and D. The strain gauges A,B and C having the length $L/3$ and D has the
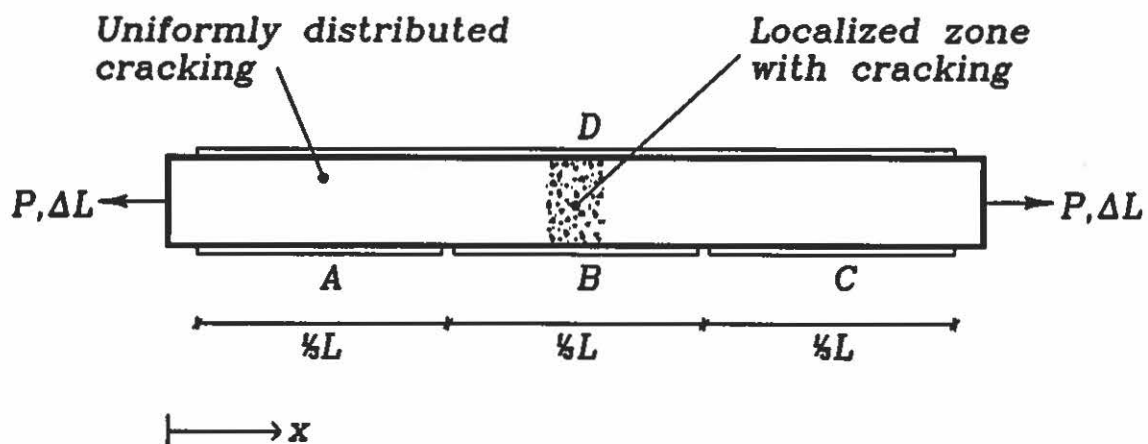
Fig. 2.9: Concrete rod subjected to displacement controlled loading.

same length as the rod. It is now assumed that the crack that eventually will split the rod into two will develop under strain gauge B. The stress-strain curves for the four strain gauge are

shown in Fig. 2.10:. The ascending branch of the four stress-strain curves are identical
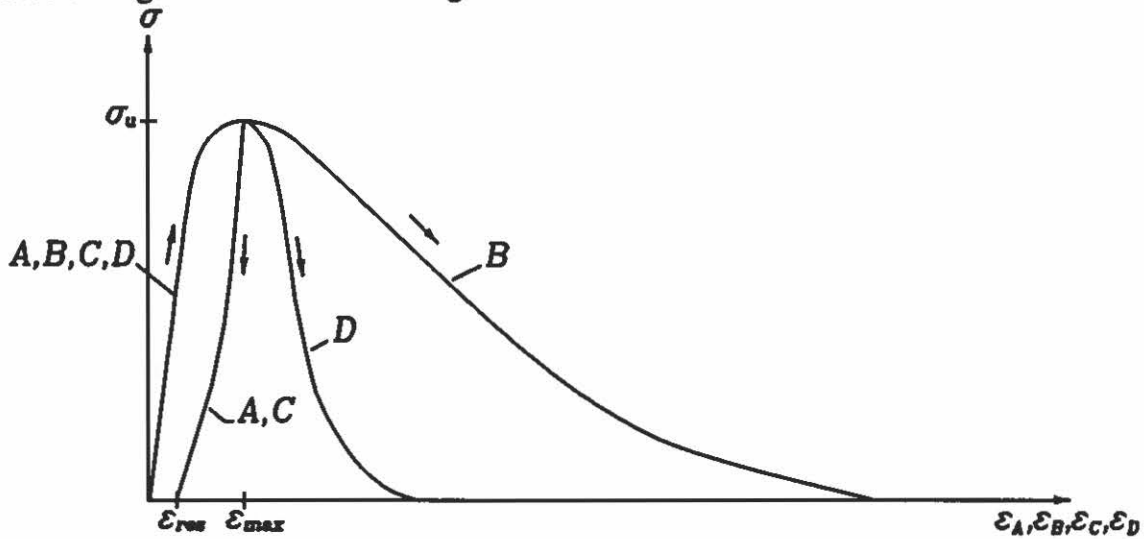
Fig. 2.10: Stress strain curves for the strain gauges A,B,C and D.

whereas the descending branch only is identical for gauges A and C. This will be explained in the following.

The elongation of the rod will in general consist of three contributions: a linear elastic part fully described by the elastic strain, ϵ_e, a non-linear part which is due to uniformly distributed cracking described by the non-linear strain, ϵ_n, and a part which is due to increased cracking in the localized zone, w. The total elongation, ΔL, can then be written

$$\Delta L = \epsilon_e L + \epsilon_n L + w \qquad (2.1)$$

The strain gauge A and C will only measure the two first contributions in eq. (2.1). Strain gauge B and D will measure all three contribution, but since strain gauge D is three times longer than B the last term will be divided by L for gauge D and only $L/3$ for gauges B. Thus, the strain measured by a strain gauge will be dependent on the length of the gauge and of the position on the rod. Each term in eq. (2.1) is shown in Fig. 2.11:.

During cracking energy will dissipate into the specimen. The dissipated energy can be categorized according to eq. (2.1). A certain amount of energy will dissipate more or less uniformly through the whole specimen and is described by the second term in eq. (2.1) the rest will be limited to the narrow zone. The total amount of dissipated energy can then be written

$$E_{disp} = \int_0^L \int_0^{\epsilon_{peak}} f_1(\epsilon_n) A\, d\epsilon_n\, dx + \int_0^L \int_{\epsilon_{peak}}^{\epsilon_{res}} f_2(\epsilon_n) A\, d\epsilon_n\, dx$$

$$+ \int_{narrow\ zone} \int_0^{w_c} f_3(w,x) t\, dw\, dx$$

(2.2)

a)

b)

$$\sigma = \begin{cases} f_1(\epsilon) & \epsilon_{non} < \epsilon_{peak} \\ f_2(\epsilon) & \epsilon_{non} \geq \epsilon_{peak} \end{cases}$$

$$A1 = \int_0^{\epsilon_{peak}} f_1(\epsilon)\, d\epsilon_{non} + \int_{\epsilon_{peak}}^{\epsilon_{res}} f_2(\epsilon)\, d\epsilon_{non}$$

c)

d)

$$E_{disp} = A_1 L + G_F$$
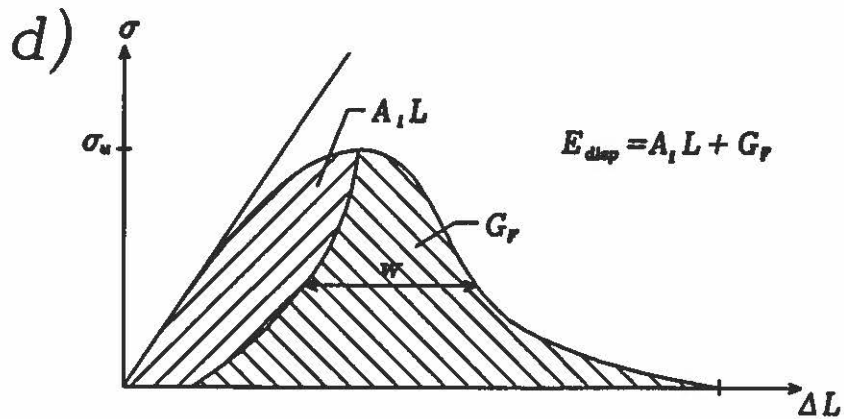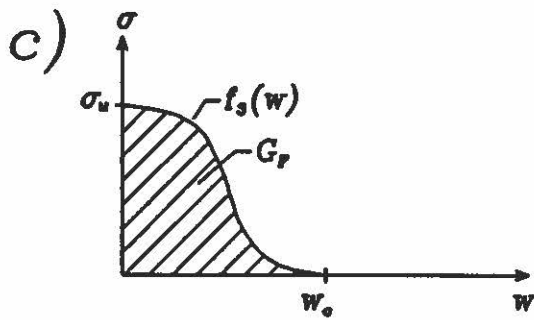
Fig. 2.11: The total elongation of a rod can be divided into three parts. a) linear elastic part b) non-linear in-elastic part and c) localized part. d) the total elongation.

20

where A, is the cross sectional area. Thus, the dissipated energy is dependent on the length of the rod, and of the three material functions $f_1()$, $f_2()$ and $f_3()$ defined in Fig. 2.11:.

An accurate model which describes the fracture behavior of concrete should, therefore, include description of all three contributions in eq. (2.1).

2.2 Linear Elastic Fracture Mechanics.

The basis of linear elastic mechanics originated with the pioneer work by Griffith (1921). Griffith considered glass rods and suggested that fracture in brittle materials arises from small inhomogeneities such as flaws and cracks. These inhomogeneities yield stress concentrations as given by Inglis (1913) and he introduced a parameter, the energy release rate, which is a state parameter related to crack extension. Until a series of catastrophic failures occurred (e.g. the liberty ships, fatigue in aero planes) researchers did not pay much attention to the theory developed by Griffith. The theory was further developed by: Irwin (1957) who introduced the stress intensity factor, Rice (1968) who defined the J-integral, Hutchinson (1968) who took yielding in front of the crack tip into consideration and Freudenthal (1968) who developed probabolistic fracture mechanics. In the following the basic ideas of LEFM will be given.

2.2.1 Basic LEFM.

The theories presented in this chapter is basic linear elastic fracture mechanics and can be found in one of the many text books on this topic e.g. Hellan (1984), Ewalds and Wanhill (1984), Alibadi and Rooke (1991), Gansted and Sørensen (1991).
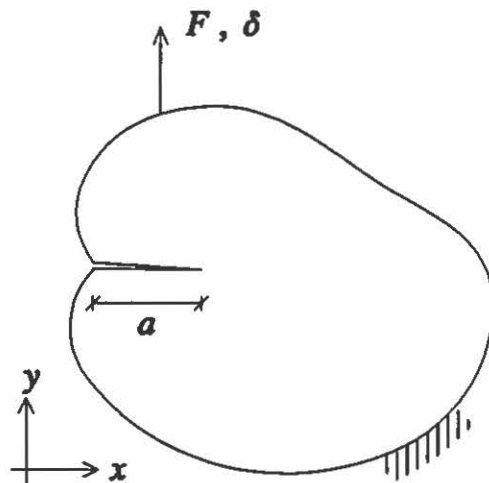
Fig. 2.12:. Arbitrary specimen with an initial crack, energy approach.

Consider a plane arbitrary elastic specimen with the thickness, t, and an initial notch of length, a, which is subjected to a set of boundary conditions and loaded remotely from the crack tip with an arbitrary load, F, see Fig. 2.12:. The total potential energy, Π, in the system is then given by

$$\Pi = \Pi_e + \Pi_F + \Pi_K \qquad (2.3)$$

where, Π_e, is the elastic energy content in the body, Π_F, is the potential of the external forces (body and surface) and, Π_K, is the total kinetic energy in the system. It is now possible to introduce a state parameter termed the energy release rate, G, defined as

$$G = -\frac{\partial \Pi}{t \partial a} \qquad (2.4)$$

The energy release rate is a pure continuum mechanical parameter and is not necessary related to crack growth.

However, if crack growth is considered then eq. (2.3) changes to

$$\Pi = \Pi_e + \Pi_F + \Pi_K + \Pi_c \qquad (2.5)$$

where, Π_c, is the fracture potential, that is the energy that dissipates during crack growth. By assuming that crack growth is only dependent on one parameter, a, the equilibrium condition becomes (the variation of the total potential shall equal zero)

$$\frac{\partial \Pi}{t \partial a} = 0 \qquad (2.6)$$

The fracture criteria can then be written as

$$G = \frac{\partial \Pi_c}{t \partial a} = R \qquad (2.7)$$

22

Where, R, is the **resistance towards crack growth**. In general R is a material, geometry and crack length dependent parameter. In LEFM, R, is assumed to be a material constant termed the **crack driving force**, G_c. The fracture criteria is then written as

$$G = G_c \qquad (2.8)$$

The crack growth is stable if the following stability condition is fulfilled (the second variation of the total potential shall be positive)

$$\frac{\partial G}{\partial a} > \frac{\partial R}{\partial a} = 0 \qquad (2.9)$$

For most structures the energy release rate, G, will be an increasing function as the crack growth, i.e $\frac{\partial G}{\partial a} > 0$.

The above outlined theory, referred to as the energy approach is, however, not adequate as a design tool and instead Irwin (1957) developed the stress intensity factor concept, which is based on stresses rather than on energy considerations.

In general fracture can take place in one of three modes or a combination of these. These modes are opening mode, shear mode and torsion mode. Here only opening mode will be considered.
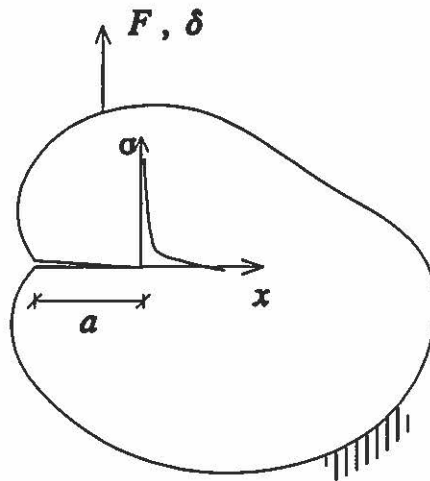
Fig. 2.13:. Arbitrary specimen with an initial crack, stress intensity approach.

Consider the specimen in Fig. 2.13:, according to linear elasticity theory the stress distribution close to the crack tip is described by

$$\sigma_{ij}(\theta,r) = \frac{K}{\sqrt{2\pi r}} \, f_{ij}(\theta) + \text{higher order terms} \qquad (2.10)$$

where, σ_{ij}, is the stress tensor, θ and r are the polar coordinates, f_{ij}, contains trigonometric

functions and, K, is the **stress intensity factor**. As the coordinate, r, approaches zero the first term approaches infinity and the extra terms are constant or tends to zero. Consequently the first term is dominating in the vicinity of the crack tip. Thus, even for infinitely small loads the stresses next to the crack tip will approach zero making a critical stress as failure condition meaningless. Irwin (1957) considered the elastic work necessary to close the crack and derived a relationship between the stress intensity factor and the energy release rate

$$K = \sqrt{GE} \tag{2.11}$$

The relationship relates the crack driving force to a **critical stress intensity factor**, K_c. The fracture criterion can thereby be written as

$$K = K_c \tag{2.12}$$

The critical stress intensity factor is usually termed the **fracture toughness**. The designing engineer is therefore only limited to determine the stress intensity factor and compares it to the critical value in order to establish if the crack growth. The stress intensity factor is often written as

$$K = \sigma\sqrt{\pi a}\, g(\text{geo}) \tag{2.13}$$

where, $g(\text{geo})$, is a dimensionless function of the geometry, which can be determined analytical or numerical e.g. the boundary element method, Alibadi and Rooke (1991).

In order to ascertain if LEFM is applicable for a given material it is then necessary to perform experiments and see if, K_c, is a material parameter. This will only be the case for elastic perfectly brittle materials.

2.2.2 LEFM and Concrete.

Many researchers have studied the applicability of LEFM to concrete and only some of the most important results will be given here, however, reference should be made to Mindess (1983) and Mindess (1986) where an annotated bibliography from 1928-1986 on fracture and cracking of concrete is presented with 595 abstracts.

The first to use LEFM on concrete was Kaplan (1964). He performed three and four point bending experiments on notched beams at different size scales. He found that K_c is a geometry and size dependent parameter. He attributed this 'size effect' to slow crack growth and to shear.

Walsh (1976) and Higgins and Bailey (1976) made experiments with notched beams of concrete and hardened cement paste respectively and they observed that K_c increases with the beam depth. They further concluded that the fracture toughness tends to a constant limiting value as the beam size increases. The same trend was observed by Modéer (1979) for concrete and he suggested that in order to measure a true material parameter the specimen size should be larger than

24

$$d > 10 \left[\frac{K_c}{\sigma_u} \right]^2 \qquad (2.14)$$

where, d, is the beam depth. The condition yields that a beam of NSC should have a beam depth of more than2overc 2-3 m.

Since HSC is considered a more brittle material than NSC, Biolzi and Tognon (1987) and Tognon and Cangiano (1989) made three-point bending experiments with NSC and HSC (Compressive strength from 50 Mpa to 170 Mpa), and they concluded that K_c is increasing with the beam size and with the strength of the concrete. For increasing notch length, K_c increased to a peak value (at notch depth ratio of approximately 0.4) and then decreased.

The reason for the requirement in eq. (2.14) and discrepancies is that a process zone of micro cracking, debonding, crack arrest etc. will develop in front of the crack tip as described in section 2.1.3. If LEFM should be applicable this zone, the **fracture process zone**, should be small compared to the overall beam dimensions. The relative size of the process zone is dependent on the size and geometry of the considered specimen and of the material used. It can therefore be concluded that LEFM is only applicable for large brittle concrete structures such as solid concrete dams or anchor blocs for large span bridges, Planas and Elices (1989).

2.3 Nonlinear Elastic Fracture Mechanics.

Since LEFM is not applicable for laboratory sized specimens several non-linear fracture mechanical models have been developed. The five most accepted models are briefly presented.

2.3.1 The Fictitious Crack Model.

The **Fictitious Crack Model** (FCM) was invented by Hillerborg, Modéer and Petersson (1978) and was formulated by Hillerborg (1977) and Petersson (1980), on the basis of the observations made of a displacement controlled tensile tests as described in section 2.1.3.
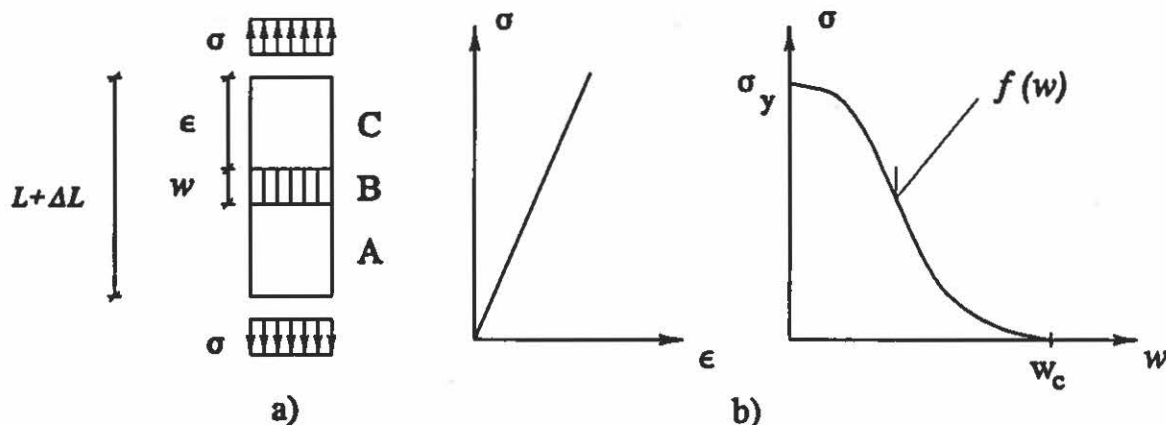
Fig. 2.14: The fictitious crack model. a) simplified rod b) the material function.

Consider the rod in Fig. 2.14: subjected to displacement controlled tensile loading. The rod is divided into three regions A, B and C. Part A and C are assumed to be linear elastic and completely described by the elasticity modulus, E, and Poisons ratio, ν. Before the tensile strength is reached part B is assumed to be infinitely small. When the first principal stress reaches the tensile strength, σ_y, a crack is assumed to develop in part B. The crack is a so-called cohesive crack, Barenblatt (1962), which is able to transfer stresses according to a material function, $f()$, only dependent on the distance between the two uncracked parts. The distance between the two uncracked parts is termed the **crack opening displacement**, w. As the crack opening displacement increases the stress will gradually fall and at some critical opening, w_c, the crack is not able of transferring stress and the specimen will split into two. Since the crack is able to transfer stresses and therefore not a real crack the crack is phrased a **fictitious crack**.

For the FCM eq. (2.1) becomes

$$\Delta L = \frac{\sigma}{E}L + w \qquad (2.15)$$

26

The dissipated energy can thereby according to eq. (2.2) be written as

$$E_{disp} = \int_0^{w_c} f(w)\,dw \qquad (2.16)$$

Since $f()$ is a material function the area under the function must be a material parameter, here termed the **fracture energy**, G_F, Hillerborg (1983).

The FCM is not well suited for analytical solutions and it is only in simple cases possible to derive analytical results. Instead the FCM is used together with numerical methods like the finite element method or the boundary element method, Hillerborg (1976), Petersson (1981), Carpinteri (1989) Brincker and Dahl (1989), Harder (1990).

The greatest problem with the FC-model is that it is extremely difficult to perform a stable displacement controlled uniaxial tensile test of a concrete rod and hitherto experiments have only been made for normal strength concrete.

The first to performed a stable tensile test on NSC, in a very stiff testing machine, where the descending branch is measured was Evans and Marathe (1968). The methods for obtaining the descending branch has become more complex and Gopolaratnam and Shah (1984) performed a large test series in a servo-controlled testing scheme. The most important work seems to have been performed at Delft University of Technology, where many experiments have been performed during the last decade, Reinhardt (1985), Wolinski et al. (1987). Among the problems which has to be overcome are:

- The axial and rotational stiffness of the testing equipment.
- The nucleation of crack growth from one side of the specimen.
- The preparation of the specimens, in order to minimize the above problem.
- Measuring of strains and displacement on the specimens.

If the above mentioned problems is not dealt with the test will either be unstable or an incorrect stress displacement relation is measured, Hillerborg (1989).

2.3.2 The Crack Band Model.

The **Crack Band Model** was invented by Bažant and Oh (1983) and Bažant (1984), and is similar to the FCM. Instead of assuming that all the deformation in the process zone localize into a zone of zero width as in the FCM, Bažant assumes that the deformation will localize into a zone with a width, h_c, which is assumed to be a material parameter (experimental fit seems to yield $h_c = 3d_{max}$ where d_{max} is the maximum size of the aggregates). The softening
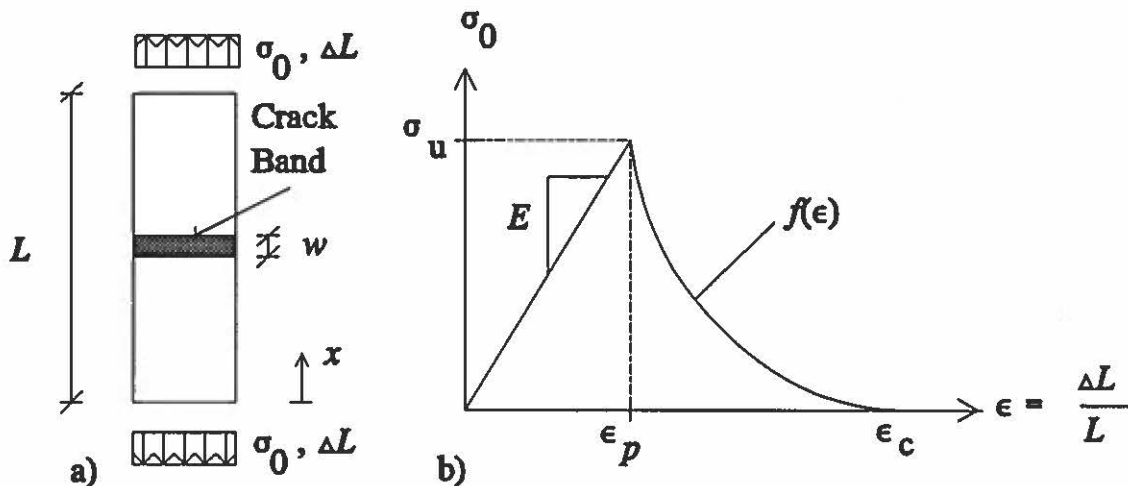
Fig. 2.15: The crack band model a) the simplified rod b) the constitutive relation for the band.

relation can then be formulated as a stress-strain relation instead of a stress - crack opening displacement relation, see Fig. 2.15:.

This leads to some advantages: a) the model is well suited for FEM calculations, b) triaxial effects are easily taken into consideration, c) some analytical solution can be obtained the most well-known is the Size Effect Law, Bazant (1984). The disadvantages are that an extra material parameter is necessary (the width of the process zone).

The dissipated energy can be written as

$$E_{disp} = \int_0^{h_c} \int_0^{\epsilon_c} \sigma(\epsilon)\, bt\, d\epsilon\, dx = \int_0^{h_c} bt g_f dx = G_F \qquad (2.17)$$

where g_f is the volumetric fracture energy, Elices and Llorca (1989).

The 'size effect law' is usually written as (only the first term of a Taylor series expansion is considered)

$$\frac{\sigma}{\sigma_u} = \frac{B_0}{\sqrt{1 + \frac{b}{\lambda_0 d_a}}} \tag{2.18}$$

where σ/σ_u is the normalized failure load, σ_u is the uniaxial tensile strength, d_a is the maximum aggregate size and B_0 and λ_0 are empirical constants usually determined by linear regression from experimental data, Bažant (1983). The size effect law will be considered further in section 2.4

2.3.3 The Two Parameter Model.

The two parameter model was proposed by Jenq and Shah (1986) and is a non-linear model which assumes a crack tip singularity in front of the real crack. The model belongs to a family of models donated cohesive crack models with crack tip singularity, Elfgren (1989).

In this model it is assumed that the peak load is reached when the stress intensity factor of an effective crack (that is the initial crack plus the cohesive crack) and the crack tip opening displacement at the initial crack tip reaches two critical values, $K_{Ic}{}^s$ and $CTOD_c$. The two state parameters K_I^s and $CTOD$ are calculated according to LEFM. It is, however, not possible to measure the $CTOD$ during experiments and instead the crack mouth opening displacement, $CMOD$, is measured. By using the inelastic $CMOD$ at peak load the effective crack length can be found and by using this crack length the two critical state parameters can be obtained.

Several investigations have been made in order to check the applicability of the two parameter model, Karihaloo and Nallathambi (1991), where it is concluded that the fracture toughness is essentially independent of specimen depth and that the variation between 0.93 and 1.53

$MPa\sqrt{m}$ is mainly due to variations in the mix properties. They did not conclude anything about $CTOD_c$, but it is observed that the variation of the $CTOD_c$ is much stronger and that it is not possible to detect a trend in the observed values, however, Brühwiler et al. concluded from wedge splitting tests that $K_{Ic}{}^s$ is size independent but $CTOD_c$ displays a significant size effect ($CTOD_c$ increases with specimen size). This phenomenon can be explained as follows. If the considered specimen outside the crack is assumed to be elastic then the crack tip opening displacement can be written according to the superposition principle

$$CTOD = CTOD_F + CTOD_{co} \tag{2.19}$$

where $CTOD_F$ is the crack tip opening displacement due to the applied load, F, and $CTOD_{co}$ is the crack opening displacement due to the cohesive stresses. In the two parameter model the last term is not taken into consideration, Cotterell and Mai (1987) and it is not always a good approximation to neglect this component. There is also no evidence for the fact that the crack tip opening displacement should take on its critical value at peak load. Actually more detailed analysis using the FC model and the boundary element method shows that the $CTOD$ takes on its critical value after the peak load, Ulfkjær, Krenk and Brincker (1991).

It is therefore concluded that the two parameter model is only a one parameter model where an effective crack length is used as controlling parameter.

2.3.4 The Effective Crack Model.

As in the two Parameter model the effective crack model assumes a sharp crack in front of the real crack as suggested by Nallathambi and Karihaloo (1986). In the effective crack model it is assumed that slow crack growth occurs prior to the peak load and an effective crack length which takes the slow crack and the reduced stiffness into consideration is introduced. The effective crack length is calculated by using the peak load and the deflection at peak load. The effective critical stress intensity factor, K_{Ic}^e is then calculated by using the effective crack length and the peak load, Nallathambi and Karihaloo (1991).

The effective crack model and the two parameter model are thus very similar, it is, however, considerably easier to calculate the effective critical stress intensity factor as described in Nallathambi and Karihaloo (1991).

2.3.5 R-Curves.

Instead of assuming that the resistance, R, is a material property a more general theory which assumes that R is a function of the crack length has been developed. The fracture criterion is then written as

$$G = R(a) \qquad (2.20)$$

and the stability condition becomes

$$\frac{\partial G}{\partial a} < \frac{\partial R(a)}{\partial a} \qquad (2.21)$$

The basic assumption is then that $R(a)$ is a material function independent of size and geometry.
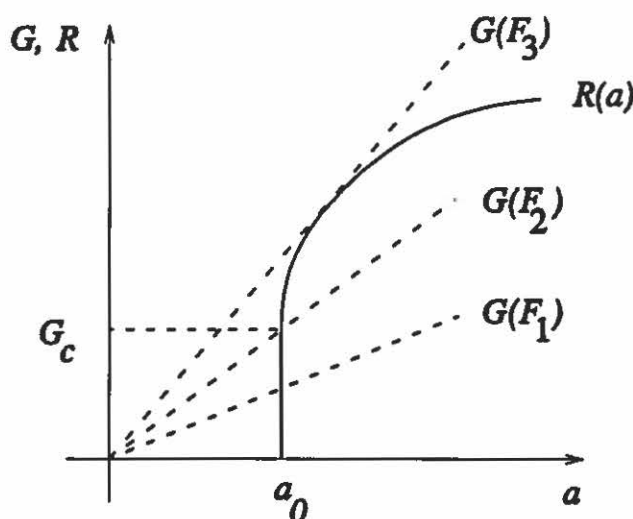
Fig. 2.16: R-curve for a specific material and initial crack length.

A correlation between the FC-model and the R-curve concept can be made. Consider an

30

arbitrary specimen without an initial notch. According to the FC-model a fictitious crack will develop when the first principal stress reaches the tensile strength. By increasing the loading the fictitious crack will grow and eventually the real crack will start to grow, see Fig. 2.17:. If the R-curve concept should be applied it is necessary to introduce an effective crack length, a_{ef}, generally defined as, Hellan (1984)
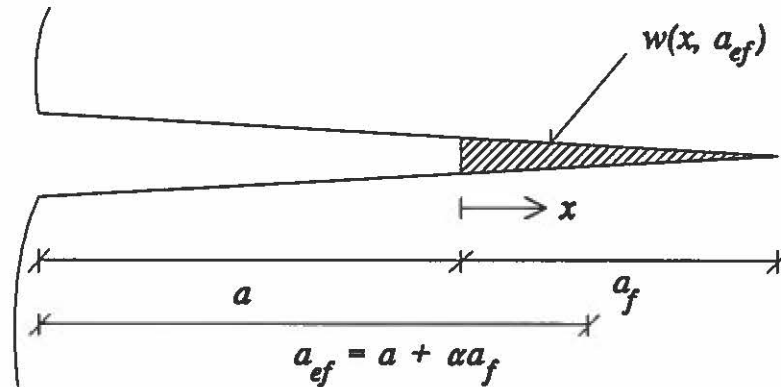
Fig. 2.17: Fictitious crack with an effective crack length.

$$a_{ef} = a + \alpha a_f \qquad \alpha \in \,]0\,;1] \qquad (2.22)$$

the dissipated energy during crack growth can then be written as

$$E_{disp} = G_F t(a_{ef} - \alpha a_f) + \int_0^{\frac{1}{\alpha}(a - a_{ef})} \varphi(x, a_{ef})\,dx \qquad (2.23)$$

where $\varphi(x, a_{ef})$ is the energy density in the fictitious crack, Brincker (1991), determined by

$$\varphi(x, a_{ef}) = \int_0^{w(x, a_{ef})} \sigma(u)\,du \qquad (2.24)$$

where $w(x, a_{ef})$ is the crack opening profile which is dependent on the size and the geometry of the considered structure. According to eq. (2.7) the resistance towards crack growth becomes

$$R = \frac{\partial E_{disp}}{\partial a_{ef}} = G_F t (1 - \alpha \frac{\partial a_f}{\partial a_{ef}}) + \varphi (\frac{1}{\alpha}(a_{ef} - a), a_{ef}) \frac{1}{\alpha}$$

$$\int_{0}^{\frac{1}{\alpha}(a_{ef} - a)} \frac{\partial \varphi (x, a_{ef})}{\partial a_{ef}} dx$$

(2.25)

since the second term is always zero eq. (2.25) becomes

$$R = \frac{1}{\alpha} G_F + \int_{0}^{\frac{1}{\alpha}(a_{ef} - a)} \frac{\partial \varphi (x, a_{ef})}{\partial a_{ef}} dx$$

(2.26)

Thus, a complicated relation exists between the FC-model and the R-curve concept revealing the fracture resistance is dependent on the size and geometry of the considered structure. It is also obvious from eq. (2.26) that the R-curve is strongly dependent on how the parameter, α, is chosen. It was shown by Brincker (1990) that if the crack profile and the stress-crack opening displacement are chosen to be linear then the R-curve will be a parable.

Similar considerations to the above have also been made by Mai (1991) but his approach seems to fail since he does not take crack growth and the fictitious crack length into consideration.

Several researchers have made experiments in order to detect if concrete has an R-curve behavior, Wecharatana and Shah (1982), Wecharatana and Shah (1983), Bažant and Cedolin (1984) and Bažant et al. (1986).

Wecharatana and Shah (1982) concluded that the R-curves seem to depend on the size and geometry of the concrete specimens considered and attributed this effect to the large process zone. Bažant concluded the same by using a linear crack band model. It seems, however, that by introducing an equivalent crack length this dependency is not very strong and he concluded that if a rough estimation of the load carrying capacity is needed R-curves seem to be suitable.

2.4 Brittleness and Size Effect.

Size effect is a term which is used more or less stringent by different researchers. The common interpretation of the word is that an assumed material parameter is not constant but is varying with the size of the structure. The author feels, however, that the word is rather misleading, since the word does not describe the problem which in reality is that for some reason the model used is not accurate enough. Therefore size effects are always related to models. Thus, an observed size effect in one model can completely disappear in another more accurate model. The problem will be further illustrated by considering the three-point bending geometry.

The usual assumption is that the beam is a Bernoulli beam with the assumption that the tensile strength (or modulus of rupture) is a material property. This is, however, a poor model since experiments show that the bending tensile strength is decreasing as the size of the beam increases, Reagel and Willis (1931).

The results of a large test series performed in USA, by the American Association of State Highway Officials, Reagal and Willis (1931), are here briefly reported for the dimensions which are similar to those used in the present investigation, see chapter 5.

The experiments were performed at four different laboratories in USA, and consisted of 64 different beam geometries, and a total of 768 beams of plain NSC were tested.
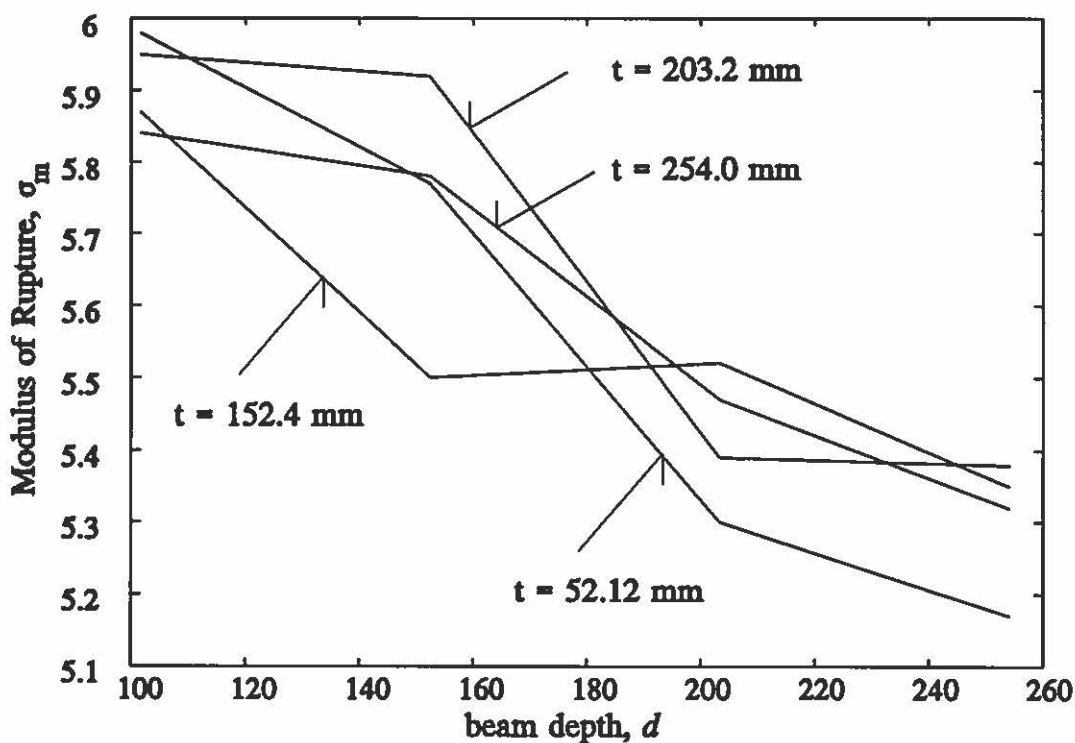
Fig. 2.18: Modulus of rupture for varying values of the beam depth, d, and thickness, t, and span equal to 762 mm, Willis and Reagel (1931).

The modulus of rupture, σ_m, was calculated from

$$\sigma_m = \frac{l(F_{max} + 3/4W)}{td^2} \qquad (2.27)$$

where, W, is the weight of the beam and , F_{max} is the peak load. The factor 3/4 on the beam weight is a mystery to the author, who expected it to be 1/2. The factor 3/4 will yield a smaller size effect than the factor 1/2. This discrepancy will in the following be ignored. The experiments performed were under high control and the coefficent of variation of the individual

33

test varied between 2% and 5.% for the considered beam dimension, and the variation between each laboratory was between 2% and 7%.

The test results for the beam with the length 762 mm are presented in Fig. 2.18:. It is seen that the modulus of rupture is decreasing with the beam depth for all beam thicknesses, and the decreasing by doubling the beam depth is 9% for the thicknesses 101.6 mm and 6% for the other thicknesses. It is also seen that the modulus of rupture is almost independent of the beam thickness.

This suggests that the Weibull size effect importance or that another cause for size effect is interacting when the beam thickness is increased, e.g. the crack profile is changing.
This size effect is known for many brittle materials and is usually explained by the Weibull effect, Weibull (1939) and Weibull (1951). The Weibull effect is based on the weakest link concept and on the assumption that the material is perfectly brittle. The mean value of the strength, R, can be expressed for homogeneous stress distributions as:

$$E[R]=x_0+x_c\Gamma\left[1+\frac{1}{k}\right]\left(\frac{V}{V_0}\right)^{-\frac{1}{k}}$$

(2.28)

where x_0 is the lower strength limit, V is the volume of the structure V_0 is a reference volume, and x_c and k are positive constants. For concrete Zech and Wittman (1977) found that $k=12$. For the considered beam (2.28) becomes for $x_0=0$:

$$E[R]=x_c\Gamma\left[1+\frac{1}{k}\right]\left[\frac{V}{V_0}\frac{1}{2(k+1)^2}\right]^{-\frac{1}{k}}$$

(2.29)

It is seen that it is only the volume and not the geometry of the beam which determine the size effect.

By using linear elastic fracture mechanics, which is a better model than the Bernoulli model, it is possible to predict a strong size effect of the form:

$$\sigma_C=\frac{K_c}{d^{1/2}}\sqrt{\frac{2}{\pi\alpha}}g(geo)$$

(2.30)

where σ_C is the failure stress, K_c is the fracture toughness, α is the normalized crack length, and d is a characteristic dimension of the structure e.g. the beam height. Yet, numerous experiments have shown that the fracture toughness is not constant when the size of the structure is changed, still a size effect, and LEFM should therefore be used with care on concrete.

In 1977 Hillerborg and co-workers showed that concrete is not a perfectly brittle material. This 'non-brittle' behaviour is due to the existence of a cohesive zone in the front of the crack tip, and can be described with a model called the fictitious crack model (FC-model). The FC-model gives a better description of the physical reality of crack growth, and by using the FC-model the modulus of rupture is size dependent.

34

One of the basic assumptions regarding the FC-model and the crack band model is that the fracture energy G_F is a material property. However, the fracture energy measured using the RILEM method displays a significant increase with beam size (the third type of size effect), Hillerborg (1985). This size effect is usually attributed to the fact that in the FC-model the energy dissipation in the bulk region has not been taken into consideration, Elices and Planas (1988).

By using dye technic Swartz (1989) showed that the crack profile is not a straight line, but is rather U-shaped. This could indicate that the strength of the concrete is lower near the surface of the specimen. If the size of this weak zone is independent of the specimen size then another cause for size effects is found.

In the following a few examples will be given which further illustrates the terms 'brittleness' and 'size effects'.

2.4.1 Example I. Size effect of plate made of a perfectly brittle/perfectly ductile material.

Consider a large plate of width $2b$ with an initial crack of length $2a$. The plate is subjected to the load σ_0 at the edges, see Fig. 2.19:. The plate is made of a material with the yield strength, σ_u,
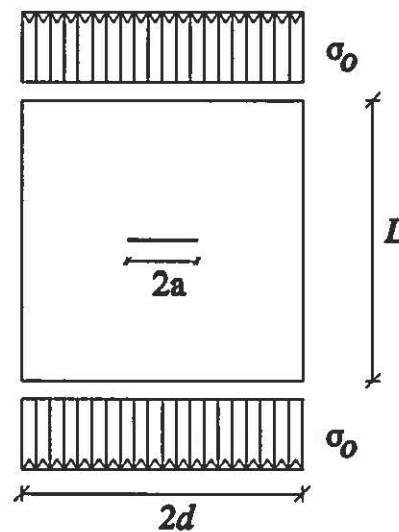
Fig. 2.19: Plate with center crack.

and with the fracture toughness, K_c. The purpose of this example is to investigate which of the two failure possibilities will occur depending on the size and geometry of the beam.

Yielding will occur in the two parts next to the crack when

$$\frac{\sigma_0}{\sigma_y} = 1 - \frac{a}{d} \qquad (2.31)$$

If the width of the beam is assumed to be much larger than the initial crack length, then the stress intensity factor can be written as

35

$$K = \sigma_0 \sqrt{\pi a} \qquad (2.32)$$

Crack propagation occurs when $K = K_c$, viz

$$\frac{\sigma_0}{\sigma_y} = \frac{K_c}{\sigma_y} \frac{1}{\sqrt{\pi \frac{a}{d}}} \frac{1}{\sqrt{d}} \qquad (2.33)$$

When similar plates are considered (e.g. $a/b = kst.$, $K_c = kst.$ and $\sigma_y = kst$) at different size scales as shown in Fig. 2.20:., then it is seen that the yielding criterion eq.(2.32) is independent of the
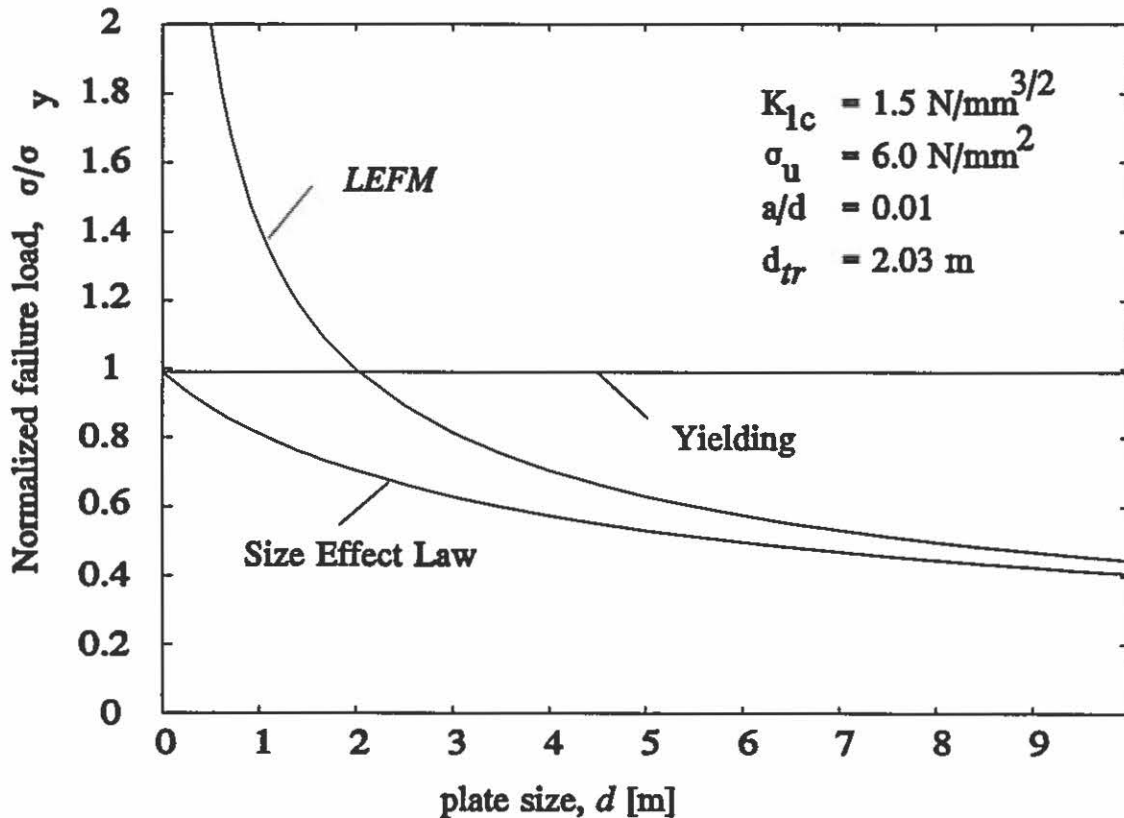
Fig. 2.20: The yielding criteria, the fracture criteria and the size effect law for the considered plate.

size scale, d, whereas the crack propagation criterion eq. (2.33) decreases rapidly with the size scale. Thus, for small sizes the plate will fail due to yielding and for large plates it will fail due to crack propagation. The transition, d_{tr}, between the two types of failure is determined by setting eq. (2.32) equal to eq. (2.33)

$$d_{tr} = \left(\frac{K_c}{\sigma_y} \right)^2 \frac{1}{\pi \frac{a}{d} \left(1 - \frac{a}{d} \right)^2} \qquad (2.34)$$

If the tensile strength is determined with such a plate then the tensile strength will be dependent on the size of the plate if the size of the beam is larger than d_{tr}, and the tensile strength is calculated according to the yielding criterion. On the other hand if fracture toughness is determined for plate sizes smaller than d_{tr} then K_c is also dependent on the beam size. These

36

phenomenons are often termed 'size effect' since an assumed material parameter is dependent on the size of the specimen. Since concrete is not a perfectly brittle material it is necessary to use huge specimens if the fracture toughness should be determined as a material parameter.

Consider now the size effect law in eq. (2.18). As the size, d, approaches zero the denominator approaches one and the normalized failure load approaches, B. As the size approach infinity the one in the square root becomes insignificant and the normalized failure becomes a function of $b^{-1/2}$. Thus, by making proper adjustment of the two constants B_0 and λ_0 the size effect law describes the two failure possibilities as limiting cases. This is done by setting

$$B = 1 - \frac{a}{d} \qquad (2.35)$$

and

$$\lambda_0 = \frac{1}{d_a}\left(\frac{K_c}{\sigma_y}\right)^2 \frac{1}{\pi\frac{a}{d}(1-\frac{a}{d})^2} = \frac{d_{tr}}{d_a} \qquad (2.36)$$

whereby the size effect law becomes

$$\frac{\sigma}{\sigma_y} = \frac{1-\frac{a}{d}}{\sqrt{1+\frac{d}{d_{tr}}}} \qquad (2.37)$$

Fig. 2.21: Load carrying capacity of plate in log-log scale.

37

The size effect law together with the yielding criterion and the fracture criterion are shown in Fig. 2.20:. Since the crack propagation criterion in loglog scale becomes a straight line with a slope of 0.5 it is common to display the failure criteria in loglog scale, see Fig. 2.21:, L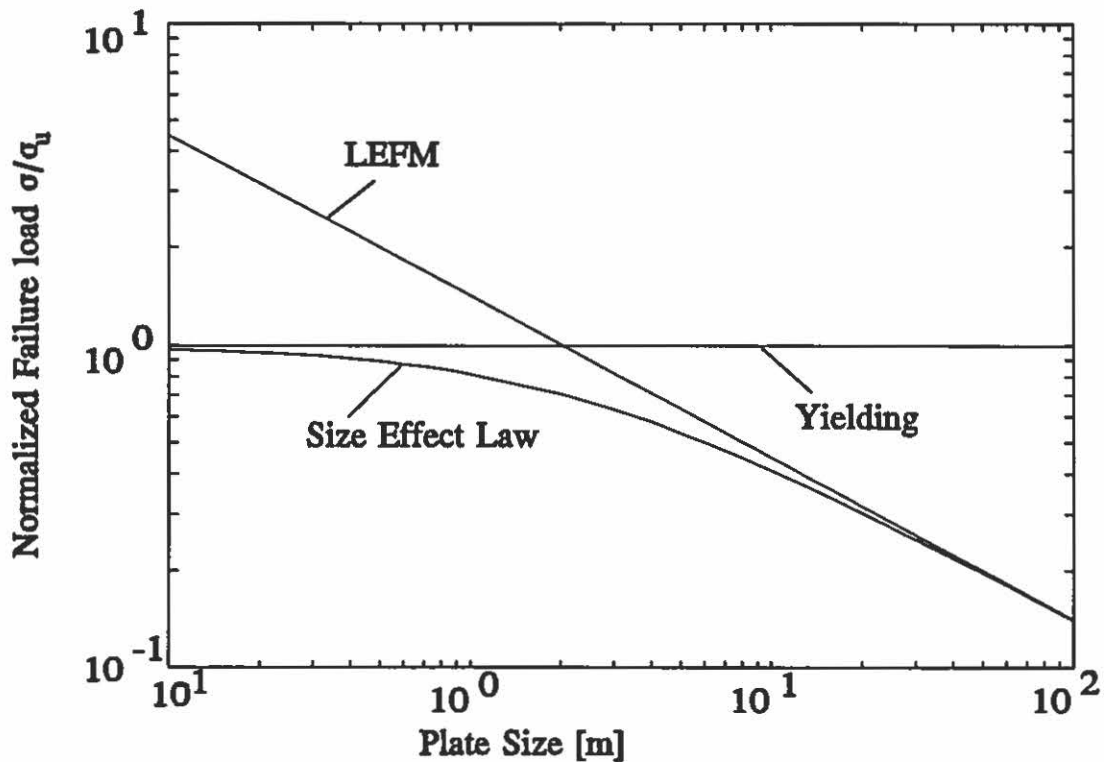eicester (1973), which makes it obvious that the Size Effect Law describes a gradual transition from the yielding criteria to the crack propagation criteria. It should, however, be emphasized that the Crack Band Model and the Fictitious Crack model would not predict any size effect in this example and the Size Effect Law is therefore only used as mathematical expression which makes the above mentioned transition.

In the example with a plate it was seen that the transition size of the plate, d_{tr}, plays a dominant role. In general plastic, elastic or visco elastic failure criteria can be written as a dimensionless function of the geometry

$$\frac{\sigma}{\sigma_y} = g_1(\text{geo}) \tag{2.38}$$

and the failure criterion for crack propagation, eq (2.8), can be rewritten as

$$\frac{\sigma}{\sigma_y} = \frac{K_c\, g(\text{geo})}{\sigma_y} \frac{1}{\sqrt{\pi \frac{a}{d}}} \frac{1}{\sqrt{d}} \tag{2.39}$$

whereby the transition size becomes

$$d_{tr} = \left[\frac{K_c}{\sigma_y} \right]^2 \frac{1}{\pi \frac{a}{d}} \left[\frac{g(\text{geo})}{g_1(\text{geo})} \right]^2 \tag{2.40}$$

and the Size Effect Law can be written as

$$\frac{\sigma}{\sigma_u} = \frac{g_1(\text{geo})}{\sqrt{1 + \frac{d}{d_{tr}}}} \tag{2.41}$$

Thus, for small ratios of $\beta_1 = d/d_{tr}$, the behavior of the structure is ductile, for large β_1 the behavior becomes more brittle, making β_1 a brittleness number. The most commonly used brittleness number is defined as the ratio between the elastic energy and the fracture energy

$$B = \frac{\text{elastic energy}}{\text{fracture energy}} = \frac{L^3 \frac{\sigma_y^2}{E}}{L^2 G_F} = \frac{L\sigma_y^2}{E G_F} \tag{2.42}$$

where L is the characteristic dimension of the structure and σ_u^2/E is the stored elastic energy at failure for a unit volume and G_F is the fracture energy, Elfgren (1989). If the relation $K_c = \sqrt{E G_F}$ is used it is seen that B is a special case of β_1 where the geometry of the structure is not taken into consideration, but only the size described by, L.

As it is seen from the previous examples the term brittleness is a word which is easy to

misinterpret. It has been common to understand brittleness as related to a material property, or to the shape of the load-displacement curve, and as was seen, is brittleness affected by the size and geometry of the considered structure, which again was reflected in the two introduced brittleness numbers. In the following brittleness will be considered on the basis of a concrete rod. A material brittleness is introduced and structural brittleness based on observations of the descending branch of the load displacement curve is defined, finally a third kind of size effect is introduced.

2.4.2 Example II. Brittleness and stability of concrete rod.

During crack growth energy will dissipate as previously described. The dissipated energy can be divided into two contributions

$$G = G_s + G_v \qquad (2.43)$$

where, G_v, is the volume dissipation and G_s is the surface dissipation during crack growth. A material brittleness can then be defined as, Brincker (1990),

$$\beta_M = \frac{G_s}{G_v} \qquad \beta_M \in [\,0\,;\,\infty\,[\qquad (2.44)$$

Structural brittleness is defined by considering the load displacement curve of a rod made of a material which behaves according to the fictitious crack model. Consider an initial uncracked concrete rod with the length, L, and the cross section, A, subjected to a displacement controlled load, F, and the corresponding displacement, u. The elastic properties are described by the elasticity modulus, E, and the softening relation is described by, $f(w)$, see Fig. 2.14:. The total potential energy in the system is given by

$$\Pi = \frac{1}{2}\frac{AE}{L}(u-w)^2 + A\int_0^w f(v)dv \qquad (2.45)$$

Equilibrium is obtained for

$$\frac{\partial \Pi}{\partial w} = \frac{AE}{L}(w-u) + Af(w) \qquad (2.46)$$

And stability is obtained through the following condition

$$\frac{\partial^2 \Pi}{\partial w^2} = \frac{\partial f(w)}{\partial w} + \frac{AE}{L} > 0 \qquad \Rightarrow$$

$$\frac{\partial f(w)}{\partial w} < \frac{AE}{L} \qquad (2.47)$$

which corresponds to infinitely slope on the descending branch of the load displacement curve. A brittleness number which includes the slope of the descending branch seems, thus, appropriate. The load displacement for the considered rod is as sketched in Fig. 2.11:. The slope on the descending branch is given by

$$\frac{\partial \sigma}{\partial \delta} = \frac{1}{\dfrac{\partial u}{\partial \sigma} + \dfrac{\partial w}{\partial \sigma}}$$

$$= \frac{1}{\dfrac{L}{E} + \dfrac{\partial w}{\partial f}} \qquad (2.48)$$

which becomes for a linear softening relation

$$\frac{\partial \sigma}{\partial \delta} = \frac{\sigma_u L - E w_c}{E \sigma_u} \qquad (2.49)$$

The advantages with this brittleness number is that it is related to a specific behavior of the load displacement curve. The disadvantages are that it is difficult to calculate, it is not dimensionless and it is not defined for all structures.

2.4.3 Example III. Stability and brittleness of glued beam.
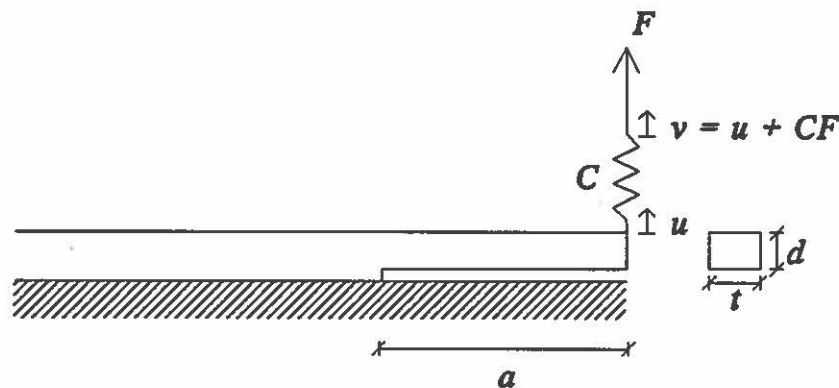
Fig. 2.22: Beam glued to an infinitely rigid foundation, subjected to deformation controlled load.

The purpose of this example is to illustrate how the stiffness of the testing machine affects the stability of the fracture process in a displacement controlled experiment. The example further illustrates the necessity in measuring the true displacement of the structure.

Consider a beam glued to an infinitely rigid support as shown in Fig. 2.22:. An initial crack with the length, a, much larger than the beam depth, b, is assumed to exist. The beam is subjected to a displacement controlled load, v. Between the load point and the beam a spring with the compliance, C, is inserted, modelling the flexibility of the testing machine. During testing the opening of the crack, u, is measured. The purpose of this example is to investigate how the flexibility of the testing machine influences the stability of the test.

Since the test is deformation controlled the potential of the load is zero and the total potential of the system becomes

$$\Pi = \frac{1}{2}uF + \frac{1}{2}CF^2 \qquad (2.50)$$

If the beam is assumed to be a Bernoulli beam the displacement becomes

$$u = \frac{1}{3}\frac{Fa^3}{EI} \tag{2.51}$$

and the energy release rate becomes

$$G = -\frac{\partial \Pi}{t\partial a} = \frac{1}{2}\frac{a^2F^2}{EIt} \tag{2.52}$$

The crack will extend when $G=G_c$ and the corresponding critical load becomes

$$F_c = \frac{\sqrt{2G_c tEI}}{a} \tag{2.53}$$

the corresponding displacement is

$$v = \left[\frac{1}{3}\frac{a^3}{EI}+C\right]F_c \tag{2.54}$$

If the fracture process shall be stable $\partial v/\partial a > 0$ yielding the following condition to the compliance of the testing machine

$$C < \frac{2}{3}\frac{a^3}{EI} \tag{2.55}$$

A set of load displacement curves for different compliances is shown in Fig. 2.23: where the controlling parameter is u (virtual crack propagation). It is seen that even in displacement controlled testing the fracture process becomes unstable for too flexible testing machines. Instead it is necessary to perform experiments where the crack opening is the controlling parameter, if the descending branch of the load displacement curve is requested. This can only be done in a closed loop servo controlled testing system, Brown and Hudson (1972).

2.5 References for Chapter 2.

Alibadi, M.H. and Rooke, D.P. (1991), Numerical Fracture Mechanics, *Kluwer Academic Publishers*, Dordrecht, The Netherlands.

Ansari, Farhad (1987), Stress-Strain Response of Micro cracked Concrete in Direct Tension, *ACI Materials Journal*, Nov-Dec 1987, pp. 481-490.

Aïtcin, P.C. (1990), Effect of Coarse-Aggregate Characteristics on Mechanical Properties of High-Strength Concrete, *ACI Materials Journal*, V. 87, No. 2, pp. 103-107.

Attiogbe, K.E. and Darwin D. (1987), Submicrocracking in Cement Paste and Mortar, *ACI Materials Journal*, Nov-Dec 1987, pp. 491-500.

Barenblatt, G.I. (1962), The mathematical theory of equilibrium cracks in brittle fracture,
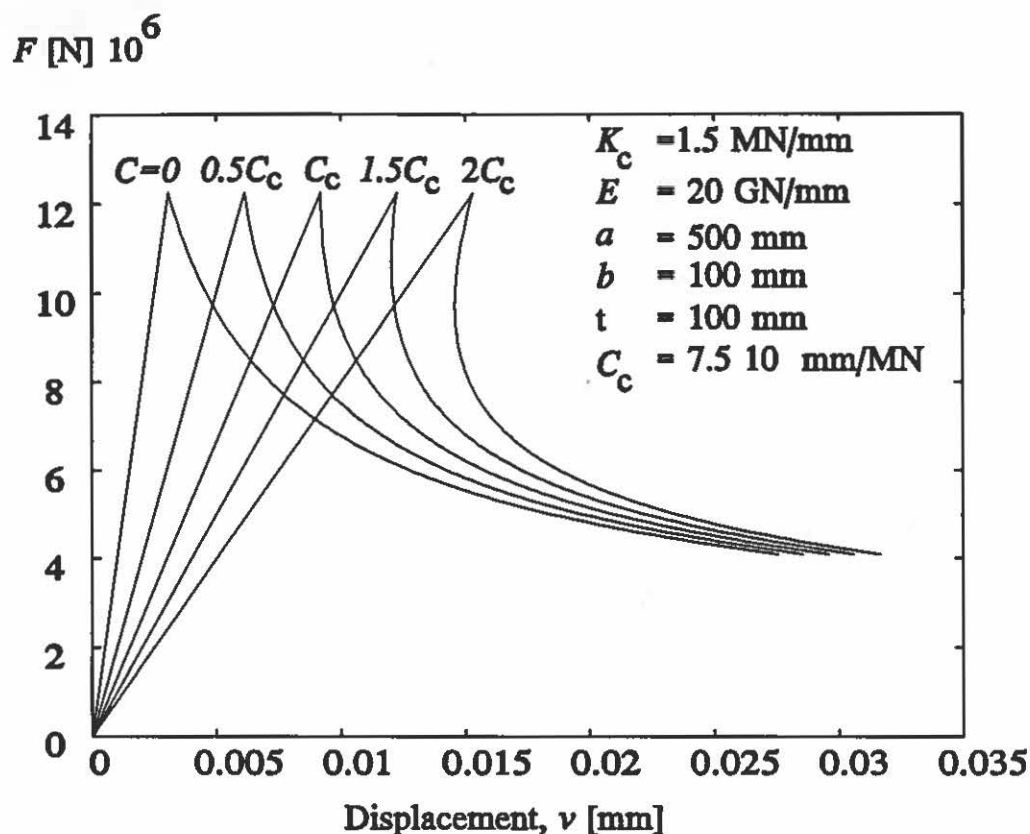
Fig. 2.23: Load displacement curves for the glued beam when the compliance of the spring is varied.

Advances in Applied Mechanics, 7, pp. 55-129.

Bažant, Z.P. and Oh, B.H. (1983), Crack Band Theory for Fracture of Concrete, *Materials and Structures*, Vol. 16, No. 93, pp. 155-177.

Bažant, Z.P. (1984), Size Effect in Blunt Fracture: Concrete, Rock, Metal, *Journal of Engineering Mechanics*, ASCE, Vol. 110, pp. 518-535.

Bažant, Z.P. and Cedolin, L. (1984), Approximate Linear Analysis of Concrete Fracture By R-Curves, *Journal of Structural Engineering*, ASCE, Vol 110, pp. 1336-1355

Bažant, Z,P, Kim J.K. and Pfeiffer, P.A. (1986), Non-linear Fracture Properties from Size Effect Tests, *Journal of Structural Engineering, ASCE*,Vol. 112, No. 2, pp. 289-307.

Biolzi, L. and Tognon,G. (1987), On the Fracture Mechanics of High and Very High Strength Concrete, *Il Cemento*, 3, pp. 251-259.

Brincker, R. and Dahl, H. (1989), Fictitious Crack Model of Concrete Fracture, *Magazine of Concrete Research*, 41, No. 147, pp. 79-86.

Brincker, R. (1990), General approach to fracture & stability, *personal communication.*

Brown, E.T. and Hudson, J.A. (1972), *Discussions of the paper Griffith Fracture Criterion and Concrete, by S.P. Shah and F.J. McGarry in Journal of Engineering Mechanics Proc. Paper 8597*, Journal of Engineering Mechanics, ACSE, 98 (EM5), pp.1310-1313

Brühwiler, E., Broz, J.J. and Saouma, V.E. (1991), Fracture Model Evaluation of Dam Concrete, *Journal of Materials in Civil Engineering*, ASCE, Vol. 3, No. 4, pp. 235-250.

Carpinteri, A. (1989), Size Effects on Strength, Toughness, and Ductility. *Journal of Engineering Mechanics*, ASCE, Vol. 115, No. 7, pp. 1375-1392.

Cotterell, B. and Mai, Y.-W. (1987), Crack Growth Resistance Curves and Size Effect in the Fracture of Cement Paste, *Journal of Materials Science*, 22, pp. 2734-2738.

Elfgren, L (1989), Fracture Mechanics of Concrete Structures - From theory to application, *Chapman and Hall*, pp.1-407.

Elices, M. and Planas, J. (1988), Material Models, *in Fracture Mechanics of Concrete Structures: From theory to applications. Edited by L.Elfgren*, pp. 16-66.

Evans, R.H. and Marathe, M.S. (1968), Microcracking and Stress-Strain Curves for Concrete in Tension, Materials and Structures, 1. pp. 61-64.

Ewalds, H.L. and Wanhill, R.J.H (1984), Fracture Mechanics, *Edward Arnold*, London.

FIP/CEB (1990), High Strength Concrete- State of the art, *FIP/CEB*, Bulletin d'information No. 197, pp 1-61.

Freudenthal, A.M. (1968), Statistical Approach to Brittle Fracture, *in Fracture, an Advanced Treatise*, Volume II, pp. 592-619.

Gansted, L. and Sørensen N.B. (1991), Introduction to Fatigue and Fracture Mechanics, *University of Aalborg*, Aalborg, Denmark.

Griffith, A.A. (1921), The Phenomena of Rupture and Flow in Solids, *Royal Society of London, Philosophical Transaction.* A, Vol 22, pp 163-198.

Gopolaratnam, V.S. and Shah, S.P. (1984), Softening Response of Plain Concrete in Direct Tension, Technological Institute Northwestern University, Evanston, Illinois, pp. 1-32.

Harder, N.A. (1990), Computer Simulated Crack Propagation in Concrete, *in Fracture Behavior and Design of Materials and Structures, Proceedings of the 8th European Conference on Fracture-ECF8* (Editor D. Firrao), Engineering Materials Advisory Services LTD, Vol. II pp. 706-712.

Higgins,D.D. and Bailey, J.E. (1976), Fracture Measurements on Cement Paste, *Journal of Materials Science*, Vol. 11, pp.773-782.

Hillerborg, A.,Modéer, M. and Petersson, P-E. (1976), Analysis of Crack Formation and Crack Growth in Concrete by means of Fracture Mechanics and Finite Elements, *Cement and Concrete Research*, Vol.6, Number 6, pp. 773-782.

Hillerborg, A. (1977), Materialbrott, *Avdelingen för byggnadsmaterialläre, rapport TVBM 3004*, Lund, Sweden, pp. 1-48.

Hillerborg, A. (1983), Analysis of One Single Crack, *in Fracture Mechanics of Concrete,edited by F.H. Wittmann*, Elsevier, pp. 223-249.

Hillerborg, A.(1985), Influence of Beam Size on Concrete Fracture Energy Determined According to a Draft RILEM Recommendation; Report to RILEM TC50-FMC, *Rapport TVBN-3021*, pp. 1-15.

Hillerborg (1989), Stability Problems in Fracture Mechanics Testing, *in Fracture of Concrete and Rock - Recent Developments, Editors S.P.Shah, S.E. Swartz and B. Barr* , Cardiff, Wales, Elsevier Applied Science, pp. 369-378.

Hellan, K. (1984), Introduction to Fracture Mechanics, *McGraw-Hill*, New York.

Herholdt, A.D., Justesen C.F.P., Nepper-Christensen P. and Nielsen A. (1985), Beton-Bogen, *CtO Aalborg Portland*, 2. Udgave, (in Danish).

Hutchinson, J.W. (1968), Plastic Stress and Strain Fields at a Crack Tip, *Journal of Mechanics, Physics and Solids*, 16, pp. 337-347.

Hsu, T.T.C., Slate, F.O., Sturman, G.M. and Winter, G. (1962), Microcracking of Plain Concrete and the Shape of the Stress-Strain Curve, *Journal of the American Concrete Institute*, Proceedings V. 60, No. 2, pp.209-223.

Inglis, C.E. (1913), Stresses in a Plate due to the Presence of Cracks and Sharps Corners. *Trans. Inst. Naval Architects*, pp. 219-241.

Irwin, G.R (1957), Analysis of stresses and Strains Near the End of a Crack Traversing a Plate, *Journal of Applied Mechanics*, Vol. 24, pp. 361-364.

Jenq, Y. and Shah, S.P. (1985), Two Parameter Fracture Model for Concrete, *Journal of Engineering Mechanics*, ASCE, Vol. 111, No. 10, pp. 1227-1242.

Kaplan, M.F. (1961), Crack Propagation and the Fracture of Concrete, *Journal of the American Concrete Institute*, Proceedings V. 58, No. 5, pp 591-610.

Karihaloo, B.L. and Nallathambi, P. (1991), Notched Beam test: Mode I Fracture Toughness, *in Fracture Mechanics Test Methods for Concrete, Edited by S.P. Shah and A. Carpinteri*,

Chapmann and Hall, pp. 1-86.

Leicester, R.H. (1973), Effect of Size on the Strength of Structures, *Forest Products Laboratory*, Division of Building Research Technological Paper No. 71, pp.1-13.

Mai, Y.-W. (1991), Fracture and Fatigue of Non-Transformable Ceramics: the role of Crack-Interface Bridging, in *Fracture Process in Concrete, Rock and Ceramics Edited by J.G.M. van Mier et al.*, Chapmann and Hall, pp. 3-26.

Mehta, P.K. (1986), Concrete: Structure, Properties, and Materials, *Prentice-Hall, Inc.*, 450 pages.

Mehta, P.K. and Aïtcin, P.C. (1990) Microstructural Basis of Selection of Materials and Mix Proportions for High-Strength Concrete, in *High-Strength Concrete ,Second International Symposium*, American Concrete Institute, pp. 265-286.

Mindess, S. (1983), The Cracking and Fracture of Concrete: An Annotated Bibliography 1928-1981, *in Fracture Mechanics of Concrete, edited by F.H. Wittmann*, Elsevier, pp. 542-671.

Mindess, S. (1986), The Cracking and Fracture of Concrete: An Annotated Bibliography 1982-1986, *in Fracture Toughness and Fracture Energy of Concrete, edited by F.H. Wittmann*, Elsevier, pp. 629-699.

Mindess, S. (1989), Interfaces in Concrete, in *Materials Science of Concrete I Edited by Jan Skalny*, The American Ceramic Society, pp. 163-190

Nallathambi, P. and Karihaloo, B.L. (1986), Determination of Specimen-Size Independent Fracture Toughness of Plain Concrete, *Magazine of Concrete Research*, Vol. 38, No. 135, pp. 67-76.

Regourd, M. (1984), Microstructure of High Strength Cement Paste Systems, in *Very High Strength Cement-Based Materials editor J.F. Young*, Materials Research Society Symposia Proceedings Vol. 42, pp. 3-18.

Petersson, P.-E. (1981), Crack Growth and Development of Fracture Zones in Plain Concrete and Similar Materials, *Division of Building Materials, Lund Institute of Technology, Report TVBM-1006*, Lund sweden, pp. 1-174.

Planas, J. and Elices, M. (1989), Asymptotic Analysis of the Development of a Cohesive Crack Zone in Mode I Loading for Arbitrary Softening Curves, *Proceedings of Fracture of Concrete and Rock* (S.P. Shah and S.E. Swartz, Editors), SEM-RILEM Conference. Houston p. 384.

Reagel, F.V. and Willis, T.F. (1931), The Effect of the Dimensions of Test Specimens on the Flexural Strength of Concrete, *Public Roads*, Vol. 12, No. 2, pp.37-46.

Reinhardt, H.W. (1985), Crack Softening Zone in Plain Concrete under Static Loading,

Cement and Concrete Research, Vol. 15, pp. 42-52.

Rice, J.R. (1968), A Path-Independent Integral and The Approximate Analysis of Strain Concentration of Notches and Cracks,, *Journal of Applied Mechanics*, 35, pp. 379-386.

Rice, R. (1977) Microstructure Dependence of Mechanical Behavior Ceramics, *Treatise on Material Science and Technology*, Vol II, Academic Press Inc., pp. 199-381.

Ziegeldorf, S. (1983), Phenomenological Aspects of The Fracture of Concrete, *in Fracture Toughness and Fracture Energy of Concrete, edited by F.H. Wittmann*, Elsevier, pp. 31-41.

Sarkar, L.S. and Aïtcen, P.C (1987), Comparative Study of the Microstructures of Normal and Very High-Strength Concretes, *Cement, Concrete and Aggregates*, The American Society for Testing and Materials, pp. 57-64.

Scrivener, K.L. (1989), The Microstructure of Concrete, in *Materials Science of Concrete I, Edited by Jan Skalny*, The American Ceramic Society, pp. 127-161.

Skalny, J. and Roberts, R.L. (1987), High-Strength Concrete, *Ann. Rev. Mater. Sci.*, 17, pp. 35-56.

Smadi, M.M. and Slate F.O. (1989), Microcraking of High and Normal Strength Concretes under Short and Long-Term Loadings, *ACI Materials Journal*, V. 86, No.2, pp. 117-127.

Stroeven, P (1975), The Influence of Volume Change on the Design and Technology of Modern Building Structures, *Karlovy Vary*, CSSR.

Swammy, R.N. (1986), Properties of High-Strength Concrete, *Cement, Concrete and Concrete and aggregates*, The American Society for Testing and Materials, pp. 33-41.

Ulfkjær, J.P., Krenk, S. and Brincker, R. (1992), Analytical Model for Fictitious Crack Propagation in Concrete Beams, *submitted for publication in Journal of Engineering Mechanics*.

Weibull, W. (1939), A Statistical Theory of the Strength of Materials, *Royal Swedish Academy of Eng. Sci. Proc.*, 151, 1-45.

Weibull, W. (1951), A Statistical Distribution Function of Wide Applicability, *Journal of Applied Mechanics*, 18, 293-297.

Wolinski, S., Hordijk, D.A., Reinhardt, H.W. and Cornelissen (1987), Influence of Aggregate Size on fracture Mechanics Parameters of Concrete, *The international Journal of Cement, Composites and Lightweight Concrete* , Vol. 9, No. 2, pp. 95-103.

3 NUMERICAL METHODS IN CONCRETE FRACTURE.

It is only in a few simple cases possible to apply the fictitious crack model in an analytical manner and instead it is necessary to use numerical methods like the finite element method or the boundary element method. In the following three different methods based on the finite element method and the boundary element method are presented. The presentation of the methods is limited to opening mode, to the three-point bending geometry and the softening relation is assumed to be piece by piece linear. Non-linear softening relations are in general applicable for all the presented methods, but then iterative procedures are necessary, Elfgren (1989). The two first models have not been implemented by the author and are only roughly presented. The last method is described in detail, implemented in computer and a serious stability problem has been solved, and this method will later be used extensively.

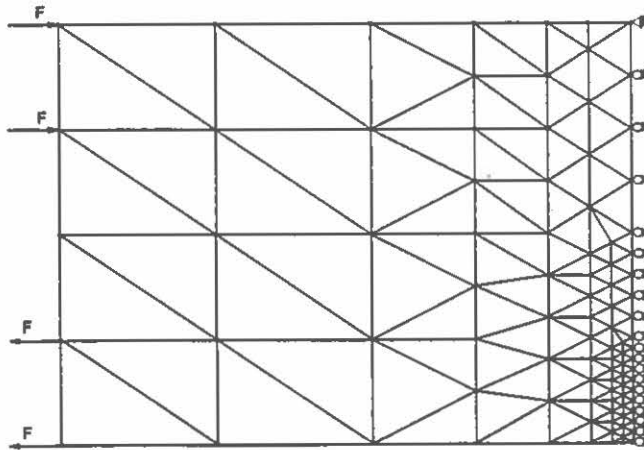## 3.1 The Hillerborg, Modeer and Petersson Methods.

Fig. 2.2 Beam and element mesh used in the calculations by Hillerborg et al. (1976).

The first method by means of the finite element method and the fictitious crack model was performed by this method, Hillerborg et al. (1976). The method is briefly outlined in the

following.

Consider the beam and the element mesh in Fig. 2.2. First the moment which yields the tensile strength in node 1 is calculated. A new special very thin element with properties according to the chosen softening relation is now inserted. As the moment increases a fictitious crack will develop in node 1, and the load which corresponds to the tensile strength in node 2 or the critical opening in node 1 is calculated. If the critical opening is reached the element at node 1 is removed and a stress free surface is achieved. If the tensile strength is reached in node 2 a new special element is inserted at node 2 and the previous step is repeated. In this way the force-displacement curve can be calculated to the peak moment and a little further.

The advantage with this method is that it is directly applicable for all geometries and loading configuration and capable of predicting multiple cracking, as long as the structure can be satisfactory modelled by the finite element method. The method is therefore also valid for reinforced concrete. The disadvantage of this method is that it is very time consuming and many different element meshes are needed, as the fictitious crack develops and advances.

Instead Modeer (1979) developed the force method, a more rapid special geometry method, which later was refined by Petersson (1981) to the sub-structure method.

3.2 The sub-structure method.

The sub-structure method was introduced by Petersson (1981) and later refined by Carpinteri (1989), who made the fracture process, fictitious crack length controlled. The method is more or less a method based on the boundary element method, since only loads at the boundary of the structure are considered. The method is superior to the method developed by Hillerborg et al. (1976) since the calculation speed is considerably higher, up to a factor 100, Brincker and Dahl (1989).

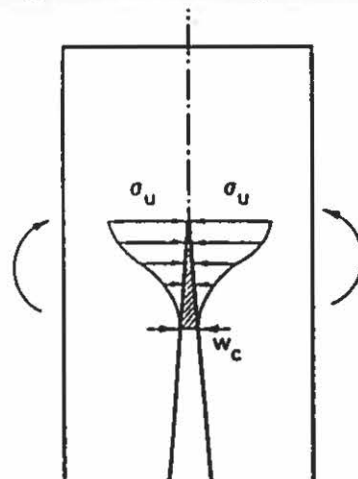Consider an arbitrary structure subjected to the displacement controlled load, F, and the

Fig. 2.3 Structure with virtual crack path, as used in the substructure method.

corresponding displacement, δ, see . The virtual crack path, γ, is assumed to be known on beforehand. The distance along the crack path is given by the coordinate y, and the virtual crack path ends at d_γ. Along the crack path closing stresses are acting according to the fictitious crack model. The crack is assumed to be long, but is not allowed to split the structure into two, as it is assumed that a certain amount of nodes are necessary if the stress and strains should be modelled in a realistic way, Petersson (1981).

First the governing equation will be derived. Then the fracture process is divided into three and the equations are discretizised.

The crack path is now assumed to consist of three parts, I) for $y=0$ to $y=a$ where the crack surfaces are stress free (the real crack), II) for $y=a$ to $y=a_f$ where the crack is loaded by cohesive stresses, $\sigma(y)$, according to the fictitious crack model, and described by the softening relation, $f(w)$, and part III) the linear elastic part where the crack opening displacement is zero.

The opening between the two virtual crack surfaces, w, can be determined by the compliances

$$w(y) = \int_0^{d_\gamma} C_1(y,y') \, \sigma(y')dy' + C_2(y)F \qquad (3.56)$$

where $C_1(y,y')$ is the displacement in x from a unit load in y', and $C_2(y)$ is the displacement in y from a external load. Similarly the load point displacement can be calculated by

$$\delta = \int_0^{d_\gamma} C_2(y)\sigma(y)dy + C_3(y)F \qquad (3.57)$$

where C_3 is the load point deflection from a unit load.

Three set of conditions must be fulfilled. At part I the virtual crack surfaces are stress free

$$\sigma(y) = 0 \qquad \text{for } 0 \le y \le a \qquad (3.58)$$

at the fictitious crack the stresses is described by the softening relation

$$\sigma(y) = f(w(y)) \qquad \text{for } a \le y \le a_f \qquad (3.59)$$

at the uncracked ligament the crack opening displacement is zero

$$w(y) = 0 \qquad \text{for } a_f \le y \le d_\gamma \qquad (3.60)$$

which constitutes the governing equations for the sub-structure method.

The structure is now discretizised along the crack path in n-nodes, with equidistant spaces between the nodes as proposed by Petersson (1981) and Carpinteri (1989). The stresses are expressed by the nodal forces, s_i, and the compliances are given by the appropriate influence coefficients

The calculations are divided into three phases: Phase I where the entire structure is assumed to be linear elastic, Phase II where the fictitious crack is developing and Phase III where the

real crack is extending.

Phase I
In all three phases the widening of each node can be calculated by using the discretiziced version of (3.56)

$$w_i = \sum_{j=1}^{n} c_{ij}^{I} s_j + c_i^{II} F \qquad (3.61)$$

where, w_i, is the crack opening displacement of node i, s_j, is the closure load in node j, c_i^I, is the opening in node i from a unit load in node j, and c_{ij}^{II} is the opening of node i due to a unit external load. The boundary compliances can be calculated by using the finite element method on the discretizised structure. By applying Maxwells-Bettis theorem it is seen that $c_{ij}^I = c_{ji}^I$, whereby the compliances reduces to $\dfrac{n(n+3)}{2}$.

Since the opening of each node is zero, the following condition must be fulfilled

$$w_i = 0 \qquad \text{for } i = 1, ..., n \qquad (3.62)$$

Eqs. (3.61) and (3.62) compose a linear algebraical system of n equations with n unknowns, that is the node forces, s_i. When the load, F, and the node forces, s_i, are known it is possible to calculate the load point displacement, δ, as

$$\delta = c_j^{II} s_j + c_F F \qquad (3.63)$$

where, c_F, is the displacement for a unit load. At this first step the load, F_1, which produces the ultimate nodal force, σ_u, at node 1 and the corresponding displacement, δ_1, is calculated by eq. (3.63), (4.95). The load-displacement curve in phase I is then the linear curve between (0,0) and (δ_1, F_1). Thus, the process is performed in load control in phase I.

Phase II
In phase II a cohesive crack develops in front of the real crack tip. The fictitious crack is assumed to form between nodes 1 and m whereby eq. (3.62) is replaced by

$$s_i = s_u \left[1 - \frac{w_i}{w_c} \right] \qquad \text{for } i = 0,...,m-1 \qquad (3.64)$$

and at the remaining ligament

$$w_i = 0 \qquad \text{for } i = m, m+1,..., n \qquad (3.65)$$

Eqs. (3.61), (3.64) and (3.65) constitutes a linear algebraical system of $2n+1$ equations with $2n+1$ unknowns, i.e, the crack opening displacements, the nodal forces and the external load, F. At the second point of the load-displacement curve the fictitious crack is between node 1 and 2 and the nodal force in node 2 is equal to the ultimate nodal force and the load, F_2 that produces that force is calculated. The displacement that corresponds to, F_2, is then calculated by using eq.(3.63), (4.95). The calculations proceed in this manner until the critical opening is reached in node 1, which ends phase II. In this way the process is fictitious crack length

controlled in phase II.

Phase III
In phase III the real crack starts to grow. The real crack is between node 0 and k-1 and the fictitious crack is between node k and m-1 whereby eqs. (3.64) and (3.65) are replaced

$$s_i = 0 \qquad \text{for } i = 1,2...,k - 1 \qquad (3.66)$$

in the fictitious crack

$$s_i = s_u \left[1 - \frac{w_i}{w_c} \right] \qquad \text{for } i = k,k + 1...,m - 1 \qquad (3.67)$$

and at the remaining ligament

$$w_i = 0 \qquad \text{for } i = m, m + 1,..., n \qquad (3.68)$$

Eqs. (3.61), (3.66), (3.67) and (3.68) constitute a **linear algebraical system of 2n+1 equations with 2n+1 unknowns.**

In phase III the controlling parameter is also the fictitious crack length, it is therefore not possible to directly calculate the real crack length, the external load and the displacement and instead an iterative procedure must be applied, Carpinteri (1989).

The sub-structure method is a specially designed method, for plain structures with one crack. The method is easy to use, and when the compliances are determined the method is applicable for all sizes of the considered structure by scaling the compliances appropriately. The calculation speed is increased tremendously compared with the Hillerborg et al. method, and by making the fictitious crack length the controlling parameter the method is applicable of predicting snap-back. If the method was not fictitious crack length controlled, but instead deflection controlled, the method becomes unstable at the point where the slope becomes infinitely. The method is, however, truncated since the crack is not allowed to divide the structure into two, but only as long as the crack is allowed to be as described previously. The problem is especially serious for ductile beams where the fictitious crack length is large compared to the beam height, whereby only a small part of the descending branch is calculated.

3.3 The Direct Sub-Structure Method.

The direct sub-structure was invented by Brincker and Dahl (1989) in order to be able to calculate the entire descending branch of the load displacement curve. Instead of making a cut in the structure as in the sub-structure method, the structure is actually divided into two in the direct sub-structure method. The method is applicable for multiple cracking, but in order of simplicity the method is only demonstrated on the three-point bending geometry. The method is described following the procedure of Brincker and Dahl (1989) and an effective method which solves the stability problem described by Brincker and Dahl (1989) is presented and demonstrated.
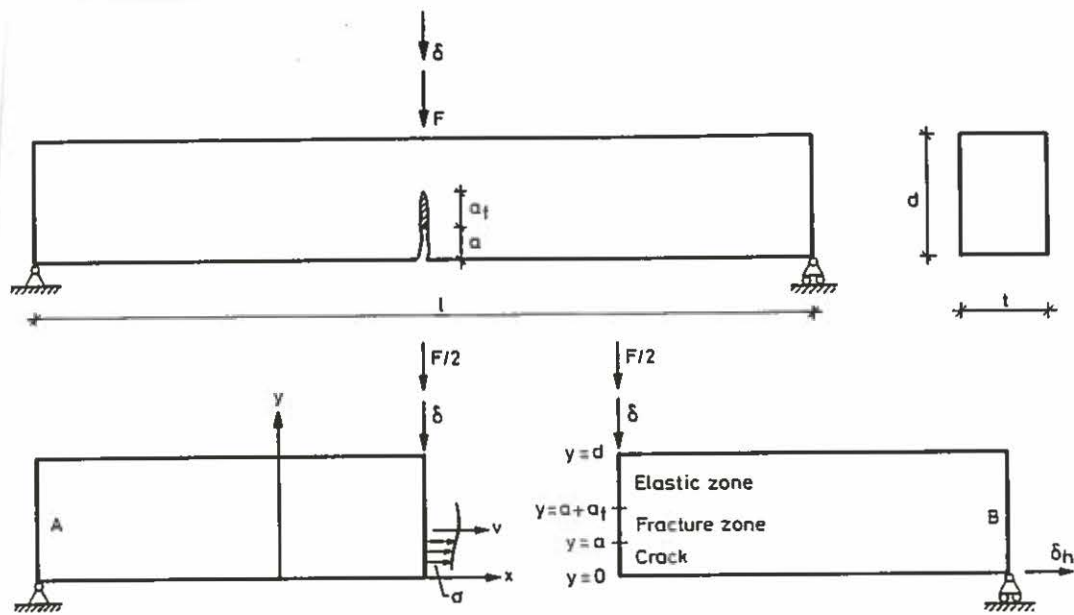
Fig. 2.4 The considered beam divided into two substructures, Brincker and Dahl (1989).

First the general equations will be derived, which are valid in all three phases, then the calculation technique for deformation control will be described.

Consider the beam in Fig. 2.4, which is split into two parts (a) and (b) by a virtual cut along what is assumed to be the crack path, γ. In general the displacements will consist of the sum of two terms: rigid body displacements, $v_a{}^r$, and elastic displacements, $v_b{}^\sigma$, of the virtual surfaces.

By assuming small displacements the rigid body displacements are calculated as

$$v_a^r(y) = \frac{2\delta}{l}y \tag{3.69}$$

and for beam part (b)

$$v_b^r(y) = \delta_h - \frac{2\delta}{l}y \tag{3.70}$$

where, $v_a{}^r$, and, $v_b{}^r$, are the displacements of the virtual crack surfaces and δ_h is the horizontal displacement of the support. The displacements caused by the stresses acting on the virtual surfaces are calculated by

$$v_a^\sigma(y) = \int_0^d \sigma(y)c(y,y')dy' \tag{3.71}$$

and for beam part (b)

$$v_b^\sigma(y) = - \int_0^d \sigma(y)c(y,y')dy' \tag{3.72}$$

where $c(y,y')$ is the compliances of the considered displacement. The opening between the virtual crack surface is then given by the difference between the total displacements fields of the two bodies (a) and (b)

$$
\begin{aligned}
v(y) &= v_b(y) - v_a(y) \\
&= -2\int_0^h \sigma(y')c(y,y')dy' + \delta_h - \frac{4\delta}{l}y
\end{aligned}
\tag{3.73}
$$

Depending on which phase is considered one or more of the following conditions must be fulfilled. The equilibrium condition

$$
\int_a^d \sigma(y)dy = 0
\tag{3.74}
$$

the constitutive condition

$$
f(w(y)) = \sigma(y) \qquad \text{for} \quad a < y \leq a + a_f
\tag{3.75}
$$

and the compatibility condition

$$
w(y) = 0 \qquad \text{for} \quad a + a_f < y < d
\tag{3.76}
$$

The external load is determined by the equilibrium condition i.e. the equivalent moment at the virtual crack faces shall outbalance the external load

$$
F = -\frac{4}{l}\int_a^d \sigma(y)ydy
\tag{3.77}
$$

As in the sub-structure method, the system is discretisized, in n nodes along the virtual crack surfaces with equidistance, a_0. The stresses are expressed by the nodal forces s_i and the compliances are expressed by the appropriate influence coefficients, c_{ij}.

The crack opening displacement is then expressed as

$$
w_i = -2\sum_{j=k}^n c_{ij}s_j + \delta_h - 4\frac{\delta}{l}y_i \qquad \text{for} \quad k \leq i < m
\tag{3.78}
$$

The equilibrium condition

$$
\sum_{j=k}^n s_j = 0
\tag{3.79}
$$

the constitutive condition is for simplicity assumed to be linear

$$
f_i = s_u(1 + \frac{w_i}{w_c})
\tag{3.80}
$$

if the constitutive relation is assumed to be piece by piece linear the two constants s_u and w_c are simply modified for the appropriate nodes. The only problem is then to establish on which

line on the softening relation each node is, Brincker and Dahl (1989). By inserting (3.78) the constitutive condition (3.80), (3.81) becomes

$$1 - 2\frac{1}{w_c} \sum_{j=k}^{n} c_{ij}s_j - \frac{4}{w_c}\frac{\delta}{l}y_i + \frac{\delta_h}{w_c} - \frac{s_i}{s_u} = 0 \qquad \text{for } k \leq i < m - 1 \qquad (3.81)$$

The compatibility condition is discretizised and combined with (3.78)

$$\sum_{j=k}^{n} c_{ij}s_j - \frac{\delta_h}{2} + 2\frac{\delta}{l}y_i = 0 \qquad \text{for } m \leq i \leq n \qquad (3.82)$$

The equations (3.79), (3.80), (3.81) and (3.82) constitute **a linear algebraical system of $2n+1$ equations with $2n+1$ unknowns**. It is seen that only $\dfrac{n(n+1)}{2}$ influence coefficients are needed. The system of linear equations can then be written

$$A\overline{x} = \overline{b} \qquad (3.83)$$

where the coefficient matrix is given by

$$A = \begin{bmatrix} 2\frac{s_u}{w_c}c_{k,k} + 1 & 2\frac{s_u}{w_c}c_{k,k+1} & \cdots & 2\frac{s_u}{w_c}c_{k,n} & -\frac{s_u}{w_c} \\ 2\frac{s_u}{w_c}c_{k+1,k} & 2\frac{s_u}{w_c}c_{k+1,k+1} + 1 & \cdots & 2\frac{s_u}{w_c}c_{k+1,n} & -\frac{s_u}{w_c} \\ \vdots & \vdots & \ddots & \vdots & \vdots \\ 2\frac{s_u}{w_c}c_{m-1,k} & 2\frac{s_u}{w_c}c_{m-1,k+1} & \cdots & 2\frac{s_u}{w_c}c_{m-1,n} & -\frac{s_u}{w_c} \\ -c_{m,k} & -c_{m,k+1} & \cdots & -c_{m,n} & 0.5 \\ \vdots & \vdots & \ddots & \vdots & \vdots \\ -c_{n,k} & -c_{n,k+1} & \cdots & -g_{n,n} & 0.5 \\ 1 & 1 & \cdots & 1 & 0 \end{bmatrix} \qquad (3.84)$$

and the right hand side is given by

$$\vec{b} = \begin{bmatrix} s_u - 4\dfrac{s_u}{w_c}\dfrac{\delta}{l}y_k \\[1.5em] s_u - 4\dfrac{s_u}{w_c}\dfrac{\delta}{l}y_{k+1} \\[1.5em] \vdots \\[1em] s_u - 4\dfrac{s_u}{w_c}\dfrac{\delta}{l}y_{m-1} \\[1.5em] 2\dfrac{\delta}{l}y_m \\[1.5em] \vdots \\[1em] 2\dfrac{\delta}{l}y_n \\[1.5em] 0 \end{bmatrix} \qquad (3.85)$$

and the solution to the system of equations is

$$\vec{x} = \begin{bmatrix} s_k \\ s_{k+1} \\ \vdots \\ s_{m-1} \\ s_m \\ \vdots \\ s_n \\ \delta_h \end{bmatrix} \qquad (3.86)$$

The non-linearity of the problem is introduced by updating the matrix A and the right hand sides $\vec{b}$. When the nodal forces are determined the crack openings are determined by (3.80), (3.81), and the external load is determined by

$$F = -\frac{4}{l}\sum_{j=k}^{n} s_j y_j \qquad (3.87)$$

The problem then consists in determining which node is the next to change state (from elastic to fictitious state or from fictitious state to complete fracture).

Two nodes are potential of changing state: node k and node m. By applying a small test load, $d\delta$, the opening in node k will change dw_k, and the stress in node m will change ds_m, whereby the following sensitivities can be calculated

$$\zeta_k = \frac{dw_k}{w_c - w_k}$$

$$\zeta_m = \frac{ds_m}{s_u - s_m}$$

(3.88)

The next node to change state will be the one with the large sensitivity. Since the system is linear the displacement increment, $\Delta\delta$, necessary for changing state is calculated by

$$\Delta\delta = \frac{d\delta}{\zeta_{max}}$$

(3.89)

It is seen that when a node is completely fractured it will simply be removed from the system of equations, reducing the calculation time as the real crack advances. In this way the entire load displacement can be calculated, in load point displacement control.

3.4 Stability of The Direct Sub-structure Method.

As was concluded by Brincker and Dahl (1989) a serious stability problem arises when the beam brittleness is increased, and an exorbitant amount of time has been used to solve this problem.

The problem can be observed in the outlined method in the way that the crack opening displacement of the nodes in the fracture zone increases, which corresponds to that the strain softening relation becomes a strain hardening relation. Therefore, it was thought that an unloading branch was necessary in order to overcome the problem. This was not the case. A method where the softening relation was a continuous function was implemented. In this case an iterative procedure is necessary since the system is non-linear. The stability problem was, however, not solved.

It was then realized that the stability problem is due to the snap-back effect. The load-displacement curve constitutes the set of points where the system is in equilibrium. If the beam is so brittle that snap-back is introduced, that means that the displacement at some point on the descending branch is decreasing, yielding a negative infinitely slope. However, the crack opening displacement will always be an increasing function.

The problem can therefore be solved by making the fracture process crack mouth opening controlled, or fictitious crack length controlled (as by Carpinteri), or crack tip opening controlled. Here crack tip opening control is presented. As is seen from the previous equations it is not possible to derive the governing equations with the crack opening as the controlling parameter. Instead a very simple and effective procedure was developed. The process is made indirectly crack tip opening displacement controlled.

The calculation are performed completely similarly to the just described method. However,

if the sensitivity of node k is then the displacement increment is calculated by

$$\Delta\delta = \frac{d\delta}{\zeta_k}$$ (3.35)

Fig. 3.5 Load displacement curve where the beam is to brittle compared to the number of nodes n=21.

Fig. 3.4 Examples of load displacement curves, calculated by using the Direct substructure method, at different size scales

Since, $\zeta_k < 0$ the displacement will decrease and snap back is introduced. This method is very stable, and a load-displacement curve is always calculated even for extremely brittle beams. The results are though not reliable if the number of nodes are too small compared to brittleness of the structure. This method will be used extensively in the rest of the thesis were many examples of load displacement curves using this method are shown.

3.5 Model Evaluation.

Three numerical methods have been presented. The Hillerborg et al. method was the first method to be used with the fictitious crack model and is a multi purpose method applicable for all geometries and loading conditions. The method is, however, very slow and many element meshes are necessary as the fictitious crack develops and as the real crack extends.

Instead the sub-structure method was developed by Petersson (1981) and Carpinteri (1989). The sub-structure is only applicable for a certain type of structures but instead it is very fast compared to the Hillerborg method. The method is also made fictitious crack length controlled, whereby very brittle structures can be analyzed. The method is, however, truncated by that the crack is not allowed to split the structure into two, and is therefore not well suited for ductile structures.

To overcome the problem of splitting the structure into two Brincker and Dahl (1989) developed the Direct sub-structure method, where the crack is extending through the entire structure and actually splits the structure into two. The method is displacement controlled and is therefore not applicable for brittle structures. The calculation speed is of the same order as in the sub-structure method.

To overcome the problem of snap-back the author has extended the direct sub-structure method, to be crack tip opening displacement controlled. The only limit to how the brittle

structures the method can analyze is thereby only limited to the amount of nodes.

The direct sub-structure is therefore applied in the rest of this thesis, since it is superior to the sub-structure method.

3.6 References for Chapter 3.

Brincker, R. and Dahl, H. (1989), Fictitious Crack Model of Concrete Fracture, *Magazine of Concrete Research*, 41, No. 147, pp. 79-86.

Carpinteri, A. (1989), Size Effects on Strength, Toughness, and Ductility. *Journal of Engineering Mechanics*, ASCE, Vol. 115, No. 7, pp. 1375-1392.

Elfgren, L (1989), Fracture Mechanics of Concrete Structures - From Theory to Application, *Chapman and Hall*, RILEM Report.

Modeer, M. (1979), A Fracture Mechanics Approach to Failure Analysis of Concrete Materials, *Division of Building Materials, Lund Institute of Technology, Report TVBM-1001*, Lund Sweden, pp. 1-102.

Hillerborg, A., Modeer, M and Petersson, P.-E. (1976), Analysis of Crack Formation and Crack Growth in Concrete by means of Fracture Mechanics and Finite Elements, *Cement and Concrete Research*, Vol. 6, pp.773-782.

Petersson, P.-E. (1981), Crack Growth and Development of Fracture Zones in Plain Concrete and Similar Materials, *Division of Building Materials, Lund Institute of Technology, Report TVBM-1006*, Lund Sweden, pp. 1-174.

4 ANALYTICAL METHODS IN CONCRETE FRACTURE.

As described in the previous section a variety of numerical methods exists which can be used to predict the load carrying capacity of plain and reinforced concrete structures in which a fictitious crack develops. It is, however, often convenient to have more simple methods which can be used to predict approximate results and more appropriate for the practical engineer. The numerical methods are in general very time consuming, and if an indirect method is used to determine the constitutive relations, as will be described in chapter 5, the numerical effort becomes enormous. In order of convenience the various models are named after the authors, who published the described methods.

4.1 Non-Reinforced Concrete.

In the following, three analytical models for plain concrete will be presented and some improvements will be suggested. The presentation is limited to linear softening relations and the notation used in each model corresponds, if possible, to the notation introduced by Ulfkjær et al. (1991).

4.1.1 The Ulfkjær, Brincker and Krenk Method.

The idea of modelling the bending failure of concrete beams by the development of a fictitious crack in an elastic layer with a thickness proportional to the beam height was introduced by Ulfkjær, Brincker and Krenk (1990), and further refined by Ulfkjær, Krenk and Brincker (1992). The following presentation is equivalent to that, and some extra results are presented.

The model is based on the assumption that the complex stress field around the crack is modelled by simple spring-action in an elastic layer around the crack, and outside the layer the deformations are modelled by elastic beam theory.

Using a linear softening relation yields that the fracture energy is given by $G_F = \frac{1}{2}\sigma_u w_c$, where, σ_u, is the ultimate tensile stress and, w_c, is the critical crack opening displacement. In the elastic layer only bending stresses are assumed to be present and the stress is assumed to depend linearly on the local elongation of the layer. By assuming a linear softening relation, the constitutive relation of the layer becomes a bi-linear relation between the axial stress, σ, and the elongation, v, see Fig. 4.1. On the ascending branch the elongation is linear elastic $v = v_e$ and no crack opening is present. The linear response is given by $v_e = \sigma h/E$ where, h, is the thickness of the layer, and, E, is Young's modulus. On the descending branch the total deformation v consists of two contributions $v = v_e + w$, where, w, is the crack opening
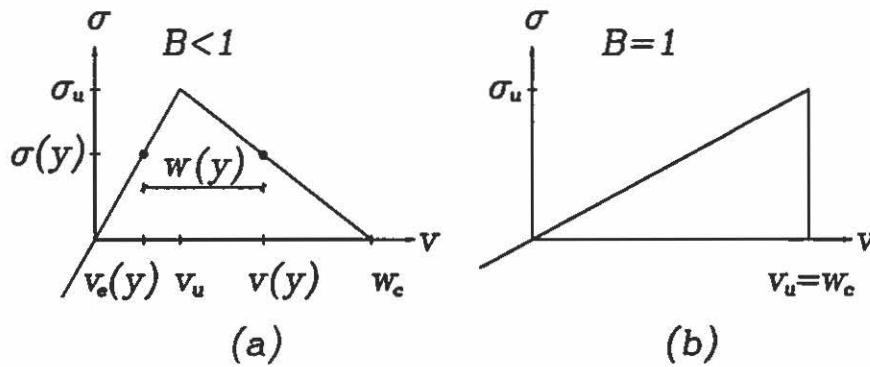
59

Fig. 4.1. Constitutive relation for the midsection of the layer a) When the layer is stable, $B<1$.. b) When the layer is unstable $B=1$.

displacement. The peak point corresponds to the deformation $v = v_u$, and total fracture corresponds to $v=v_c$. Therefore, the critical crack opening displacement corresponds to $w_c=v_c$.

If the elastic layer should be stable in displacement controlled loading the following condition must be fulfilled

$$v_u < v_c \qquad (4.91)$$

In the present method it is convenient to define the brittleness number, in eq. (2.38), as

$$B = \frac{\sigma_u^2 h}{2G_F E} \qquad (4.92)$$

corresponding to a characteristic size of the structure equal to $h/2$. The stability condition (4.91) can then be written as

$$B < 1 \qquad (4.93)$$

Thus, in this model the brittleness number, B, varies between zero corresponding to ideal ductile behavior and one corresponding to ideal brittle behavior. The thickness h of the elastic layer, is assumed to be a linear function of the beam depth $h=kd$. In general the factor, k, is a function of the beam geometry, the beam size, the fictitious crack length and the real crack length. In this model the factor, k, is assumed constant and is found using the DSS demanding that the peak load is predicted correctly.

As a first approximation only rigid body displacement is assumed of the beam parts outside the elastic layer, see Fig. 4.2.

The calculations are, as in the numerical method, divided into three phases. Phase I): Before the tensile strength is reached in the tensile side of the beam, phase II): Development of a
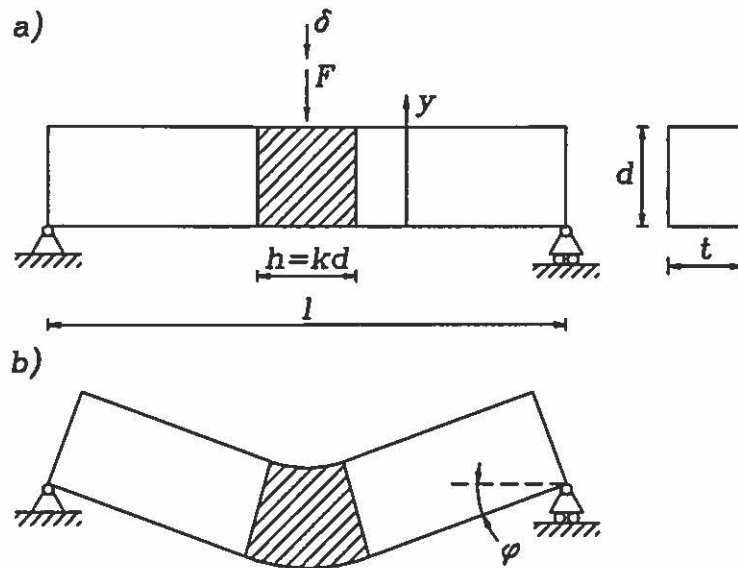
60

a)

b)

Fig. 4.2 a) The considered beam where the hatched area is the elastic layer. b) Deformed beam where only rigid body displacements are considered.
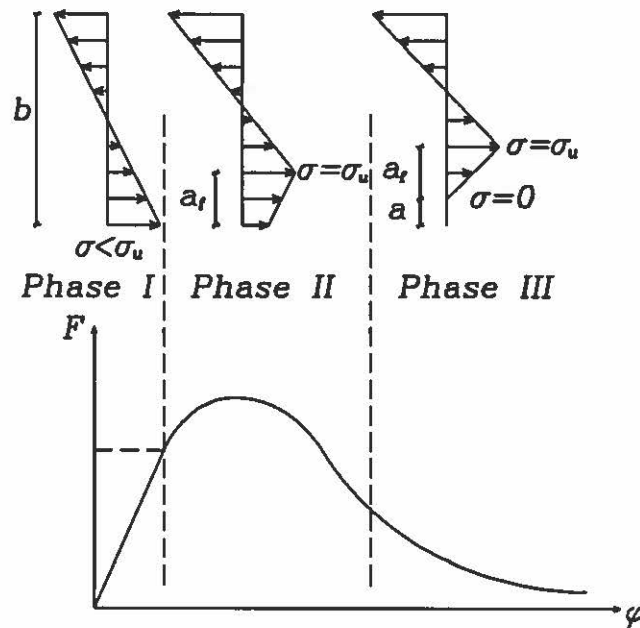
Fig. 4.3. The stress distributions of each phase a) Phase I where the stress distribution is elastic. b) Phase II where the fictitious crack is developed. c) Phase III where the real crack starts to grow. d) The load-displacement curve.

fictitious crack in the layer, and phase III): Crack propagation. The stress distribution in each phase of the fracture process is illustrated in Fig. 4.3

Phase I.

In phase I a linear elastic constitutive relation is used for all parts of the layer $v_e = \sigma h / E$. By simple geometric considerations it is seen that $v_e = \varphi (d-2y)$ where φ is the rotation, d is the
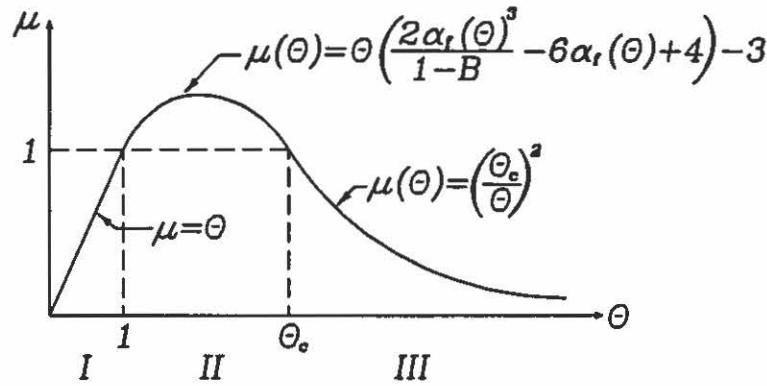
Fig. 4.4 The moment rotation curve of the beam when only rigid body displacements are considered.

beam depth and y is the vertical coordinate. The neutral axis is at the mid-point of the beam corresponding to $y = d/2$. Instead of the bending moment M and the rotation φ it is convenient to introduce the dimensionless bending moment

$$\mu = M\frac{6}{\sigma_u d^2 t} \tag{4.94}$$

and the corresponding dimensionless displacement

$$\theta = \varphi\frac{dE}{h\sigma_u} = \varphi\frac{E}{k\sigma_u} \tag{4.95}$$

giving the simple load-displacement relation

$$\mu(\theta) = \theta \tag{4.96}$$

In the limit situation of phase I the stress for $y=0$ equals the tensile strength, and the dimensionless bending moment equals one. Thus, in phase I the load-displacement curve is a straight line between origo and $(\theta,\mu) = (1,1)$, see Fig. 4.4.

Phase II.
In phase II the size of the elastic tensile zone is determined by simple geometrical considerations. When the fictitious crack develops, it is necessary to determine the crack opening displacement. By assuming that the stress in the fictitious crack is equal to the stress in the elastic layer, the crack opening displacement becomes

$$w = \frac{2\varphi}{1-B}(a_f{-}y) \tag{4.97}$$

where a_f is the length of the fictitious crack. Thus, this corresponds to a linear crack profile.

If the linear softening relation is expressed as

$$\sigma = \sigma_u(1{-}\frac{w}{w_c}) \tag{4.98}$$

then the length of the fictitious crack can be determined by combining (4.98) with the equilibrium condition (the resultant axial force equal to zero). The result reduces to

$$\alpha_f(\theta) = \frac{a_f}{d}(\theta) = 1 - B - \sqrt{(1-B)(\frac{1}{\theta}-B)} \qquad (4.99)$$

The equivalent moment is determined by integrating the axial stresses

$$\mu(\theta) = \theta \left[\frac{2\alpha_f(\theta)^3}{1-B} - 6\alpha_f(\theta) + 4 \right] - 3 \qquad (4.100)$$

In order to stay in phase II the crack opening displacement at the bottom of the beam must be smaller than the critical crack opening $w(0) < w_c$, which by use of (4.97), (4.99) and (4.100) can be reformulated as

$$\mu(\theta) > 1 \quad \text{or} \quad 1 < \theta < \theta_c \qquad (4.101)$$

where

$$\theta_c = \frac{1+\sqrt{B}}{2B} \qquad (4.102)$$

Thus, during the development of the fictitious crack the moment increases from 1 to its ultimate value and then decreases again. When the moment reaches the value 1 at the descending branch corresponding to $\theta = \theta_c$ the real crack starts to grow, see Fig. 4.4. The real crack will therefore only propagate on the descending branch of the load displacement curve as found by Harder (1991).

Phase III.

In phase III the real crack starts to grow. The real crack length is termed a, see Fig. 4.3. The size of the elastic tensile zone is determined by the condition that $w(a+a_f) = w_u$. The size of the fictitious crack, a_f, is obtained by the condition $w(a) = w_c$ giving

$$\alpha_f = \frac{1}{2\theta}\frac{1-B}{B} \qquad (4.103)$$

The crack length a is determined through the equilibrium condition that the resultant axial force is equal to zero

$$\alpha = \frac{a}{d} = 1 - \frac{\theta_c}{\theta} \qquad (4.104)$$

As in phase II the dimensionless bending moment is determined by integrating the axial stresses. The result is

$$\mu(\theta) = \left[\frac{\theta_c}{\theta} \right]^2 \qquad (4.105)$$

When, θ_c, is suitably modified this result is general in the sense that it is valid for all softening relations. The results for the moment-rotation curve including only rigid body displacements of the beam parts are shown in Fig. 4.4.

Beam Depth, d [mm]	100.0
Beam Width, t [mm]	100.0
Beam Length, l [mm]	800.0
Notch depth, a_i [mm]	0.0
Specific Fracture Energy, G_F [Nmm/mm^2]	0.100
Tensile Strength, σ_u [N/mm^2]	3.0
Modulus of Elasticity, E [N/mm^2]	20,000
Brittleness number, B	0.1125

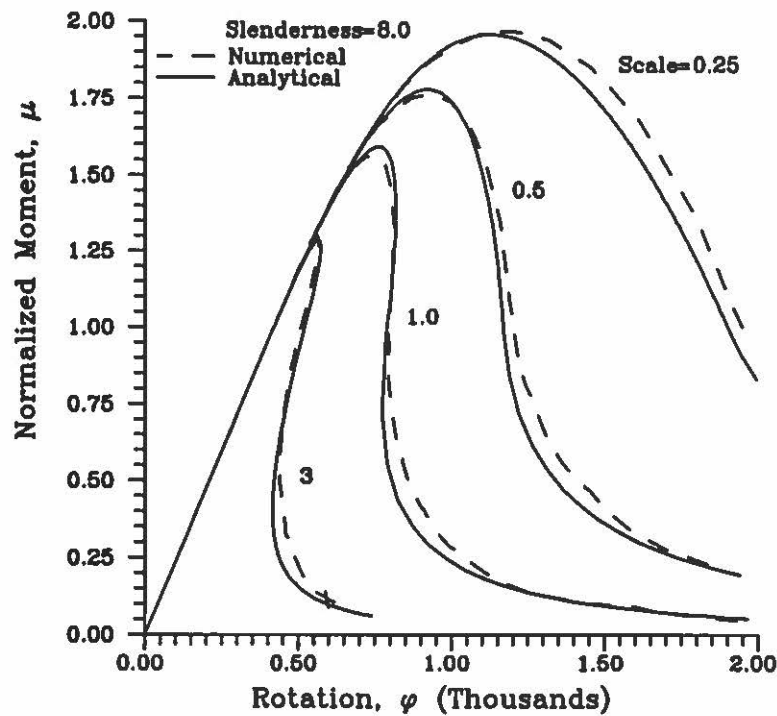Tabel 4.1 Geometry and materials parameters for standard beam.

In Fig. 4.5

Fig. 4.5. Comparison between the analytical model and DSS using the standard beam at 4 different size scales.

Elastic deformations in the beam parts outside the elastic layer are taken into account by subtracting the elastic deformation, $\theta = \mu(\theta)$, from the elastic layer leaving only deformations due to crack growth and adding the elastic deformations of the whole beam using a solution for a Timoshenko beam, Timoshenko S. (1955). The Timoshenko displacements are

$$\delta_e = \frac{Ml^2}{12EI}\beta(\lambda) \qquad (4.106)$$

where EI is the bending stiffness of the beam, β, is a factor describing the influence of shear $\beta = 1 + 2.85\lambda^2 - 0.84\lambda^3$, and, λ, is the slenderness ratio $\lambda = l/d$. Introducing the elastic rotation similar to equation (3.63), (4.95)

$$\theta_e = 2\frac{\delta_e}{l}\frac{dE}{h\sigma_u} \qquad (4.107)$$

the relation (4.106) can be written in dimensionless form

$$\theta_e = \gamma\mu \qquad (4.108)$$

where

$$\gamma = \frac{\beta(\lambda)\lambda}{3k} \qquad (4.109)$$

and the total deformation is then given by subtracting the elastic deformation in the layer and then adding the deformations of the Timoshenko beam

$$\theta_t = \theta - \mu(\theta) + \theta_e = \theta + (\gamma - 1)\mu(\theta) \qquad (4.110)$$

Hence, the complete moment rotation curve is fully determined by the brittleness number B, and the slenderness ratio λ.

The numerical results are obtained by the direct sub-structure method (DSS), Dahl and Brincker (1989). Four-node elements and an element mesh with 21 nodes in the midsection were used. Results for one beam geometry (slenderness ratio $\lambda = 8$) are compared at different brittleness levels in order to see how well the model predicts the load-displacement curve. It is assumed that the size of the elastic layer is proportional to the beam depth $h = kb$ where the factor k is assumed to be 0.5. A beam geometry similar to the RILEM beam and material parameters corresponding to a normal strength concrete is chosen as standard beam, see Tabel 4.1. With the chosen material parameters the maximum beam depth is according to (4.93) 888 mm corresponding to that all dimensions of the beam are scaled by a factor of 8.88 (scale factor = 8.88).

a comparison is shown between the analytical model and the numerical results for the standard beam on 4 different size scales (0.25, 0.5, 1.0 and 3.0). It is observed that the shape of the moment-rotation curves is almost identical and that the model predicts the ultimate load quite well. However, in the analytical model the snap-back effect is more pronounced which implies that the analytical model is a little too brittle.

In Fig. 4.6 results for the size of the fictitious crack are compared. It is seen that the size of the fictitious crack calculated by the analytical model is slightly smaller than that calculated by the numerical method before the real crack starts to grow (the ascending branch of the curves) and larger at the descending branch. The small kinks on the numerical curve are due to the discretization made in the numerical model. With a larger number of nodes in the midsection these kinks would disappear. In Fig. 4.8 the real crack lengths for the two models are compared. It is seen that the real crack grows faster in the numerical model.
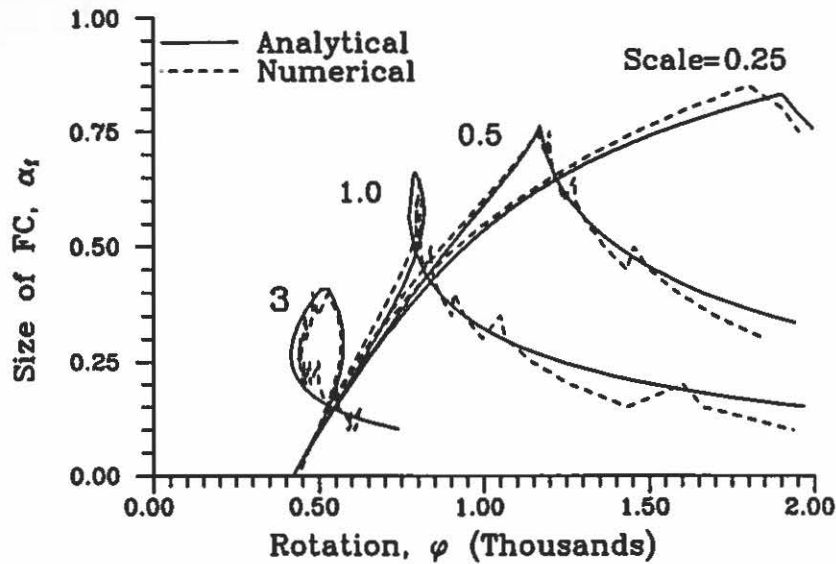
Fig. 4.6. Size of the fictitious crack for the analytical model and DSS. The loops are due to snap-back.
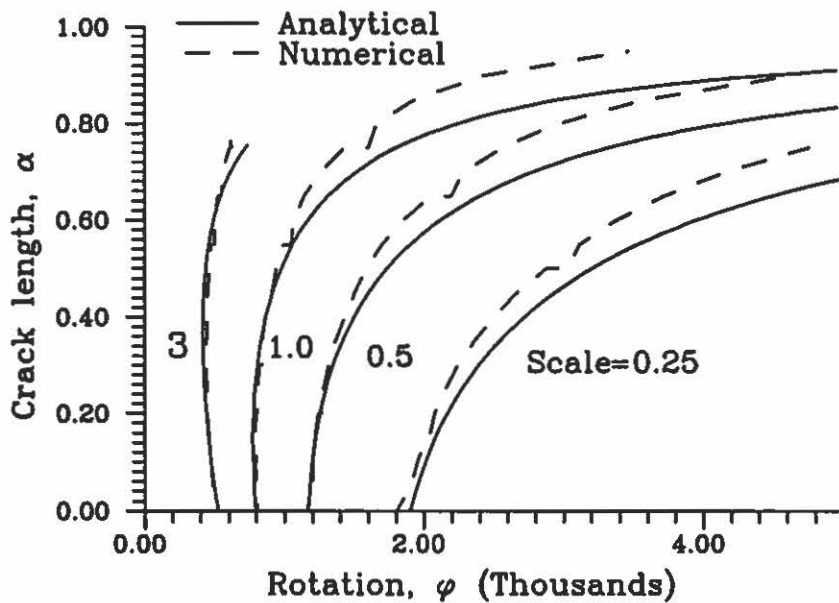

Fig. 4.7. Length of real crack for the analytical model and DSS.

In order to check the influence of the slenderness of the beam on the load displacement curves two additional slenderness number are considered. The slenderness is regulated by changing the beam length whereby a scale factor of 1.0 always corresponds to the beam height 100 mm. The results are seen in Fig. 4.8 and Fig. 4.9. It is seen that the analytical predicted by the analytical model still is almost identical to the numerical method. The stiffness of the beam with the slenderness ratio equal to 4 is, however, not identical. This is not a surprise since the Timoshenko assumptions are not accurate enough for beams with low slenderness ratios.

The peak loads, μ_{max}, predicted by the analytical and the numerical models are shown in
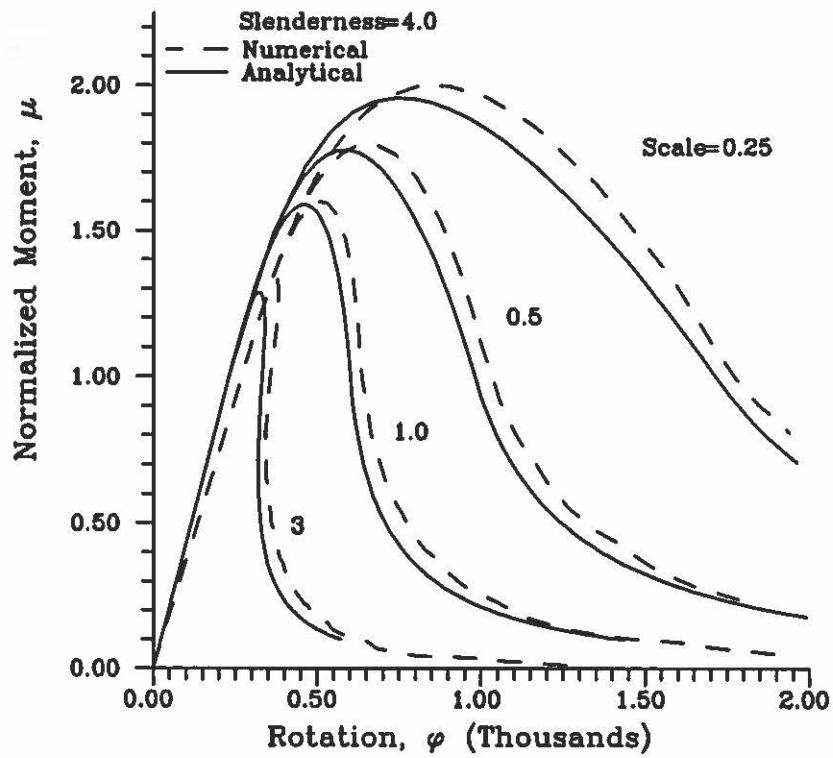
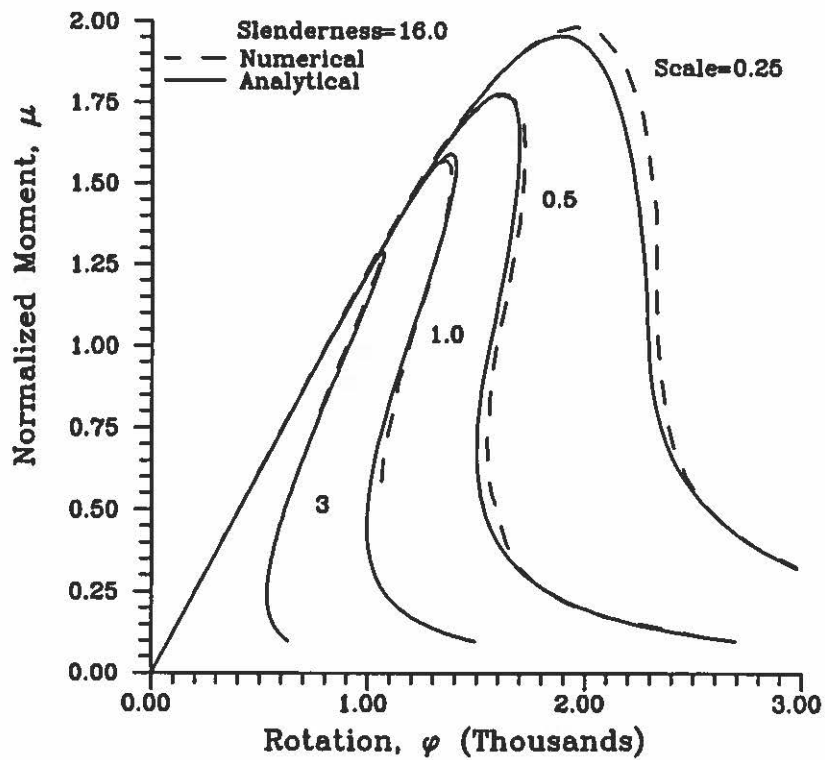Fig. 4.8 Load displacement curves for the slenderness ratio equal to 4.0.

Fig. 4.9 Load displacement curves for beam with slenderness = 16.0.

log-log scale in Fig. 4.10. Since there is no stress singularity included in the two models there
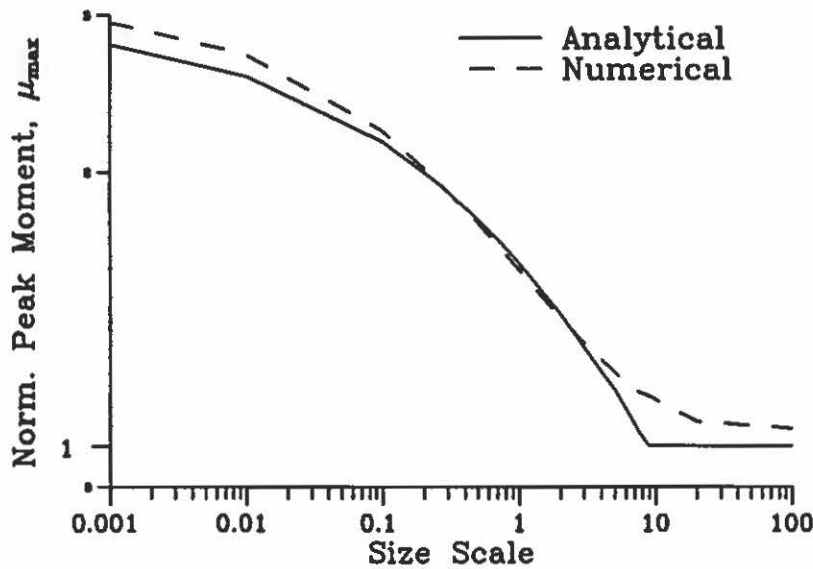
67

Fig. 4.10. Peak load at different size scales predicted by the model and by the DSS.

is no size effect beyond the critical size of the models. In the numerical model this limit will depend upon the material parameters and the number of nodes there are in the midsection (here the critical size scale is approximately 20).
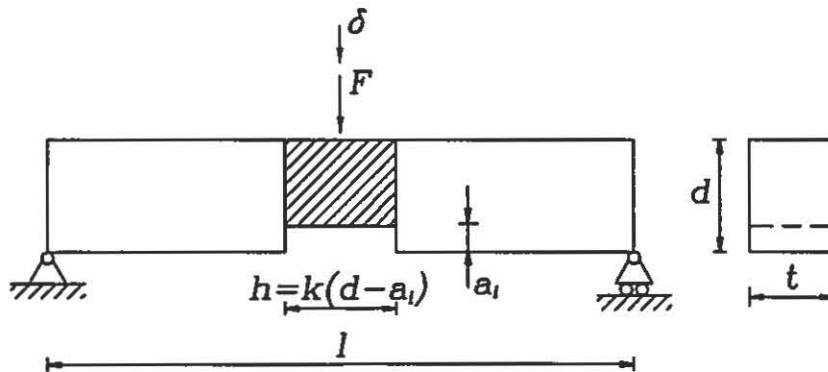

Fig. 4.11. Model of notched beam.

The model is extended to notched beams as indicated in Fig. 4.12 . The idea is to keep the width/depth ratio of the elastic layer by setting the width of the layer equal to k times the effective beam depth of the notched beam section $h = k(d-a_i)$, $k = 0.5$ where a_i is the depth of the notch. The modifications thus introduced imply that the brittleness number B for the layer is multiplied by a factor $(1-a_i/d)$. The total beam depth is still used in the formulas (4.94), (3.63), (4.95) and (4.106) whereas the effective beam depth $d_e = b-a_i$ is used in all other formulas. Results for different notch depth's are shown in Fig. 4.12 .

Comparing numerical results with results for the analytical model it can be concluded that deviations are relatively small. The errors introduced by the elastic layer and the assumption
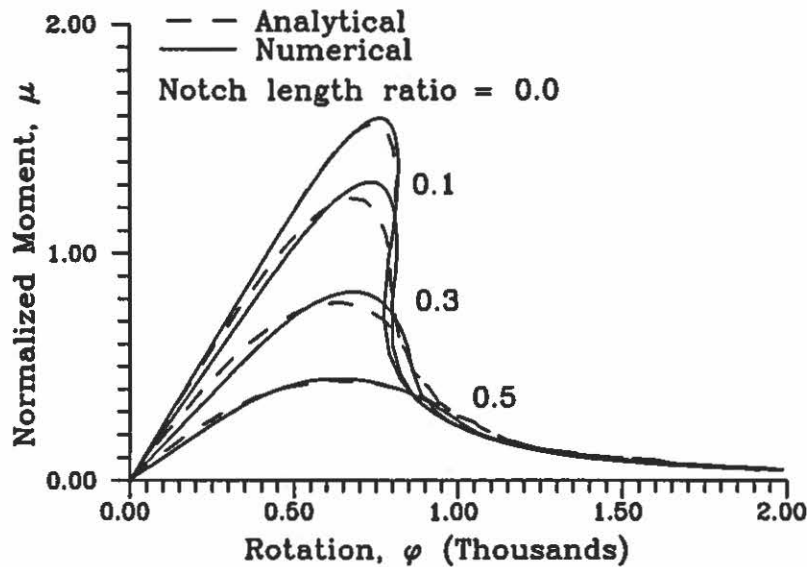
68

Fig. 4.12. Moment displacement curves for notched beams with three different notch depths.

of wedge-like crack-opening are typically smaller than errors due to the simple linear softening relation, Brincker and Dahl (1989).

When the size of the beam changes, the stress distribution in the partially fractured mid-section changes and so does the shape of the load-displacement curve. In the following a few closed form solutions are given for these size effects predicted by the analytical model.

An important parameter describing the stress distribution in the partially fractured mid-section, is the maximum size $a_{f,max}$ of the fictitious crack. Since $\partial a_f/\partial\theta > 0$ in phase II and $\partial a_f/\partial\theta < 0$ in phase III, a_f is largest at the end of phase II. Thus, the maximum size of the fictitious crack is found by combining eq. (4.99) and (4.101)

$$a_{f,max} = d(1-\sqrt{B}) \tag{4.111}$$

Thus, for small ductile beams the relative size of the fictitious crack is large and for large brittle beams the relative size of the fictitious crack approaches zero.

The way the load-displacement curve changes with size is more difficult to describe. One important parameter of the load-displacement curve is the peak load, μ_{max}. The peak load might be obtained from the condition $\partial\mu/\partial\theta_t =0$. However, no simple expressions have been derived for this case.

Another key-parameter for the load-displacement curve is the maximum slope S on the descending branch. The slope is found by taking the derivative of eq. (4.110)

$$1 = \frac{\partial\theta}{\partial\mu}\frac{\partial\mu}{\partial\theta_t}+(\gamma-1)\frac{\partial\mu}{\partial\theta_t} \tag{4.112}$$

from which

69

$$\frac{\partial \mu}{\partial \theta_t} = \left[\gamma - 1 + \frac{\partial \theta}{\partial \mu} \right]^{-1} \tag{4.113}$$

The steepest point on the descending branch of the load-displacement curve is at the transition from phase II to phase III, i.e. for $\theta = \theta_{cr}$. Thus, the minimum value of $\partial \theta / \partial \mu$ is found from eq. (4.105) and eq.(4.102) which together with eq. (4.113) yield the results

$$S = \frac{4B}{1 + \sqrt{B} - 4(\gamma - 1)B} \tag{4.114}$$

The quantity S is a kind of brittleness number for the structure, as described in Chapter 2. The larger maximum slope on the descending branch, the more brittle the behavior of the beam will be. The brittleness number varies between zero corresponding to ideal ductile behavior and infinity corresponding to the case where the maximum slope becomes infinite. If the point of infinity slope is exceeded, snap-back occurs, and the brittleness number S becomes meaningless. Thus, the brittleness number S only describes the brittleness of structures without snap-back on the load-displacement curve.
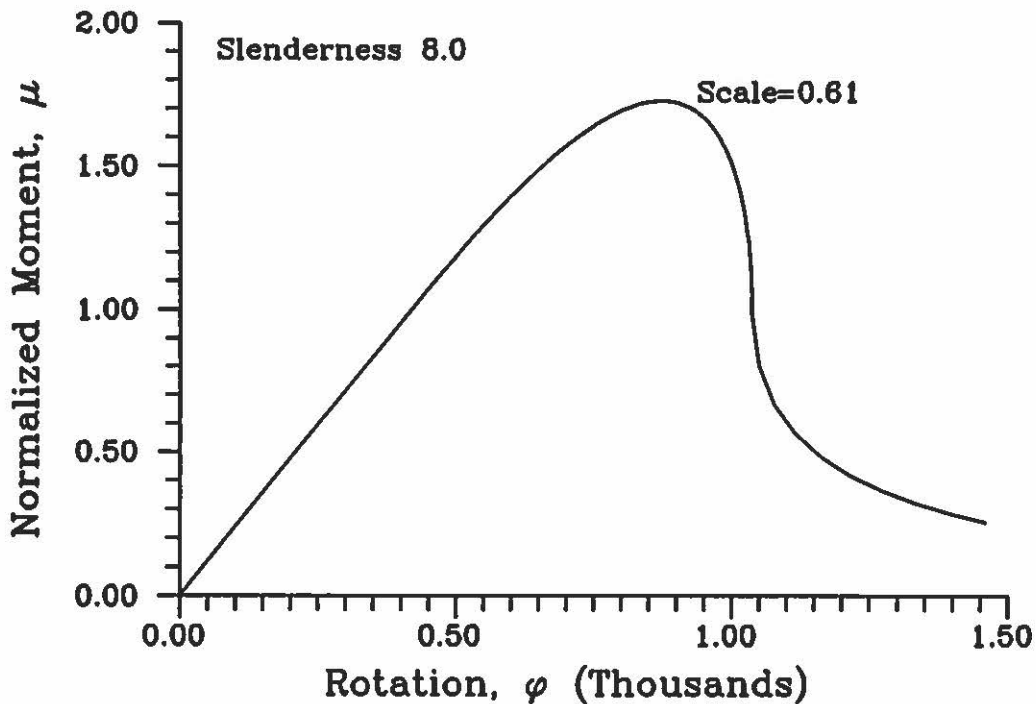

Fig. 4.13. Moment displacement curve for the beam with the slenderness = 8.0, on the critical size scale.

The maximum slope on the descending branch becomes infinite when the denominator in eq. (4.114) vanishes, i.e. when

$$1 + \sqrt{B} - 4(\gamma - 1)B = 0 \tag{4.115}$$

The solution to this equation defines a critical brittleness number for the elastic layer
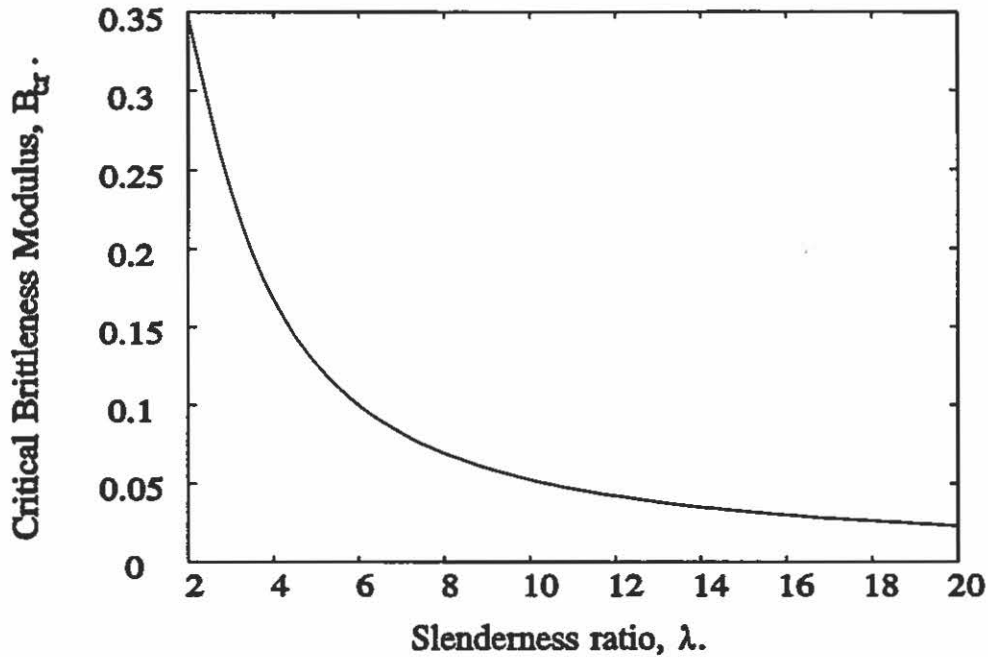
Fig. 4.14 The critical brittleness number as a function of the slenderness.

$$B_{cr} = \left[\frac{1+\sqrt{1+16(\gamma-1)}}{8(\gamma-1)} \right]^2 \qquad (4.116)$$

If the brittleness number B of the layer is larger than the critical brittleness number B_{cr} then there is snap-back on the load-displacement curve. Otherwise there is no snap-back. The critical brittleness number as dependent of the slenderness is seen in Fig. 4.14, and it is seen as the slenderness increases the critical brittleness decreases. This was also seen in the moment-rotation curves for the different slenderness numbers. For the standard beam the critical brittleness number is found as B_{cr}=0.069 corresponding to a scale factor of 0.615. The case is illustrated Fig. 4.13 where the results for the analytical model are shown for $B = B_{cr}$.

In the method presented by Ulfkjær et al. the equations are derived assuming that the beam is loaded with a concentrated load at the midsection and that the strain distribution in the elastic layer is constant. These two assumptions are conflicting, but this conflict is easily removed by assuming that the beam is loaded in four point bending, whereby the equivalent moment becomes constant between the loads.

It is also concluded that the model is not applicable for beams with a brittleness number equal to or larger than one. This restriction is not necessary, as it can be replaced by a condition stating that phase II is absent for brittleness numbers equal to or larger than one. Beyond this value the peak load can eventually be calculated by using LEFM, yielding the strong size effect described in chapter 2.

4.1.2 The Chuang and Mai Method.

This method was introduced by Chuang and Mai (1989) and is based on the crack band model. In the original paper four point bending specimens were considered and the descending branch of the constitutive relation was a power relation of the type

$$\sigma = \sigma_u \left[1 - \left(\frac{\epsilon - \epsilon_u}{\epsilon_c - \epsilon_u} \right)^n \right] \tag{4.117}$$

where , σ, is the stress, ϵ, is the strain, σ_u, is the tensile strength, ϵ_p, is the strain at peak load, ϵ_c, is the strain that corresponds to no stress transmission and, n, is the softening coefficient. Thus, all the parameters are material constants, see Fig. 2.15. By setting the minor span (the distance between the two loads) to zero and $n=1$, a three-point bending configuration with a linear softening relation is obtained. The procedure for establishing the governing equations is very similar to the previously presented method and the Chuang and Mai method will therefore only be roughly presented.

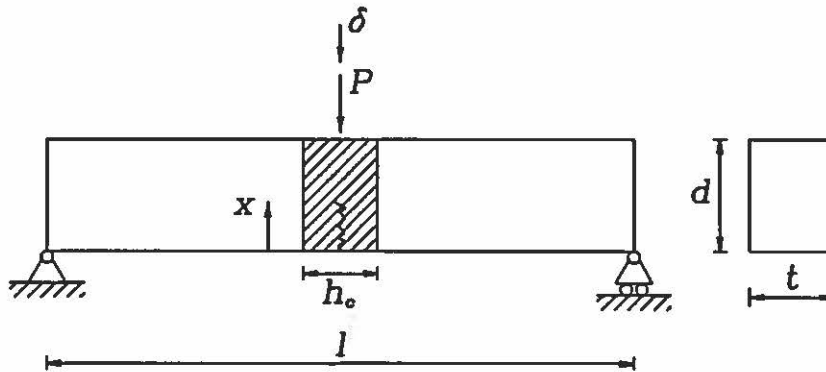Consider a beam with the length, L, depth, d, and thickness, t, with a crack band introduced

Fig. 4.15 The considered beam with a crack band around the midsection.

around the midsection with the thickness, h_c, see Fig. 4.15. The calculations are again divided into three phases, corresponding to those defined in the previous section. As a first approximation the two beam parts outside the crack band are assumed to perform rigid body deformations. The strain distribution in each phase are shown in Fig. 4.16, the stress distributions are as in the previous presented model, see Fig. 4.3.

Phase I
In phase I all the material is assumed to be linear elastic. By demanding equilibrium it is seen that the neutral axis is at $x=d/2$ whereby the normalized bending moment becomes

$$\mu(\kappa) = \frac{6M}{\sigma_u d^2 t} = \frac{\kappa}{2\eta} \tag{4.118}$$

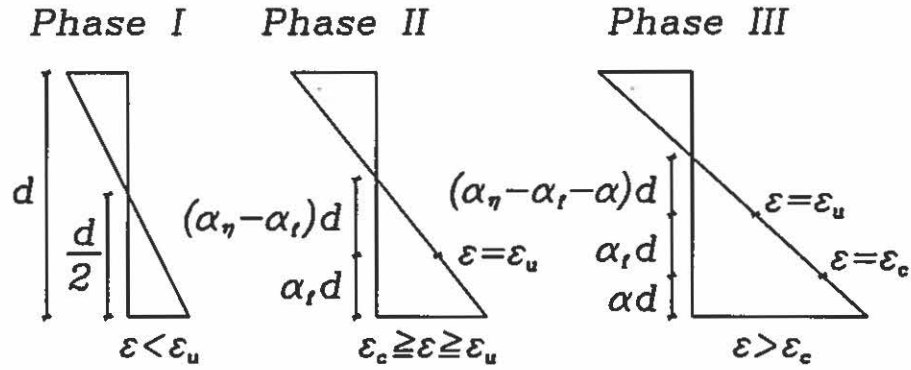where, M, is the moment in the midsection and the normalized curvature, κ, is defined as

72

Fig. 4.16. Strain distribution in the three phases.

$$\kappa = \frac{\epsilon^* \eta}{\epsilon_u x} \tag{4.119}$$

where ϵ^* is the strain at the lowest part of the elastic tensile zone and α_ηs the normalized size of the elastic tensile zone and $\eta = \dfrac{\epsilon_u}{\epsilon_c}$ is a material parameter which relates the maximum elastic strain to the separation strain. At the end of phase I the normalized moment and normalized curvature becomes

$$\mu = 1 \qquad \kappa = 2\eta \tag{4.120}$$

Thus, as in the Ulfkjær, Brincker and Krenk model a linear relationship is obtained.

Phase II
In this phase the fictitious crack starts to develop. The normalized size of the elastic tensile zone, α_η, is obtained by the condition that the strain at the tip of the process zone equals, ϵ_p, yielding: $\alpha_\eta = \eta/\kappa$, and the size of the softening zone, α_f, is obtained by requiring equilibrium

$$\alpha_f = 1 - \eta - \sqrt{(1-\eta)(\frac{2\eta}{\kappa} - \eta)} \tag{4.121}$$

It is immediately seen that the length of the process zone is only dependent on the curvature and the material parameter, η. This is in strong contradiction to the Ulfkjær, Brincker and Krenk model, where, α_f, also is a function of the size of the structure. Observe, however, the remarkable similarity between equations (4.121) and (4.99).

The corresponding normalized moment can be expressed as

$$\mu(\kappa) = \frac{2(1-\alpha_\eta-\alpha_f)^3}{\alpha_\eta} + 2\alpha_\eta^2 + 6\alpha_f\alpha_\eta + 3\alpha_f^2 - \left[\frac{\eta}{1-\eta}\right]\left[3\alpha_f^2 + 2\frac{\alpha_f^3}{\alpha_\eta}\right] \tag{4.122}$$

Phase II ends when the strain in the lowest fibre equals, ϵ_c, yielding the following condition to the curvature in phase II

$$2\eta \leq \kappa \leq \kappa_c \tag{4.123}$$

73

where $\kappa_c = 1 + \sqrt{\eta}$ is the normalized curvature which ends phase II. This corresponds to that the normalized moment is one in both limits, completely equivalent to the Ulfkjær, Brincker and Krenk method.

Phase III

The governing equations in the crack growth regime is obtained similarly to the previous phases. The size of the elastic tensile zone is obtained by considering similarly triangles, the size of the process zone is determined by the condition that the strain at the tip of the zone must equal, ϵ_u,

$$\alpha_f = \frac{\eta - 1}{\kappa} \tag{4.124}$$

the real crack length, α, is obtained by requiring equilibrium

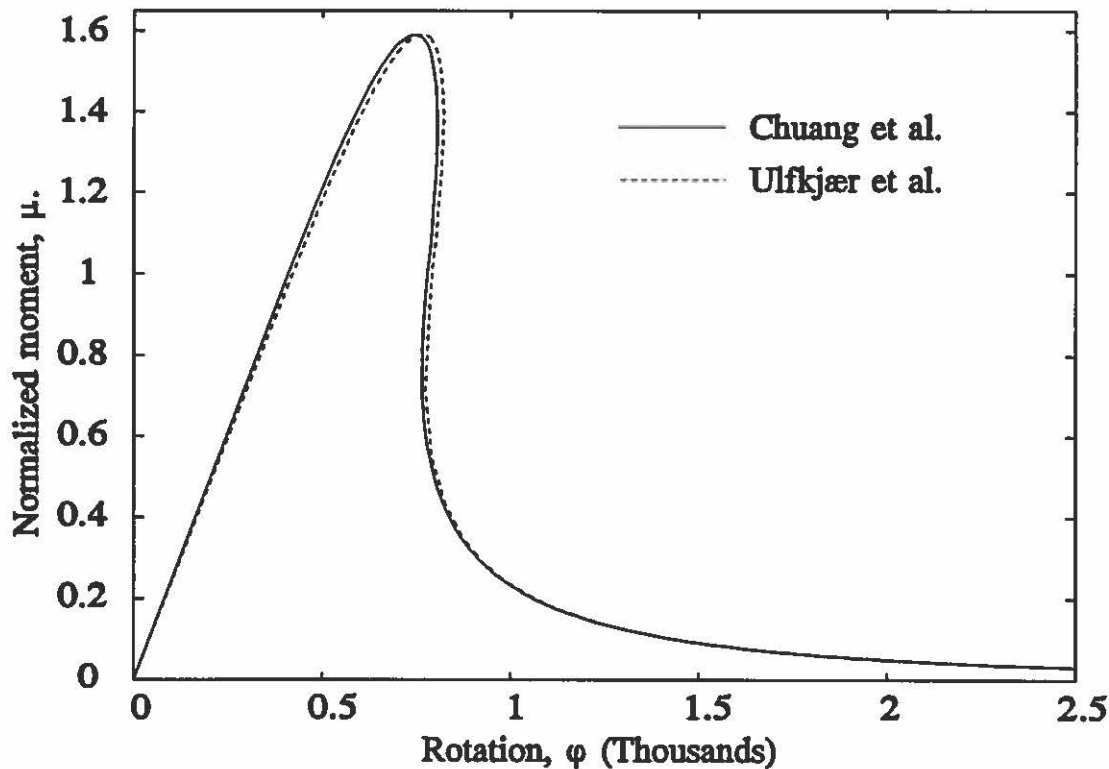$$\alpha = 1 - \frac{\kappa_c}{\kappa} \tag{4.125}$$

Fig. 4.17 Moment rotation curves predicted by the Chuang and Mai model and The Ulfkjær, Brincker and Krenk model.

and the equivalent normalized moment becomes

74

$$\mu(\kappa) = \left[\frac{\kappa_c}{\kappa}\right]^2 \qquad (4.126)$$

Again a remarkable similarity is seen between the two models, however, with the important difference that the governing parameters in the Chuang and Mai model are independent of the beam size.

The displacement, δ, is obtained by adding the displacement in the crack band to the displacement in the rest of the beam. Since the curvature in the crack band is constant, the deflection will be a circular arch with the radius $1/\kappa$, the deformations in the parts outside the crack band are calculated by assuming that the parts are cantilever beams loaded by, F, at the end. The total deflection, δ, becomes

$$\frac{\delta}{d} = \frac{L}{2d}\tan[\sin^{-1}(\frac{h_c\kappa\epsilon_c}{2d})] + \frac{1}{6}\eta\epsilon_c\gamma_2\mu \qquad (4.127)$$

where

$$\gamma_2 = \frac{\left[\frac{L}{d}-\frac{h_c}{d}\right]^3 - 2\left[\frac{h_c}{d}\right]^3 + 3\left[\frac{h_c}{d}\right]^2\left[\frac{L}{d}-\frac{h_c}{d}\right]}{\frac{L}{d}} \qquad (4.128)$$

For the standard beam introduced in the previous section, the size of the crack band, h_c, is set to 50 mm (which is the same as the size of the elastic layer) whereby, $\epsilon_u=0.00015$ and $\epsilon_c=0.00133$.

The normalized moment-rotation curve, where the rotation is determined by $\varphi = \frac{2\delta}{l}$, predicted by the Chuang and Mai model and the Ulfkjær Brincker and Krenk model are shown in Fig. 4.17. It is seen that the curves are almost identical and the difference is attributed to the difference in the method of calculating the elastic deformations. Normalized moment-rotation curves, with the same material properties, at different size scales, predicted by the Chuang and Mai method, are shown in, Fig. 4.18. It is seen that the peak value is not affected by the size scale and that the shape of both the ascending and the descending branch is changed.

The only equations where the size of the beam is included are in the deflection equations. This is due to the fact that during derivation of the governing equation an increase of the beam size alters the normalized amount of elastic energy stored in the beam parts outside the crack. It can therefore be concluded that the Chuang and Mai model is not able to predict size effects, but can only determine the difference in load carrying capacity for different materials. The Chuang and Mai model will therefore not be considered further.

4.1.3 The Llorca and Elices Method.

As was shown in chapter 2, virtual crack propagation can be considered by using LEFM. For the three-point bending geometry this has been done by Carpinteri (1982), Carpinteri (1986), Carpinteri (1989) and Biolzi et al. (1989). The Llorca and Elices method is an extension of
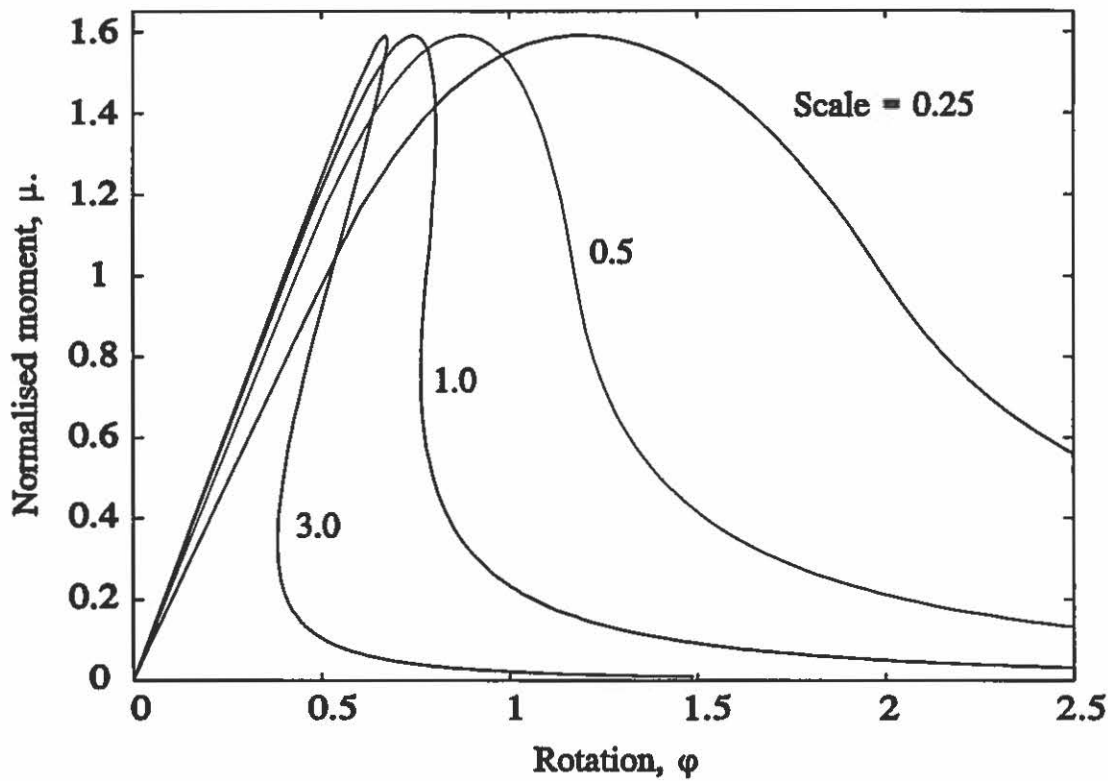
75

Fig. 4.18 Normalized moment rotation curves, as described by the Chuang and Mai model for the standard beam at different size scales.

this method since it assumes a linear elastic beam with a crack with the length, $a+a_f$, and a cohesive stress distribution acting on the crack edges described by the FC-model, see Fig. 4.19.

The method is based on findings of Foote et al. (1986), but the equations of the model described here are derived on basis of the work by Llorca and Elices (1990). The method is in general applicable for all structures and all loading conditions as long as it is possible to determine the appropriate stress intensity factors. Here the method will be tested on the three-point bending configuration.

The basic hypothesis of the model is that the crack opening profile is a known function, completely described by the length of the fictitious crack, a_f. Here it will be assumed that the crack profile is a straight line described by the function

$$w(x) = \frac{w_c}{a_f}(a+a_f-x) \qquad \text{for } 0 \leq x \leq a + a_f \qquad (4.129)$$

where, a, is the real crack length, a_f, is the length of the fictitious crack and, w_c, is the critical crack opening displacement. The beam is assumed to be linear elastic, loaded at the load point with the force, F, and at the crack tip with cohesive stresses (internal loading) described by the constitutive relation, $f(w)$, and the crack opening profile, $w(x)$. Since the beam is linear elastic the stress intensity factor, K, is determined by using the principle of
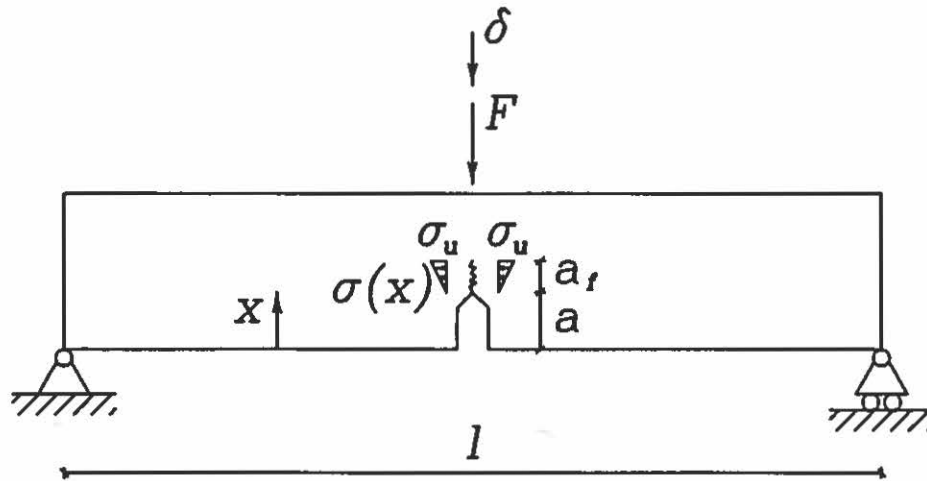
76

Fig. 4.19 The considered beam geometry, with a cohesive crack in front of an initial real crack tip.

superposition

$$K = K_\sigma + K_F \tag{4.130}$$

where, K_σ, is the stress intensity factor due to the cohesive stresses and, K_F, is the stress intensity factor due to the external load. One of the basic assumptions in the FC-model is that there is no stress intensity at the crack tip, which implies that the stress intensity factor is equal to zero

$$K = 0 \quad \Rightarrow \quad K_\sigma = -K_F \tag{4.131}$$

For the three-point bending specimen with an initial notch of length, a, the stress intensity factor for the external load, K_F, can be determined by, ASTM (1974),

$$K_F = \frac{3lF}{2d^2t}\sqrt{a}\, Y_F\,(a/d) \tag{4.132}$$

where the dimensionless shape function, $Y_F(a/b)$, for $\lambda = 8$ is given by

$$Y_F\,(a/d) = 1.93 - 3.07(a/d) + 14.53(a/d)^2 - 25.11(a/d)^3 + 25.8(a/d)^4 \tag{4.133}$$

The stress intensity factor for a concentrated unit load at, x, on the crack edge for an infinitely long beam is determined by, Tada et al. (1973)

$$K_{con}(a,x,d) = \frac{2}{t\sqrt{\pi a}}\, Y_{con}(a/d, x/a) \tag{4.134}$$

where

$$Y_{con}(a/d,x/a) = \frac{3.52(1 - x/a)}{(1 - a/d)^{3/2}} - \frac{4.35 - 5.28x/a}{\sqrt{1 - a/d}}$$

(4.135)

$$+ \left\{ \frac{1.30 - 0.30(x/a)^{3/2}}{\sqrt{1 - (x/a)^2}} + 0.83 - 1.76x/a \right\} [1 - (1 - x/a)a/d]$$

and by applying the principal of superposition the stress intensity factor for the stress distribution, $\sigma(w\{x\})$, becomes

$$K_\sigma(a,a_f) = \int_a^{a + a_f} \frac{2}{\sqrt{\pi(a + a_f)}} \, Y_{con}(\frac{a + a_f}{d}, \frac{x}{a + a_f}) \, \sigma\{w(x)\} \, dx$$

(4.136)

whereby the external load, F, can be determined by using eq. (4.131).

In order to obtain compatibility it is necessary to check if the assumed crack opening profile corresponds to the one calculated by using displacement formulas according to LEFM. In the following the necessary displacement and crack opening displacement equations will be derived using the energy principals described by Llorca and Elices (1990a) and Bosco et al. (1990).

Instead of considering the entire cohesive stress distribution a concentrated force, F_2, at the crack edge is considered together with the applied load, F_1, with the corresponding
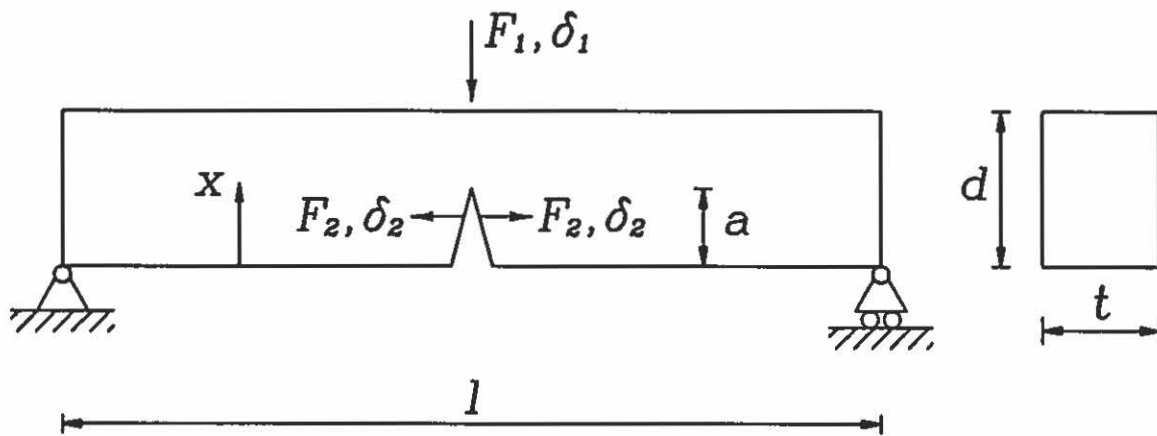

Fig. 4.20 Beam with two concentrated loads for determination of compliances.

displacements, u_1 and, u_2, see Fig. 4.20. The total potential energy, Λ, stored in the system is

$$\Pi = - \frac{1}{2}F_1\delta_1 - \frac{1}{2}F_2\delta_2$$

(4.137)

where the displacements are given by the compliances

78

$$\delta_1 = C_{11}F_1 + C_{12}F_2$$
$$\delta_2 = C_{21}F_2 + C_{22}F_2 \tag{4.138}$$

The energy release rate is given by

$$G = - \frac{\partial \Pi}{t \partial a}$$
$$= \frac{1}{2}F_1^2 \frac{\partial C_{11}}{t \partial a} + \frac{1}{2}F_2 \frac{\partial C_{22}}{t \partial a} + F_1 F_2 \frac{\partial C_{12}}{t \partial a} \tag{4.139}$$

where Maxwell-Bettis theorem has ben applied. The energy release rate can be written as

$$G = \frac{K^2}{E} = \frac{(K_1 + K_2)^2}{E}$$
$$= \frac{K_1^2}{E} + \frac{K_2^2}{E} + \frac{2K_1 K_2}{E} \tag{4.140}$$

Since the terms in (4.140) are linearly independent the compliances are determined as

$$C_{ij}(a + a_f) = \frac{2t}{E} \int_0^{a + a_f} K_i K_j \, d\omega \tag{4.141}$$

where, K_i, and, K_j, are the stress intensity factors for a unit load. The displacements can then be determined by using eq. (4.138). When a distributed stress distribution is applied along the crack faces the principle of superposition can be applied

$$\delta_F = C_{FF}(a + a_f)F + \int_a^{a + a_f} C_{Fx}(a + a_f, x) \, \sigma(x) \, t \, dx \tag{4.142}$$

$$\delta(x) = C_{xF}(a + a_f, x)F + \int_a^{a + a_f} C_{x\check{x}}(a + a_f, \check{x}, x) \, \sigma(\check{x}) \, t \, d\check{x}$$

where $C_{x\check{x}}$ is the displacement in, x, from a unity load in, $\check{x}$, is given by

$$C_{x\check{x}}(a + a_f, \check{x}, x) = \frac{2t}{E} \int_{\max(x,\check{x})}^{a + a_f} K_{\check{x}}(\omega, x) K_x(\omega, \check{x}) \, d\omega \tag{4.143}$$

The deflection of the beam is then given as the sum of the deformation due to the crack and the deformation of an uncracked beam.
By setting $x = a_f$ in eq. (4.142) the crack tip opening displacement, *CTOD*, is calculated

$$CTOD = \delta(a + a_f) = C_{aF}(a + a_f) F + \int_a^{a + a_f} C_{ax} \, \sigma\{w(x)\} \, t \, dx \tag{4.144}$$

where

$$C_{aF}(a,a_f) = \frac{2t}{EF} \int_0^{a+a_f} K_F(a + a_f)K_{con}(x,a + a_f)\,dx$$

$$C_{ax}(a,a_f,x) = \frac{2t}{E} \int_x^{a+a_f} K_{con}(\omega,x)\,K_{con}(\omega,a + a_f)\,d\omega$$

(4.145)

By comparing the, $CTOD$, with the assumed value, w_c, it is possible to check if the assumed crack opening profile described by, a_f, is correct. If the, $CTOD$, is higher than, w_c, then, a_f, has to be increased, and vice versa. The actual length of the fictitious crack is then calculated following an iteration procedure. The above formulas can only be calculated numerically, and care should be taken with the singular stress intensity factors during the numerical integration.

Llorca and Elices suggest that by using this known value of, a_f, it is possible to calculate the entire force-displacement relation. This seems to be a crude approximation. According to the numerical methods and to the Ulfkjær, Brincker and Krenk method, where it was shown that, a_f, initially is zero then growing to its maximum value and then decreasing, and it was seen that the maximum size of, a_f, was obtained when $CTOD=w_c$. Thus, in order to improve the model Llorca and Elices have calculated, a_f, in each loading step in a subsequent paper, Llorca and Elices (1990b), however, without comparing the method with numerical results or with the previous sketched method and without giving the results of, a_f.

As was seen in the previous section, it is only at the descending branch the real crack starts to grow, and it seems evident that the method should be extended, so the development of the fictitious crack can be calculated. Actually the peak value is reached during the development of the fictitious crack.

The method here suggested is equivalent to the Llorca and Elices method, but is divided into two phases. In the first phase the fictitious crack develops and in the second phase the real crack grows. At the first loading steps the desired opening is not set to the critical opening, but an opening which is a certain fraction of the critical opening, e.g. $w_{des}=w_c/n$, where, n, is the fraction and w_{des} is the new desired opening. The above outlined iteration method is then applied until the $CTOD$ is equal to the desired value. The desired opening is then increased and the iteration is performed again. This is done, n, times corresponding to that the desired opening is equal to the critical opening. Then the second phase begins which corresponds to the extended Llorca and Elices method. The method corresponds to that the loading in phase I is crack tip opening displacement controlled and in phase II is crack length controlled. This suggestion will yield a considerable improvement of the Llorca and Elices method, and will only yield a small increase in the total calculation time since it is known that in the initial phase, a_f, there is an increasing function of the desired opening and a decreasing function in the second phase of the real crack length.

In the following the different procedures of this method are compared, see Fig. 4.21.

4.1.4 Model Evaluation.

Three methods based on three different assumptions have been presented.
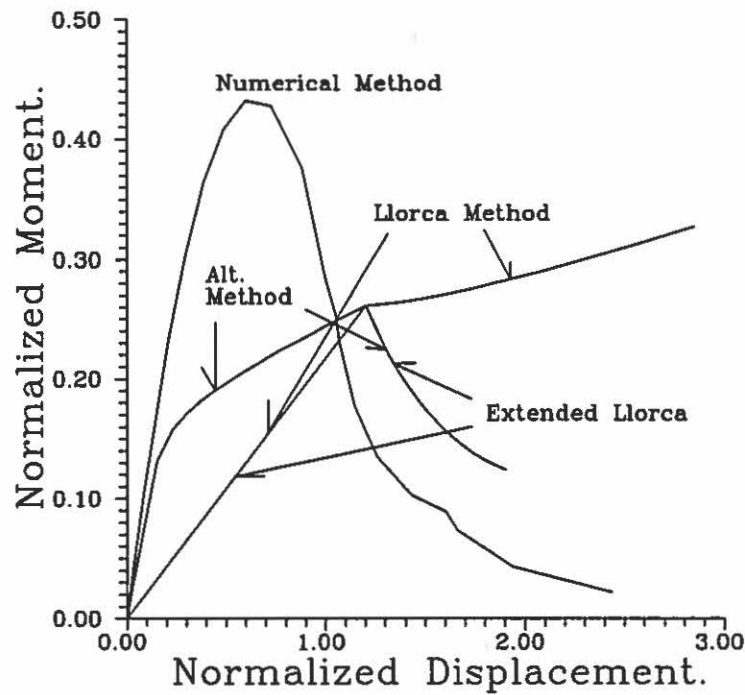
Fig. 4.21 The different methods as introduced by Llorca and the author.

The Ulfkjær et al. model is based on the development of a fictitious crack with a linear softening relation in the midsection of an elastic layer. The layer is assumed to be linearly dependent on the beam depth. The moment rotation curves calculated by the model is almost identical to the ones calculated using a numerical model at different size scales and slenderness ratios. The great advantages of the model are its simplicity and that the governing equations are simple and explicit whereby the calculating time is minimal. Further it is possible to derive analytical results, e.g. the maximum size of the fictitious crack and the slope of the descending branch. The disadvantage is that the model is only applicable for a linear or piece by piece linear softening relation and that a size effect relation has not been found. However, approximate solutions can be obtained for other softening relations than the linear by assuming that the displacement field in the midsection of the layer is linear.

The Chuang and Mai model is based on the crack band model, on the Bernoulli assumptions, and on an exponential softening relation. The governing equations is derived on the basis of the same stress distributions as in the Ulfkjær et al. model and by assuming a linear softening relation the equation becomes almost identical, with the important difference that the Chuang and Mai model not is able of predicting size effects, which is a great disadvantage of the model. The model is, however, able of comparing the load carrying capacity of identical structures with different softening relations.

The third model is based on LEFM and on the assumption that closing stresses acts on the edges at the crack tip, described by the fictitious crack model. By assuming that there is no stress intensity factor at the crack tip, the external load and the crack tip opening displacement can be calculated, which shall equal the critical crack opening displacement. By performing an iterative procedure, which involves numerical integration of a double integral, the length of the fictitious crack can be calculated. By using this length the load displacement curve can

be calculated, this approximate procedure is used in order to make the method simple and fast. The model is then extended by the author whereby the formation of the fictitious crack is calculated.

Though the basic idea appears to be sound, results obtained by using this model is disappointing. By using the original method the even descending branch is missing, and the stiffness of the structure is miscalculated. By using the extended version where the length of the fictitious crack is calculated at each loading step, the descending branch is obtained, and some similarity between a numerical method is observed. However, the stiffness and the peak load is estimated unsatisfactory. In the procedure suggested by the author the initial stiffness is predicted better, but the shortcoming is that the peak load not is predicted with sufficiently accuracy. It is therefore concluded that more research is needed in order to improve the method.

4.2 Reinforced Concrete.

To the authors knowledge only two analytical models which describe crack propagation in reinforced concrete exist. The two models are conceptual different since the first model, the Carpinteri model, is based on LEFM whereas the later is based on the fictitious crack model and an elastic layer in the midsection. The two models are presented, compared and evaluated.

4.2.1 The Carpinteri Method.

This method is based strictly on LEFM and was introduced by Carpinteri (1981), Carpinteri(1984), Carpinteri (1985), Carpinteri (1988) and later refined by Bosco et al.(1991).
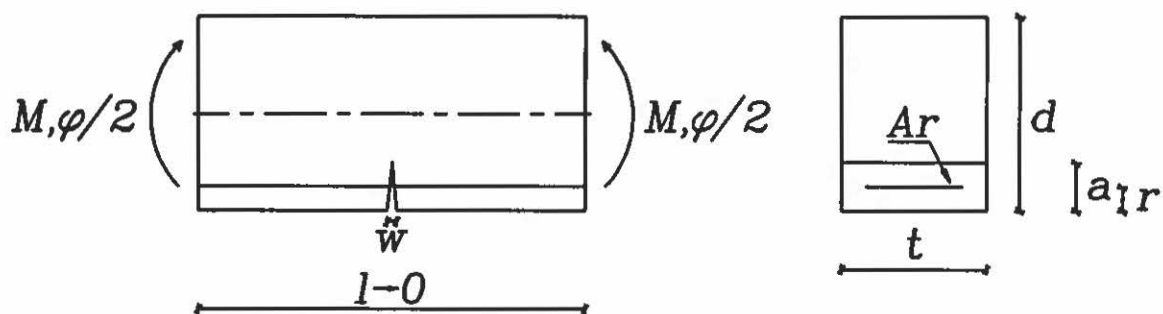

Fig. 4.22 Beam segment from reinforced beam made of a perfectly brittle material.

Consider the reinforced concrete beam segment in Fig. 4.22, with the depth, d, thickness, t, crack length, a, and the reinforcement area, A_r, in the depth, r, loaded with the external moment, M. The concrete is assumed to be linear elastic, perfectly brittle described by the modulus of elasticity, E, and the fracture toughness, K_c, and the reinforcement is assumed to be rigid, perfectly ductile described by the yielding strength, σ_y.

The reinforcement is now removed and an external steel force, F_s, is introduced which corresponds to the stress state in the reinforcement. The stress intensity factor, K, for the beam segment is then written as

$$K = K_M + K_{F_s} \tag{4.146}$$

where, K_M, is the stress intensity factor due to the external moment and, K_{F_s}, is the stress intensity factor due to the steel force. The stress intensity factors are given in Tada et al. (1973) as

$$
\begin{aligned}
K_M &= \frac{M}{d^{3/2}t} Y_M(a/d) \\
K_{F_s} &= \frac{-2F_s}{h^{1/2}t} Y_{F_s}(a/d, r/d)
\end{aligned}
\tag{4.147}
$$

where

$$
Y_M(a/d) = 6(1.99(a/d) - 2.47(a/d)^{3/2} + 12.97(a/d)^{5/2} - 23.17(a/d)^{7/2} + 24.8(a/d)^{9/2})
\tag{4.148}
$$

$$
Y_{F_s}(a/d, r/a) = \frac{2}{\sqrt{\pi d}} Y_{con}(a/d, r/a)
$$

where, $Y_{con}(a/d, r/a)$, is given in eq.(4.135). The additional rotation, ϕ, of the segment due to the crack, produced by the two loads are given by the compliances

$$\phi(a/d, h/a) = C_{MM}(a/d)\, M + C_{MF_s}(a/d, r/a)F_s \tag{4.149}$$

and the crack opening displacement, $w(x)$, at the center of the reinforcement is given by

$$w(a/d, r/a) = C_{F_sM}(a/d, r/a)M - C_{F_sF_s}(a/d, r/a)F_s \tag{4.150}$$

The compliances can be derived by using energy principles similar to the one shown in section 4.1.3, Bosco et al. (1990)

$$
\begin{aligned}
C_{MM} &= \frac{2}{Etd^2} \int_0^{a/d} Y_M(\omega)^2 \, d\omega \\
\\
C_{F_sF_s} &= \frac{2}{Et} \int_{r/d}^{a/d} Y_{F_s}(\omega, r/d)^2 \, d\omega \\
\\
C_{MF_s} &= \frac{2}{Etd} \int_{r/d}^{a/d} Y_M(\omega) Y_{F_s}(\omega, r/d) \, d\omega
\end{aligned}
\tag{4.151}
$$

before the steel is yielding the crack opening displacement is assumed to be zero

$$w = 0 \quad \Rightarrow$$

$$\frac{M}{F_s d} = r'' \ (a/d, r/a) \tag{4.152}$$

where

$$r'' \ (a/d, r/a) = \frac{C_{F_s F_s}(a/d, r/a)}{C_{F_s M}(a/d, r/a) d} \tag{4.153}$$

from which the force in the reinforcement caused by the external moment is calculated. In the limit of plastic flow the moment becomes

$$M_p = F_s^p d r'' \tag{4.154}$$

where $F_s^p = \sigma_y A_r$. By considering eq.(4.146) the fracture moment, M_F (the crack is extending when $K = K_c$) can be determined as

$$\frac{M_F}{K_c b^{3/2} t} = \frac{1}{Y_M} + \frac{Y_{F_s}(a/d, h/a)}{Y_M(a/d)} N_p \frac{F_s^F}{F_s^P} \tag{4.155}$$

where , F_s^F, is the steel force at fracture and, N_p, is a brittleness number defined by

$$N_p = \frac{\sigma_y d^{1/2}}{K_c} \frac{A_r}{A} \tag{4.156}$$

where, $A = t d$, is the cross sectional area. Before the steel is yielding , F_s^F, is determined through eq.(4.153), whereby the fracture moment becomes

$$\frac{M_F}{K_c h^{3/2} t} = \frac{1}{Y_M - \dfrac{Y_{F_s}}{r''}} \qquad \text{for} \qquad \varphi(F_s^F) \leq \varphi(F_s^p) \tag{4.157}$$

and when the steel is yielding, $F_s^F = F_s^p$, viz

$$\frac{M_F}{K_c h^{3/2} t} = \frac{1}{Y_M} + \frac{Y_{F_s}}{Y_M} N_p \qquad \text{for} \qquad \varphi(F_s^F) > \varphi(F_s^p) \tag{4.158}$$

It is hereby possible to consider virtual crack propagation, where the controlling parameter is the crack length, a/d.

In the limit state of virtual crack growth the ultimate moment becomes

$$M_u = F_s^p (1 - r/d) \qquad \Rightarrow$$

$$\frac{M_u}{K_c d^{3/2} t} = N_p (1 - r/d) \tag{4.159}$$

Bosco et al. concluded hereby that the moment-rotation curve will consist of three phases, a

linear elastic part until the fracture moment is reached given by eq. (4.155) . As the crack length increases the moment decreases until the minimum moment, M_{min}, is reached. If the minimum moment is less than the ultimate moment the fracture moment will eventually increase until it reaches the ultimate moment, which the author agrees upon. However, as will be shown this conclusion can not be made with the presented shape functions.

In order to be able to make comparisons between experiments and the model the load displacement curves should be considered. The load-displacement curves can be determined by considering the sum of the displacement due to the cracking, δ_c, caused by, ϕ, and the elastic deformation of a Timoshenko beam without a crack, δ_e, as suggested by Hededal and Kroon (1991)

$$\delta = \delta_t + \delta_e = \frac{\phi L}{4} + \delta_e \qquad (4.160)$$

In order to check the Carpinteri model it has been implemented on computer. The results are, however, disturbed by an erroneousness shape function, Y_{con}, which in Bosco et al. is given as

$$Y_{con}(a/d,x/a) = \frac{3.52(1 - x/a)}{(1 - a/d)^{3/2}} - \frac{4.35 - 5.28x/a}{(1 - a/d)^{3/2}}$$

$$\qquad (4.161)$$

$$+ \left\{ \frac{1.30 - 0.30(x/a)^{3/2}}{(1 - (x/a)^2)^{-1/2}} + 0.83 - 1.76x/a \right\} \left[1 - (1 - x/a) \right]$$
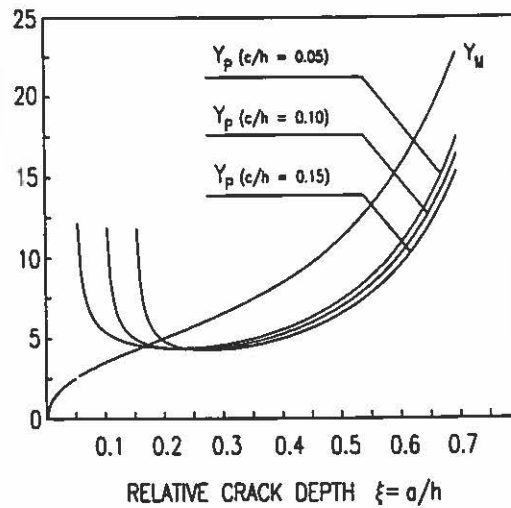
Fig. 4.23 The shape functions as presented in Bosco et al. (1990).

By using this shape function the fracture moments calculated for virtual crack propagation are negative, and they are therefore not consistent. The shape functions used by Bosco et al. are, however, also presented graphically and are shown in Fig. 4.23. The shape functions calculated using eq.(4.161) and eq.(4.148), (4.161) are shown in Fig. 4.22, Fig. 4.25, and it
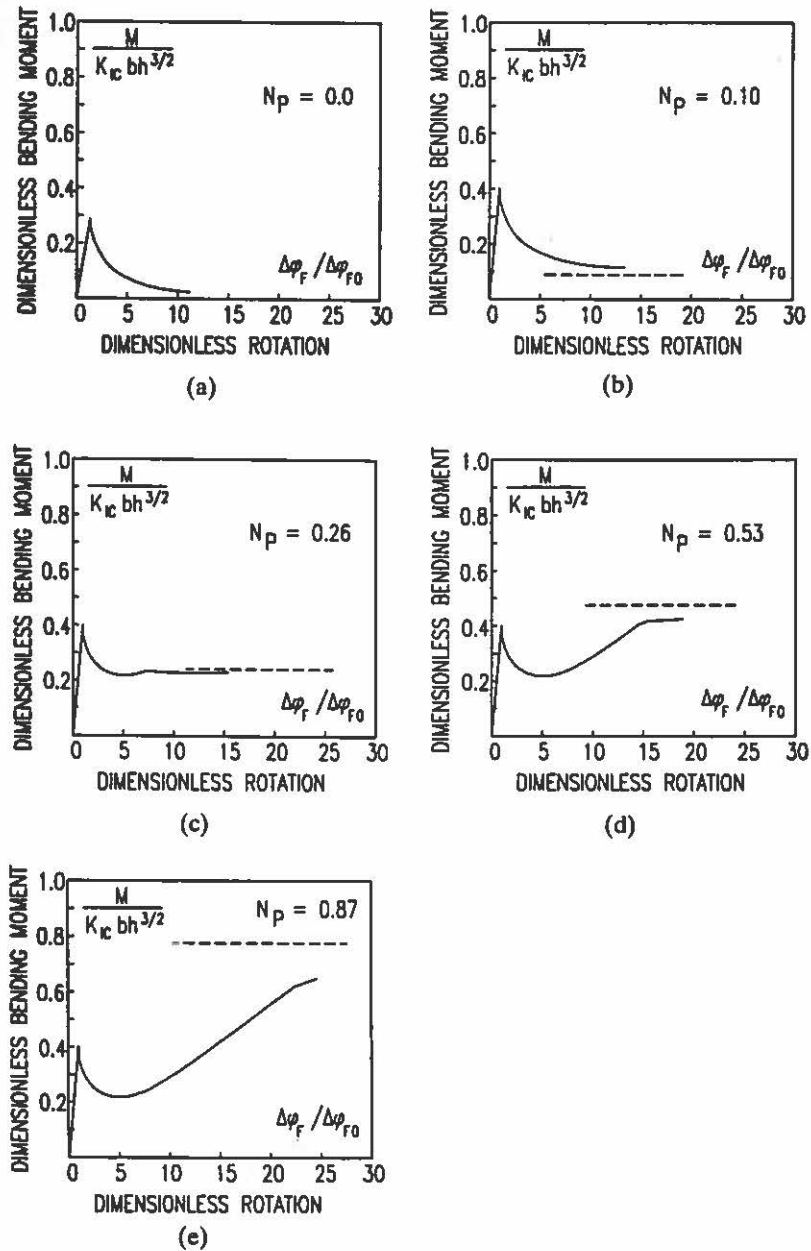
Fig. 4.24 Moment rotation curves for different brittleness numbers as presented in Bosco et al. (1990).

is seen that Y_{F_s} is completely different from the one used by Bosco et al. (1990) while Y_M is exactly the same.

For the standard beam the fracture toughness is calculated according to $K_c = \sqrt{EG_F}$. The other material parameters are shown in Tabel 4.2. By using the presented method a normalized moment-rotation curve for the reinforced standard beam is shown in Fig. 4.26, where the rotation is normalized to the first cracking rotation, ϕ_0.

The initial shape of the moment rotation curve is equivalent to Bosco et al., however, the rest
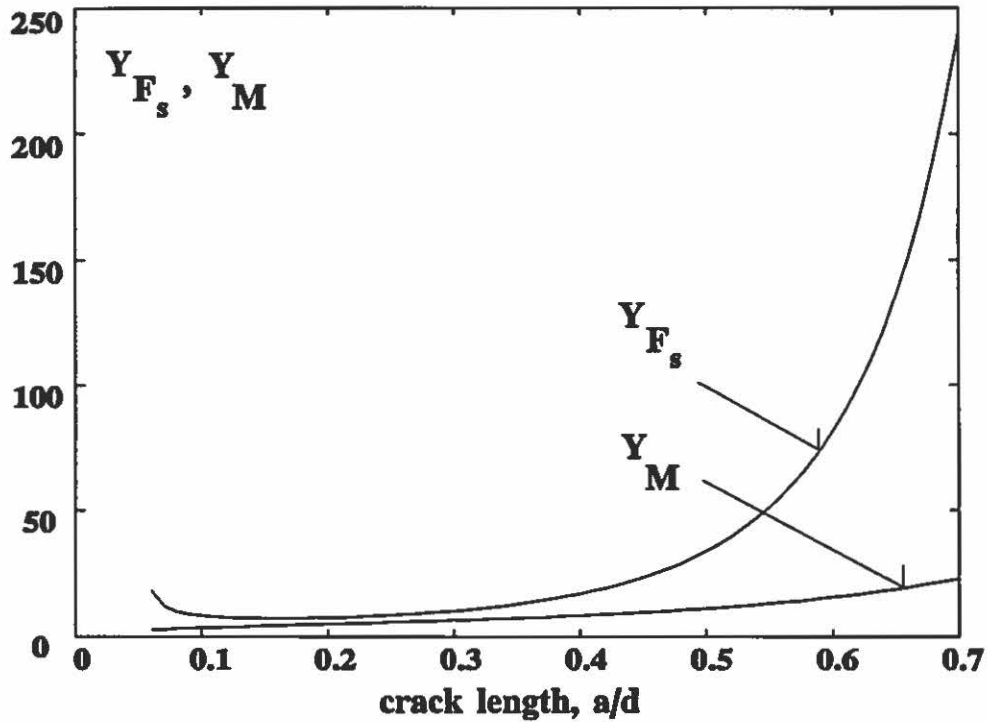
Fig. 4.25 Shape functions according to Tada et al. (1973).

Fracture Toughness, K_c [Nmm$^{-3/2}$]	44.7
Reinforcement area, A_r [mm^2]	29
Relative reinforcement position, r/d	0.05
Brittleness number, N_p	0.26
Yielding strength, σ_y [N/mm^2]	400

Tabel 4.2 Parameters which describe the reinforced standard beam.

of the curve is completely different. The minimum moment is much larger using the presented indeed different from the one shown in Fig. 4.23, and it is actually larger than the ultimate moment. The second kink on the curve indicates where the steel starts to yield, and after that rotation the moment was supposed to decrease, and as is seen that is not the case. When the steel is yielding eq.(4.158), is applied. Since the first term is decreasing, and N_p is constant the moment-rotation curve is highly dependent by the ratio $\dfrac{Y_{F_s}}{Y_M}$, see Fig. 4.27. If the shape of the moment rotation curves should be as found by Bosco et al., then this ratio should be decreasing or at least constant.
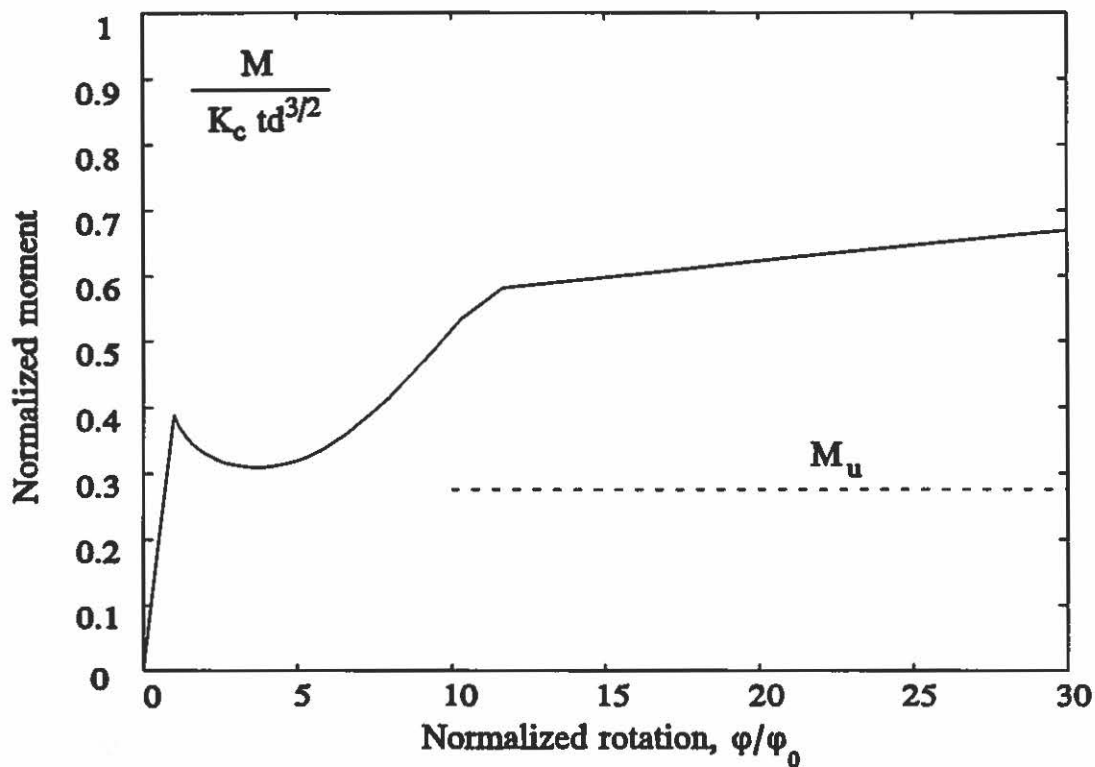
Fig. 4.26 Normalized moment-rotation curves by using the Carpinteri method.

The author feel that the basic ideas describing the Carpinteri model is sound, but it has not been possible to determine, moment rotation curves as described in Bosco et al. (1990). It would indeed be nice to see the mathematical expressions used to describe the shape functions used by Bosco et al. (1990).

4.2.2 The Hededal, Kroon, Ulfkjær and Brincker Method.

This method is an extension of the Ulfkjær, Brincker and Krenk Method with reinforcement introduced in the elastic layer. The model was developed in junction with the Masters thesis of Hededal and Kroon (1991) and this presentation follows their approach.

Consider the beam in Fig. 4.28, reinforced with the reinforcement area, A_r, introduced in the depth, r. The reinforcement is assumed to be linear elastic, perfectly plastic described by the modulus of elasticity, E_s and the yielding strength, σ_y. The concrete is described as in section 4.1.1. The approach of obtaining the governing equations is identical to the method without reinforcement. Thus, three phases are considered, however, each phase is divided into two: a) the steel remains elastic or b) the steel yields. The strain condition in the steel in the elastic layer is assumed to be equal to the strain condition in the layer. The stress distribution and the shape of the load displacement curve are shown in Fig. 4.29.

The strain distribution, $\epsilon(y)$, in the midsection is obtained by considering similar triangles
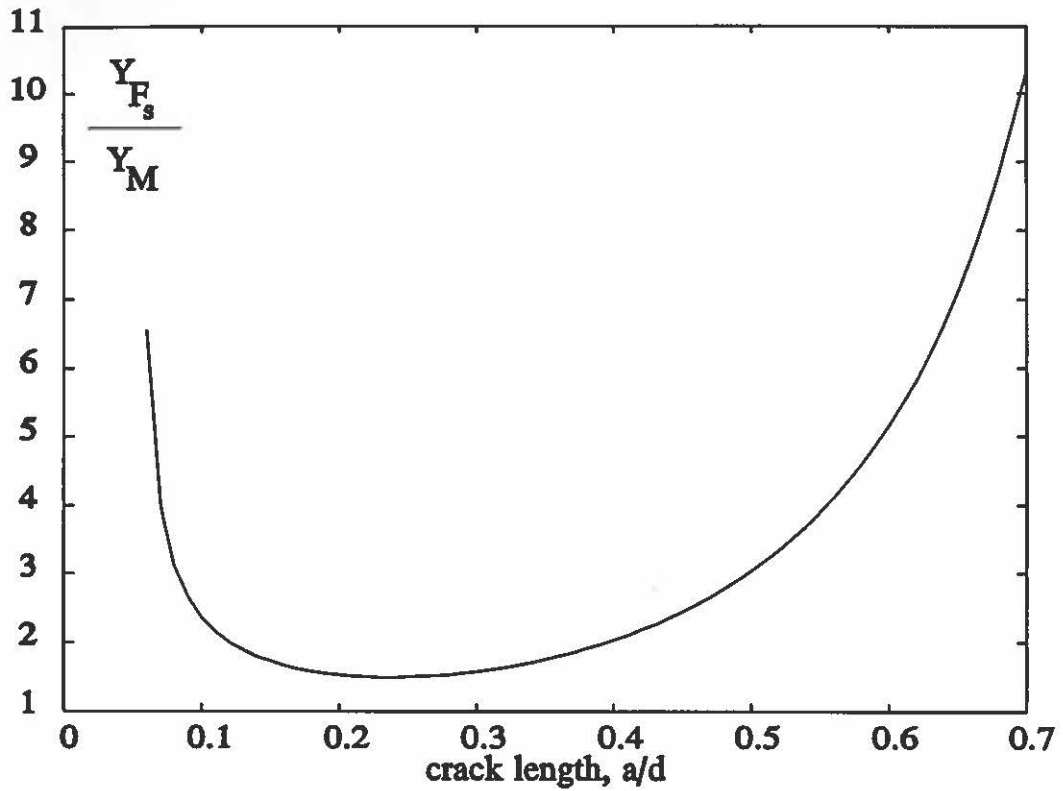
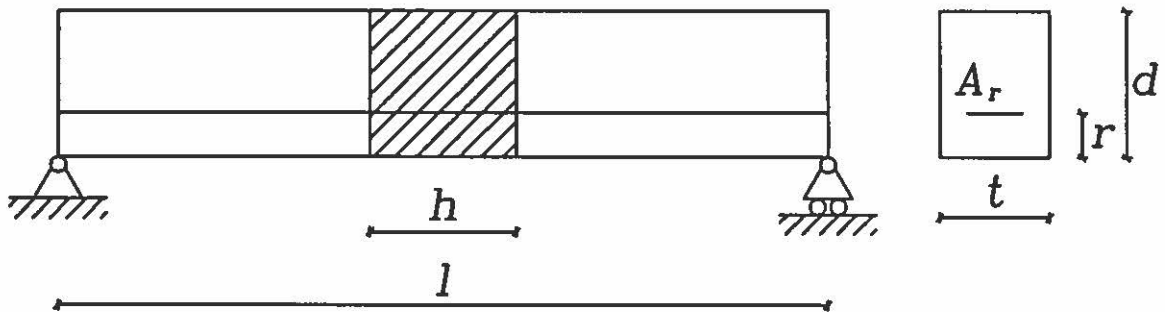Fig. 4.27. The ratio between the two shape functions used in the Carpinteri method.

Fig. 4.28 The considered beam used in the Hededahl et al. method.

$$\epsilon(y) = 2\theta\epsilon_u(\alpha_\eta - \frac{y}{d}) \qquad (4.162)$$

where, θ, is defined in section, 4.1.1., α_η, is normalized position of the neutral line, ϵ_u, is the ultimate concrete strain and, y, is the coordinate.

Phase I.
In this phase the concrete is assumed to be linear elastic. By taking horizontal equilibrium the position of the neutral axis, α_η, is determined as

Fig. 4.29 Sketch of the load-displacement curve for reinforced concrete where the three phases are indicated.

$$\alpha_\eta = \frac{1}{2}\left[\frac{1 + 2\zeta\rho\alpha_r}{1 + \zeta\rho}\right] \qquad \text{for} \qquad \epsilon_s \leq \epsilon_y$$

$$(4.163)$$

$$\alpha_\eta = \frac{1}{2}\left[1 - \rho\frac{\sigma_y}{\sigma_u}\frac{1}{\theta}\right] \qquad \text{for} \qquad \epsilon_s > \epsilon_y$$

where, $\zeta = \dfrac{E_s}{E}$, is the flexibility ratio between steel and concrete, $\rho = \dfrac{A_r}{td}$, is the reinforcement ratio and, $\alpha_r = \dfrac{r}{d}$, is the normalized position of the reinforcement. The equivalent moment becomes

$$\mu(\theta) = \theta(4 - 6\alpha_\eta) - 6\frac{\sigma_s(\theta)}{\sigma_u}\rho\alpha_r \qquad (4.164)$$

where, σ_s is the steel stresses which is determined by using eq. (4.162). Phase I ends when the strain in the bottom equals, ϵ_u, yielding the following condition to the normalized rotation

$$\theta \leq \frac{1}{2\alpha_\eta} \qquad (4.165)$$

Thus, the moment rotation curve is a linear curve in phase I if the steel is not yielding, and bi-linear if the steel yields.

Phase II.

In phase II the fictitious crack develops. The size of the elastic tensile zone is found by the condition that the strain at the fictitious crack tip is, ϵ_u, yielding $\eta = \dfrac{1}{2\theta}$. The position of the neutral axis is determined by taking horizontal equilibrium

$$\alpha_f = (1 + \zeta\rho)(1 - B)$$

$$\pm \sqrt{(1 + \zeta\rho)^2(1 - B)^2 - (1 + 2\zeta\rho\alpha_r)(1 - B) + (\frac{1}{\theta}(1 - B)(1 + \zeta\rho)} \quad \text{for } \epsilon_s \leq \epsilon_y$$

$$\alpha_f = (1 - B) \pm \sqrt{\frac{1}{\theta}(1 - B)\left[1 + \frac{\sigma_y}{\sigma_u}\rho\right]} \qquad \text{for } \epsilon_s > \epsilon_y \tag{4.166}$$

and the equivalent moment becomes

$$\mu(\theta) = \theta\left[\frac{2\alpha_f(\theta)^3}{1 - B} - 6\alpha_f(\theta) + 4\right] - 3 + \frac{\sigma_s(\theta)}{\sigma_u}\rho\alpha_r \tag{4.167}$$

which is completely equivalent to the un-reinforced model, except for the last term taking the account of the steel and the modified equation for description of the size of the fictitious crack.
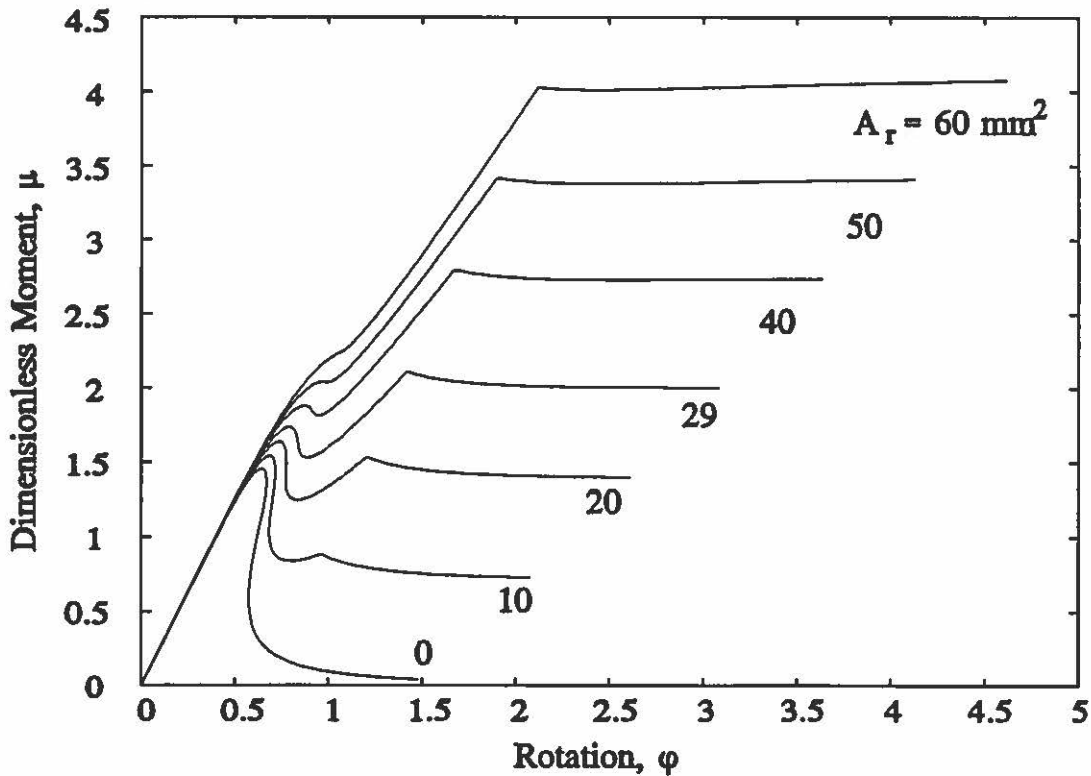

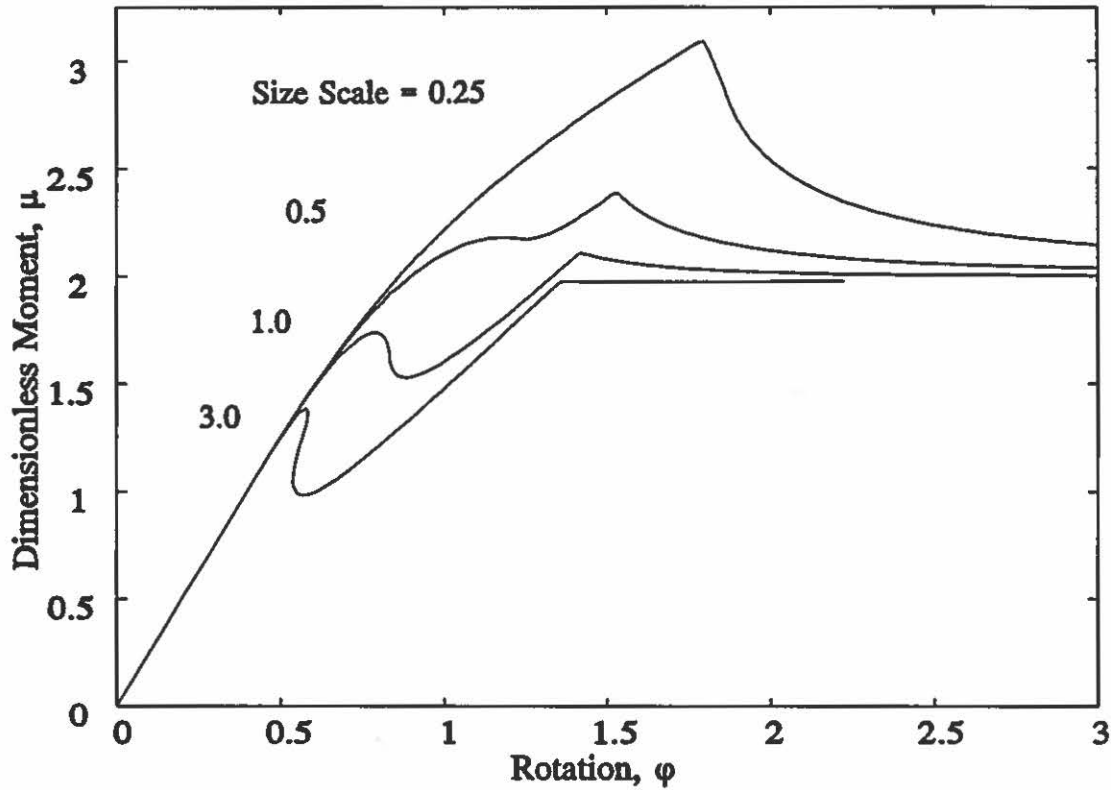Fig. 4.30 Moment-rotation curves for the Hededal et al. model with different reinforcement ratios.

Fig. 4.31 Moment rotation curves for the reinforced standard beam, with constant reinforcement ratio at different size scales.

Phase III.

In phase III the real crack starts to grow. The size of the elastic tensile zone is as in phase II: $\frac{1}{2\theta}$. The condition that the strain at the real crack tip is, ϵ_c, and by considering similar triangles the size of the fictitious crack is determined as

$$\alpha_f = \left[\frac{1-B}{B}\right]\frac{1}{2\theta} \qquad (4.168)$$

which is the same as in the un-reinforced situation. The length of the real crack is determined be requiring horizontal equilibrium

$$\alpha = 1 + \zeta\rho - \frac{1}{2B\theta} \pm \sqrt{\zeta\rho(\zeta\rho + 2(1-\alpha_r)) + B\left[\frac{1}{2B\theta}\right]^2} \qquad \text{for} \quad \epsilon_s \leq \epsilon_y$$

$$\qquad (4.169)$$

$$\alpha = 1 - \frac{1}{2B\theta} \pm \sqrt{2\rho\frac{\sigma_y}{\sigma_u}\frac{1}{2\theta} + B\left[\frac{1}{2B\theta}\right]^2} \qquad \text{for} \quad \epsilon_s > \epsilon_y$$

92

and the equivalent moment becomes

$$\mu(\theta) = \theta \left[4 - 6 \left[\frac{1}{2B\theta} + \alpha \right] + \frac{2(\alpha + \alpha_f)^2 - 2B\alpha^3}{1 - B} \right] + 6\frac{\sigma_s}{\sigma_u}\rho\alpha_r \qquad (4.170)$$

As in the Ulfkjær et al. method, is this method based on the assumption that the curvature is constant in the elastic layer, and the model is therefore derived for four point bending. Modifications must, however, be made in order to calculate the elastic displacement, according to the four point bending geometry.

In Fig. 4.30 normalized moment-rotation curves as calculated using the method for different reinforcement areas. it is seen that the shapes are as described under the carpinteri method, which is the expected behavior. In Fig. 4.31 normalized moment-rotation curves for the standard beam at different size scales with constant reinforcement ratios are shown.

The governing equations are simple and explicit, which makes the calculation speed very high compared to the Carpinteri method.

The peak moment is seen to be dependent on both the reinforcement area and on the size of the structure.

It is seen that there is a small kink on the curves. This kink is due to that the constitutive relation for the steel also have a kink and it was shown by Hededahl and Kroon (1991), that the kink on the moment-rotation curve disappears when the kink on the constitutive condition is removed, e.g. by making the constitutive relation parabolic-perfectly plastic.

There have not been made any comparison between the Carpinteri method and the Hededal et al. method since it is assumed that the Carpinteri method is erroneousness as it is presented here.

4.2.3 Model Evaluation.

The first method presented was the Carpinteri method. The method is strictly based on LEFM and that the reinforcement is rigid-plastic. The model requires numerical integration of double integrals. The results presented here are, however, disturbed by an erroneousness results compared to the ones presented in the original paper, and further conclusions seems meaningless, until is solved if the errors are due to the shape functions or due to the model concept.

The second method, the Hededal et al. method, is based on the development of a fictitious crack with a linear softening relation in an elastic layer around the midsection of the beam and that the reinforcement is linear elastic-perfectly plastic. The results fits very well with what was expected. The model is powerful in the sense that the governing equations are explicit and the calculation speed is therefore very high.

4.3 References for Chapter 4.

ASTM (1974). E399-74: Method of test for plane strain fracture toughness of metallic materials.

Biolzi, L., Cangiano, S., Tognon, G. and Carpinteri, A. (1989), Snap-back Softening Instability in High-Strength Concrete beams, *Materials and Structures*, 22, pp. 429-436.

Bosco, C. and Carpinteri, A. (1990), Fracture Mechanics Evaluation of Minimum Reinforcement in Concrete Structures, *in Application of Fracture Mechanics to Concrete Structures, Edited by A. Carpinteri*, Elsevier Applied Science, Politecnico di Torino, Italy, pp. 347-377.

Carpinteri, A. (1981), A Fracture Mechanics Model for Reinforced Concrete Collapse, *IABSE Colloquium*, Report of the working commission, Delft University of Technology, Delft, Vol. 34, pp.17-30.

Carpinteri, A. (1982), Notch Sensitivity in Fracture Testing of Aggregative Materials, *Engineering Fracture Mechanics*, Vol. 16, No. 4 pp.467-481.

Carpinteri, A. (1984), Stability of Fracturing Process in RC Beams, *Journal of Structural Engineering*, ASCE, Vol. 110, No. 3, pp. 544-558.

Carpinteri, A. (1985), Scale Effects in Fracture of Plain and Reinforced Concrete Structures, *in Fracture Mechanics of Concrete: Structural Application and Numerical Simulation, Editors: G.C. Sih and A. Di Tommaso*, pp. 95-140.

Carpinteri, A. (1986), Size Effects on The Brittleness of Concrete Structures, *Il Cemento*, 4, pp.375-388.

Carpinteri, A. (1988), Snap-Back and hyper-strength in Lightly Reinforced Concrete Beams, *Magazine of Concrete Research*, Vol. 40, No. 145, pp. 209-215.

Carpinteri, A. (1989), Fracture Mechanics and Post-Peak Structural Behavior of Plain and Reinforced Concrete, *in Fracture Toughness and Fracture Energy; Test Methods for Concrete and Rock, Editors: H. Mihashi, H. Takahashi and F.H. Wittmann*, A.A. Balkema, Tohoku, Japan, pp. 13-28.

Chuang, T.-J. and Mai, Y.-W. (1989), Flexural Behavior of Strain Softening Solids, *International Journal Solids Structures*, Vol. 25, No. 12, pp. 1427-1443.

Foote, R.M., Mai, Y-W. and Cotterell, B. (1986), Crack Resistance Curves in Strain Softening Materials, *Journal of the Mechanics and Physics of Solids*, 34, pp.593-607.

Harder, N.A. (1991), A Theorem on Brittleness, University of Aalborg, ISSN 0902-7513-R9126, pp. 1-17.

Hededal, O. and Kroon, I.B. (1991), Lightly Reinforced High-Strength Concrete, *M.Sc Thesis at University of Aalborg*, pp. 1-88.

Llorca, J. and Elices, M. (1990a), A Simplified Model to Study Fracture Behavior in Cohesive Materials, *Cement and Concrete Research*, Vol. 20, pp. 92-102.

Llorca, J. and Elices, M. (1990b), Fracture Toughness, Crack Growth Resistance and Ductility of Fibre-Reinforced Ceramics, *Structural Ceramics - Processing, Microstructure and Properties, Editors. Bentzen et al.*, Risø National Laboratory, pp. 403-411.

Tada, H., Paris, P. and Irwin, G. (1985), The Stress Analysis of Stress Handbook, *Del research Corporation*.

Timoshenko, S. (1955), *Strength of Materials, Part 1, Elementary Theory and Problems*, Third edition, D. Van Nostrand Company Inc., New York, p. 174.

Ulfkjær, J.P., Brincker, R. and Krenk, S. (1990), Analytical Model for Moment-Rotation Curves of Concrete Beams in Bending Fracture Behavior and Design of Materials and Structures, *Proceedings of the 8th European Conference on Fracture-ECF8* (Editor D. Firrao), Engineering Materials Advisory Services LTD, Vol. II pp.612-617.

Ulfkjær, J.P., Krenk, S. and Brincker, R. (1992), Analytical Model for Fictitious Crack Propagation in Concrete Beams, *submitted for publication in Journal of Engineering Mechanics*.

5 EXPERIMENTAL DETERMINATION OF FRACTURE PROPERTIES OF HIGH-STRENGTH CONCRETE.

With the different numerical and analytical methods presented, it is possible to analyze plain, lightly reinforced and other structures of normal and high-strength concrete where the tensile strength is a governing factor. It is, however, necessary to investigate if the size effects introduced in chapter 2 are present. For three of the models presented in chapter 2 the fracture parameters are determined, the results are presented and the size effects observed are commented.

As was described in chapter 2, it is very difficult to determine the constitutive parameters in the fictitious crack model and for high-strength concrete, only the fracture energy has been determined, and only by using the RILEM recommendation developed by Hillerborg and co-workers, RILEM 50-FMC (1985). Instead indirect methods can be applied, e.g. the fracture parameters are determined through three-point bending experiment. Here the experimental results, in form of load displacement curves, are compared with numerical results obtained by using the direct sub-structure method, described in chapter 3, and the fracture parameters are then assumed to be those who minimize a certain function, which in some way describes the difference between the experiment and the numerical result. Three of such functions are tested on 8 different beam geometries, and two different optimization techniques have been used. This method of determining the constitutive parameters is evaluated, and conclusions are drawn.

In order to measure the crack profile and to detect causes for size effects, dye experiments are performed on ordinary specimens and on specimens which are saw cut out.

5.1 Size Effect Experiments.

5.1.1 Materials.

A high strength concrete similar to the one used at the Great Belt project in Denmark has been used. The largest aggregate size in this concrete is, however, only 8 mm. Table 5.1 shows the mix of the concrete and Table 5.2 shows the mechanical properties. The modulus of elasticity, the cylinder compressive strength and the cylinder splitting strength were determined using conventional procedures.
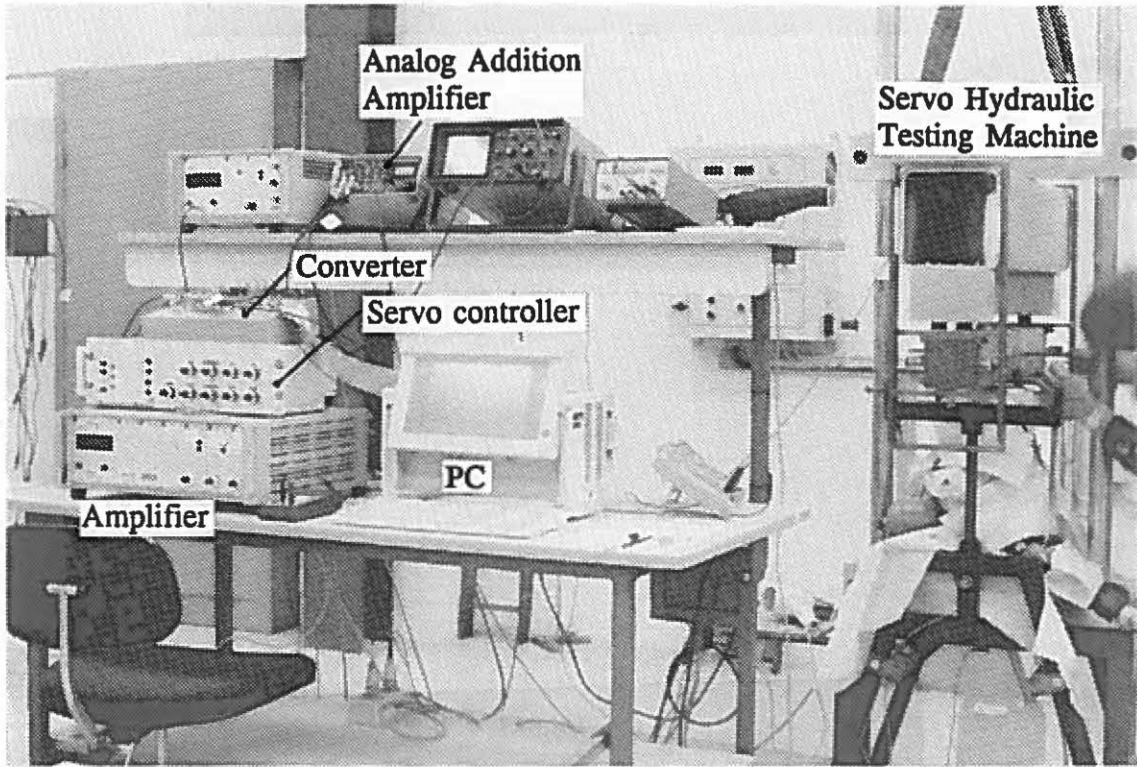
Fig. 5.5 Testing equipment for three-point bending testing.

Cement	Fly ash	Silica fume	Water	Plast. (*)	Super Plast.	Sand	Gravel
312	44	29	122	1.56	8.58	614	1238

(*) Melamine-Naphthalene based plasticizer; Units are [kg/m^3]

Table 5.1 Mix proportions.

The experiments were carried out on 8 different beam sizes as shown in Table 5.3. These geometries were chosen for two reasons. Firstly, in order to be able to study statistical and structural size effects separately, and secondly because of the limitations of the testing equipment. The beams were made out of three batches (40 l each) and beams of 8 different sizes were cast on the same day. A total amount of 40 beams were cast over a period of 4 weeks. The beams were named after size, cast day and batch number (e.g. A-3a is beam size A cast on day 3 from the first batch). The day after casting the beams were striped from their molds and cured 7 days in water (37°C). Then a notch of rectangular cross section was saw cut in the beams and the beams were further cured under water (20°C) for 7 days.

97
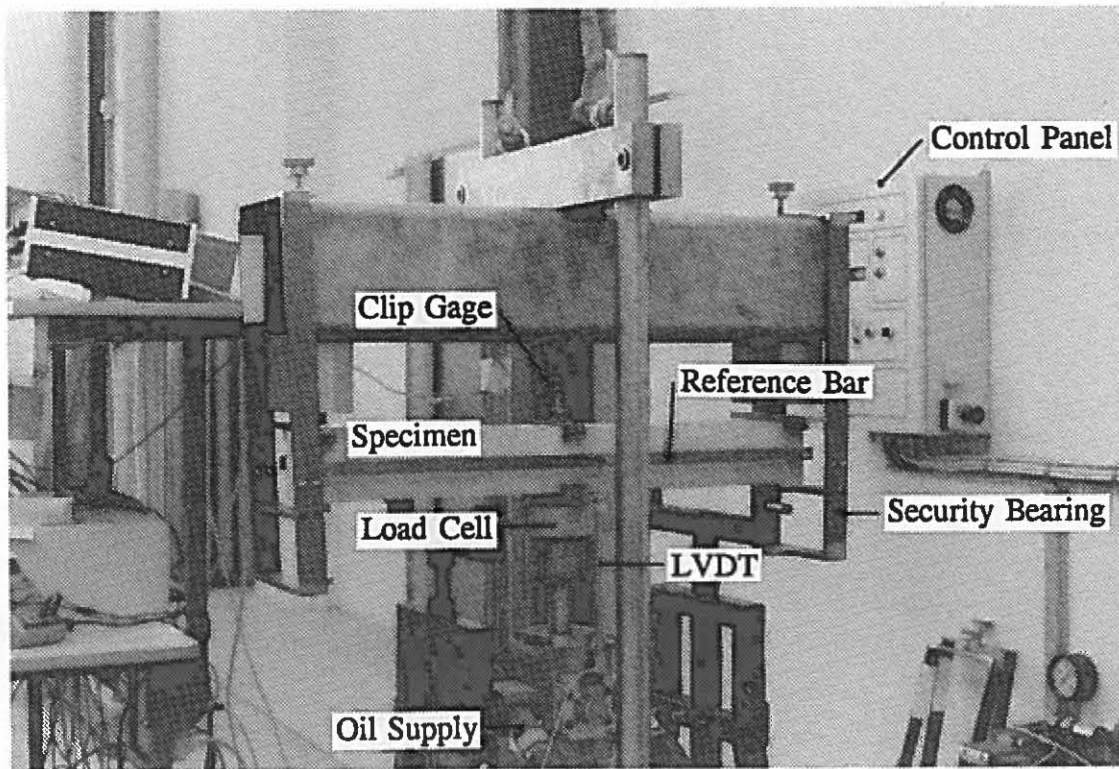
Fig. 5.6 Phot of reference bar.

Cylinder compres-sive strength		Cylinder splitting strength		Young's modulus	
Mean	S.Dev	Mean	S.Dev.	Mean	S.Dev.
81,7	5.0%	5.55	8.1%	42660	2.5%

Units are [MPa]

Table 5.2 Mechanical properties of tested concrete.

Hereafter, the beams were stored in the laboratory at relative humidity of 100% at 20°C until the day of testing.

5.1.2 Testing equipment and procedure.

The beams were submitted to three-point bending in a servo controlled materials testing system, see Fig. 5.5. In order to measure the true beam deflection a reference bar was placed on each side of the beam, and the beam deflection was measured as the distance from the
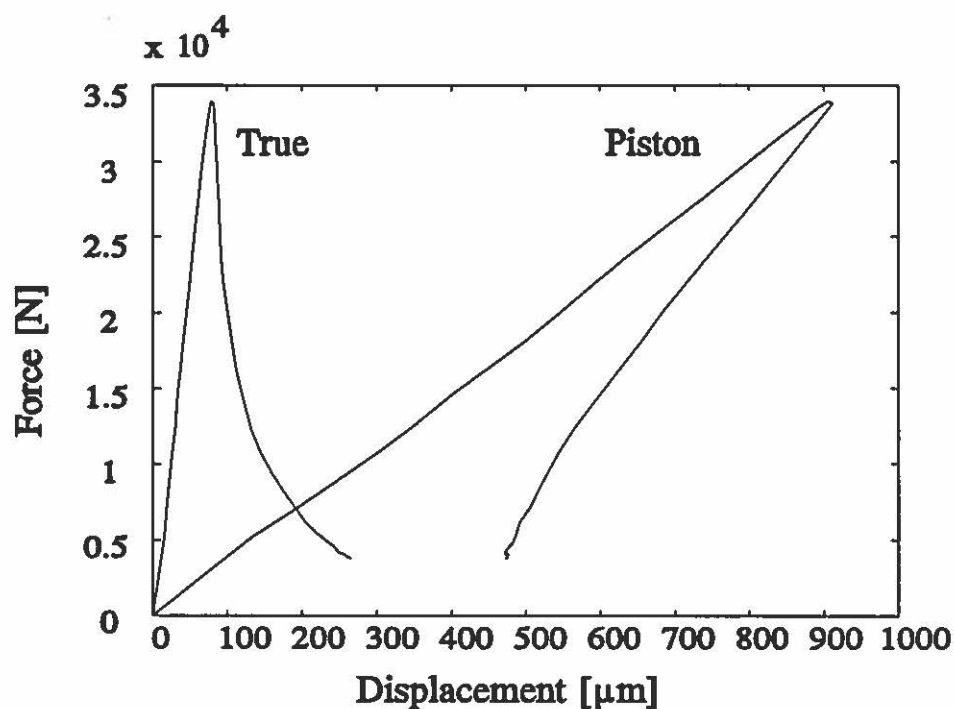
Fig. 5.7 Difference between the true displacement and the piston displacement for beam type H-5c.

Type	Length [mm]	Depth [mm]	Width [mm]	Notch depth [mm]
A	840.0	50.0	50.0	5.0
B	840.0	50.0	100.0	5.0
C	840.0	100.0	50.0	10.0
D	840.0	100.0	100.0	10.0
E	840.0	100.0	200.0	10.0
F	840.0	200.0	50.0	20.0
G	840.0	200.0	100.0	20.0
H	840.0	200.0	200.0	30.0

Table 5.3 Sizes of the beams tested, the dimensions was all within +/- 2.0 mm.

load point to the reference bar using two LVDT's with a base of 20.0 mm and a sensitivity of 0.5 V/mm, see Fig. 5.6. The piston displacement was measured using the build-in LVDT

with a base of 5.0 mm and a sensitivity of 2.0 V/mm. The difference between the 'true displacement and the piston displacement, which usually is assumed to be the beam deflection, is seen in Fig. 5.7, for beam type H-5c. The crack opening displacement was measured using a clip-gauge with a base of 2.0 mm and with a sensitivity of 5.0 V/mm, see Fig. 5.6. The load was measured using a 50.0 kN load cell with a sensitivity of 0.2 V/kN. A schematic of the test set-up is shown in Fig. 5.8.

All signals together with the time, t, were recorded using an analog to digital converter and an AT Personal Computer. The test was controlled by a feedback signal that included contributions from both the piston displacement and the COD. The feed back signal, δ, was
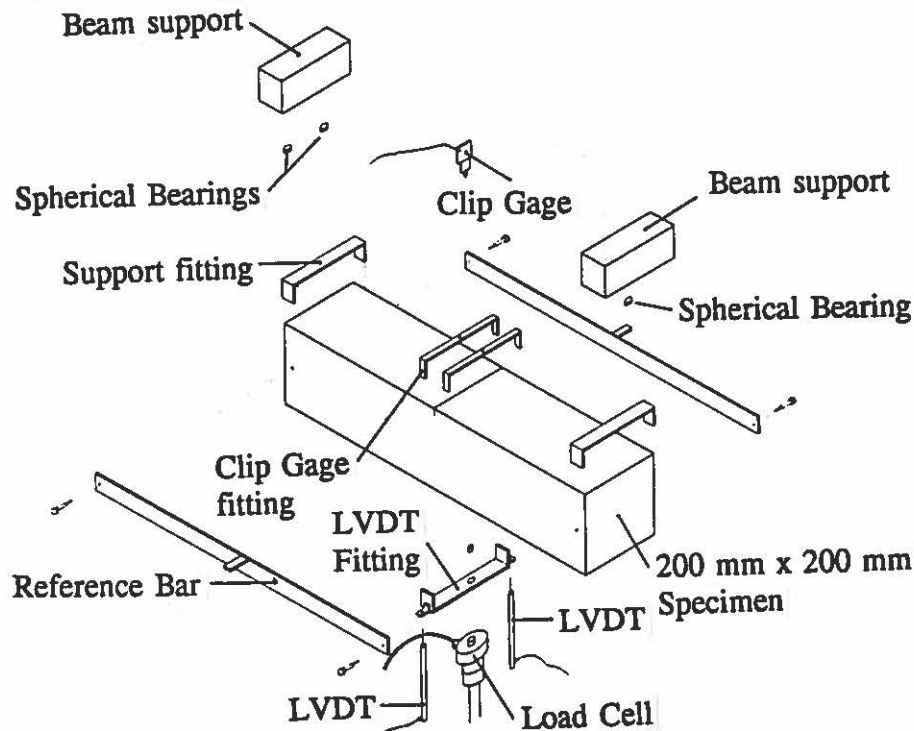
Fig. 5.8 Schematic of the test set-up.

created by analog addition of the corresponding signals:

$$\delta = \alpha \delta_{COD} + \beta \delta_p \tag{5.171}$$

where, δ_{COD}, is the crack opening displacement and, δ_p, is the piston displacement. The weight factors, α, and, β, were chosen to $\alpha = 10.0$, 5.0 and 2.5 and $\beta = 1.0$, where α is decreasing with the beam depth.

The idea of using this combined signal as feedback is that each term in (5.171) plays a dominant role in the different stages of the test. Before the fracture process starts the piston displacement plays the dominant role. When the fracture process starts the COD is increasing rapidly. In this way a stable test is obtained, see Fig. 5.9 , where the load-COD curve is plotted together with the load-piston displacement curve and the feed-back signal for beam

100
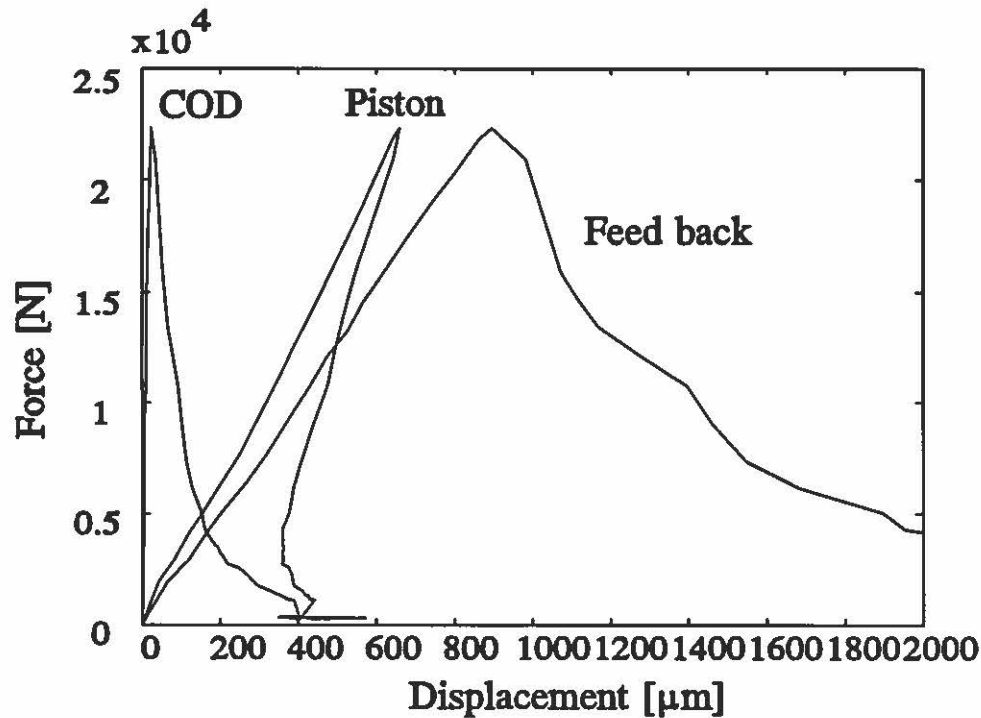
Fig. 5.9 Displacement, crack opening displacement and feed-back signal for beam type G-4a.

G-4a. It is obvious from this example that if the test was piston displacement controlled an instability would occur immediately after the peak load.

The reference signal, a linear ramp, was generated with the same AT PC using a digital to analog converter. The control arrangement is shown in Fig. 5.10.

The measured load displacement curves are shown in Appendix A2, categorized according to the geometry. The peak load and the displacement at peak load are shown in Appendix A3.

5.2 Fracture Parameter Results.

Fracture parameters from three different models are calculated:

A: The bending tensile strength according to Bernoulli (modulus of rupture).
B: The critical stress intensity factor K_C according to LEFM.
C: The modulus of elasticity, E, the fracture energy, G_F, the uniaxial tensile strength, σ_u, and the coordinates of the kink of a bi-linear σ-w relation, according to the FC-model.

101
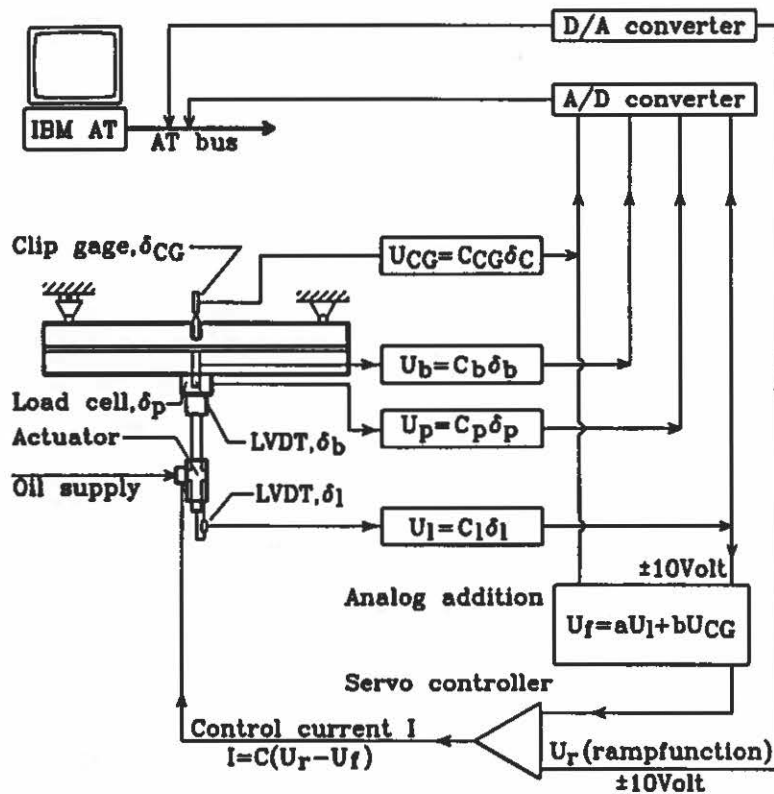
Fig. 5.10 Control Arrangement.

5.2.1 The Modulus of Rupture.

The modulus of rupture is calculated as the bending tensile strength of a Bernoulli-Euler beam

$$\sigma_m = \frac{3F_{max}l}{2(d - a_i)^2 t} \qquad (5.172)$$

where, F_{max}, is the peak load when the load displacement curve is adjusted for the beam weight. The modulus of rupture for all the beams are shown in Appendix A3, together with the mean values, the standard deviation and coefficient of variation. In Fig. 5.11 the mean value of the modulus of rupture is drawn as a function of the beam depth, for the different beam thickness. It is seen that except for the smallest beam (d = 50 mm, t = 50 mm) the same trend is seen as in the Reagel and Willis (1931) experiments, thus, the modulus of rupture is decreasing with the beam depth. The decrease in modulus of rupture by doubling the beam depth is 4% for the thicknesses 50 mm and 100 mm and 10% for the beam thickness 200 mm which is of the same order as in the experiments by Reagel and Willis (1931).

102
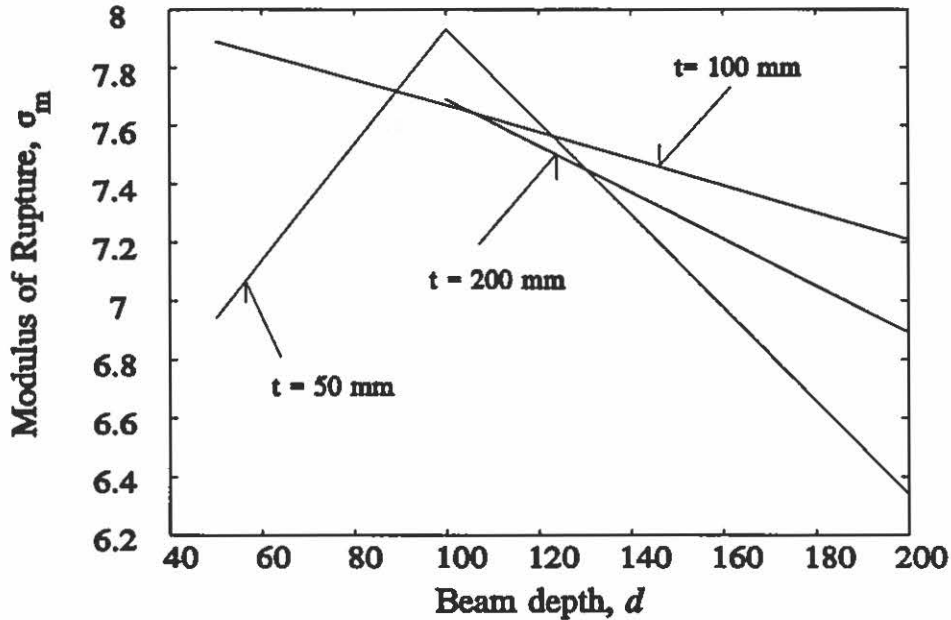
Fig. 5.11 Mean values of modulus of rupture as function of the beam depth for the three beam thickness.

The reason for the unexpected behavior of test series A could be that the specimens have been too small to make a homogeneous structure of the specimens, however, visual inspection of the specimens did not indicate any difference in the structure of the smaller specimens than that of the larger. It is therefore assumed that the decrease in strength of the smallest beam size is due to some edge effect, which e.g. is introduced by the mould.

5.2.2 The Fracture Toughness.

The fracture toughness, K_c is calculated according to ASTM:

$$K_c = \frac{3}{2} \frac{F_{max} l \sqrt{a}}{bd^2} f\left[\frac{a}{d}\right] \tag{5.173}$$

where

$$f\left[\frac{a}{d}\right] = 1.93 - 3.07\left[\frac{a}{d}\right] + 14.53\left[\frac{a}{d}\right]^2 - 25.11\left[\frac{a}{d}\right]^3 + 25.8\left[\frac{a}{d}\right]^4 \tag{5.174}$$

F_{max} is the peak load and d, t and a is the beam depth, thickness and notch depth, respectively.

103

The critical stress intensity factor for each beam is shown in Appendix A3, and the mean values are plotted in Fig. 5.12. It is seen that the fracture toughness is strongly increasing with the beam depth, and is almost independent of the beam depth. The increase by doubling the beam depths is 53% for $t=50$ mm, 46% for $t=100$ mm and 65% for $t=200$ mm. Thus, a distinct size effect is observed, when LEFM is used.
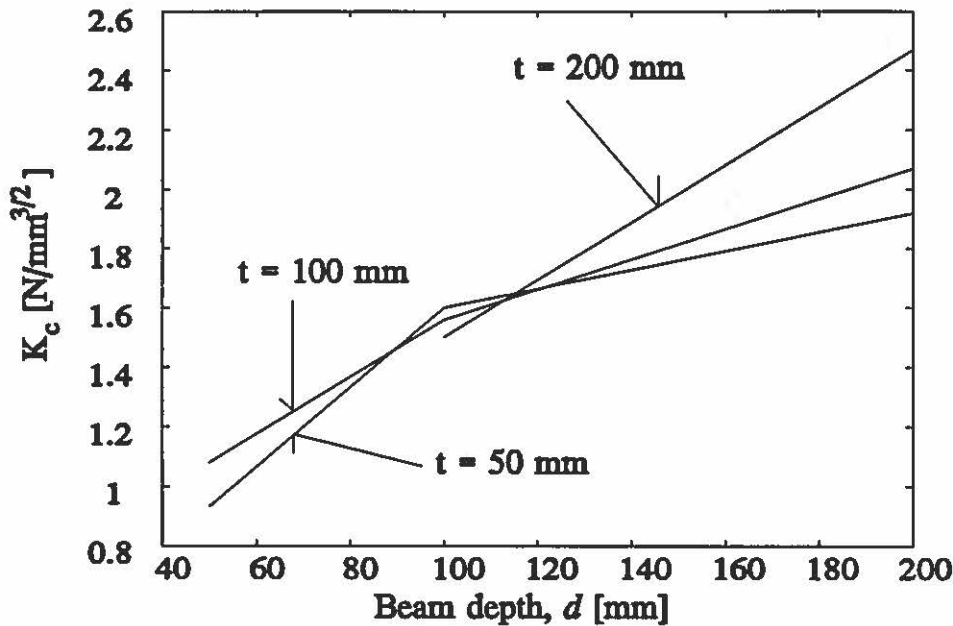
Fig. 5.12 Mean value of the critical stress intensity factor.

5.2.3 Fracture Energies According to RILEM.

According to the RILEM recommendation, RILEM TC-50 (1985), the fracture energy should be determined on a specimen with the dimensions $l = 800$ mm, $d = 100$ mm, $t = 100$ and initial notch depth $a_i = 50$ mm, the maximum aggregate size should not be larger than 16 mm. In this test series the initial notch depth ratio was chosen to be only 1/10 of the normalized beam depth, because as stated in chapter 2, LEFM is only applicable for small notch depth. By using this reduced notch depth the amount of energy dissipated outside the fracture will increase. Therefore it can be expected that a certain size effect will be measured by using the RILEM method, since the energy dissipated in the bulk is not taken into consideration by using this method.

Different areas are calculated in connection with the RILEM method. Consider the load-displacement curve in Fig. 5.13. The experiments are usually terminated before the load is decreased to zero, due to the fact that the piston displacement speed is very slow at the

descending branch. The experiment will therefore end at the load, F_1, and the corresponding displacement, δ_1, and the remaining area under the load-displacement curve must be estimated.

According to the Ulfkjær et al. model the descending branch in Phase III is described by

$$F = \left(\frac{\delta_1}{\delta}\right)^2 \qquad (5.175)$$

the remaining contribution to the fracture energy, A_1, can then be determined by

$$A_1 = \frac{1}{t(d - a_i)} \int_{\delta_1}^{\infty} \frac{\delta_c^2}{\delta^2} d\delta \qquad (5.176)$$

By applying the condition

$$F_1 = \left(\frac{\delta_c}{\delta_1}\right)^2 \qquad (5.177)$$

the remaining fracture energy becomes

$$A_1 = \frac{F_1 \delta_1}{t(d - a_i)} \qquad (5.178)$$

The fracture energies (the sum of the area under the measured curve and the remaining area divided by the ligament) and the remaining fracture energy, A_1, for each experiment are shown in Appendix A3. The mean value of the fracture energies for each geometry is shown in Fig. 5.14. It is seen that the fracture energy is increasing with the beam depth, and is almost independent of the beam thickness. The increase by doubling the beam depth is for $t = 50$ mm 19%, for $t = 100$ mm 8% and for $t = 200$ mm 16%. The fracture energy for test series A, is quite low, which is due to the experiment A-5a, where the fracture energy is very low. Visual inspection of the cracked surfaces did not indicate that this specimen in any sense was weaker than the others. The reason for the size dependency of the fracture energy is attributed to the fact that energy dissipation in the bulk is not taken into consideration.

5.2.4 Fracture Parameters According to the Fictitious Crack Model and Data fitting.

The fracture energy, the tensile strength, the modulus of elasticity, the coordinates of the kink on a bi-linear σ-w relation were estimated by solving the minimizing of an objective function which in some manner describes the difference between the measured load displacement relation and one calculated using a numerical method. Three different objective functions and two different optimization procedures were tested in order to obtain the best estimate of the constitutive parameters. The functions will be presented in the order they were tested by the author, and the shortcomings of each function will be given.

Objective function I:

The first objective function to be tested were

$$\min_{\overline{z}} \frac{\sum_{i=1}^{N} \left[(\hat{F}_i^I(\overline{z}) - F_i^I)^2 \ (F_i^I)^2 \right]}{F_{max}^4} \qquad (5.179)$$

$$\overline{z} = [\hat{\sigma}_u \ \hat{w}_c \ \hat{E} \ ]^T$$

where F_i^I is the experimental load deflection curve at the applied displacement δ_i, which were calculated at equidistant displacements and $\overline{z}$ is the state vector. No bounds were imposed on the elements in the state vector. $\hat{F}_i^I(\overline{z})$ is a load deflection curve determined using the direct sub-structure method (DSS-method), Brincker and Dahl (1988), described in chapter 3. Using the finite element method for determination of influence coefficient, four-node
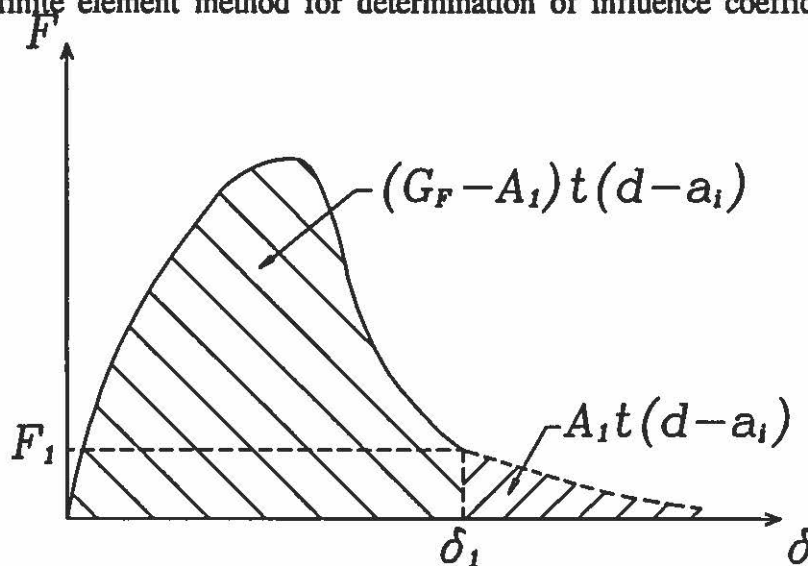
Fig. 5.13 Areas calculated in order to determine the fracture energy, using the RILEM method.

element were chosen and the number of nodes in the midsection were 21. The σ-w relation was assumed to be bi-linear with the normalized kink-coordinate at (0.16,0.31). $\hat{\sigma}_u$, $\hat{w}_c$ and $\hat{E}$ are the estimated uniaxial tensile strength, critical crack opening displacement and the modulus of elasticity modulus respectively. The term $(F_i^I)^2$ is a weight, that emphasizes the importancee of the peak.

The optimization problem was solved using the Nelder and Mead algorithm, see e.g. Gill et al. (1981) or Vanderplaats (1984) on a 386 20 MHz Personal Computer implemented in a MATLAB shell, MATLAB (1989) and it took about 1 hour for each optimization. However, in order to avoid local minima several runs were necessary. Using this objective function
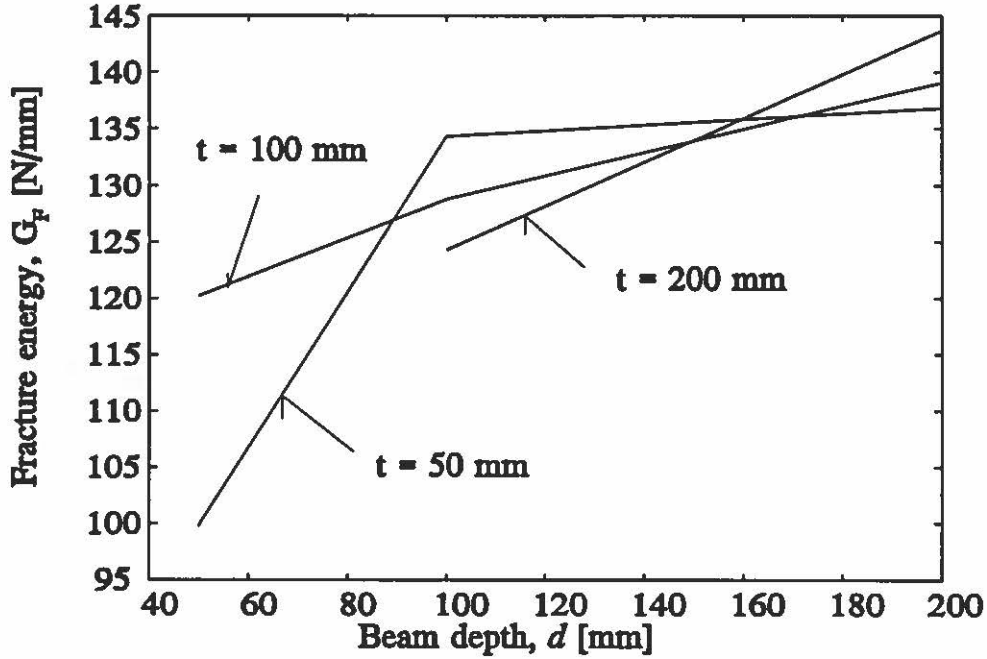
Fig. 5.14 Fracture energies determined according to the RILEM recommendation.

initially rather good results were obtained and it was concluded that the method was rather good. However, as the results became more, and more scattered and as it was observed that the fitting results were very poor, especially at the descending branch. It was therefore concluded that another objective function was needed, so that the descending branch could be fitted better.

Objective function II:
The second objective function is similar to the first, however, the normalized coordinates of the kink point $(\hat{w}_1/\hat{w}_c, \hat{\sigma}_1/\hat{\sigma}_u)$ of the strain softening relation is taken into account

$$\min_{\underline{z}} \frac{\sum_{i=1}^{N} \left[(\hat{F}_i^{II}(\vec{z}) - F_i^{II})^2 \ (F_i^{II})^2 \right]}{F_{max}^4} \tag{5.180}$$

$$\vec{z} = [\ \hat{\sigma}_u \ \ \hat{G}_F \ \ \hat{E} \ \ \hat{w}_1/\hat{w}_c \ \ \hat{\sigma}_1/\hat{\sigma}_1 \ ]^T$$

and the state vector is subjected to the following constraints

107

$$0 < \quad \hat{\sigma}_u \quad < \quad 10.0 \text{ MPa}$$

$$0 < \quad \hat{E} \quad < \quad 80{,}000 \text{ MPa}$$

$$0 < \quad \hat{w}_c \quad < \quad 0.5 \text{ mm}$$

$$0 < \quad \hat{w}_1/\hat{w}_c, \; \hat{\sigma}_1/\hat{\sigma}_u \quad < \quad 0{,}5$$

(5.181)

Another important difference is that the loads F_i^{II}, were calculated at equidistance points at the load-displacement curve and not just on the displacement curve. By doing so the descending branch was weighted equally as much as the ascending branch, and even snap back is taken into account by this method. The number of points, N, was set to 350. In order to increase the calculation speed the objective function was implemented using the C programming language, and instead of the Nelder and Mead scheme the NLPQL scheme developed by Schittkowski (1980) implemented in the programming language FORTRAN was used.

The NLPQL algorithm is a very effective method where each iteration consists of two steps. The first is the determination of a search direction by solving a quadratic optimization problem formed by a quadratic approximation of the Lagrange function of the non-linear optimization problem and a linearization of the constraints at the current design point. The second step is a line search with an augmented Lagrangian merit function, Enevoldsen et al. (1990). NLPQL requires estimates of the gradients of the objective function and the constraints, and is in this case done numerically.

In this way a more complicated objective function with two additional parameters is used with almost the same calculation time as the previous function. However, as in the case of the first objective function it is necessary to try more than one start guess, in order to find the true minimum.

In most cases this object function yields very satisfactory results, however, it is in some cases not possible to obtain an acceptable agreement at the tail at the descending branch, which usually results in a too large fracture energy. An example of such an optimization result is seen in Fig. 5.15.

Objective function III:
In order to solve the above outlined problem a third objective function was designed

$$\min_{z} \frac{\sum_{i=1}^{N} \left[\left(\hat{F}_i^{II}(\vec{z}) - F_i^{II} \right)^2 \left[\left(\frac{F_i^{II}}{F_{max}} \right)^2 + \left(\frac{\delta_i^{II}}{\delta_{max}} \right)^2 \right] \right]}{F_{max}^2}$$

(5.182)

$$\vec{z} = [\; \hat{\sigma}_u \; \hat{G}_F \; \hat{E} \; \hat{w}_1/\hat{w}_c \; \hat{\sigma}_1/\hat{\sigma}_u \;]^T$$
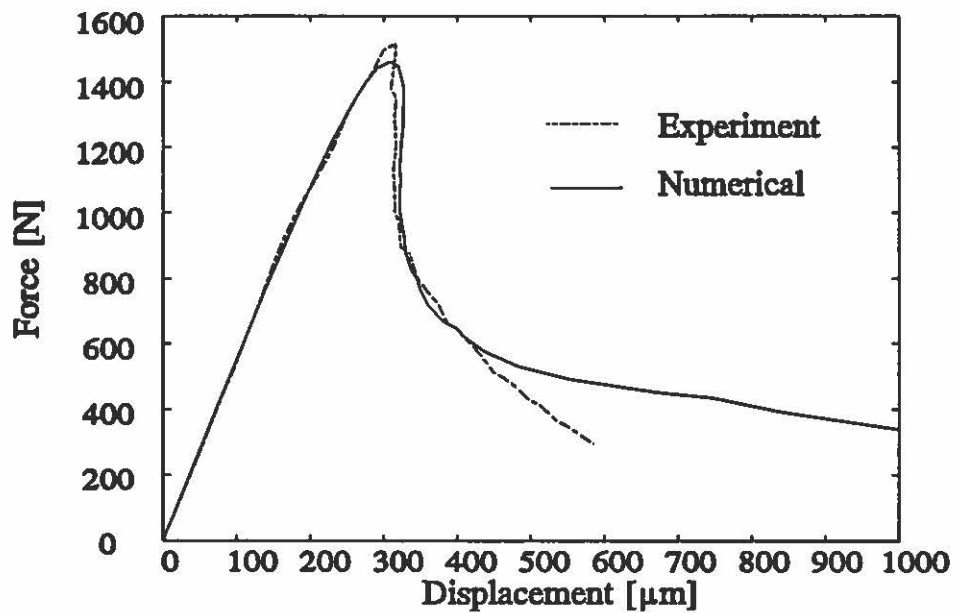
subjected to the following constraints

108

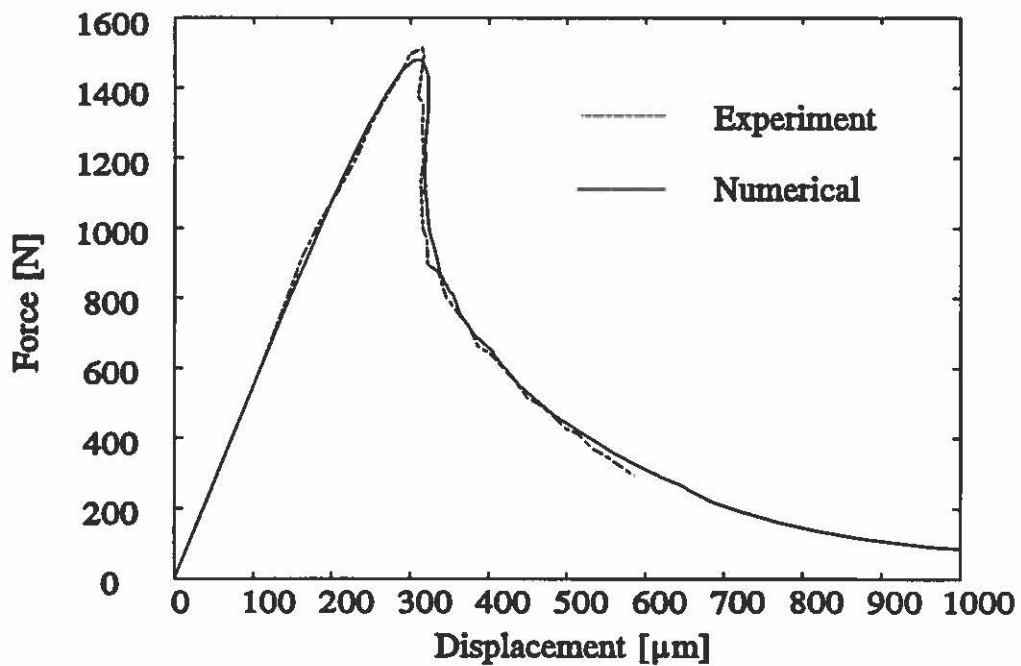Fig. 5.15 Optimization result where the second objective function fails.

Fig. 5.16 Optimization result from using the third objective function.

$$0 < \quad \hat{\sigma}_u \quad < \quad 10.0 \text{ MPa}$$

$$0 < \quad \hat{E} \quad < \quad 80,000 \text{ MPa}$$

$$0 < \quad \hat{w}_c \quad < \quad 0.5 \text{ mm}$$

$$0 < \hat{w}_1/\hat{w}_c, \ \hat{\sigma}_1/\hat{\sigma}_u \quad < \quad 0.5$$

(5.183)

which are equivalent to objective function II, but weighted with the square of the normalized

displacement $\left(\dfrac{\delta_i^{II}}{\delta_{max}}\right)^2$. By using this objective function the optimization result in Fig. 5.15

changes to Fig. 5.16.
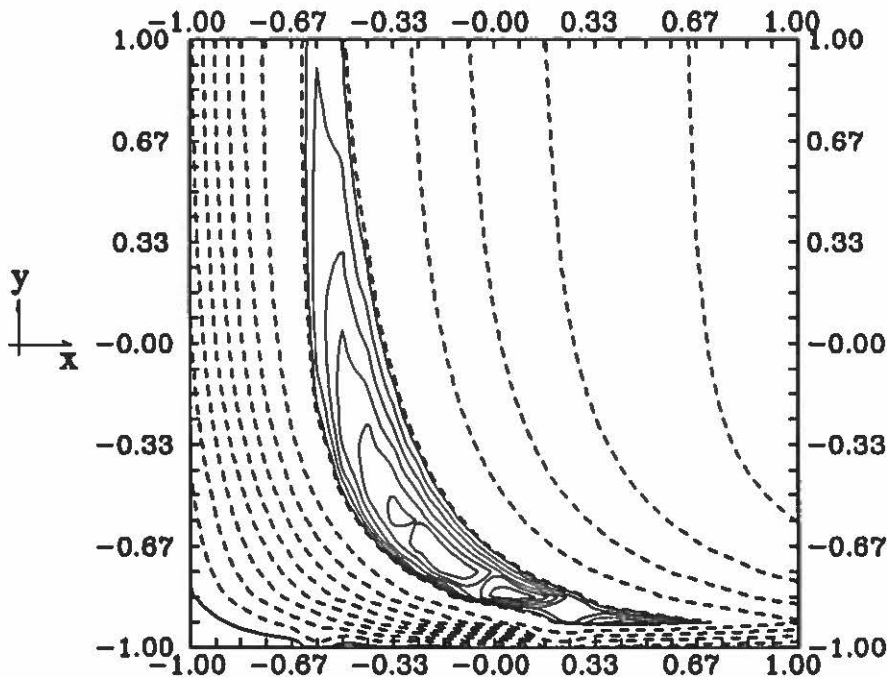
Fig. 5.17 Contour plot of the object function for beam A-4a.

A contour plot of the objective function for beam A-4a is plotted in Fig. 5.17 where the optimal values of E = 43086 MPa, $\hat{w}_1/\hat{w}_c$ = 0.14 and $\hat{\sigma}_1/\hat{\sigma}_u$ = 0.22 are used. The corresponding surface plot is shown in Fig. 5.18. The plot consist of a square grid of 51*51 points and it took over 26 hours to perform the calculations on a 386 33 MHz Personal Computer. The solid contour lines are plotted with equidistance of 3,000 and the dashed contour lines are plotted with equidistance of 30,000. The two variables x and y are defined so that -1.0 at the x-axis corresponds to σ_u= 10 MPa and 1.0 corresponds to σ_u= 10.0 MPa, at the y-axis -1.0 corresponds to w_c= 0.05 mm and 1.0 corresponds to w_c= 1.0 mm. The minima of the function is at (x,y) = (0.08, -0.84) and is equal to 107.96 the maxima is at (x,y) = (-1.0, -1.0) and is equal to 318260. The minimum corresponds to that w_c = 0.09 mm and σ_u = 5.86 MPa, the values shown in Appendix A3 found by NLPQL are w_c = 0.09 mm and σ_u = 5.42 MPa.

It is seen that the objective function is 'banana' shaped with a very deep valley. At the bottom of the valley the objective function is very flat for constant brittleness numbers, and a lot of local minima are present. It is therefore very difficult to find the true minimum of the objective function and often several start guesses are necessary in order to get a good fit.

110
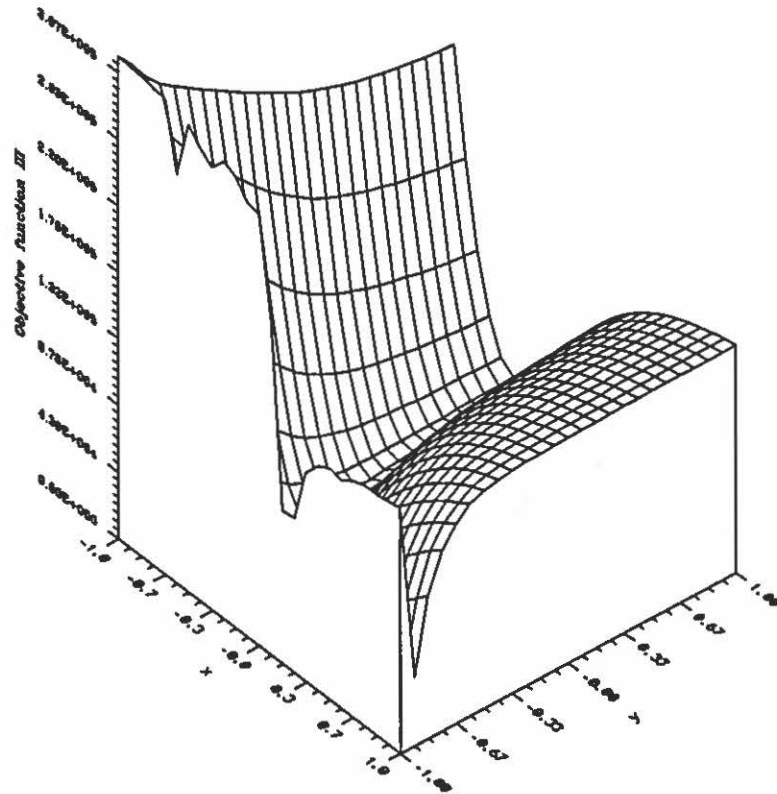
Fig. 5.18 Surface plot of the object function for beam A-4a.

The optimization results for all the beams are shown in Appendix A4, and the estimated parameters are shown in Appendix A3.

The mean value of the estimated fracture energies are shown in Fig. 5.19, and the trend observed in the RILEM method is also observed here, which is due to the fact that the fitting is made so the curve will be as equal as possible and that the energy dissipation in the bulk is not taken into consideration in this method. The increase in the fracture energy by doubling the beam depth is 15% for $t = 50$ mm and $t = 200$ mm and 10% for $t = 100$.

The mean values of the uniaxial tensile strength, σ_u, are shown in Fig. 5.20. No distinct trend is observed from the estimated uniaxial tensile strength. The tensile strength is smallest for the small specimens, are then increasing and then decreasing a little. It is observed that the uniaxial tensile strength is smaller than the modulus of rupture, which is in agreement with the results presented in chapter 4.

The mean values of the normalized kink point of the softening relation are shown in Fig. 5.21. It is also seen that the normalized kink coordinate is decreasing with the beam size and that the values are lower that that of NSC ((0,16,0.31)), indicating that HSC is more brittle than NSC.
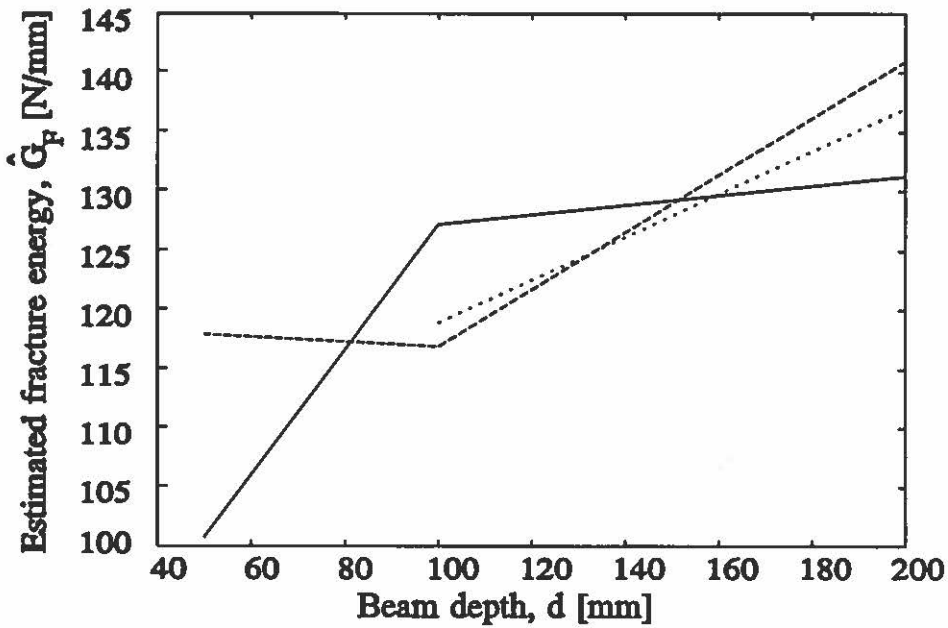
Fig. 5.19 Estimated fracture energies.
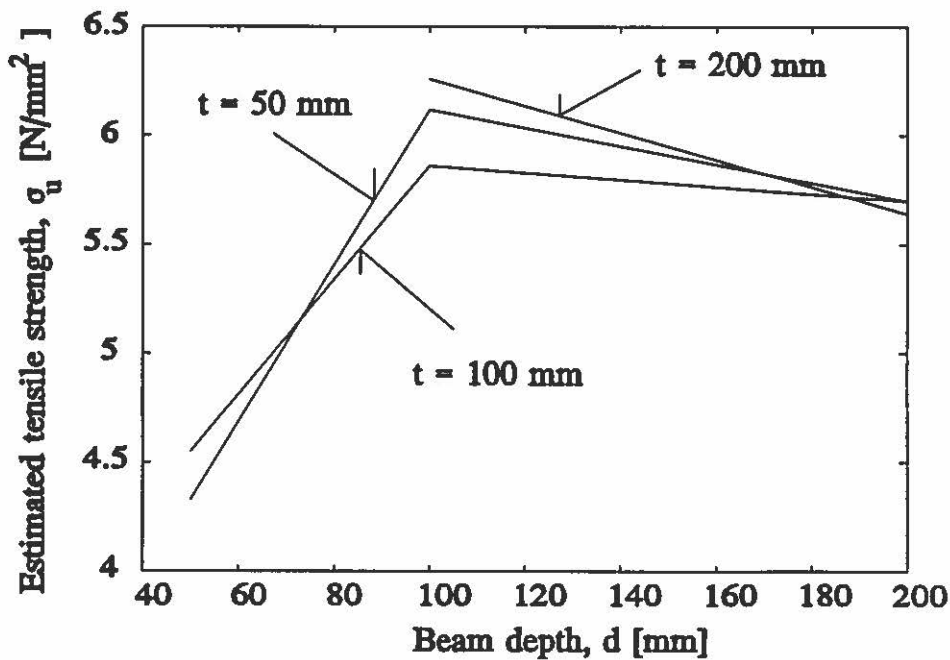
Fig. 5.20 Estimated uniaxial tensile strength.

When this work was finished the author became aware of a work by Roelfstra and Wittmann (1986) and Bruhwiler et al. (1990) who also have determined the fracture parameters through
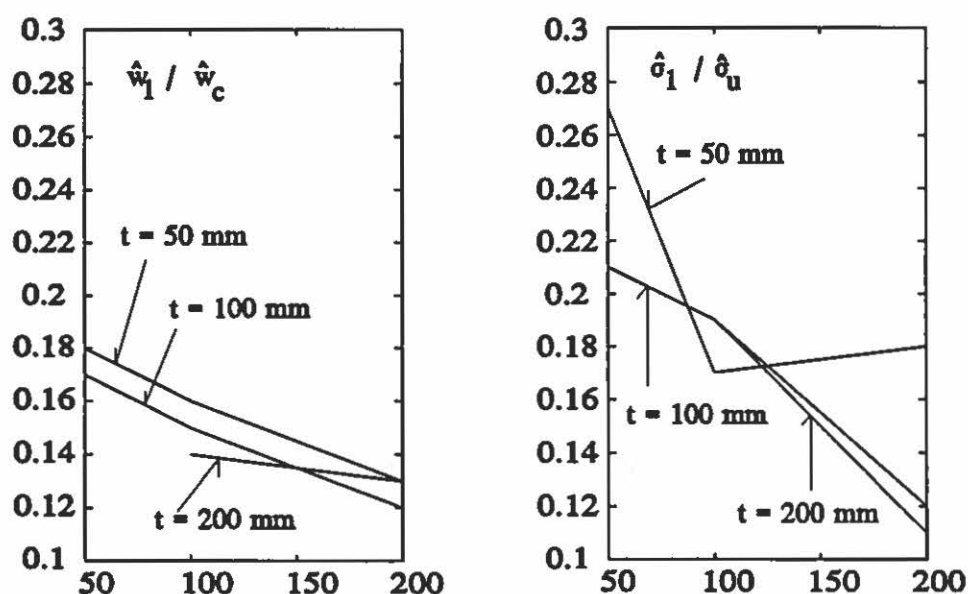
Fig. 5.21 Estimated results for the normalized kink coordinate of the softening relation.

a method similar to the one under objective function I on NSC. They did, however, not use a weight on the objective function, and their estimation of the peak load is not as that good as with objective function I.

5.2.5 Conclusions on Size Effect Experiments.

For all the three models it were seen that there were a significant size effect. The size effect on the modulus of rupture was of the same order as that of experiments performed by Reagel and Willis (1931). The increase on the fracture toughness with the increasing beam depth was very large and it is concluded that LEFM, is not applicable for HSC concrete of laboratory size. The size effect on the fracture energies wase also significant, and the RILEM method for determining the fracture energy seems inappropriate. By using the data fitting technique the uniaxial tensile strengths and the kink coordinate on the descending branch were determined and it was observed that the tensile strength was both decreasing and increasing with the beam depth. The normalized kink coordinates were decreasing with the beam depth. For all parameters it was concluded that they were independent of the beam thickness. It appears, thus, that edge effects are present, since the Weibull in some way is outbalanced.

5.3 Dye Experiments.

In order to determine the crack profile and to investigate why the thickness of the beam does not influence on any of the determined fracture parameters, a series of dye experiments similar to the ones performed by Swartz and Refai (1989) has been performed, with emphasis on studying edge effects.

In the method developed by Swartz and Rafai (1989), two Aluminum sheets were glued to the beam using silicone. The specimen was then loaded beyond the peak load, where after the dye, Blue Vanish (a fluid soap), was poured into the reservoir. The beam is then load-cycled, with the maximum load being app. 1/3 of the peak load. The reservoirs were then removed and the beam was split whereby the cracked profile corresponding to the unloading load is revealed. The crack was then measured immediately after testing, since the dye disappears after about an hour. The crack profile measured by Swartz was rather U-shaped indicating the possibility of the existence of a weak zone at the edges of the specimen. The reason for this weak zone could be that the structure of the concrete is not the same at the edges of the beam. Another reason could be that the stress intensity factor for a crack on the edge of the structure is up to a factor of 2.0 of that of an internal crack. That means that a crack at the surface will propagate for a load which is only the half of that for an internal crack. A third explanation could be that the used dying technic is responsible for the shape of the measured crack profiles.

Almost the same testing procedure test set-up as used by Swartz is utilized in this investigation, see Fig. 5.22. Though, the dye used was instead Rotamin, a red colored dye used in women lip-sticks, and is in the concentrated form used here almost impossible to remove. A specimen which was dyed approximately a year ago, placed in the authors office, has not changed at all since the day of dyeing!. The drying procedure in this investigation was done by using a hot air canon whereby the drying time was very short. Also the reservoirs were not glued on to the specimen, but were hinged to the top of the beam, and then a little silicone was used to make the connection waterproof. It is thereby assumed that the stiffness of the beam has not changed, due to the reservoirs.

In order to check if the crack profiles change as the structure of the surfaces changes, four specimens which were saw cut out were produced, and four reference specimens of beam type D were cast. The procedure just outlined was then followed. The crack profile measured and drawn. The profiles are shown in appendix A5, and as seen it is not possible to see any difference in the measured crack profiles.
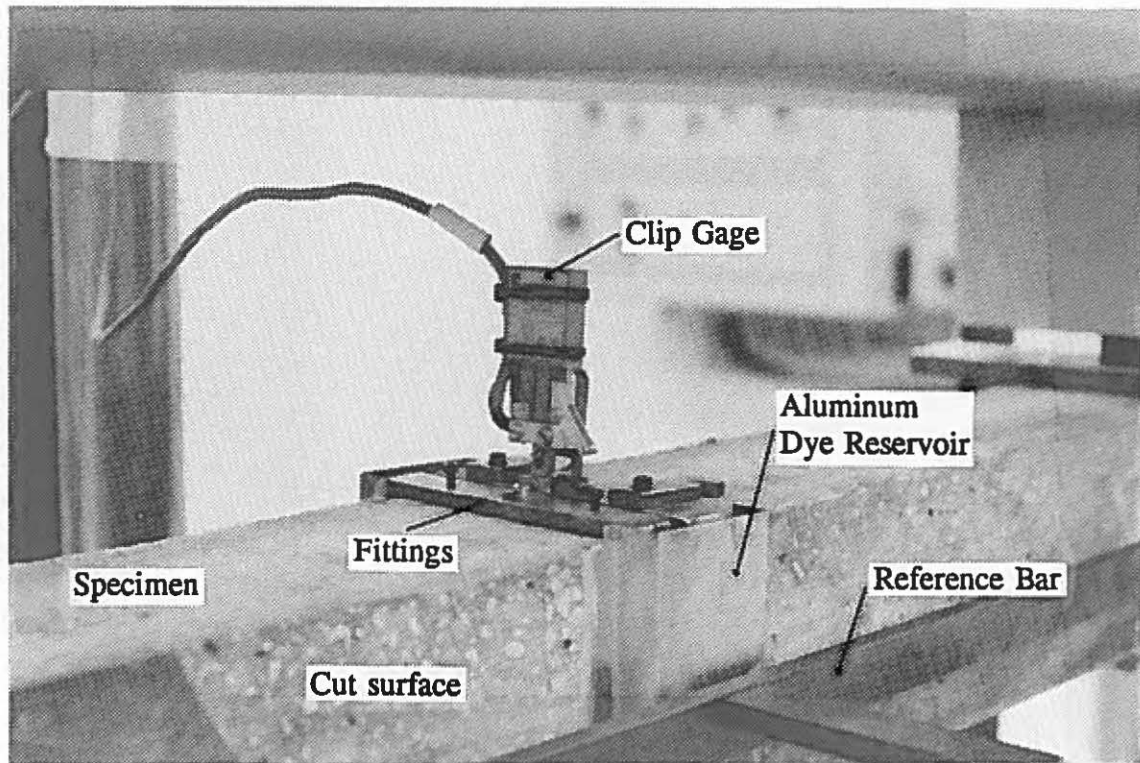
5.4 Conclusions of Chapter 5.

114

Fig. 5.22 Test set up used in the dyeing experiments, with the aluminum reservoir.

An experimental investigation on 40 high-strength concrete beams in three point bending have been performed. The beams consisted of eight different geometries where the beam depth and the thickness were varied. The experiments were made in a combination of piston displacement and crack opening displacement control, whereby the same controlling parameter was used throughout the entire experiment. The fracture parameters according to three different models were determined. That is the Bernoulli beam theory, linear elastic fracture mechanics, and the fictitious crack model.

Explicit formulas are available for the two first theories. The results for the Bernoulli beam theory showed that the bending tensile strength or the modulus of rupture is decreasing with the beam depth, but not with the beam thickness. The decrease was approximately 10% by doubling the beam depth. The fracture toughness determined according to LEFM displayed a significant size effect, as the increase was approximately 50% by doubling the beam depth. Also here there was no significant size effect by increasing the beam thickness. These results are parallel to other similar investigations.

Two different methods were used in connection with the fictitious crack model. The RILEM method and a novel method were the fracture parameters determined through curve fitting. The fracture energy calculated by using the RILEM method displayed a size effect when the beam depth was increased by 15% No size effect was observed by increasing the beam

thickness. The data fitting was done by minimizing a function which describes the difference between the results from a numerical method and the experimental results. Three such functions, objective functions, were tested and the third one was the peak load and the tail were weighted gave the best results. The method is disturbed by the fact that the objective function has a very deep flat valley with many local minima, which makes it very difficult to find the true minimum of the function even when powerful optimization techniques are applied. This problem makes it also very time consuming to determine the fracture parameters.

The material parameters determined using the data fitting technique showed the size effects as the other related parameters. The normalized kink coordinates on the softening relation, which only can be used by using this technique were decreasing with the beam size and were in general smaller than those of normal strength concrete indicating that normal strength concrete is more brittle than high strength concrete.

For all the parameters it was observed that the thickness of the beam was not a governing factor and instead extra experiments were performed in order to check for edge effects due to the mould. Dying experiments were performed on standard specimens and on specimens saw cut out. No difference in the cracking profiles was observed.

5.5 References for Chapter 5.

ASTM (1974), E399-74: Method of test for plane strain fracture toughness of metallic materials.

Bruhwiler, E., Wang, J. and Wittmann, F.H. (1990) Fracture of AAC as Influenced by Specimen Dimension and Moisture, *Journal of Material in Civil Engineering*, ASCE, Vol. 2, No. 3, pp. 136-146.

Enevoldsen, I., Sørensen, J.D. and Sigurdsson, G. (1990), Reliability-Based Shape Optimization Using Stochastic Finite Element Methods, *3rd IFIP WG 7.5 Working Conference*, Berkeley, USA, pp. 75-89.

Gill, P.E., Murray, W. and Wright, M.H. (1981), Practical Optimization, Academic Press, Inc.

Hillerborg, A.(1985), Influence of Beam Size on Concrete Fracture Energy Determined According to a Draft RILEM Recommendation; Report to RILEM TC50-FMC. Rapport TVBN-3021, pp. 1-15.

Karihaloo, B.L. and Nallathambi, P. (1990), Final Report of Sub-committee A (Chairman B.L. Karihaloo) Notched Beam Test Mode I Fracture Toughness RILEM TC89

FMT,(Chairman S.P. Shah), 1-86.

MATLAB (1989), MATLAB^{TM} for MS-DOS Personal Computers, *The MATH Works Inc.*, 21 Eliot Street, , South Natick MA 01760, USA. pp 1-365.

Reagel, F.V. and Willis, T.F. (1931), The Effect of the Dimensions of Test Specimens on the Flexural Strength of Concrete, *Public Roads*, Vol. 12, No. 2, pp.37-46.

RILEM 50-FMC (1985), Determination of the Fracture Energy of Mortar and Concrete by Means of Three-Point Bend tests on notched beams, *Materials and Structures*, Vol. 18, No. 106, pp. 285-290.

Roelfstra, P.E. and Wittmann F.H. (1986), Numerical Method to Link Strain Softening with Failure of Concrete, *in Fracture Toughness and Fracture Energy of Concrete, Edited by F.H. Wittmann*, Elsevier, pp. 163-175.

Swartz, S.E. and Refai, T. (1989), Cracked Surface Revealed by Dye and its Utility in Determining Fracture Parameters, *in Fracture Toughness and Fracture Energy - Test Methods for Concrete and Rock, Eds. Mihashi et al.*, pp.509-520.

Schittkowski, K. (1985), A FORTRAN subroutine Solving Constrained Non-Linear Programming Problems, *Annals of Operation Research*, Vol. 5, pp. 485-500.

Vanderplaats, G.N. (1984), Numerical Optimization Techniques for Engineering Design, *McGraw-Hill Book Company*.

6 CONCLUSIONS.

This chapter has three sections. The first contains a summary of the different chapters of the thesis. The second section gives an overall conclusion of the thesis. This conclusion is based on the evaluation made at the end of chapters 2-5. Finally future research needs and applications are presented and discussed.

6.1 Summary of Thesis.

Chapter 1
Chapter 1 contains the introduction to this thesis. The scope of the thesis is partly to investigate different numerical and analytical models based on fracture mechanical ideas, which are able to predict size effects, and partly to perform an experimental investigation on high-strength concrete.

Chapter 2
A description of the factors which influence the strength and cracking of concrete and high strength concrete is made. Then basic linear fracture mechanics is outlined followed by a description and evaluation of the models used to describe concrete fracture in tension. The chapter ends with a description of the different types of size effects. Three examples which discuss the two terms 'size effect' and 'brittleness' and the importance of a stiff test rig. Finally some brittleness numbers are defined.

Chapter 3
In chapter 3 the most well-known numerical methods which use the fictitious crack to describe fracture in concrete are presented. Two of the methods are combined into a power method which is stable for all brittleness numbers and which is able of calculating the entire load-displacement curve even for very ductile beams. This method is used extensively in the rest of the thesis.

Chapter 4
Since analytical methods are very time consuming different analytical models have been developed. Three methods for plain concrete are presented, where one of the methods is developed by the author. The method is based on three different fracture models. Also two models applicable for lightly reinforced concrete are presented.

Chapter 5

An experimental investigation is performed in a closed-loop testing setup where high-strength concrete in three-point bending is tested. In order to determine the material parameters in the fictitious crack model an estimation procedure based on the solving of an optimization problem is developed. The material parameters and the load-displacement curves obtained by using this procedure are presented. Different size effects are observed, and it is concluded that edge effects play a dominant role. Dyeing experiments were performed on ordinary specimens and specimens which are saw-cut out.

6.2 General Conclusions.

One of the major problems solved in this thesis is the stability problem described in chapter 3. The direct sub-structure method is thereby complete, and is a strong tool, when analyzing structures of quasi brittle materials. The only limit of the method is now the number of nodes used in the midsection. When a fictitious crack develops, the normalized size of this zone is dependent on the brittleness of the structure. The more brittle the structure the smaller the fracture process zone, and consequently many nodes are necessary for describing this zone.

The analytical methods described in chapter 4 show very different results. The analytical method developed by the author, R. Brincker and S. Krenk, seems to be the most promising. This method is capable of predicting the size effect on the modulus of rupture. Further more it is based on basic principles and the governing equations are explicit and simple. These properties of the model make it a very powerful tool, which is applicable for the designing engineer. The method is also extended to reinforced concrete, where the results look very promising.

The large experimental investigation on high-strength concrete seems to have been too small However, some general results were obtained. It is observed that the decrease in the modulus of rupture with the increase of beam depth is of the same order as that of normal strength concrete. The fracture toughness is increasing with the beam depth, making LEFM inadequate for high-strength, even though high-strength is considered to be a brittle material. The data fitting performed by finding the minimum of three different function which describes the difference between a numerical and an experimental load displacement curve turned out to be very time consuming. If the constitutive parameters are wanted for high strength concret this method is then the only applicable. The method is, however, not recommended.

6.3 Future Perspective.

The following items and problems are suggestions for future research in the field of fracture

mechanics of concrete

- Developing analytical methods where the softening relation is bi-linear.
- Perform experiments with high-strength where the beam depths and span are varying with more than a factor 5
- Development of direct experimental techniques whereby the softening relation can be determined for ultra brittle materials.
- Development of simple models, where the bulk dissipation is included.
- Development of models, which describes the bonding between steel and concrete.
- Development of stochastic methods, whereby the reliability and lifetime of cracked structures can be calculated.

APPENDIX A1
NOTATION.

The following symbols are used in this thesis:

a	=	Crack length.
a_e	=	Effective crack length.
a_{ef}	=	Effective crack length.
a_f	=	Fictitious crack length.
a_i	=	Initial crack length.
a_0	=	Distance between nodes.
B	=	Brittleness number.
B_0	=	Material geometry dependent parameter in the size effect law.
C	=	Compliance, or greens function.
c_{ij}, c_j	=	Influence coefficients.
$CTOD$	=	Crack tip opening displacement.
d	=	Characteristic size of structure (e.g. beam depth).
d_y	=	Length of virtual cut in structure.
E	=	Modulus of elasticity.
E_{disp}	=	Dissipated energy.
F	=	Force.
F_{max}	=	Peak load.
$f()$	=	Material function.
$g()$	=	Geometry function.
G	=	The energy release rate.
G_c	=	The crack driving force.
G_F	=	The fracture energy.
I	=	Moment of Inertia.
K	=	The stress intensity factor.
K_c	=	The critical stress intensity factor.
l	=	Length of structure.
Δl	=	Elongation of structure.
$LEFM$	=	Linear elastic fracture mechanics.
R	=	Resistance towards crack growth.
r	=	Position of reinforcement.
s_j	=	Nodal force.
s_u	=	Ultimate nodal force.
t	=	Thickness of structure.
u, v	=	Displacement of virtual surface.
w	=	Crack opening displacement.
w_c	=	Critical crack opening displacement.

x,y	$=$	Cartesian coordinates
α	$=$	Normalized crack length.
α_f	$=$	Normalized fictitious crack length.
α_r	$=$	Normalized position of reinforcement.
α_η	$=$	Normalized position of neutral axis.
β	$=$	Brittleness number.
γ	$=$	Crack path.
δ	$=$	Displacement.
δ_{max}	$=$	Displacement at peak load.
ϵ	$=$	Strain.
ϵ_e	$=$	Linear elastic strain.
ϵ_n	$=$	Nonlinear part of strain.
ϵ_{peak}	$=$	Strain at peak load.
ϵ_{res}	$=$	Residual strain
$\phi()$	$=$	Energy density.
Π	$=$	Total potential energy of the considered system.
Π_e	$=$	The elastic energy content in structure.
Π_F	$=$	The potential of external forces.
Π_K	$=$	The kinetic energy.
Π_c	$=$	The fracture potential.
η	$=$	Position of neutral axis.
σ	$=$	Stress, or arbitrary external load.
σ_{ij}	$=$	Stress tensor.
σ_m	$=$	Modulus of rupture.
σ_u	$=$	Tensile strength.
σ_y	$=$	Yield strength.
θ,r	$=$	Polar coordinates.
j		

APPENDIX A2

LOAD DISPLACEMENT CURVES.

On the following pages the load displacement curves are plotted. The beams are plotted according to beam size.

a_1c, a_2a, a_4a and a_5a

Max a_1c = 543.1
Max a_2a = 663.7
Max a_4a = 683.8
Max a_5a = 616.9
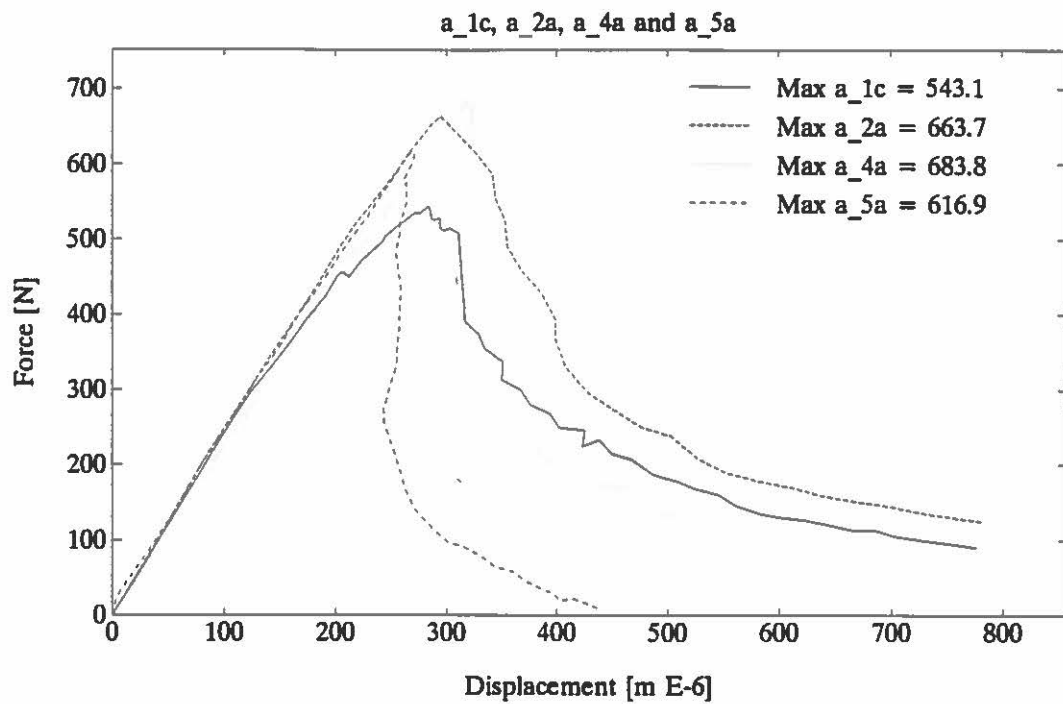
Figure A2.1: Load displacement curves for beam series A.

b_2a, b_4aand b_5a

Max b_2a = 1197.9
Max b_4a = 1514.9
Max b_5a = 1701.0
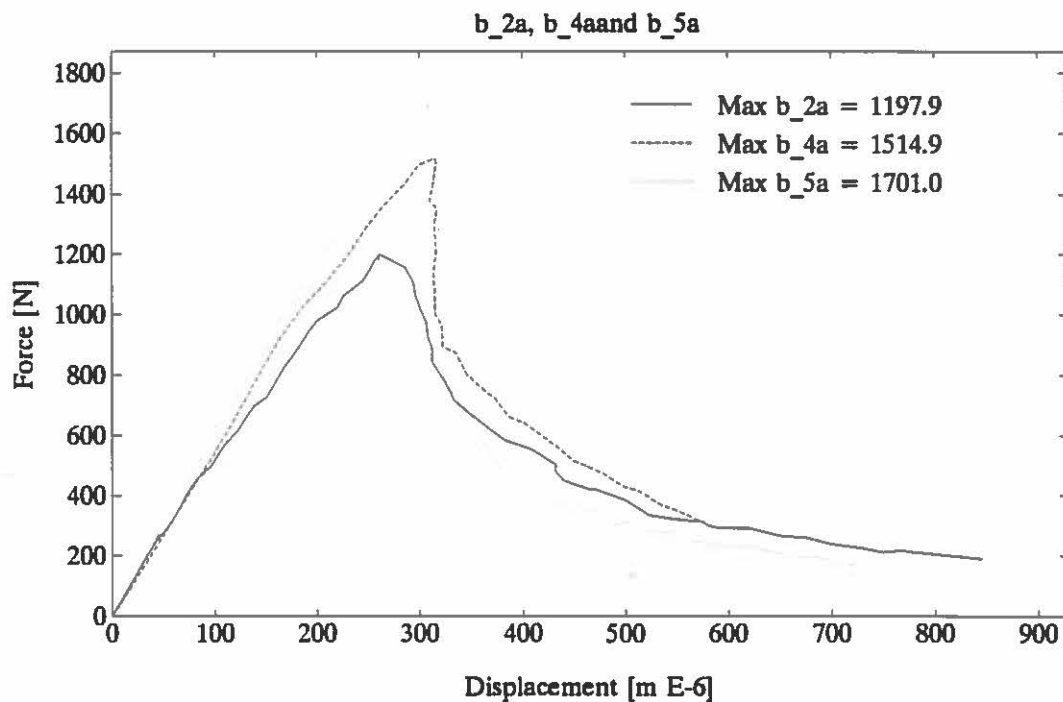
Figure A2.2: Load displacement curves for beam series B.
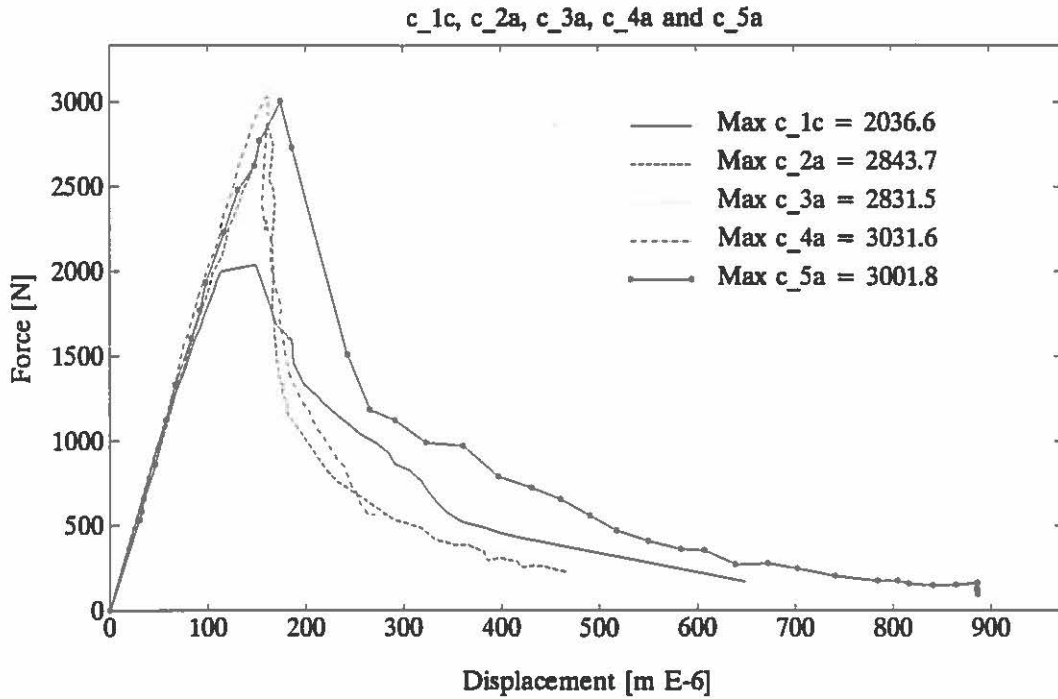
Figure A2.3: Load displacement curves for beam series C.
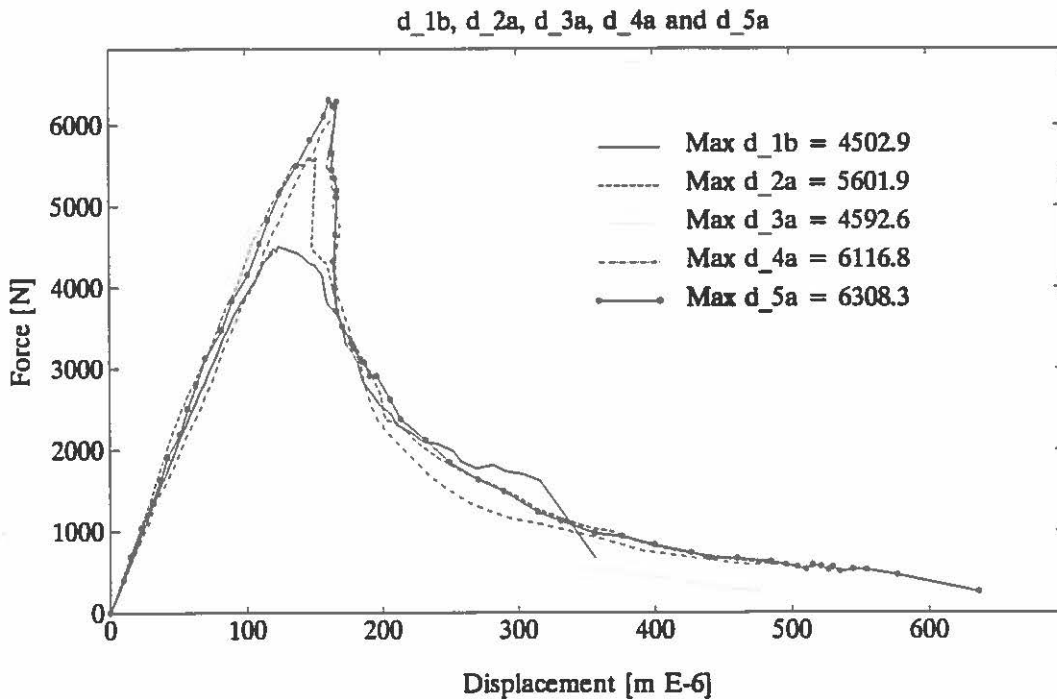
Figure A2.4: Load displacement curves for beam series D.

e_1c, e_2b, e_3b, e_4b and e_5b
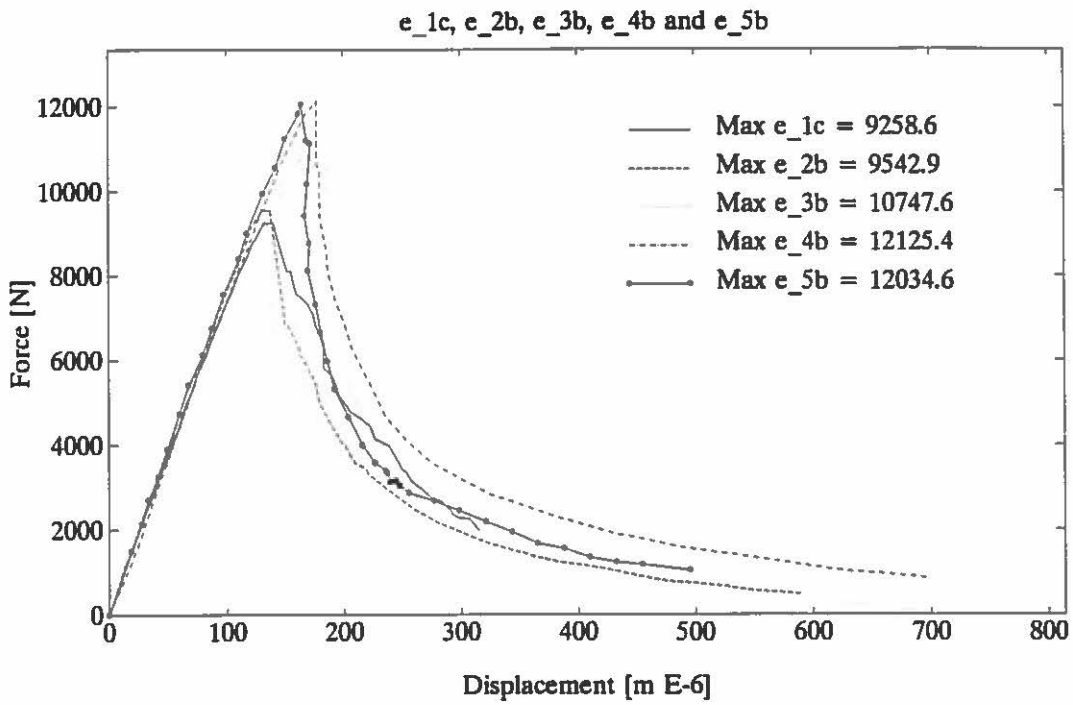
Figure A2.5: Load displacement curves for beam series E.

f_1c, f_2b, f_3b, f_4b and f_5b
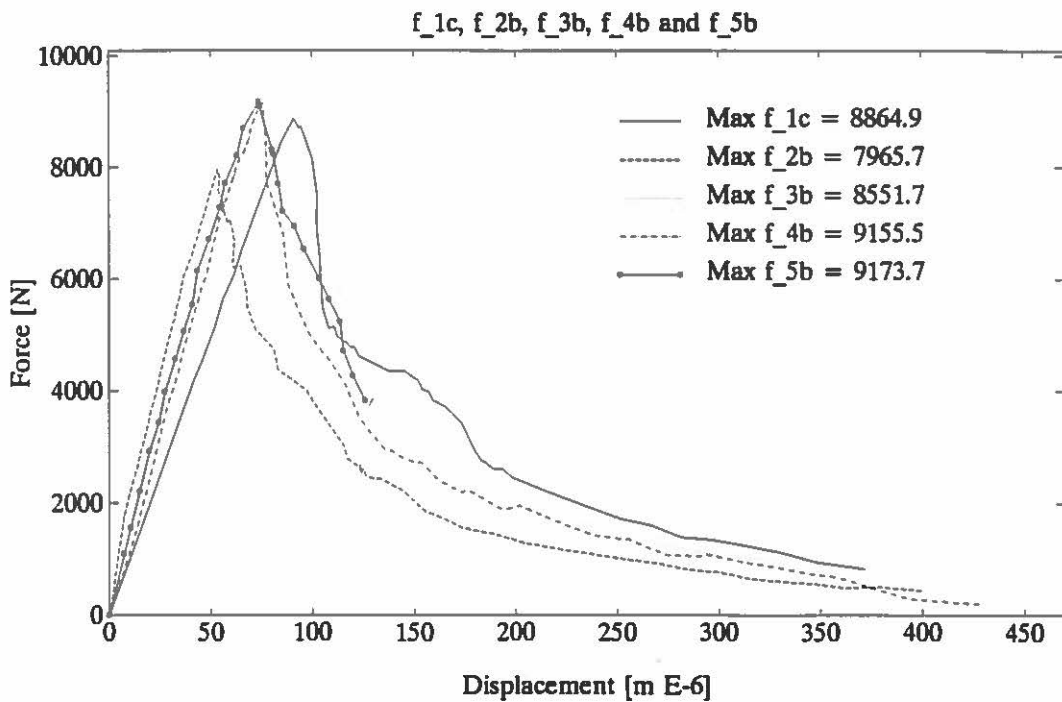
Figure A2.6: Load displacement curves for beam series F.
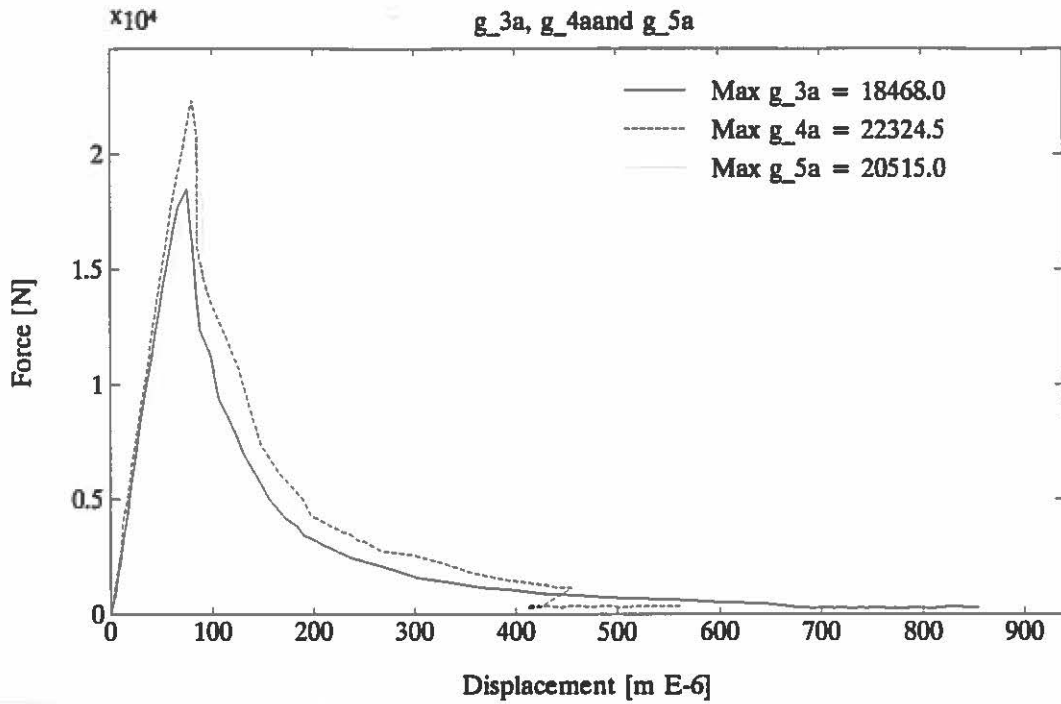
Figure A2.7: Load displacement curves for beam series G.
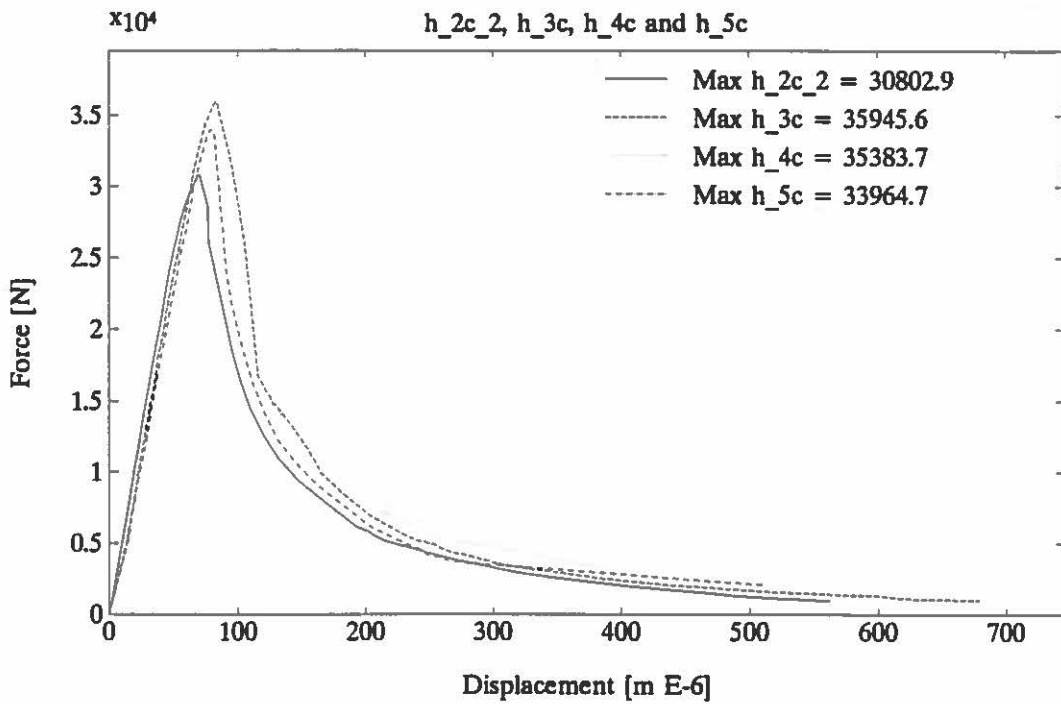
Figure A2.8: Load displacement curves for beam series H.

APPENDIX A3
FRACTURE PARAMETERS.

On the following pages the fracture parameters determined in chapter 5 are presented.

In table A3.1 and A3.2 the modulus of rupture, The fracture toughness, the peak load and the peak displacements are shown.

In Table A3.3 and A3.4 the Fracture energy, the remaining fracture energy and the fracture energy obtained through optimization are presented.

In table A3.5 and A3.6 the parameters determined through the optimization technique described in chapter 5 are shown.

Specimen	Mod. of rupture [N/mm^2]	K_c [N/mm$^{3/2}$]	Peak load [N]	Peak displacement [μm]
A1	6.50	1.14	543	284
A2	7.18	0.87	663	294
A3	%	%	%	%
A4	7.43	0.94	684	318
A5	6.68	0.78	617	271
Mean ± S.dev	6.94 ± 0.43	0.93 ± 0.15	627 ± 62.5	295 ± 33.2
Coeff.of Var.	0.062	0.16	0.10	0.11
B1	%	%	%	%
B2	6.51	0.917	1198	262
B3	%	%	%	%
B4	8.21	1.13	1515	314
B5	8.94	1.18	1710	311
Mean ± S.dev	7.89 ± 1.25	1.08 ± 0.14	1474 ± 258	296 ± 29.2
Coeff.of Var.	0.16	0.13	0.18	0.09
C1	6.43	1.39	2160	135
C2	7.97	1.57	2843	161
C3	8.25	1.69	2831	154
C4	8.54	1.69	3032	162
C5	8.45	1.67	3002	175
Mean ± S.Dev	7.93 ± 0.87	1.60 ± 0.13	2773 ± 355	157 ± 14.6
Coeff.of Var.	0.11	0.08	0.13	0.09
D1	6.58	1.52	4502	124
D2	7.97	1.65	5601	152
D3	6.54	1.36	4593	126
D4	8.53	1.62	6117	167
D5	8.74	1.66	6308	162
Mean ± S.dev	7.67 ± 1.05	1.56 ± 0.13	5424 ± 842	146 ± 20.1
Coeff.of Var.	0.14	0.08	0.16	0.14

Table A3.1 Estimated fracture parameters for beam type A-D.

Specimen	Mod. of rupture [N/mm²]	K_c [N/mm³/²]	Peak load [N]	Peak displacement [μm]
E1	6.9	1.52	9259	133
E2	6.87	1.37	9543	131
E3	7.56	1.41	10748	165
E4	8.66	1.68	12125	178
E5	8.44	1.53	12034	165
Mean ± S.dev	7.69 ± 0.84	1.50 ± 0.12	10741 ± 1343	154 ± 21.1
Coeff.of Var.	0.11	0.081	0.13	0.14
F1	6.37	1.92	8865	90.8
F2	5.85	1.79	7966	%
F3	6.13	1.78	8552	69.4
F4	6.62	2.03	9155	75.6
F5	6.73	2.07	9174	73.7
Mean ± S.dev	6.34 ± 0.36	1.92 ± 0.13	8742 ± 503	77.4 ± 9.32
Coeff.of Var.	0.057	0.069	0.057	0.120
G1	%	%	%	%
G2	%	%	%	%
G3	6.65	1.96	18468	75.5
G4	7.82	2.24	22324	80.3
G5	7.17	2.02	20515	63.6
Mean ± S.Dev	7.21 ± 0.59	2.07 ± 0.15	20436 ± 1929	73.1 ± 8.60
Coeff.of Var.	0.081	0.071	0.094	0.12
H1	%	%	%	%
H2	6.33	2.31	30803	69.4
H3	6.98	2.33	35946	82.3
H4	7.36	2.75	35383	81.5
H5	6.9	2.47	33964	78.4
Mean ± S.dev	6.89 ± 0.42	2.47 ± 0.20	34024 ± 2304	77.9 ± 5.91
Coeff.of Var.	0.062	0.12	0.068	0.076

Table A3.2 Estimated fracture parameters for beam type E-H.

Specimen	G_F^{Hil}	A_1	G'_P
A1	115	31.2	105
A2	140.0	41.1	126.2
A3	%	%	%
A4	93.7	27.7	85.0
A5	40.5	0.0	87.0
Mean//S.dev	98.8 ± 42.3	%	100.8 ± 19.2
Coeff.of Var.	0.42	%	0.19
B1	%	%	%
B2	122.2	34.0	117.5
B3	%	%	%
B4	123.5	36.6	120.0
B5	114.8	25.4	117.0
Mean//S.dev	120.2 ± 4.69	%	118 ± 1.6
Coeff.of Var.	0.04	%	0.01
C1	140.7	24.1	132.1
C2	109.6	34.0	111.0
C3	123.0	31.2	103.6
C4	114.0	32.9	102.0
C5	184.0	17.8	188.0
Mean/S.Dev	134.3 ± 30.3	%	127.3 ± 36.0
Coeff.of Var.	0.23	%	0.28
D1	145.2	56.0	136
D2	140.5	30.7	118
D3	93.0	13.5	81.0
D4	130	29.9	124.2
D5	135.4	17.3	126
Mean//S.dev	128.8 ± 20.8	%	117.0 ± 21.2
Coeff.of Var.	0.16	%	0.18

Table A3.3 Fracture Energies for beam types A-D.

131

Specimen	G_F^{Hil}	Al	G'_F
E1	119.4	34.7	108
E2	107	15.6	99
E3	100.9	0.79	105
E4	163.4	30.1	159.4
E5	131	27.9	128
Mean//S.dev	124.3 ± 24.7	%	119.9 ± 24.6
Coeff.of Var.	0.20	%	0.21
F1	158.1	33.1	159
F2	113.8	19.5	107.1
F3	161	34.4	154
F4	120.8	9.17	121.3
F5	130.5	53.3	115
Mean//S.dev	136.8 ± 21.6	%	131.3 ± 23.6
Coeff.of Var.	0.16	%	0.18
G1	%	%	%
G2	%	%	%
G3	138.7	13.5	143
G4	153.6	9.62	154
G5	125.1	44.8	128.3
Mean/S.Dev	139.1 ± 14.3	%	141.8 ± 12.9
Coeff.of Var.	0.10	%	0.09
H1	%	%	%
H2	127.1	15.1	123.2
H3	152.6	19.2	142
H4	168.6	26.6	159.8
H5	126.5	28.8	124.6
Mean//S.dev	143.7 ± 20.6	%	137.4 ± 17.2
Coeff.of Var.	0.14	%	0.13

Table A3.4 Fracture Energies for beam types E-H.

Specimen	σ_u'	w_c'	x'	y'	α
A1	3.60	0.12	0.19	0.28	1.14
A2	3.97	0.12	0.22	0.31	1.12
A3	%	%	%	%	%
A4	5.42	0.086	0.14	0.22	1.01
A5	%	%	%	%	%
Mean±S.dev	4.33 ± 0.96	0.11 ± 0.02	0.18 ± 0.04	0.27 ± 0.05	1.09 ± 0.07
Coeff.of Var.	0.22	0.18	0.22	0.17	0.06
B1	%	%	%	%	%
B2	3.31	0.15	0.20	0.26	1.20
B3	%	%	%	%	%
B4	5.14	0.12	0.15	0.24	1.23
B5	5.19	0.15	0.17	0.13	1.35
Mean±S.dev	4.55 ± 1.07	0.14 ± 0.02	0.17 ± 0.03	0.21 ± 0.07	1.26 ± 0.08
Coeff.of Var.	0.24	0.12	0.15	0.33	0.06
C1	4.15	0.14	0.18	0.29	1.26
C2	6.14	0.19	0.12	0.07	1.18
C3	6.91	0.10	0.14	0.16	1.32
C4	7.87	0.08	0.16	0.16	1.26
C5	5.53	0.18	0.18	0.19	1.26
Mean±S.Dev	6.12 ± 1.41	0.14 ± 0.05	0.16 ± 0.03	0.17 ± 0.08	1.26 ± 0.05
Coeff.of Var.	0.23	0.35	0.17	0.45	0.04
D1	4.12	0.16	0.18	0.23	1.31
D2	6.47	0.11	0.15	0.20	1.38
D3	6.25	0.07	0.13	0.27	1.27
D4	6.69	0.15	0.14	0.12	1.23
D5	5.77	0.16	0.14	0.14	1.25
Mean±S.dev	5.86 ± 1.03	0.13 ± 0.04	0.15 ± 0.02	0.19 ± 0.06	1.29 ± 0.06
Coeff.of Var.	0.18	0.30	0.13	0.32	0.05

Table A3.5 Estimated fracture parameters for beam type A-D.

Specimen	σ_u'	w_c'	x'	y'	α
E1	5.12	0.09	0.19	0.30	1.25
E2	6.15	0.11	0.12	0.20	1.23
E3	6.63	0.09	0.16	0.19	1.13
E4	6.61	0.18	0.12	0.15	1.19
E5	6.80	0.18	0.11	0.10	1.21
Mean±S.dev	6.26 ± 0.68	0.13 ± 0.05	0.14 ± 0.03	0.19 ± 0.07	1.20 ± 0.05
Coeff.of Var.	0.11	0.35	0.24	0.39	0.04
F1	5.95	0.26	0.09	0.12	1.06
F2	5.23	0.16	0.09	0.17	1.72
F3	5.24	0.17	0.14	0.21	1.37
F4	6.18	0.15	0.12	0.15	1.39
F5	5.90	0.08	0.19	0.27	1.47
Mean±S.dev	5.7 ± 0.44	0.16 ± 0.06	0.13 ± 0.04	0.18 ± 0.06	1.40 ± 0.24
Coeff.of Var.	0.08	0.39	0.33	0.32	0.17
G1	%	%	%	%	%
G2	%	%	%	%	%
G3	5.48	0.21	0.11	0.14	1.47
G4	7.57	0.16	0.11	0.14	1.51
G5	6.17	0.20	0.13	0.09	1.28
Mean±S.Dev	6.41 ± 1.06	0.19 ± 0.026	0.12 ± 0.012	0.12 ± 0.03	1.42 ±0.12
Coeff.of Var.	0.17	0.14	0.10	0.23	0.09
H1	%	%	%	%	%
H2	5.38	0.18	0.12	0.14	1.49
H3	5.11	0.24	0.15	0.08	1.34
H4	5.75	0.28	0.11	0.09	1.43
H5	6.31	0.17	0.12	0.11	1.32
Mean±S.dev	5.64 ± 0.52	0.22 ± 0.05	0.13 ± 0.02	0.11 ± 0.03	1.40 ± 0.08
Coeff.of Var.	0.09	0.24	0.14	0.25	0.06

Table A3.6 Estimated fracture parameters for beam type E-H.

APPENDIX A4

OPTIMIZATION RESULTS.

On the following pages the fitted load displacement curves are plotted. The experimental curve is the dashed curve and the solid curve is the fitted curve.
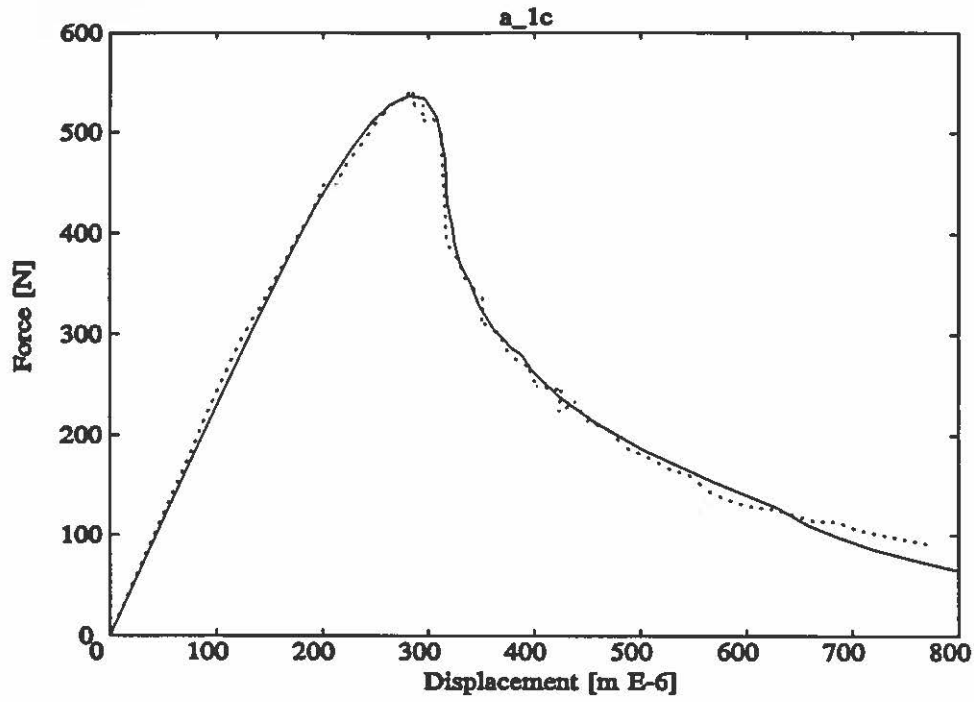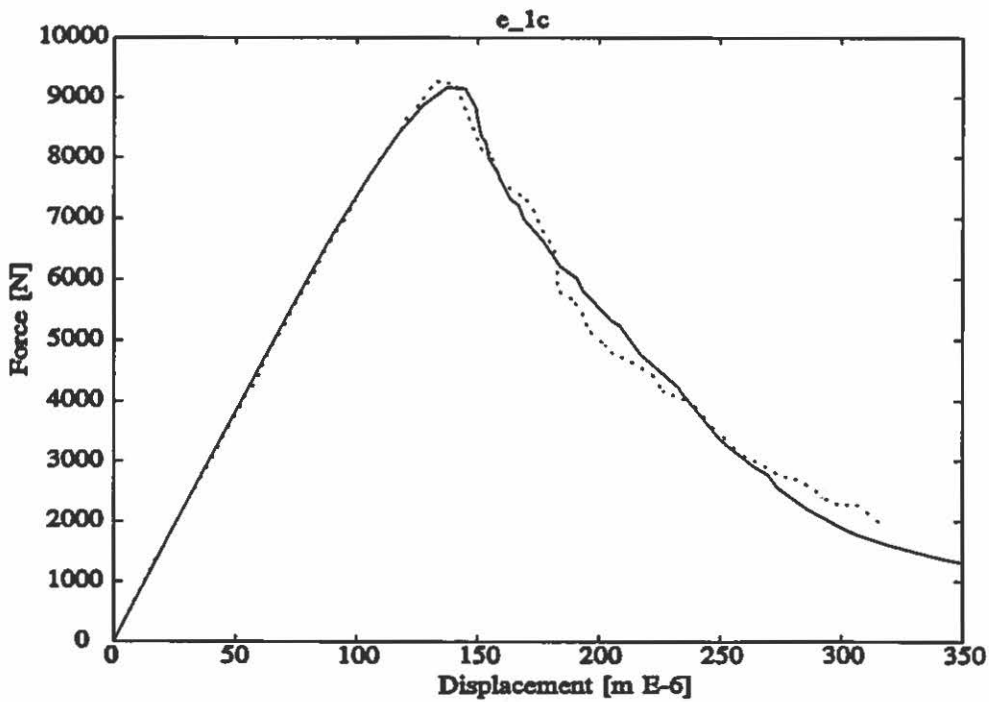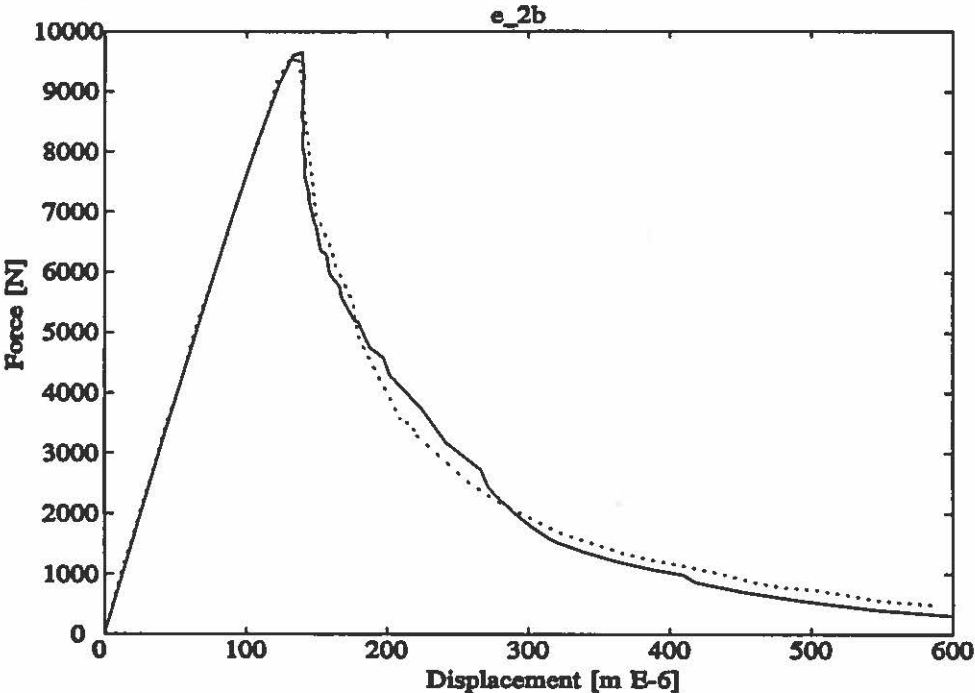
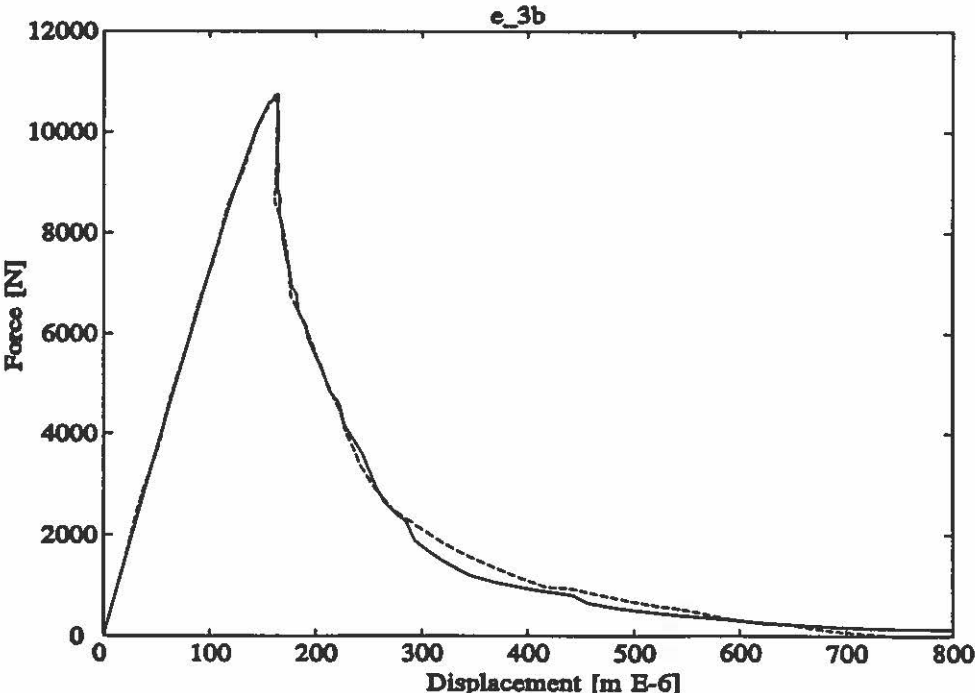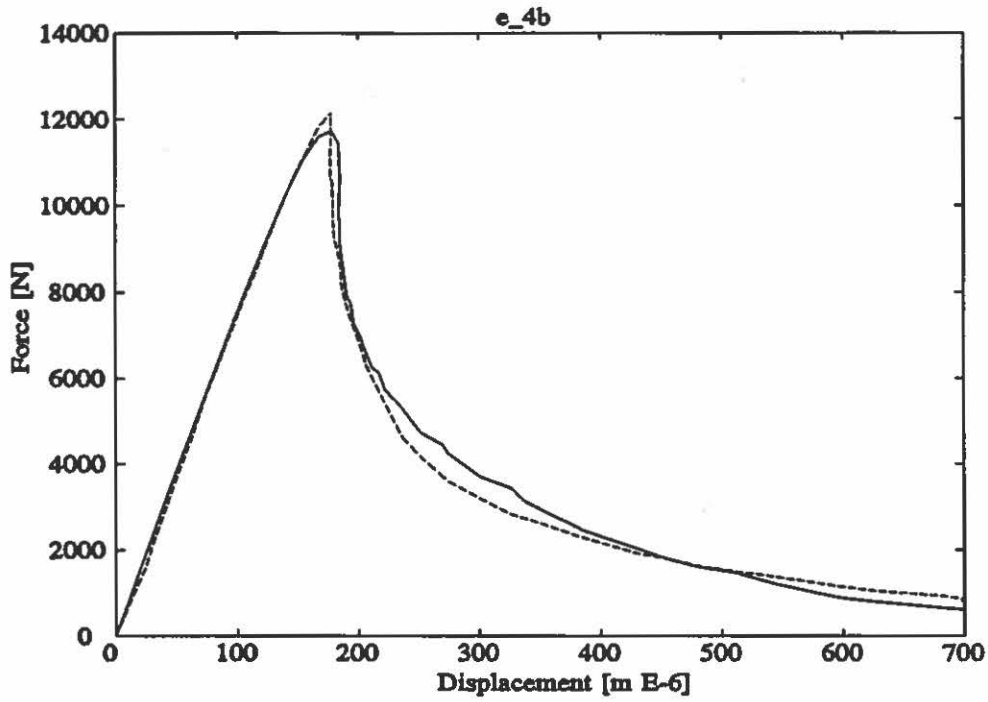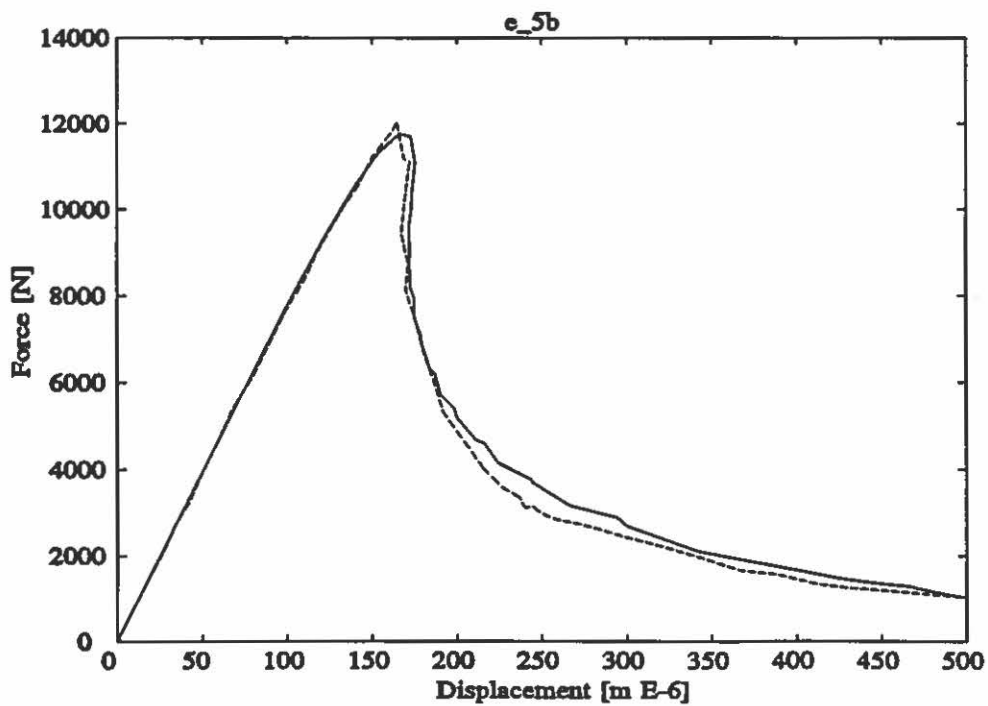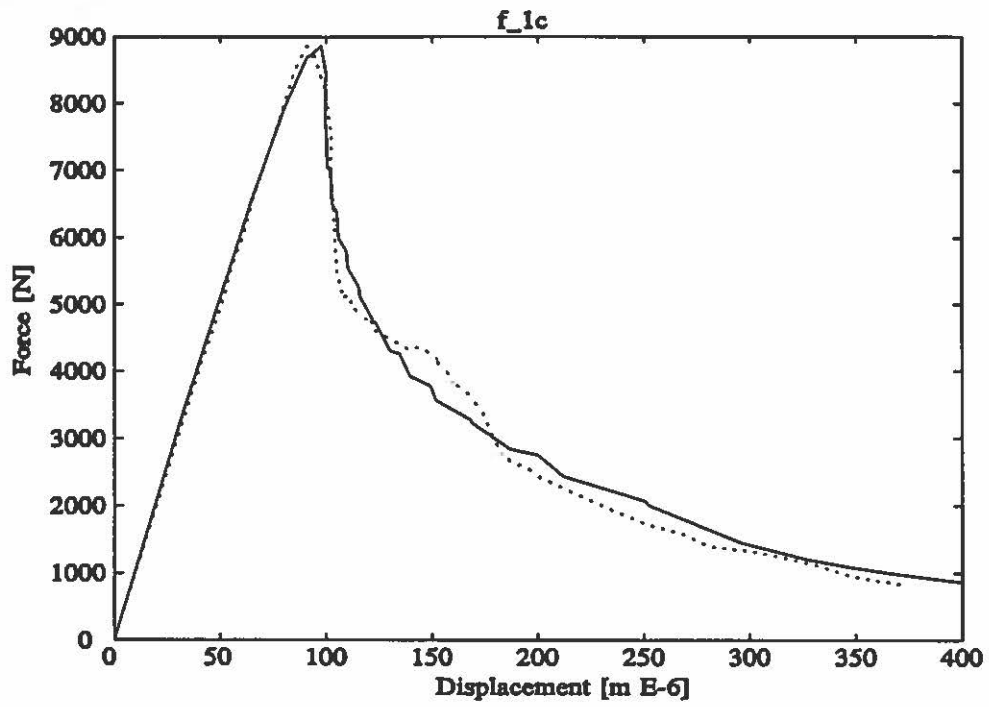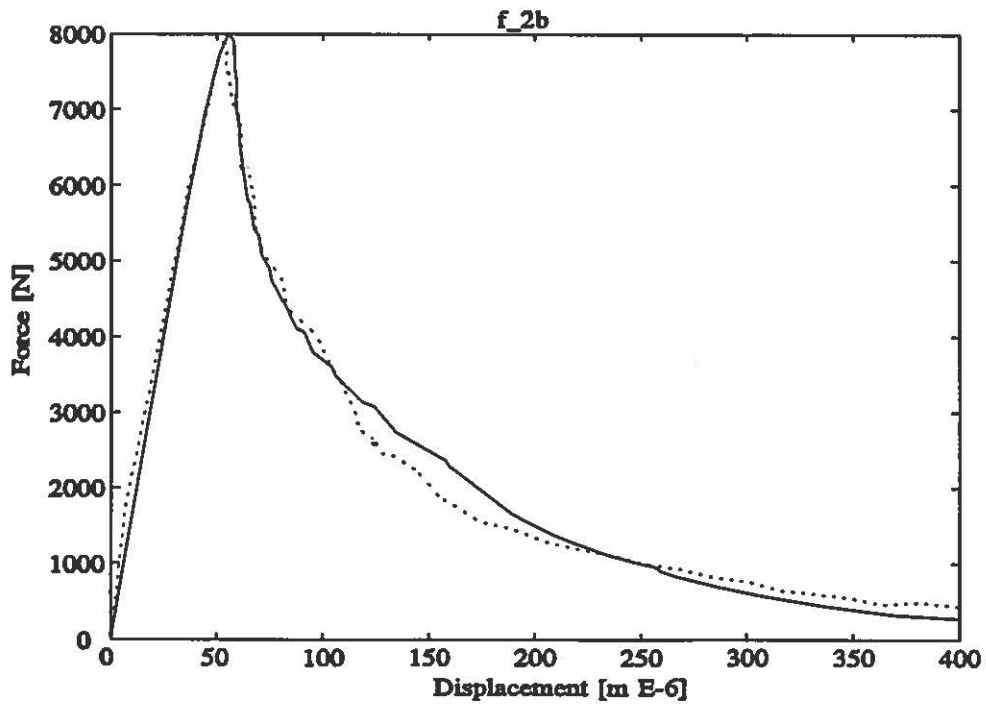Figure A2.1: Fitted results for beam A-1C.
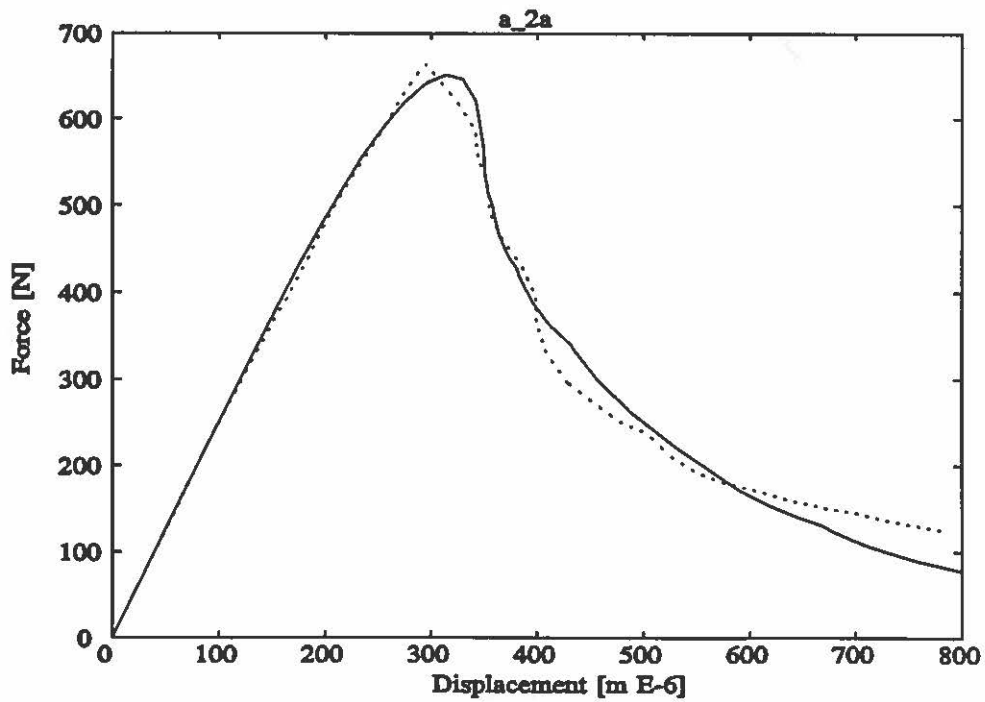
Figure A2.2: Fitted results for beam A-2a.
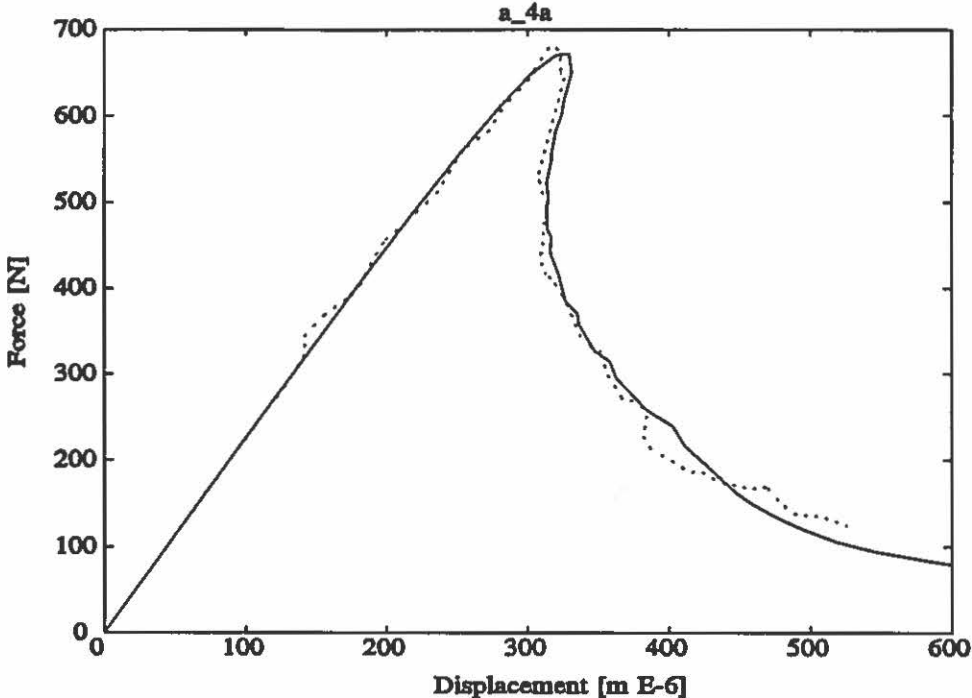
Figure A2.3: Fitted results for beam A-4a.
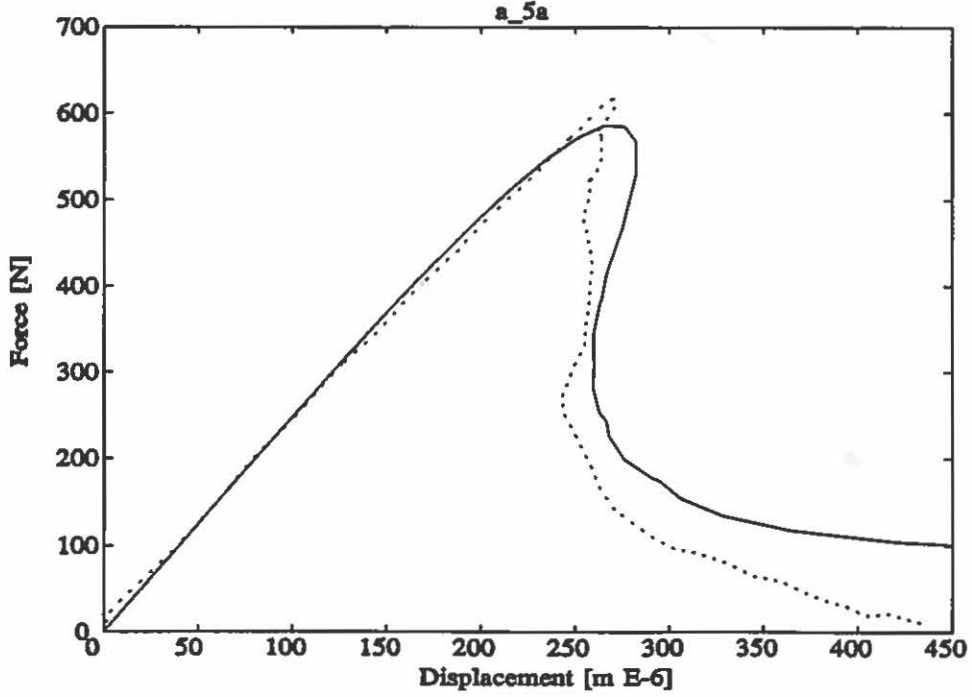
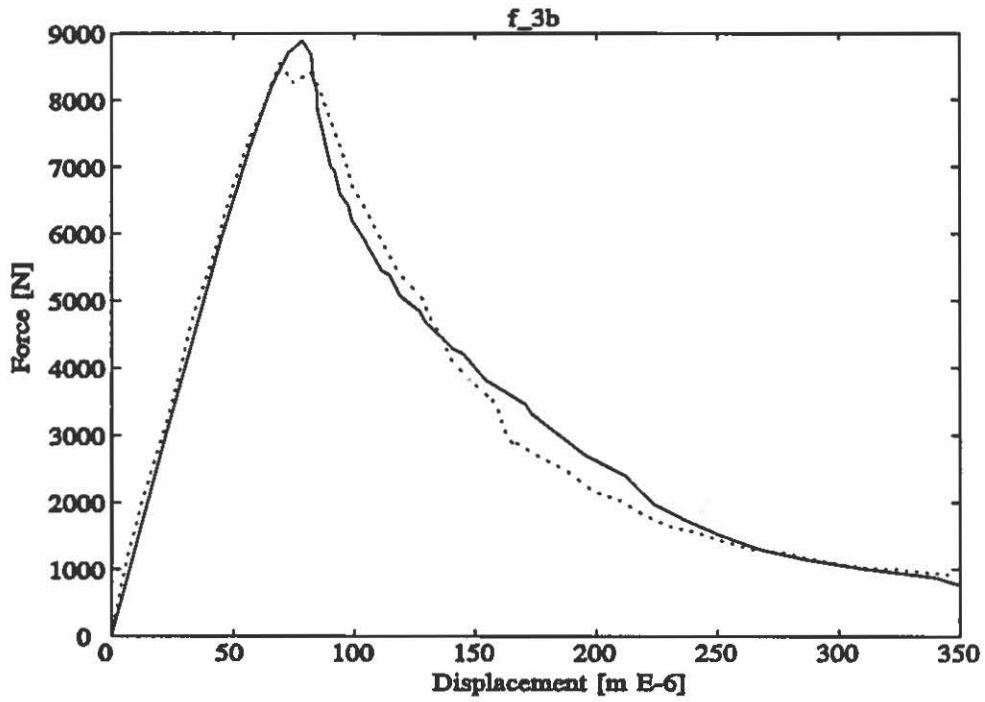Figure A2.4: Fitted results for beam A-5a.
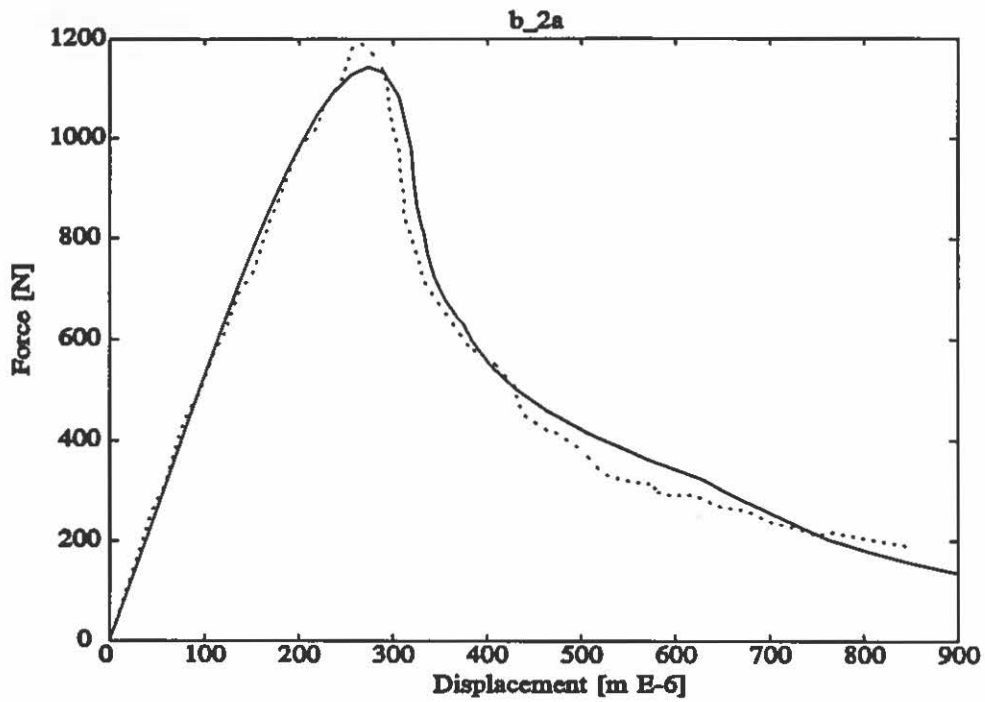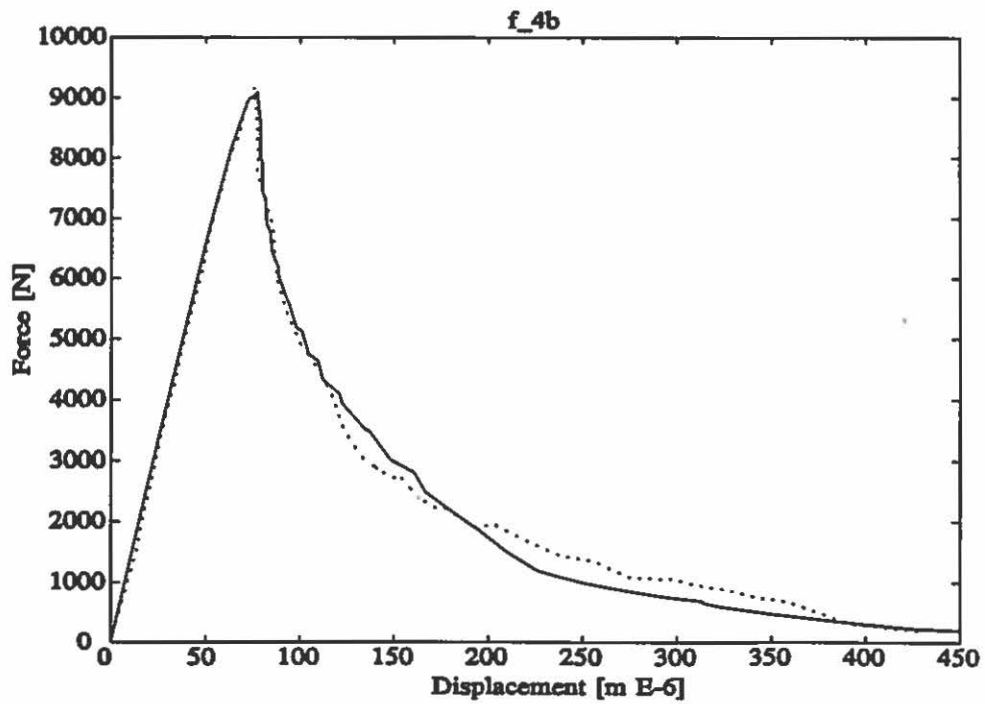
Figure A2.5: Fitted results for beam B-2a.
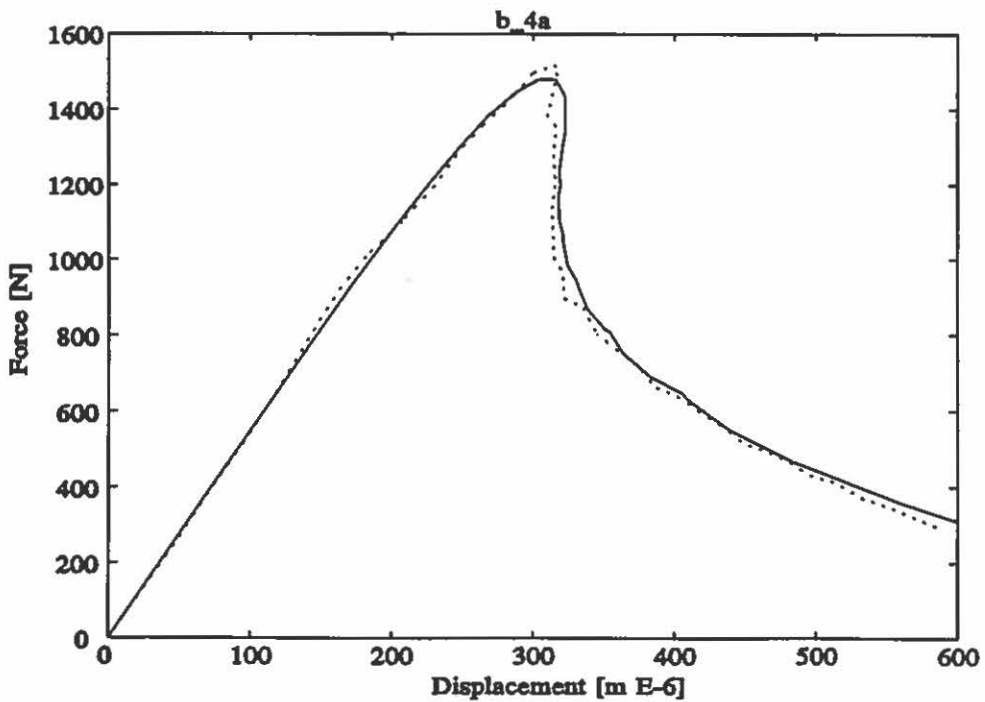
Figure A2.6: Fitted results for beam B-4a.

138
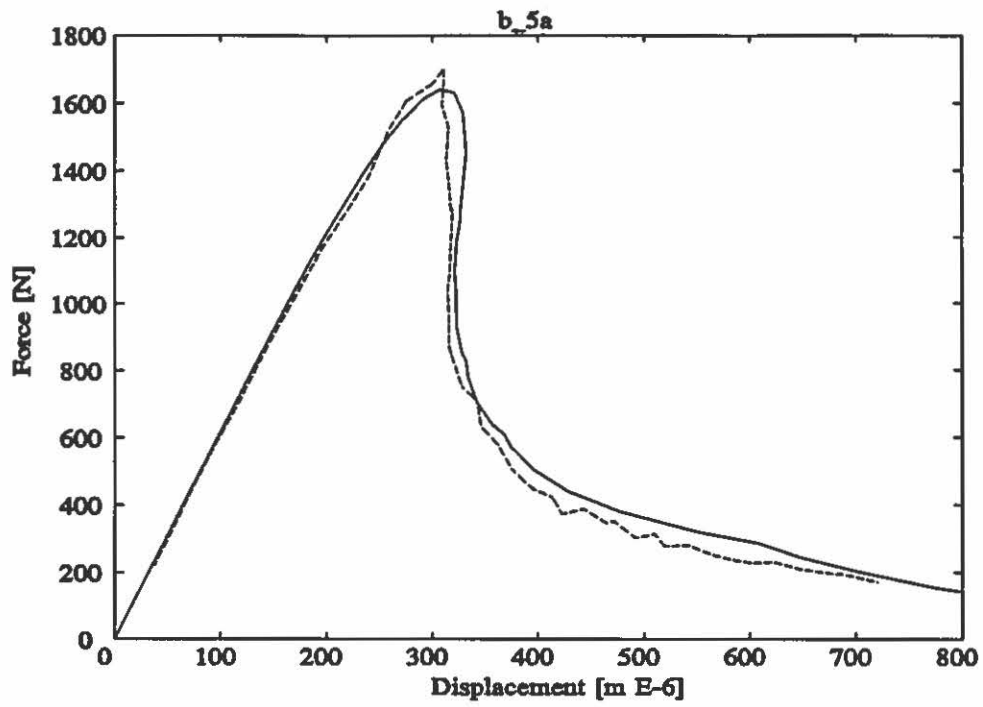
Figure A2.7: Fitted results for beam B-5a.
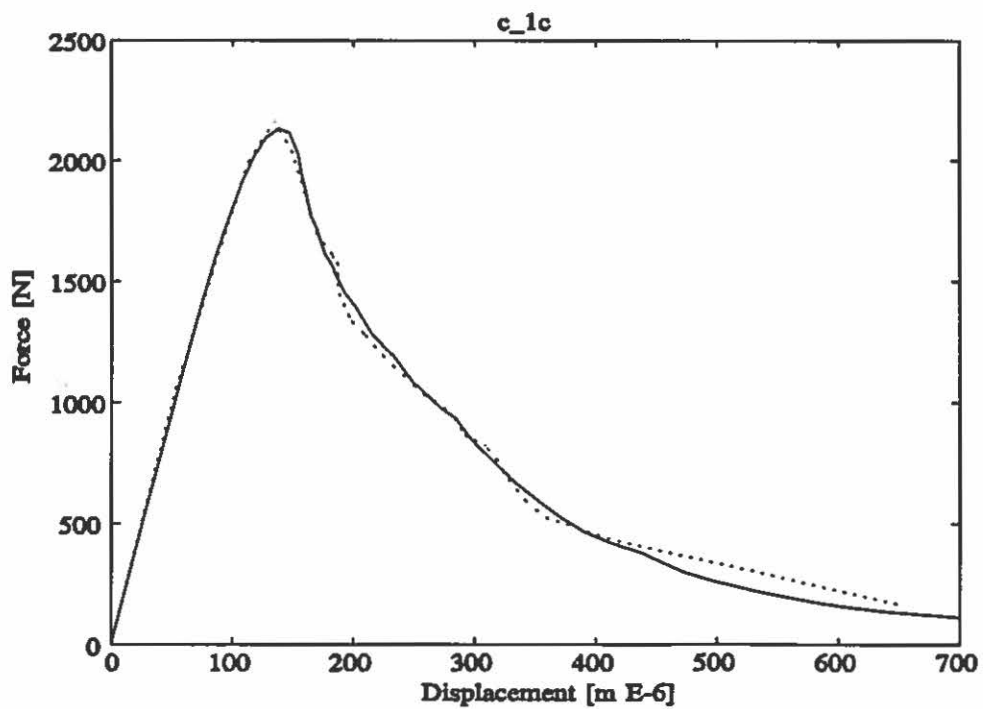
Figure A2.8: Fitted results for beam C-1c.
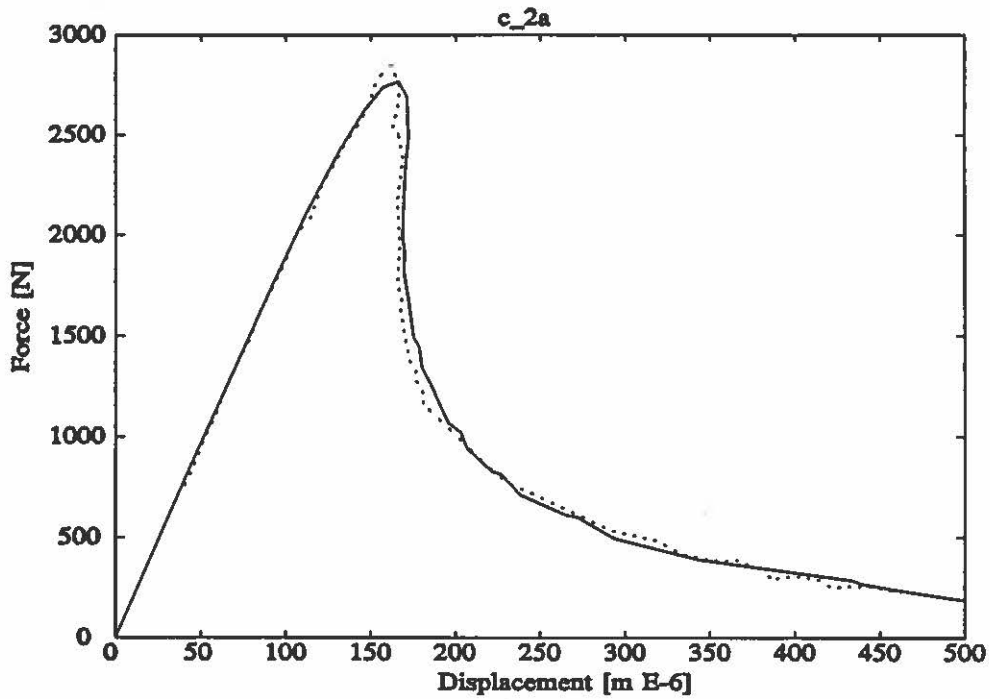
Figure A2.9: Fitted results for beam C-2.
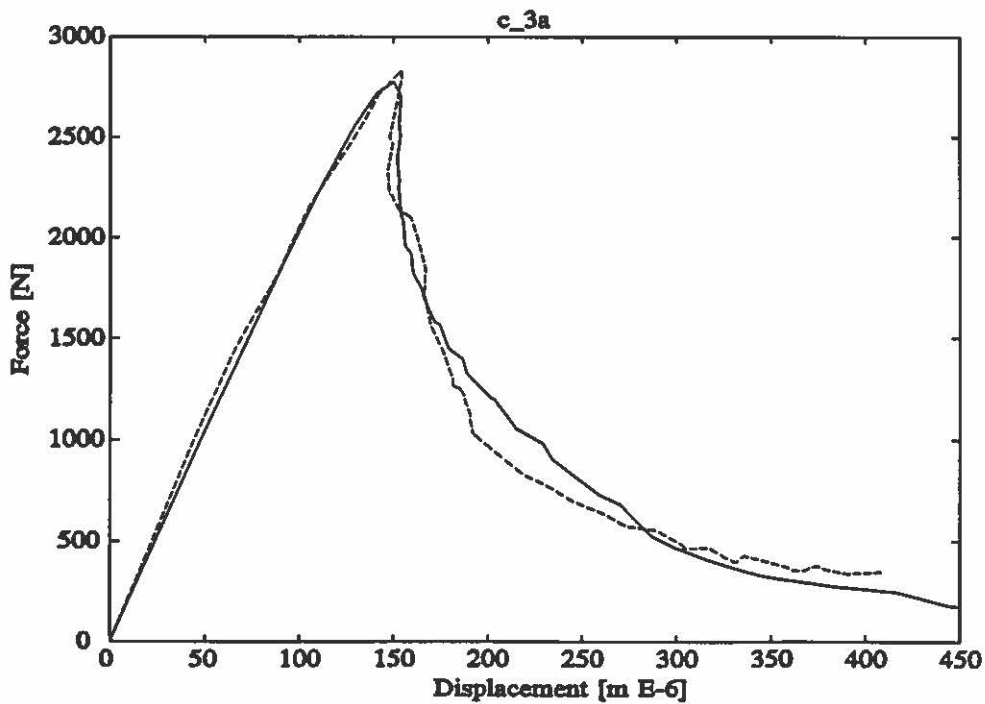
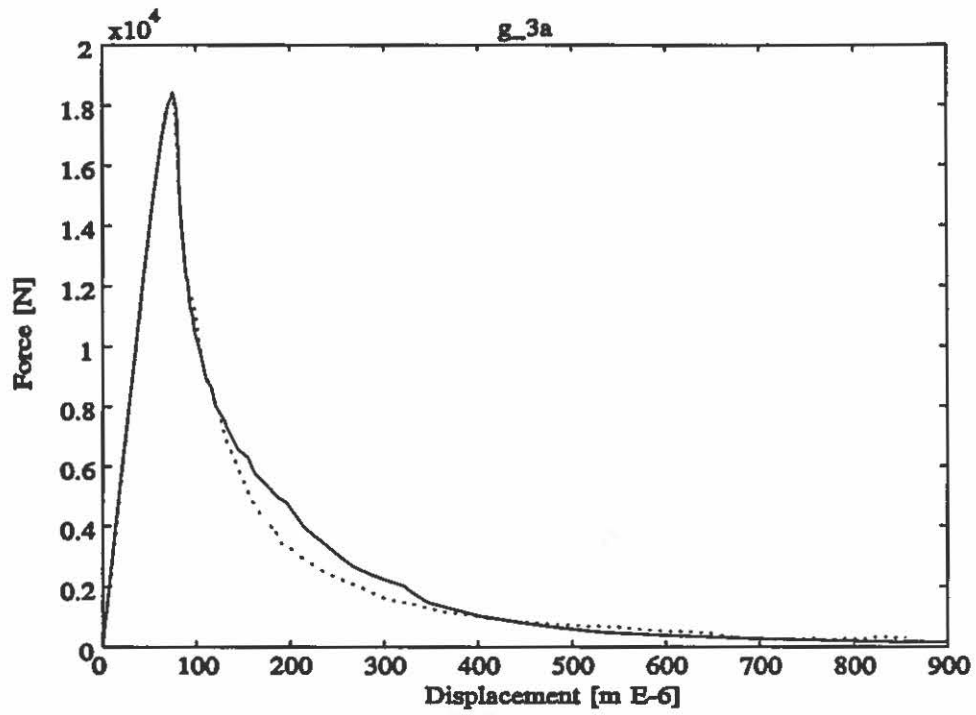Figure A2.10: Fitted results for beam C-3.
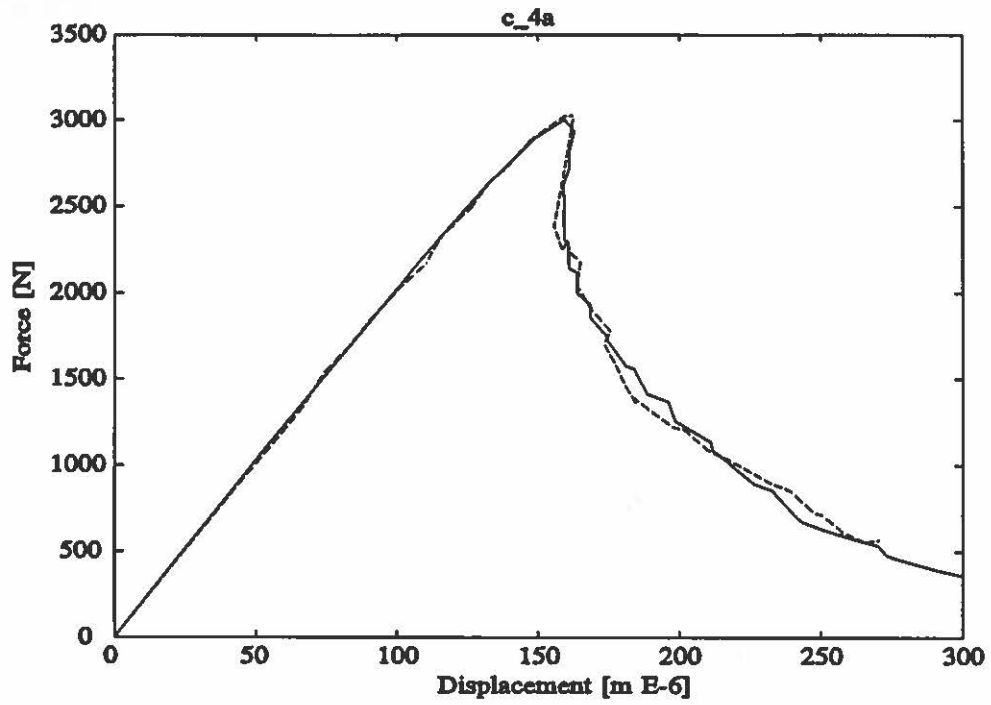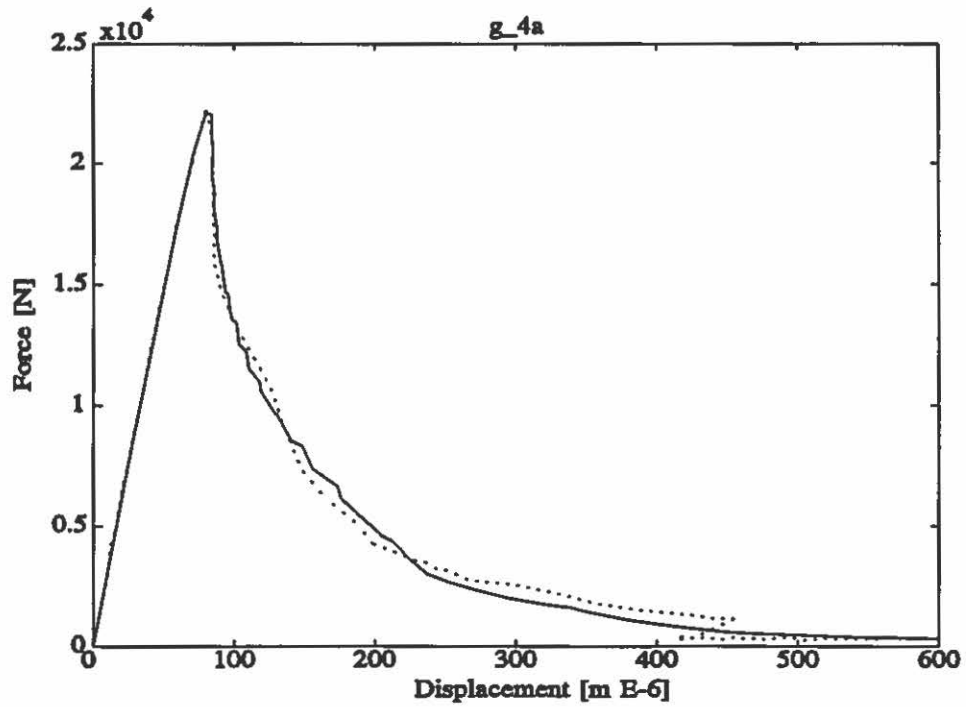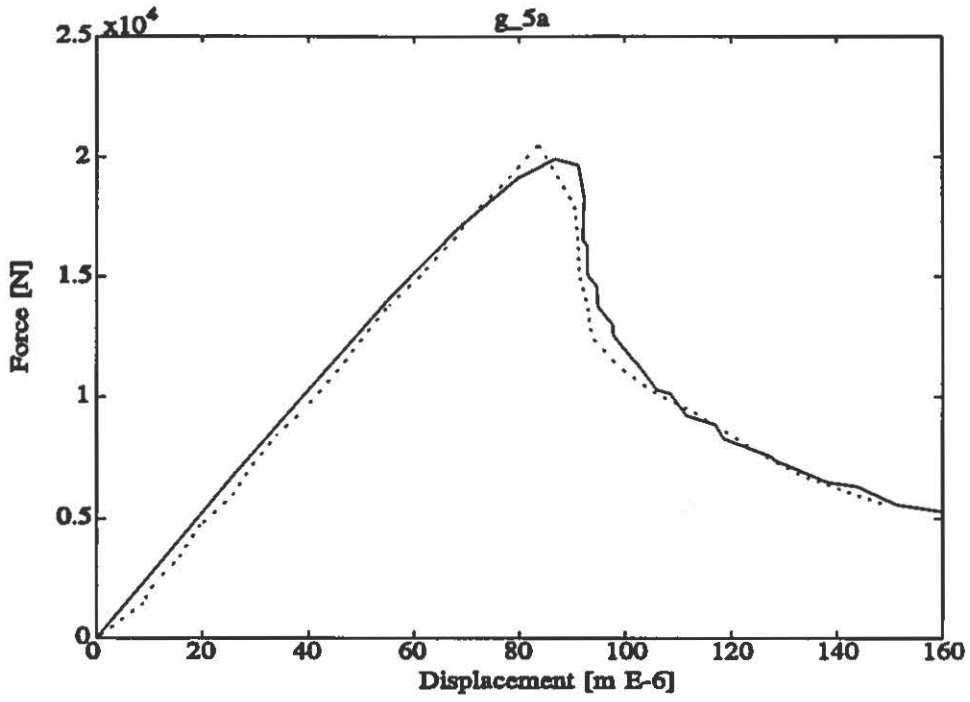
Figure A2.11: Fitted results for beam C-4.
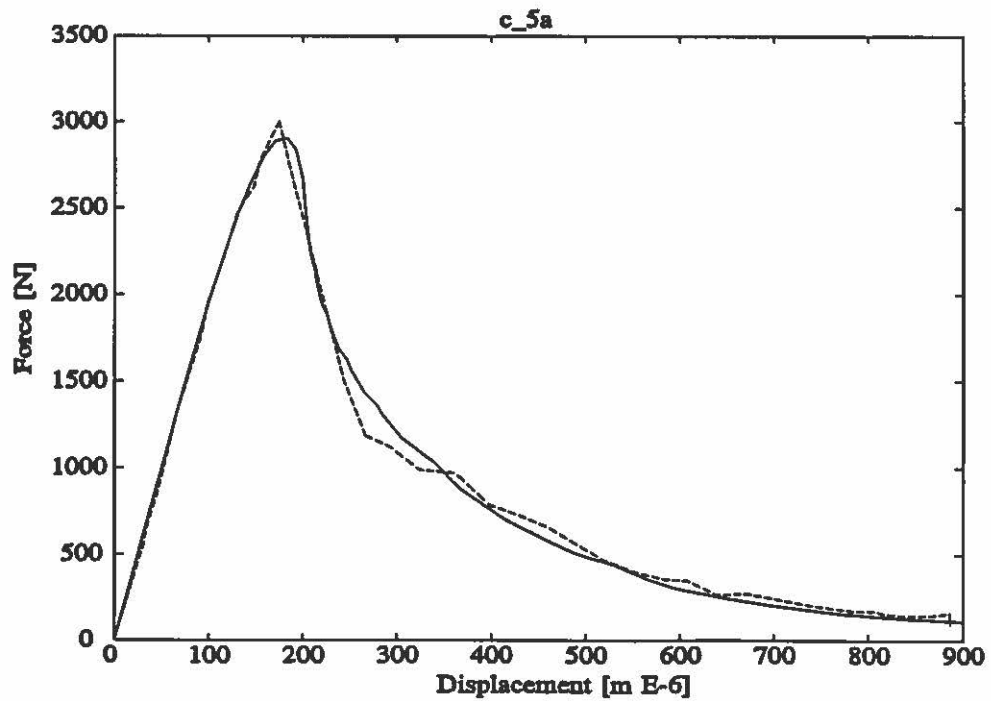
Figure A2.12: Fitted results for beam C-5.
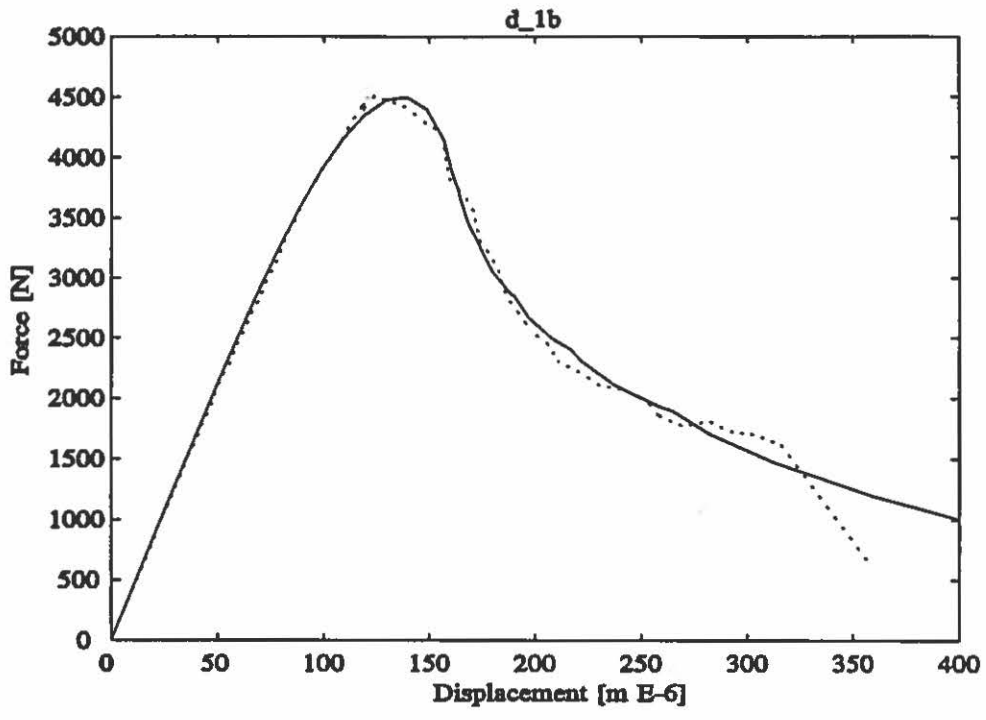
Figure A2.13: Fitted results for beam D-1.
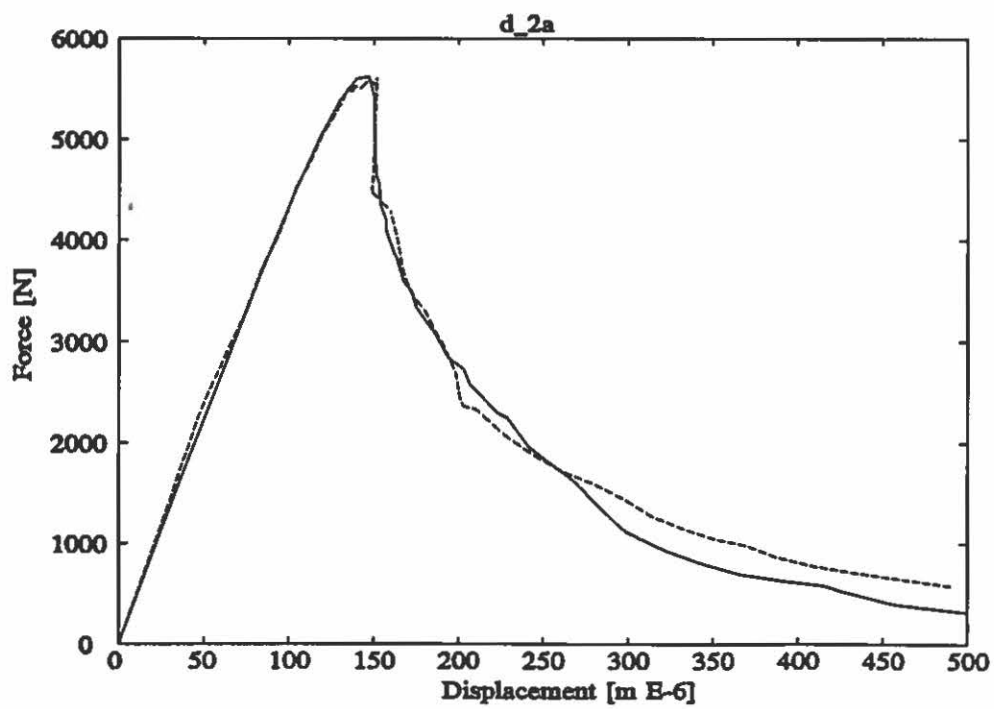
Figure A2.14: Fitted results for beam D-2.
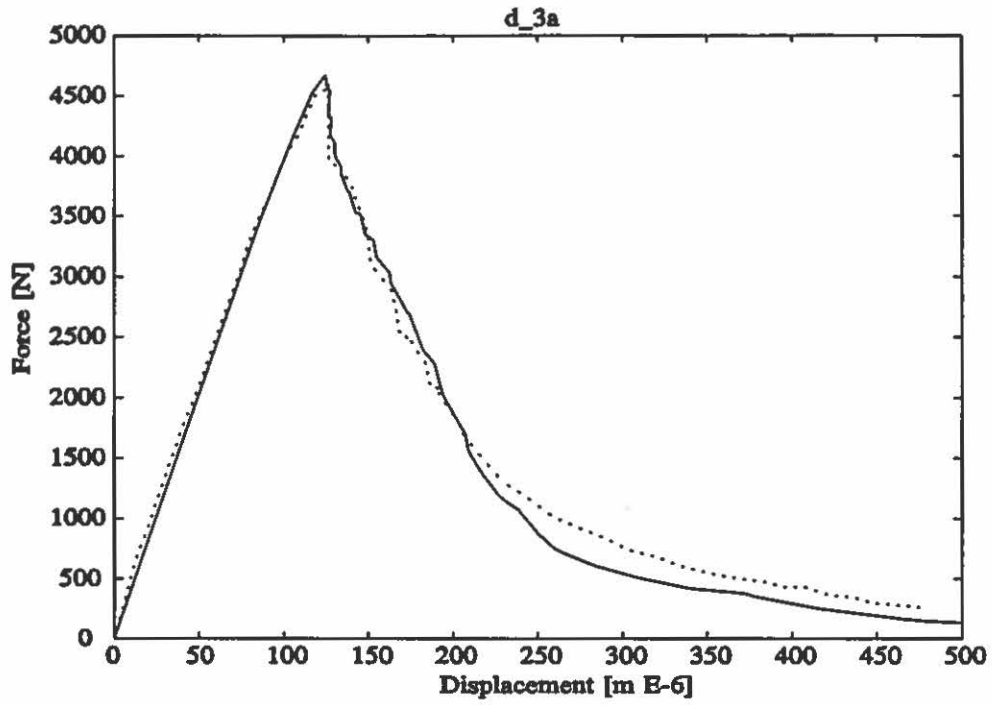
Figure A2.15: Fitted results for beam D-3.
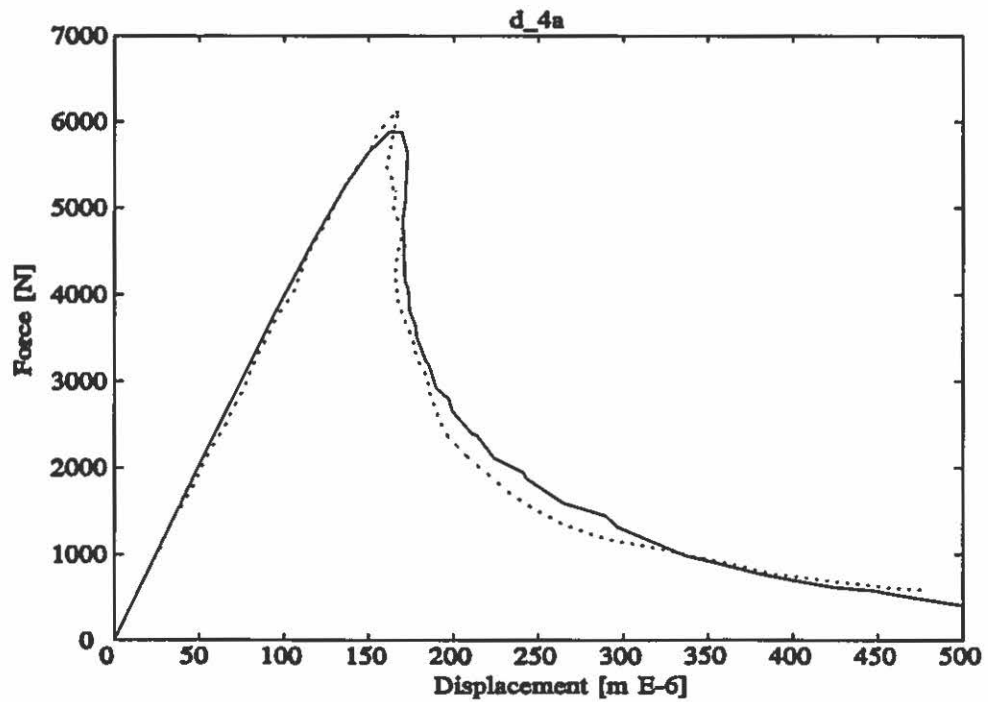
Figure A2.16: Fitted results for beam D-4.

143
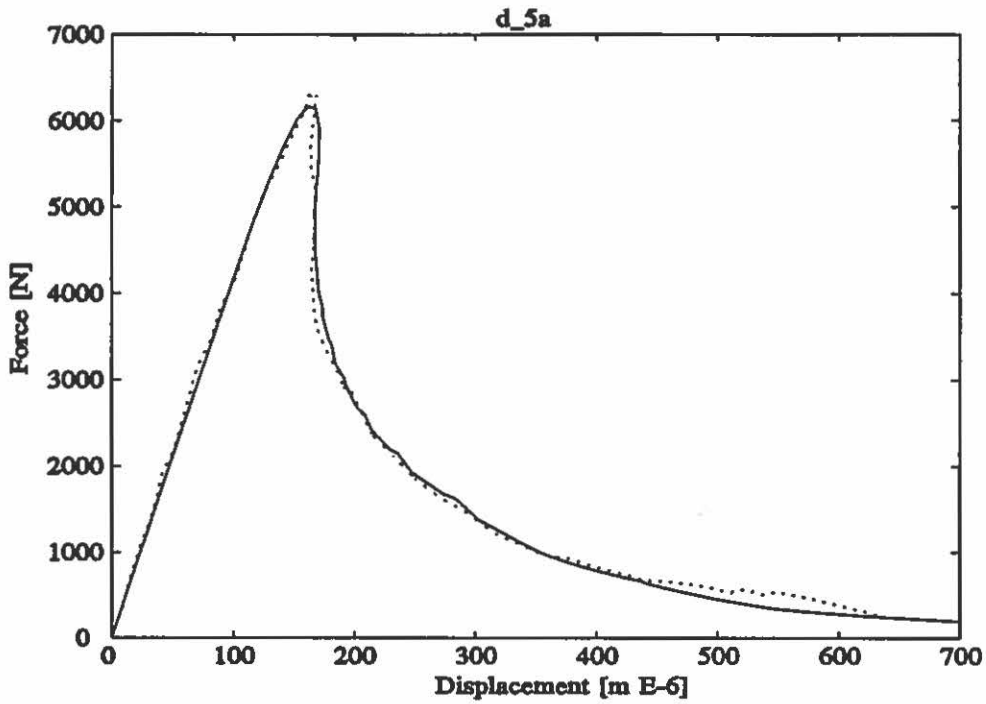
Figure A2.17: Fitted results for beam D-5.
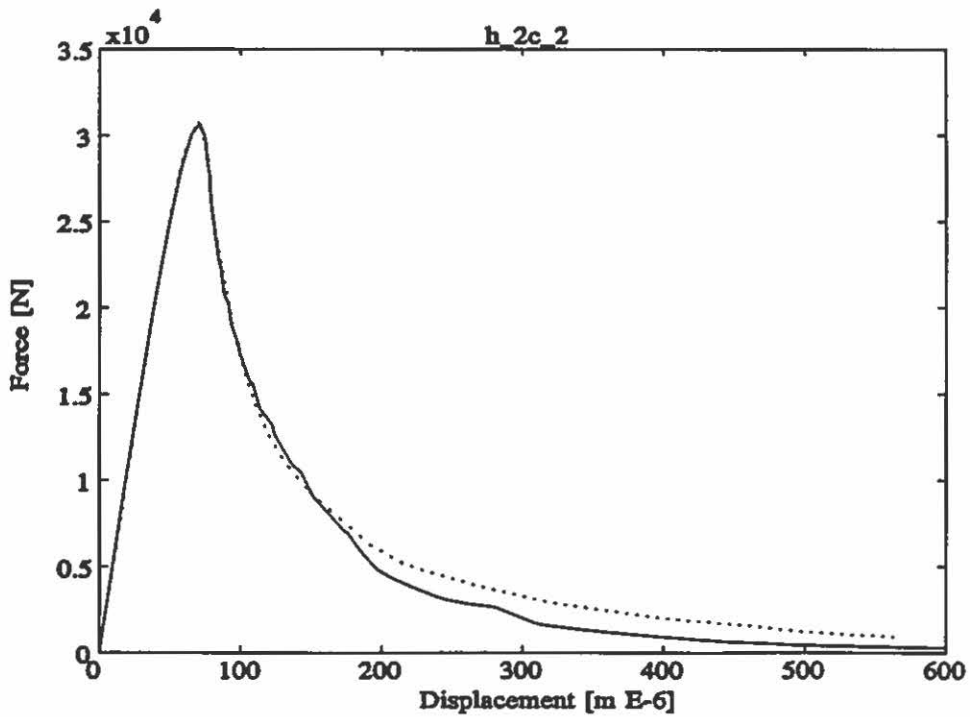

Figure A2.18: Fitted results for beam E-1.

Figure A2.19: Fitted results for beam E-2.

Figure A2.20: Fitted results for beam E-3.

Figure A2.21: Fitted results for beam E-4.

Figure A2.22: Fitted results for beam E-5.

146

Figure A2.23: Fitted results for beam F-1.

Figure A2.24: Fitted results for beam F-2b.

Figure A2.25: Fitted results for beam F-3b.

Figure A2.26: Fitted results for beam F-4b.

148

Figure A2.27: Fitted results for beam G-3a.

Figure A2.28: Fitted results for beam G4-a.

Figure A2.29: Fitted results for beam G-5a.
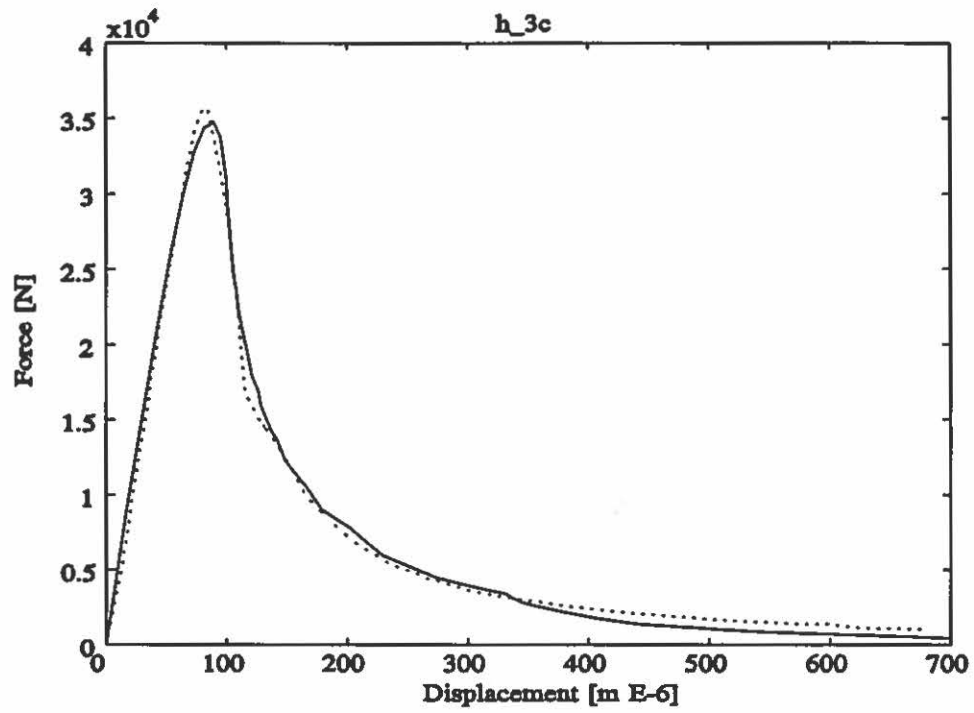

Figure A2.30: Fitted results for beam H-2c.

Figure A2.31: Fitted results for beam H-3c.

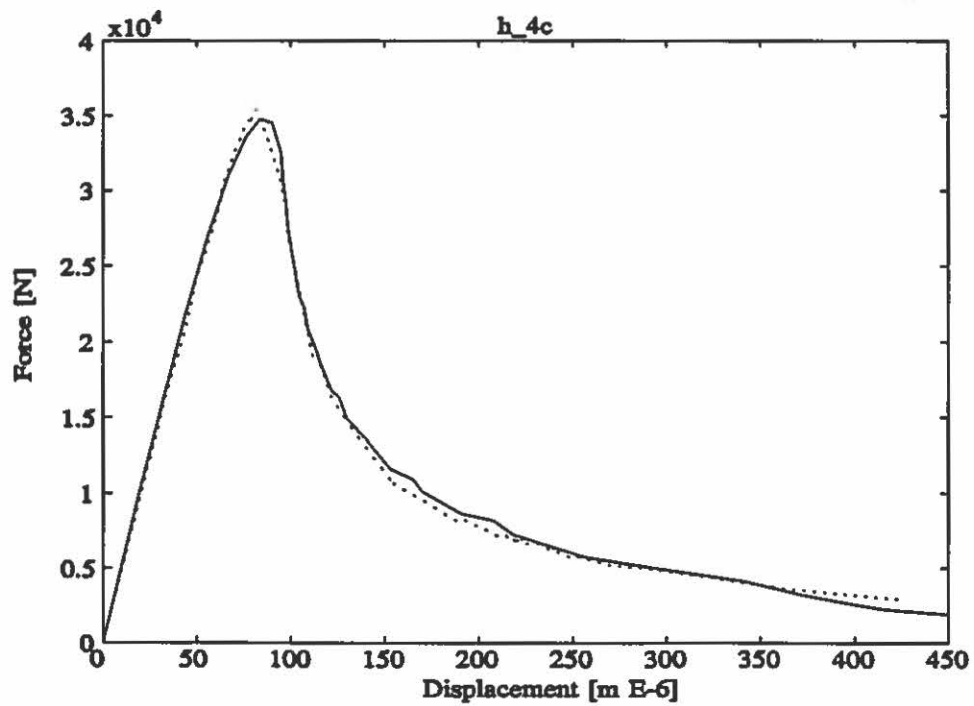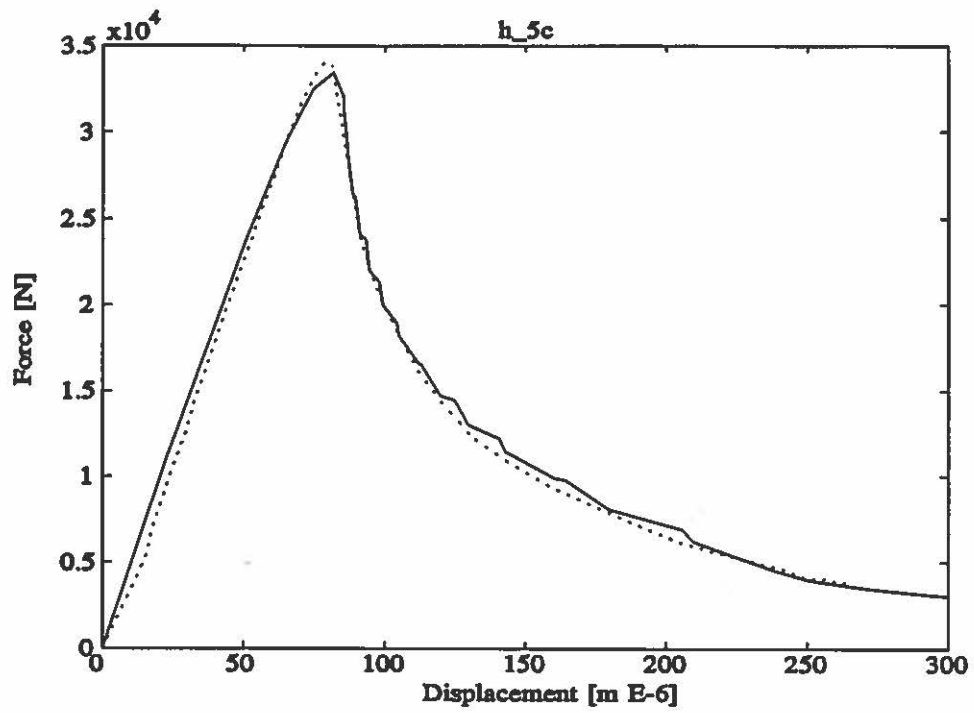Figure A3.1: Fitted results for beam H-4c.

Figure A3.2: Fitted results for beam H-5c.

APPENDIX A5
CRACKING PROFILES.

On the following pages the measured cracking profiles described in chapter 5 are shown. The specimens S1-S4 are the standard specimens, and specimens K1-K4 are the saw cut specimens. The profiles are meassured for both fracture surfaces, and are almost identical.

The dashed line indicates the position of the notch, and the solid line shows the dye edge, which is assumed to be near the real crack tip.
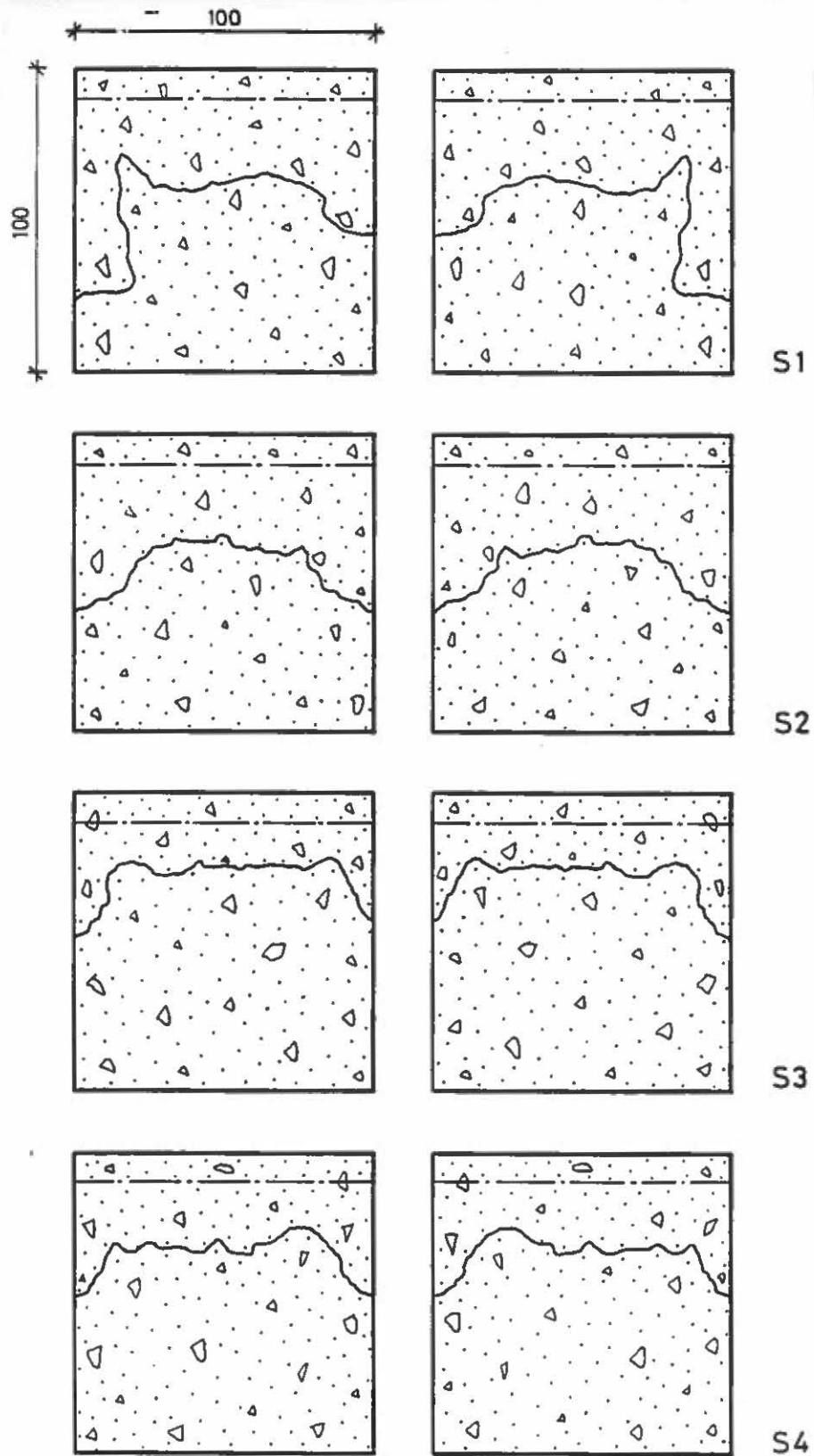
Figure A5.1: Dyeing profiles for the standard specimen type D.
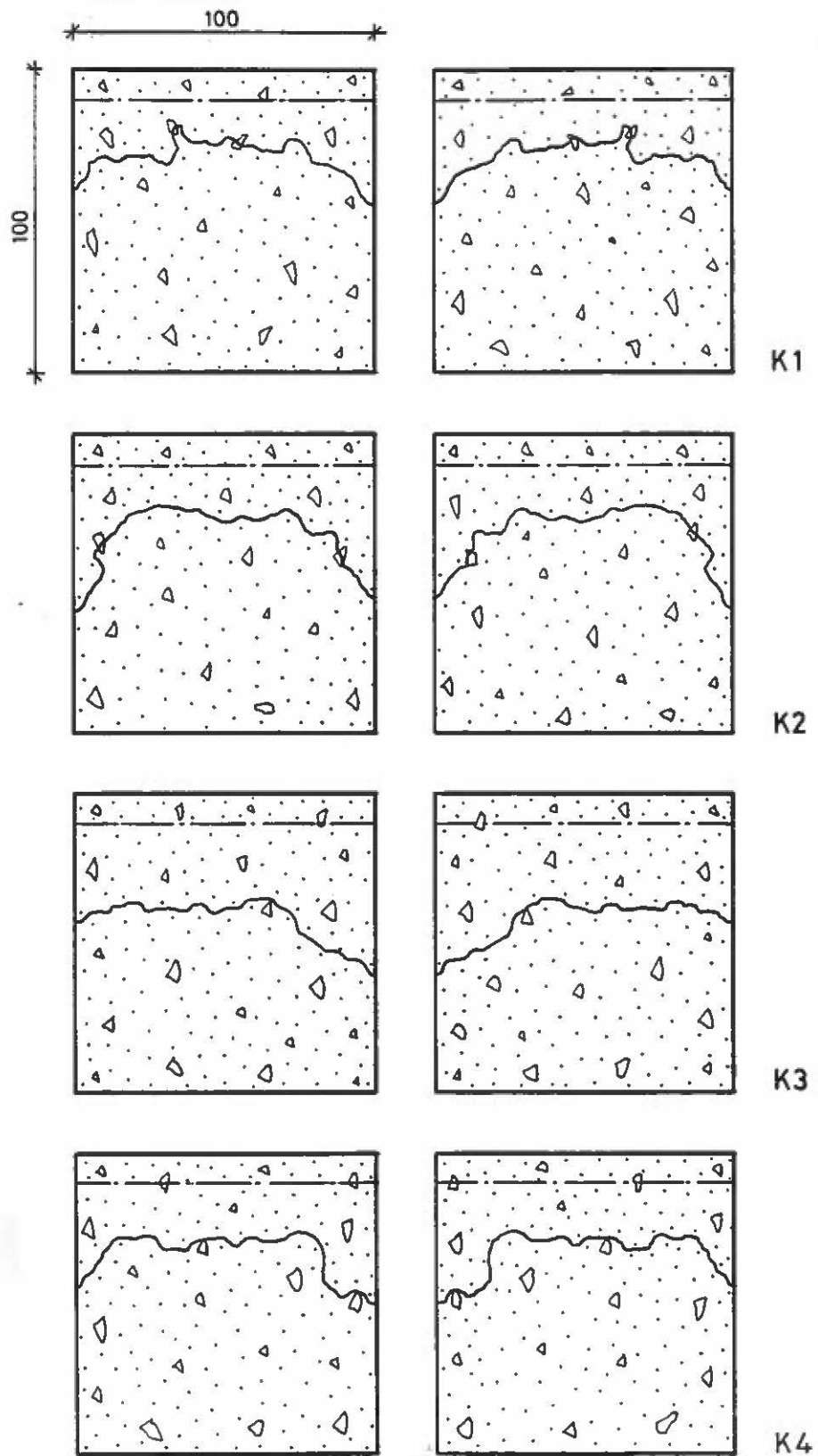
Figure A5.2: Dyeing profiles for the saw cut specimen, of size D.

APPENDIX A6
RESUMÉ IN DANISH.

Titlen på afhandlingen er

Brudmekanik for beton

Som titlen beskriver omhandler projektet brudmekanik for beton. Projektet er en del af et større forskningsprogram under Statens Teknisk Naturvidenskabelige Forskningsråd med titlen:

"Højkvalitetsbetoner i 90'erne"

Brudmekanik er en forholdsvis ny disciplin og de udviklede teorier har fortrinsvis været rettet mod stål hvor en lineær teori ofte giver gode resultater. For beton har lineær brudmekanik generelt vist sig at give dårlige resultater og i stedet er der udviklet en række nye modeller. Den mest kendte af disse er den fiktive revnes model udviklet af Arne Hillerborg. Denne model har gjort fagområdet bredt tilgængeligt og indenfor de seneste år har stadig flere fundet interesse for fagområdet, der er inde i en rivende udvikling. Brudmekanik er en mere nøjagtig metode at beskrive konstruktioner på end de mere almindelige anvendte teknikker (elasticitet teori og plasticitetsteori), og kan derfor beskrive visse fænomener som de førnævnte teorier ikke kan forklare. I Danmark er der dog stadig kun få, der har beskæftiget sig indgående med emnet (H.H. Bache, H. Stang og N.A. Harder). Det var på denne baggrund projektet blev startet.

I denne afhandling er der især fokuseret på fænomenet 'størrelseseffekter', hvor betegnelsen størrelseseffekter er opfattet bredt (størrelseseffekter på vilkårlige materiale parametre).

I kapitel 2 af afhandlingen gives en grundig beskrivelse af brudprocessen i beton og højstyrkebeton gående fra mikro- til makroniveau. Derefter følger en beskrivelse af de mest anvendte brudmodeller for beton. Kapitlet afsluttes med forskellige eksempler, der ved hjælp af lineær elastisk brudmekanik illustrerer begrebet størrelseseffekter.

Efter beskrivelsen af disse modeller er der valgt at fokusere på den fiktive revnes model. Der er desuden foretaget den afgrænsning, at der udelukkende betragtes bjælker udsat for tre punkts bøjning.

I kapitel 3 beskrives det hvorledes den fiktive revnes model kan anvendes i tilknytning til numeriske metoder. De to mest kendte metoder udviklet af P.E. Petersson og A. Carpinteri præsenteres. En ny metode baseret på randelementmetoden præsenteres. Der er i forbindelse med projektet lagt et stort arbejde i at udvikle og implementere denne metode.

Da numeriske modeller ikke altid er særlig hensigtsmæssige er der udviklet en analytisk metode hvor den fiktive revnes model er anvendt således at den fuldstændige arbejdskurve kan beregnes. Modellen beskrives i detaljer og sammenlignes med to modeller, der er udviklet af Y.W. Mai, baseret på revnebåndsmodellen, samt en metode af J. Llorca, der er baseret på den fiktive revnes model. Modellen er endvidere udvidet til at gælde for armeret beton.

I forbindelse med projektet er der udført forsøg med omkring 50 bjælker af uarmeret og svagt armeret beton i en nyudviklet servostyret revneåbningkontrolleret forsøgsopstilling. Der er genemført forsøg til belysning af størrelseseffekter og forsøg med henblik på at bestemme revne profiler i udsavede prøveemner. Der er endvidere forsøgt at bestemme materialeparametre i den fiktive revnes model ved at tilpasse arbejdskurver bestemt ved den numeriske metode med arbejdskurver målt ved forsøg. Dette er gjort ved anvendelse af et generelt ikke-lineært optimerings program. Forsøg og forsøgsresultater er beskrevet i kapitel 5.

Rapporten afsluttes med en konklusion der opsummerer de opnåede resultater, samt giver forslag til den videre forskning indenfor området.